이학박사 학위논문

Near-Infrared Study of Galactic Supernova Remnants

우리 은하 초신성 잔해에 대한 근적외선 연구

2017년 8월

서울대학교 대학원
물리·천문학부 천문학전공
이 용 현

Near-Infrared Study of Galactic Supernova Remnants

우리 은하 초신성 잔해에 대한 근적외선 연구

지도교수 구 본 철

이 논문을 이학박사 학위논문으로 제출함
2017년 4월

서울대학교 대학원
물리·천문학부 천문학전공
이 용 현

이용현의 이학박사 학위논문을 인준함
2017년 6월

위 원 장	(인)
부 위 원 장	(인)
위 원	(인)
위 원	(인)
위 원	(인)

Near-Infrared Study of Galactic Supernova Remnants

by

Yong-Hyun Lee

A dissertation submitted in partial fulfillment of the
requirements for the degree of
Doctor of Philosophy
in
Astronomy

in

Astronomy Program
Department of Physics and Astronomy
Seoul National University

Committee:

Professor	Myung Gyoon Lee
Professor	Bon-Chul Koo
Professor	Myungshin Im
Professor	Woong-Tae Kim
Doctor	Ho-Gyu Lee

Abstract

The Galactic supernova remnants (SNRs) play a crucial role in the evolution of our Galaxy, since it is responsible for interstellar turbulance, large galactic structures, and various types of heavy elements. I present near-infrared (NIR) imaging and spectroscopic studies for the Galactic SNRs in this thesis which is composed of four individual parts. The first two parts are concerned with [Fe II] 1.64 μm and H_2 2.12 μm emission line studies for the "evolved" SNRs interacting with their surrounding medium, and the last two parts deal with NIR spectroscopic studies for one of the youngest Galactic SNR (Cassiopeia A) where the imprints of SN explosion remain.

In the first part, I report the detection of [Fe II] 1.64 μm and H_2 2.12 μm line features around the Galactic SNRs using UWIFE and UWISH2 surveys that cover the first galactic quadrant of $7^\circ < l < 62^\circ$ and $|b| < 1.3^\circ$. Among the 79 Galactic SNRs fully covered by both surveys, I detect a total of 19 [Fe II]-emitting and 19 H_2-emitting SNRs which is corresponding to the overall detection rate of $\sim$ 24%. Eleven SNRs show both emission features. The detection rate of [Fe II] is highest at the Galactic longitude of 40°–50°, whereas that of H_2 peaks at l = 30°–40°. The different peaks may be due to different SN populations along the Galactic longtitude. The total [Fe II] flux we estimated is at least a few times fainter than the expected [Fe II] flux from the SN rate of our Galaxy, implying either that there are many SNRs whose [Fe II] lines are undetected in the survey, or that there are many missing SNRs that have not been known so far. Five out of the 11 SNRs emitting both emission lines clearly show "[Fe II]-H_2 reversal;" the H_2 emission lines are detected far beyond the [Fe II]/radio boundary. From NIR spectra for the extended H_2 emission lines, I find that the H_2 lines may arise from collisionally excited H_2 gas, but their exciting sources remain to be explored.

In the second part, I report the results of high resolution NIR spectroscopy of the five Galactic SNRs (G11.2−0.3, KES 73, W44, 3C 396, W49B), showing the extended H_2 filaments far beyond the strong NIR [Fe II] lines and radio continuum in the border of the remnants. H_2 1–0 S(1) 2.12 μm and 1–0 S(0) 2.22 μm lines are clearly detected in all slits. Their radial velocities are well consistent with the systematic velocity of

the remnants, and these imply that they are indeed physically associated with the remnants. They also show the broad line width ($\gtrsim$ 10 km s^{-1}) as well as the flux ratios analogous to thermal excitation, which imply that the extended H_2 filaments are collisionally excited by shock. I suggest three possibilities of the origin of the shock: (1) magnetic precursor ahead of the supernova (SN) shock, (2) projection effect of the SN shock, and (3) slow non-dissociative C-shock produced by pre-SN wind. I discuss about the origin of the extended H_2 emission features detected around each SNR.

In the third part, I report the results of broadband (0.95–2.46 μm) NIR spectroscopic observations of the Cassiopeia A SNR. Using a clump-finding algorithm in two-dimensional dispersed images, I identify 63 'knots' from eight slit positions and derive their spectroscopic properties. All of the knots emit [Fe II] lines together with other ionic forbidden lines of heavy elements, and some of them also emit H and He lines. I identify 46 emission line features in total from the 63 knots and measure their fluxes and radial velocities. The results of our analyses of the emission line features based on principal component analysis show that the knots can be classified into three groups: (1) He-rich, (2) S-rich, and (3) Fe-rich knots. The He-rich knots have relatively small, $\lesssim$ 200 km s^{-1}, line-of-sight speeds and radiate strong He I and [Fe II] lines resembling closely optical quasi-stationary flocculi of circumstellar medium, while the S-rich knots show strong lines from O-burning material with large radial velocities up to $\sim$ 2000 km s^{-1} indicating that they are SN ejecta material known as fast-moving knots. The Fe-rich knots also have large radial velocities but show no lines from O-burning material. I discuss the origin of the Fe-rich knots and conclude that they are most likely "pure" Fe ejecta synthesized in the innermost region during the SN explosion. The comparison of [Fe II] images with other waveband images shows that these dense Fe ejecta are mainly distributed along the southwestern shell just outside the unshocked ^{44}Ti in the interior, supporting the presence of unshocked Fe associated with ^{44}Ti.

In the last part, I present the results of extinction measurements toward the main ejecta shell of the Cassiopeia A SNR using the flux ratios between the two NIR [Fe II] lines at 1.26 and 1.64 μm. I find a clear correlation between the NIR extinction

($E(J-H)$) and the radial velocity of ejecta knots, showing that redshifted knots are systematically more obscured than blueshifted ones. This internal "self-extinction" strongly indicates that a large amount of SN dust resides inside and around the main ejecta shell. At one location in the southern part of the shell, I measure $E(J-H)$ by the SN dust of 0.23 ± 0.05 mag. By analyzing the spectral energy distribution of thermal dust emission at that location, I show that there are warm ($\sim$ 100 K) and cool ($\sim$ 40 K) SN dust components and that the latter is responsible for the observed $E(J-H)$. I investigate the possible grain species and size of each component and find that the warm SN dust needs to be silicate grains such as $MgSiO_3$, Mg_2SiO_4, and SiO_2, whereas the cool dust could be either small ($\lesssim 0.01$ μm) Fe or large ($\gtrsim 0.1$ μm) Si grains. I suggest that the warm and cool dust components in Cassiopeia A represent grain species produced in diffuse SN ejecta and in dense ejecta clumps, respectively.

Keywords: dust, extinction — infrared: ISM — ISM: individual objects (Cassiopeia A, G11.2−0.3, KES 73, W44, W49B, 3C 396) — ISM: molecules — ISM: supernova remnants — line: identification — surveys

Student Number: 2011-30129

Contents

List of Tables

List of Figures

Chapter 1

Introduction

1.1 Supernovae and Supernova Remnants

Supernovae (SNe) are one of the most violent events in the Universe, and had been revealed as gigantic explosions marking the catastrophic ends of evolved stars. Based on the progenitor types, the SNe can be classified into two major groups: core-collapse and themonuclear SNe. The core-collapse SNe result from the gravitational collapse of innermost Fe core of the massive stars ($\gtrsim 8\ M_{\odot}$) at the end of their evolutions. The collapsed Fe core with a small amount of fall-back materials produces a compact central source (a single neutron star or black hole), and the bounce of the infalling materials on the surface of the compact source produces the initial SN shock which propagates outward. The bounce shock with a shock revival process heats and accelerates the infalling materials which result in high speed, metal-enriched SN ejecta. In observation, the core-collapse SNe can be divided into sub-groups (e.g., Type II-P/L, Type I-b/c) depending on their spectral characteristics and light curves which are strongly affected by the inital masse of the progenitor. The thermonuclear SNe (also called Type Ia SNe), on the other hand, seem to occur when a white dwarf exceed the Chandrasekhar mass limit ($\sim 1.4\ M_{\odot}$) (1) by mass accretion from a non-degenerate companion (e.g., main-sequence, red-giant; single degenerate senario) or (2) by merging of two white dwarfs in a binary system (double degenerate senario). And then, the carbon/oxygen core of the white dwarf might be ignited, which leads to a thermonuclear deflagration/detonation

process. Since all the Type Ia SNe occur in a white dwarf with a final mass of $\sim$ 1.4 $M_{\odot}$, their total luminosity, spectral characteristics, and light curves seem to be almost the same. These properties make them extremely useful as a distance indicator. The detailed process of the SN explosion is highly uncertain, and not well studied in observations. But the general concensus of multi-dimensional numerical simulations is that the explosion should be asymmeric and turbulent especially near the progenitor core.

The supernova remnant (SNR) is all materials governed by the SN shock, and is composed of the SN ejecta expelled by the SN blast wave and the swept-up circumstellar/interstellar medium (CSM/ISM). The SNRs play a crucial role in the evolution of galaxies in several aspects. First, a huge amount of kinematic energy of the SN shock might be the major source of interstellar turbulence, and sometime it is responsible for the large interstellar structure like "bubble" or "chimney" in galaxies. Furthermore, the shock wave propagating into ISM heats the interstellar gas, dissociate the molecules, and destroy the dust, so it changes the physical condition of the ISM. Finally, a large amount of heavy elements synthesized in the massive progenitor is spread out via the SN ejecta, and it enriches the ISM with a various types of heavy elements. Therefore, studying SNRs is very important to understand the evolution of galaxies as well as the origin of life on Earth.

1.2 Galactic Supernova Remnants

Around 300 Galactic SNRs have been identified up to this time (Green, 2014), and have been studied in multi-wavebands. Two of the most interesting topics conserning the Galactic SNRs are their origins (where they come from) and evolutions (how to evolve after the explosion).

The origin (progenitor type or SN type) is a very important factor for studying the SNRs, because the releasing evergy, mass of ejecta/dust, and surrounding environments highly depends on their progenitor types. For very young SNRs like Cassiopeia A and Tycho SNRs, the SN type can be directly derived from (1) their SN spectra obtained

from the observations of their light echos and (2) their light curves written in historical records. For evolved SNRs, however, we cannot use such direct estimations. Instead, there are several indirect ways to do this by using (1) multi-component spectral fitting of X-ray spectrum, (2) kinematic/chemical properties of optical/infrared nebulosity, (3) existance of compact source or companion, and so on. Since the evolved SNRs are relatively faint compared to the young SNRs, most of their origins have not yet been determined so far, and the various multi-wavebands observations and studies are required.

The evolution of SNRs is concerned with the physical and chemical processes after the SN explosions. Several issues for evolusion of SNRs have been discussed: (1) explosion mechanism, (2) SN ejecta and dust, (3) interaction of SNR with surrounding molecular clouds. All these issues, however, are still not well-known so far.

1.3 Supernova Remnants in Near-Infrared Waveband

The Galactic SNRs have been widely studied in radio and X-ray wavebands during the last several decades by using various radio telescopes and arrays (e.g., Very Large Array, Green Bank, Effelsburg), and space-based X-ray observatories (e.g., Chandra, ROSAT, XMM-Newton). In near-infrared (NIR) wavebands, however, a limited number of observations and studies have been reported, because of low sensitivity and resolution of early NIR detectors and instruments. Since 1980's, (1) several dedicated NIR telescopes were constructed (e.g., UKIRT, IRTF, VISTA), (2) the sensitivity and resolution of NIR detector were dramatically improved (developments of Focal Plane Array with HgCdTe and InSb material), and (3) various types of NIR instruments were developed. Therefore, the NIR observations with high quality are available in these days.

1.3.1 Advantage of Near-Infrared

Near-infrared (NIR) waveband which ranges from 1 μm up to 5 μm has unique advantages compared to other wavebands.[1] First, there are various types of emission lines falling in the waveband: (1) forbidden lines from various mettallic atoms (e.g., [Fe II], [P II], [S II]), (2) H/He revombination lines, (3) molecular lines (e.g., H_2, CO). And their line ratios can be used as astrophysical diagnostics (e.g., extinction, electron density/temperature, abundance). Second, since the interstellar extinction in NIR is smaller than that in visible waveband, NIR is a more useful tool for investigating the Galactic SNRs which experience heavy interstellar obscuration. Finally, NIR can be observable in ground-based telescopes so that we can access various types of NIR instruments with high spatial resolution. Therefore, NIR observations are useful to see the detailed structure of the Galactic SNRs, and to understand their evolutions.

1.3.2 Previous Near-Infrared Studies

The previous NIR studies were limited to only a small number of bright SNRs, but found very interesting characterisics of the SNRs.

For evolved SNRs, two bright emission lines, [Fe II] and H_2, were detected in surrounding circumstellar/interstellar medium, and various excitation mechanisms have been suggested. In shock-dominated regions like SNRs, it is most likey that [Fe II] and H_2 lines arise from the SN shock. The fast ($v_s > 50$ km s^{-1}), atomic J-shock make extensive partially ionized zone where the Fe^+ and e^- coexist, and the [Fe II] lines could arise from this post-shock cooling region behind the shock front (Mouri et al., 2000). There is a possibility that the [Fe II] line arises from upstream/preshock gas, when the strong X-ray emission from the shock can make another partially ionized zone ahead of the shock front (e.g., Draine, 2011). If there are non-thermal X-ray sources (like pulsar wind nebula) around the remnants, we may also expect [Fe II] lines (Graham et al., 1990). Since the NIR [Fe II] (> 0.8 μm) lines have relatively high

[1] The definition and range of NIR is somewhat controversal. Historically, NIR stars around 0.75 μm where the average human eyes loses all sensitivity. Technologically speaking, however, it starts at 1 μm where optical charged coupled devices (CCDs) cease to be useful but NIR detectors (e.g., HgCdTe, InSb) start to be sensitive. The "end point" of NIR is generally accepted to be 5 μm.

collisional strengths compared to optical [Fe II], most of detected [Fe II] lines in NIR result from collisional process, not from the UV pumping (Mouri et al., 2000). If the shock is fast (like atomic J-shock; > 50 km s^{-1}), on the other hand, H_2 molecules will be distroyed. Therefore, the H_2 lines are expected to arise from slow (< 50 km s^{-1}), non-dissociative C-shock. We cannot rule out a possibility that they are from the far downstream of fast J-shock where the H_2 molecules are significantly reformed (Hollenbach & McKee, 1989; Neufeld & Dalgarno, 1989), or from magnetic precursors ahead of the J-shock front where the H_2 molecules can be collisionally excited (e.g., Draine, 2011). Sometimes, the fluorecsence of the H_2 by UV-pumping is possible if there are strong UV/X-ray sources (like pulsar wind nebula) around SNRs.

The young SNRs like Cassiopeia A (Cas A), give us an unique opportinity to study the detailed explosion mechanism and the production of ejecta/dust, since their SN ejecta are not yet significantly mixed with their surrounding medium. The previous NIR spectroscopic studies for Cas A show that the SN ejecta are dominated by forbidden lines from oxygen-burning meterials, whereas the dense circumstellar medium show bright He I 1.083 μm with H I emission lines (Gerardy & Fesen, 2001; Lee et al., 2017) The different line ratios of the metalic emission lines in the SN ejecta seem to reflect their different abundances (Koo et al., 2013).

1.4 Purpose of Thesis

The main purpose of this thesis is to investigate the origin and evolution of Galactic SNRs by using characteristics of NIR emission lines, and I use various NIR imaging and spectroscopic data. This thesis consists of four individual parts. The first two parts are concerned with the evolved SNRs emitting strong [Fe II]-1.64 μm and H_2-2.12 μm emission lines, and the next two parts deal with one of the youngest SNR, Cassiopeia A, showing the bright forbidden lines from metalic elements.

In Chapter 2, I will introduce the UWIFE and UWISH2 surveys that are [Fe II]-1.64 μm and H_2-2.12 μm narrow-band imaging surveys covering the first galactic quadrant of $7^\circ < l < 62^\circ$ and $|b| < 1.3^\circ$. Using their detectrion rates, I discuss about the SN

populations along the Galactic longitude and effects of interstellar extinction through the Galactic plane. And then, the origin and excitation mechanism of the emission lines are discussed from their morphologies and spectroscopic properties. In Chapter 3, "[Fe II]-H_2 reversal" in several bright SNRs detected in the UWIFE and UWISH2 surveys will be dicussed in more detail. In order to reveal the origin of H_2 filaments extended beyond radio and [Fe II] boundary, I derive the H_2 line ratios and their line widths using IGRINS, a NIR spectrograph with high spectral resolution (R 40,000). In Chapter 4, I will show the NIR spectral characteristics of knots detected in the young SNR, Cassiopeia A. Using principal component analysis, I classify the knots into three major groups and discuss about their origins. In Chapter 5, the properties of the SN dust in Cassiopeia A will be discussed. Using the flux ratio of [Fe II] at 1.26 μm and 1.64 μm, I find the "self-extinction" due to the internal SN dust, and derive the possible dust properties that can explain both the NIR self-extinction and the mid-/far-infrared dust continuum.

Biblography

Draine, B. T. 2011, Physics of the Interstellar and Intergalactic Medium by Bruce T. Draine. Princeton University Press, 2011. ISBN: 978-0-691-12214-4,

Gerardy, C. L., & Fesen, R. A. 2001, AJ, 121, 2781

Graham, J. R., Wright, G. S., & Longmore, A. J. 1990, ApJ, 352, 172

Green, D. A. 2014, Bulletin of the Astronomical Society of India, 42, 47

Hollenbach, D., & McKee, C. F. 1989, ApJ, 342, 306

Koo, B.-C., Lee, Y.-H., Moon, D.-S., Yoon, S.-C., & Raymond, J. C. 2013, Science, 342, 1346

Lee, Y.-H., Koo, B.-C., Moon, D.-S., Burton, M. G., & Lee, J.-J. 2017, ApJ, 837, 118

Mouri, H., Kawara, K., & Taniguchi, Y. 2000, ApJ, 528, 186

Neufeld, D. A., & Dalgarno, A. 1989, ApJ, 340, 869

Chapter 2

Supernova Remnants in UWIFE and UWISH2 Surveys

2.1 Introduction

Supernovae (SNe) are one of the most powerful events in the Universe as the catastrophic ends of evolved stars, and play a crucial role in the evolution of galaxies in several aspects. A huge amount of kinematic energy of the SN shock might be the major source of interstellar turbulence, and is responsible for the large interstellar structures like "bubble" or "chimney" in galaxies. Furthermore, the shock wave propagating into interstellar medium (ISM) heats the interstellar gas, dissociate the molecules, and destroy the dust, so it changes the physical condition of the ISM. Finally, a large amount of heavy elements synthesized in the massive progenitor is spread out via the SN ejecta, and it enriches the ISM with various types of heavy elements. Therefore, studying the Galactic SNRs is very important to understand the evolution of our Galaxy.

The atomic and molecular gas swept up by SN shock can radiate various types of emission lines from radio to γ-ray wavebands. Previous near-infrared (NIR; 1 μm–5 μm) studies have reported the detection of two strong emission lines around the Galactic SNRs: (1) forbidden lines of single ionized Fe ([Fe II]) and (2) molecular hydrogen (H_2), and found that they mainly arises from the swept-up circumstellar/interstellar gas (e.g., Graham et al. 1987 for IC 443, Oliva et al. 1990, Burton & Spyromilio 1993

for RCW 103, Koo et al. 2007 for G11.2−0.3, Keohane et al. 2007 for W49B, Lee et al. 2009 for 3C 396). Cassiopeia A SNR, the second youngest $\sim$ 340 years old Galactic SNR, is exceptional, because most of NIR emission arises from the SN ejecta. Their NIR spectra are dominated by a dozen forbidden lines from various metallic atoms (e.g., [Si VI], [P II], [S II], [Fe II]; Gerardy & Fesen, 2001; Lee et al., 2017), and may reflect the chemical abundance of the nucelar burning materials (Koo et al., 2013). The NIR [Fe II] ($\gtrsim$ 0.8 μm) lines are believed to be predominantly populated by electron collision and arise from partially ionized region where the Fe^+ and e^- are coexist (Mouri et al., 2000). The partially ionized region can be extended either by shock heating or by power-law photoionization (Mouri et al., 2000). Therefore, the strong [Fe II] lines detected around SNRs could arise from the post-shock cooling region just behind of fast ($v_s > 50$ km s^{-1}), atomic J-shock. If there is a strong non-thermal continuum source like a pulsar wind nebula, we may also expect collisionally excited [Fe II] lines from dense medium photo-ionized by the non-thermal continuum (Graham et al., 1990). The ground state of H_2 also can be excited by SN shocks via collisional process, and then radiates strong rotational-vibrational H_2 lines in near- and mid-infrared wavebands. However, the fast ($v_s > 50$ km s^{-1}) J-shock can efficiently dissociate H_2. The H_2 emission lines, therefore, are expected to arise from either (1) the post-shock cooling region of slow ($v_s < 50$ km s^{-1}), non-dissociative C-shocks (Draine, 1980; Chernoff et al., 1982; Draine & Roberge, 1982), or (2) the far downstream ($n_H \sim 10^{18-21}$ cm^{-2}) of dissociative J-shocks where the H_2 can be reformed (Hollenbach & McKee, 1989; Neufeld & Dalgarno, 1989). Another important excitation mechanism of H_2 is absorption of far-ultraviolet (FUV; 11.2 eV – 13.6 eV) photons. The radiative cascade of the excited H_2 downward to the ground state also produces strong H_2 lines (e.g., Black & Dalgarno, 1976; Black & van Dishoeck, 1987). Since the shocked hot plasma and pulsar wind nebulae are strong UV and X-ray emitters, we may also expect strong H_2 lines by UV fluorescence around the remnant. The two strong NIR emission lines detected around SNRs, therefore, are highly connected to the SN activity as well as their environments. Among around 300 Galactic SNRs (Green, 2014), however, only a limited number of NIR studies for the SNRs have been done so far.

Recently, two NIR [Fe II] 1.64 μm and H_2 2.12 μm narrow-band imaging surveys called UWIFE and UWISH2 (UKIRT Widefield Infrared Survey for Fe^+ and H_2) had been done for the first galactic quadrant of our Galaxy (Froebrich et al., 2011; Lee et al., 2014). These systematic and unbiased NIR emission surveys together with follow-up NIR spectroscopic observations will give us unique opportunity to understand the origin and environments of the SNRs. This paper is organized as follows. In Section 2.2, we outline the two NIR imaging and spectroscopic observations and their data reduction/analysis. The statistical results of the imaging surveys as well as the spectroscopic results for four Galactic SNRs are presented in Section 2.3. We discuss about the origin and environment of the SNRs in Section 2.4, and the summary of this paper is listed in Section 2.5.

2.2 Observations and Data Analysis

2.2.1 Near-Infrared Narrow-band Imaging Surveys

Brief descripsion of surveys

The [Fe II] and H_2 narrow-band imaging surveys that constitute UWIFE and UWISH2 were carried out with the Wide-Field Camera (WFCAM) at the United Kingdom Infrared Telescope (UKIRT; Froebrich et al., 2011; Lee et al., 2014). The WFCAM consists of four separated Rockwell Hawaii-II 2048 $\times$ 2048 detectors with a pixel scale of $0\farcs4$ and each detector places at a spacing with 90% of the detector size. The basic observing unit of a single WFCAM tile is composed of 2×2 macro-stepping sequence in order to fill the spacing, so the tile covers a continuous field of view of $0\farcm8 \times 0\farcm8$. Additional 2×2 micro-stepping sequence with an interlacing technique has been used during the entire surveys in order to prevent under-sampling at a good seeing condition (less than $0\farcs8$) and therefore the final stacked image provide $0\farcs2$ pixel resolution. The single exposure time per-frame is 60 seconds, but the 2×2 micro-stepping and three jittering observations give a total integration time per-pixel ($0\farcs4$) of 720 seconds. The [Fe II] narrow-band filter were used in the UWIFE survey, that has a mean wavelength (λ_0) of 1.645 μm and a bandwidth ($\Delta\lambda$) of 284 Å. Those of the H_2 1-0 S(1) filter used

Table 2.1. Specifications of [Fe II] and H_2 Narrow-band Filters

Filter	BW[a] (Å)	λ_0[b] (μm)	λ_{iso} (μm)	$F_\lambda(\lambda_{iso})$[c] (W m^{-2} μm^{-1})	In-Band[d] (W m^{-2})
[Fe II]	284	1.645	1.666	1.15E-9	3.27E-11
H_2	211	2.122	2.122	4.66E-10	9.84E-12

[a] Equivalent band width defined by BW = $\int R(\lambda)\ d\lambda$ / R_{max}, where R_{max} is the maximum throughput of the filter response function ($R(\lambda)$).

[b] Mean wavelength of the filter defined by $\lambda_0 = \int \lambda R(\lambda) d\lambda / \int R(\lambda) d\lambda$.

[c] Zero-point level for Vega continuum. It is described by $F_\lambda(\lambda_{iso}) = \int \lambda F_\lambda(\lambda) R(\lambda)\ d\lambda$ / $\int \lambda R(\lambda)\ d\lambda$, where $F_\lambda(\lambda)$ are the spectral energy distribution of Vega (Rieke et al., 2008). λ_{iso} denotes the "isophotal wavelength" at which the $F_\lambda(\lambda_{iso})$ equals the flux density of Vega continuum (See Tokunaga & Vacca (2005) and Rieke et al. (2008) for more information).

[d] Total in-band flux of Vega spectrum falling in the passband. It was derived from the $F_\lambda(\lambda_{iso})$ multiplied by the band width.

in the UWISH2 survey are $\lambda_0 = 2.122$ μm and $\Delta\lambda$ =211 Å. The detailed descriptions for the both filters are listed in Table 2.1. The both surveys fully cover the first Galactic quadrant of $7° < l < 62°$ and $|b| < 1.^\circ3$. (Note that the UWISH2 together with the extended UWISH2 survey (UWISH2-E; Froebrich et al., 2015) were mapped for the larger areas, but we do not take those into account because no further [Fe II] survey has been done so far.) The median seeing of the UWIFE and the UWISH2 is $0.''8$ and $0.''7$, respectively, and the surface brightness limit of the both surveys goes down to 10^{-19} W m^{-2}arcsec^{-2}. The detailed information is described in Lee et al. (2014) for the UWIFE survey and Froebrich et al. (2011) for the UWISH2 survey.

Data Reduction and Continuum Subtraction

All WFCAM data are pre-processed by the Cambridge Astronomical Survey Unit (CASU) and are distributed through a dedicated archive hosted by the Wide Field Astronomy Unit (WFAU). During the process, astrometric and photometric calibration have been made with 2MASS catalog. The detailed description of the process is presented in Dye et al. (2006).

To search the extended [Fe II] and H_2 emission features more efficiently, we performed continuum-subtraction for the both narrow-band imaging data using the broad *H*- and *K*-band image obtained as part of the UKIDSS GPS (Lucas et al., 2008). We first smoothed either a narrow- or a broad-band image that observed at a better seeing condition in order to make same width of the point spread function (PSFs). And then we scaled the broad-band image to match their fluxes. In order to suppress the residuals of the bright stars as much as possible, we performed PSF-fitting photometry by using an empirical PSF model image constructed by the well-sampled, bright reference stars. For this, we utilized StarFinder, an IDL-based code for deep analysis of stellar fields (Diolaiti et al., 2000). And then, the bright stars in both narrow- and broad-band images are removed by each flux-scaled PSF image. The final continuum-subtracted [Fe II] and H_2 images are obtained from the image-to-image subtraction of the "bright point source removed" narrow- and broad-band images. The detailed processing step of the continuum-subtraction is described in Section 3.3 of Lee et al. (2014).

Identification and Flux Measurement

Among 294 known galactic SNRs (Green, 2014), 79 SNRs are fully covered by the both survey area and are listed in Table 2.2.

Table 2.2. H_2 and [Fe II] Detection of the Galactic SNRs

G-Name	Other Name	Size[a] (arcmin)	Type[b]	Detection Levels			
				GR[c]	MP[d]	H_2[e]	[Fe 2][f]
G7.2 + 0.2	...	12	S	-	-	...	...
G8.3 − 0.0	...	5 × 4	S	-	-	...	...
G8.7 − 0.1	...	45	S?	-	-	...	Y
G8.9 + 0.4	...	24	S	-	-	...	...
G9.7 − 0.0	...	15 × 11	S	-	-	...	...
G9.8 + 0.6	...	12	S	-	-	...	...
G9.9 − 0.8	...	12	S	-	-	Y	...
G10.5 − 0.0	...	6	S	-	1	...	...
G11.0 − 0.0	...	11 × 9	S	-	3	...	...
G11.1 − 1.0	...	18 × 12	S	-	-	...	...
G11.1 − 0.7	...	11 × 7	S	-	3	...	...
G11.1 + 0.1	...	12 × 10	S	-	1	...	...
G11.2 − 0.3	...	4	C	1	1	Y	Y
G11.4 − 0.1	...	8	S?	3	3	...	...
G11.8 − 0.2	...	4	S	-	2	...	...
G12.0 − 0.1	...	7?	?	3	3	...	...
G12.2 + 0.3	...	6 × 5	S	-	3	...	...
G12.5 + 0.2	...	6 × 5	C?	-	1	...	...
G12.7 − 0.0	...	6	S	-	3	...	...
G12.8 − 0.0	...	3	C?	-	3	...	...
G13.5 + 0.2	...	5 × 4	S	3	3	Y	...
G14.1 − 0.1	...	6 × 5	S	-	1	...	...
G14.3 + 0.1	...	5 × 4	S	-	1	...	...
G15.4 + 0.1	...	15 × 14	S	-	3	...	...
G15.9 + 0.2	...	7 × 5	S?	3	1	...	Y
G16.0 − 0.5	...	15 × 10	S	-	3	Y	...
G16.4 − 0.5	...	13	S	-	1	...	...
G16.7 + 0.1	...	4	C	3	2	...	...
G17.0 − 0.0	...	5	S	-	2	...	...
G17.4 − 0.1	...	6	S	-	3	...	...
G18.1 − 0.1	...	8	S	-	4	Y	Y
G18.6 − 0.2	...	6	S	-	1	...	...
G18.8 + 0.3	kes 67	17 × 11	S	3	3	...	...
G18.9 − 1.1	...	33	C?	-	-	Y	Y
G19.1 + 0.2	...	27	S	-	3	...	...
G20.0 − 0.2	...	10	F	3	3	...	...
G20.4 + 0.1	...	8	S	-	1	...	...
G21.0 − 0.4	...	9 × 7	S	-	3	...	...
G21.5 − 0.9	...	4	C	3	1	...	Y
G21.5 − 0.1	...	5	S	-	1	...	...
G21.6 − 0.8	...	13	S	-	-	Y	...
G21.8 − 0.6	kes 69	20	S	1	1	Y	Y
G22.7 − 0.2	...	26	S?	1	2	...	...
G23.3 − 0.3	W41	27	S	2	2	...	Y

There are several additional SNRs which are partially covered by the survey coverage, but we do not consider those SNRs for our statistical analysis. From the continuum-subtracted images, we checked [Fe II] and H_2 emission features around the SNRs by eyes and also cross-checked our detection result with the previously published detection lists which are done by an automated code (Froebrich et al. 2015; Kim et al. 2017 in preparation). We found various morphologies of the emission lines that seems to be associated with the SNRs. The continuum-subtracted narrow-band images of the [Fe II]- and/or H_2-emitting SNRs together with their short descriptions are presented in Appendix A.

Before measuring the fluxes of the detected emission features in the continuum-subtracted images, we first performed median filtering with the "window" size of 10 pixels, and masked the star-residuals around saturated stars with H- and Ks-band magnitude of > 14 mag using 2MASS catalog in order to prevent a few artificial pixels (e.g., hot pixels by cosmic ray hit, residuals around saturated star, etc; See Froebrich et al. 2015 in more detail) from dominating the total fluxes. It is worth noticing that the *H*- and *K*-band images used for the continuum-subtraction (see Section 2.2.1) also include a small portion of [Fe II] and H_2 emission lines. In order to compensate such "line subtraction," we multiplied the continuum-subtracted images by a factor of 1.15 for [Fe II] and 1.10 for H_2 images. These two correction values derived from the assumption that there is only a [Fe II] 1.64 μm line in *H*-band and a H_2 2.12 μm line in *K*-band, respectively. We measured the line fluxes in the continuum-subtracted images with an appropriate circular or elliptical region encircling the line emission features. The local background level can be measured from an annulus with a radius of 1.5 times larger than the source region. Note that in most cases the total background flux is considerably smaller than the total flux of the line emission, since almost all continuum-subtracted image have stable zero-level background unless the bright emission features are extended more than a half of the detector FOV. The total flux (F) of [Fe II] and H_2 line emission can be derived from the equation below.

$$F = F_0 \left(\frac{DN}{t_{exp}} \right) 10^{-0.4 \cdot ZP} \tag{2.1}$$

Table 2.2 (cont'd)

G-Name	Other Name	Size[a] (arcmin)	Type[b]	Detection Levels GR[c]	MP[d]	H_2[e]	[Fe 2][f]
G23.6 + 0.3	...	10?	?	3	1	...	...
G24.7 − 0.6	...	15?	S?	4	4	...	...
G24.7 + 0.6	...	30 × 15	C?	3	2	Y	...
G27.4 + 0.0	kes 73	4	S	3	1	Y	Y
G27.8 + 0.6	...	50 × 30	F	3	3	Y	Y
G28.6 − 0.1	...	13 × 9	S	3	1	...	Y
G29.6 + 0.1	...	5	S	4	3	...	...
G29.7 − 0.3	kes 75	3	C	3	1	...	...
G30.7 + 1.0	...	24 × 18	S?	-	-	...	...
G31.5 − 0.6	...	18?	S?	3	2	...	...
G31.9 + 0.0	3C391	7 × 5	S	1	1	Y	Y
G32.1 − 0.9	...	40?	C?	3	3	Y	...
G32.4 + 0.1	...	6	S	-	2	...	...
G32.8 − 0.1	kes 78	17	S?	3	3	Y	Y
G33.2 − 0.6	...	18	S	3	2	Y	...
G33.6 + 0.1	kes 79	10	S	2	1	...	...
G34.7 − 0.4	W44	35 × 27	C	1	1	Y	Y
G35.6 − 0.4	...	15 × 11	S	-	1	...	...
G36.6 − 0.7	...	25?	S?	2	3	...	...
G39.2 − 0.3	3C396	8 × 6	C	1	1	Y	Y
G40.5 − 0.5	...	22	S	4	2	...	...
G41.1 − 0.3	3C397	4.5 × 2.5	S	1	1	...	Y
G41.5 + 0.4	...	10	S?	-	-	...	Y
G42.0 − 0.1	...	8	S?	-	-	...	...
G42.8 + 0.6	...	24	S	4	4	...	...
G43.3 − 0.2	W49B	4 × 3	S	1	1	Y	Y
G45.7 − 0.4	...	22	S	2	2	...	...
G46.8 − 0.3	(HC30)	17 × 13	S	3	3	...	...
G49.2 − 0.7	W51C	30	S?	3	3	...	Y
G54.1 + 0.3	...	1.5	F?	3	3	...	...
G54.4 − 0.3	(HC40)	40	S	1	1	Y	...
G55.0 + 0.3	...	20 × 15?	S	2	2	...	...
G57.2 + 0.8	(4C21.53)	12?	S?	4	3	...	...
G59.5 + 0.1	...	15	S	3	3	...	...
G59.8 + 1.2	...	20 × 16?	?	-	-	...	...

[a]Sizes taken from Green's SNR Catalog (Green, 2014). If it is asymmetry, two dimensions with the major and minor axis of the ellipse are given.

[b]This represents the morphology of the remnant in radio observations, and is taken from Green's SNR Catalog. The abbreviation, "S", "F", and "C" represents "shell", "filled-center", and "composite", respectively.

[c]GLIMPSE survey: Reach et al. (2006). Detection classifications are as follows: 1 (detected), 2 (possible detections), 3 (not conclusive), and 4 (not detected). The object that is not covered by the survey area is marked by hyphen (-).

[d]MIPSGAL survey: Pinheiro Gonçalves et al. (2011). Detection classifications are same as Reach et al. 2006

[e]UWISH2 survey: this paper. Detection classifications are as follow: Y (detected), ... (not detected)

[f]UWIFE survey: this paper. Detection classifications are same as above.

Table 2.3. Log of NIR Spectroscopy

Target	Slit Number	Slit Position [α(J2000) δ(J2000)]	Filter	Exposure Time (seconds)
G11.2−0.3	Slit 1	18:11:26.5 −19:22:29	Ks	120 × 16
	Slit 2	18:11:34.0 −19:26:17	Ks	120 × 8
KES 69	Slit 1	18:33:12.6 −10:12:18	Jl, H, Ks	120 × 2
KES 73	Slit 1	18:41:18.3 −04:57:02	Jl, H	120 × 2
3C 391	Slit 1	18:49:21.7 −00:55:34	H	120 × 2
	Slit 2	18:49:33.8 −00:56:20	H	120 × 2

where F_0 is a total in-band flux of each narrow-band filter for Vega star (See Table 2.1), DN is a digital number, and t_{exp} is an effective exposure time of the surveys which is fixed to 60 seconds. ZP is a zero-point magnitude at each target image. The total flux uncertainty can be derived from the quadrature sum of (1) absolute calibration uncertainty and (2) standard deviation of the background variation. Since the background level around the source is quite stable, the most of the flux error arises from the calibration uncertainty. The typical calibration error measured from the uncertainty of the zero-point magnitude over the survey data, is 0.06 mag for UWIFE and 0.04 mag for UWISH2, that corresponding to the 6% and 4% of the total flux, respectively. Even in severe case, the total uncertainty does not exceed the 10% of the total flux.

2.2.2 Near-Infrared Spectroscopy

We carried out long-slit NIR spectroscopic observations for four Galactic SNRs (G11.2−0.3, KES 69, KES 73, and 3C 391) in which the bright [Fe II] and/or H_2 emission lines are detected. The observations were performed with IRIS2 (Infrared Imager and Spectrograph; **?**) attached on 3.9 m Anglo-Australian Telescope, which provides a spectral resolution of $\sim$ 2400 together with a pixel resolution of $0\farcs45$ per-pixel in each of the J, H, and K-bands. Two slit observations for G11.2−0.3 were done in 2012 April 7–8, whereas the other was observed in 2011 June 27. Figure 2.1 shows the position of the slits and the observation logs are listed in Table 2.3. All the observations were done by On-Off nodding sequence in order to remove sky air-glow

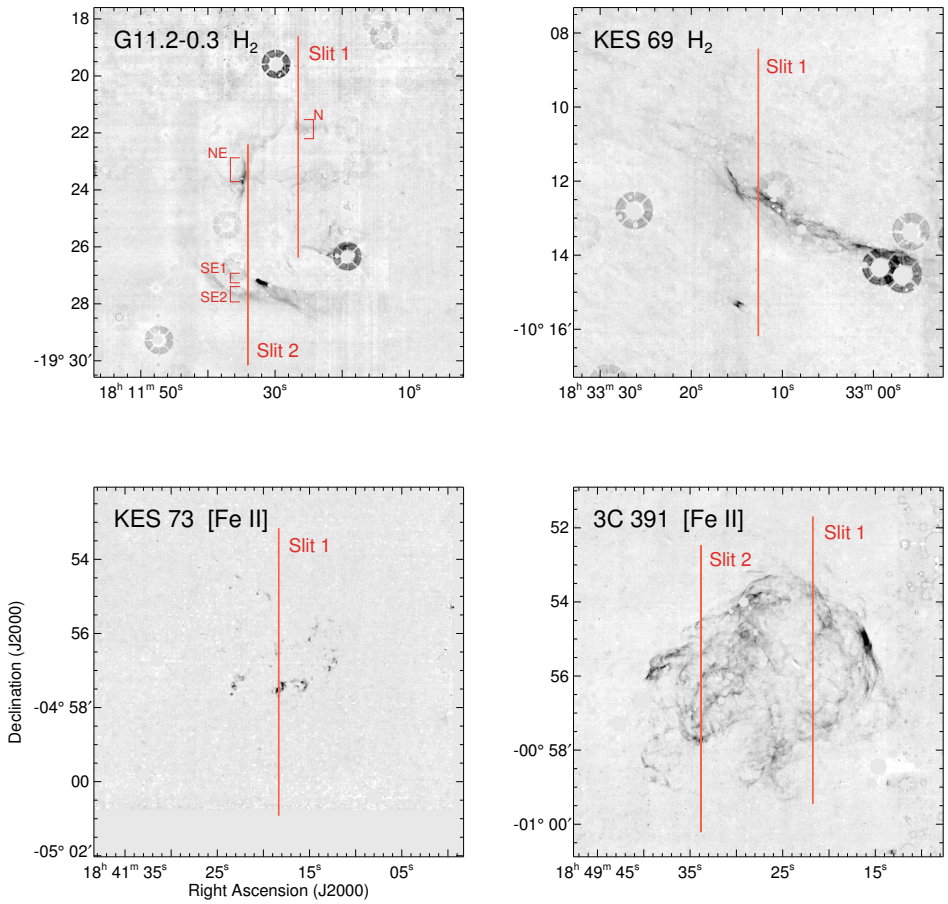

Figure 2.1 Slit positions (red vertical bars) of NIR spectroscopy for four SNRs. The background images are the continuum-subtracted H_2 of G11.2−0.3 and KES 69, and [Fe II] of KES 73 and 3C 391. For G11.2−0.3 (upper-left), source names and their positions are also marked.

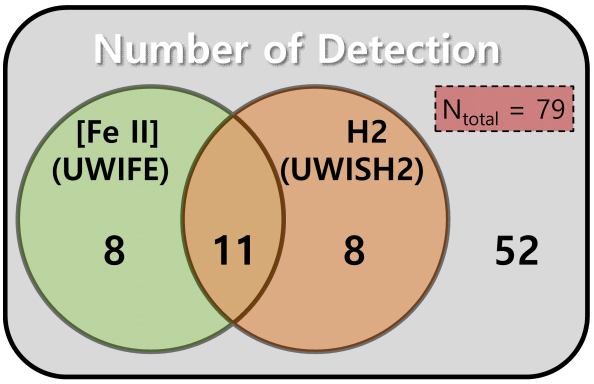

Figure 2.2 Venn diagram for the number of the detection. The numbers encircled by the green and red area represent the total numbers of [Fe II]- and H_2-emitting SNRs, respectively.

emission lines within the wavebands.

We followed the general data reduction procedure. First, all the observed raw spectra were subtracted by the dark frame and then were divided by the normalized flat frame. Using bright OH airglow emission lines, we derived the two dimensional wavelength solution for each science frame. The sky background including OH airglow emission lines and thermal continuum in K-band was subtracted by the Off-position frame. Finally, we performed an absolute photometric calibration for all the spectra by comparing the observed spectrum of A0V type standard star with the Kurucz model spectrum[1]. The 1-sigma uncertainty of the absolute flux calibration reaches up to 30% of its flux, but the relative uncertainty within each band is very low.

2.3 Results

2.3.1 Statistics of Imaging Surveys

All the 79 SNRs falling in the survey area are listed in Table 2.2, and we marked "Y" in the last two columns when if the emission lines are detected. Figure 2.2 shows the Venn diagram visualizing the result of our identification. In UWIFE survey, we found a total of 19 SNRs with [Fe II] emission features, and therefore the detection

[1] `http://kurucz.harvard.edu/`

rate is 24% (19 out of 79). Six of them were already confirmed the existence of [Fe II] lines by previous NIR imaging and spectroscopic observations: G11.2−0.3 (Koo et al., 2007), G21.5−0.9 (Zajczyk et al., 2012), 3C 391 (Reach et al., 2002), W44 (Reach et al., 2005), 3C 396 (Lee et al., 2009), W49B (Keohane et al., 2007), whereas the rest (13 out of 19; $\sim$ 70%) are newly-confirmed [Fe II]-emitting SNRs that have never been reported in previous studies. It is worth noticing that the detection rate is considerably lower than that in extra-galaxies (for example, the detection rate in M82 and NGC 253 is approximately 30–50%; Alonso-Herrero et al., 2003). This lower detection rate may result from the high interstellar extinction through the galactic disk (see next paragraph). In UWISH2 survey, on the other hands, bright H_2 emission lines are detected around another 19 SNRs, 14 of which are new discoveries. Note that 5 out of 19 were already confirmed the existence of NIR H_2 lines in previous studies (G11.2−0.3 (Koo et al., 2007), 3C 391 (Reach et al., 2002), W44 (Reach et al., 2005), 3C 396 (Lee et al., 2009), W49B (Keohane et al., 2007)). The detection rate is 24% (19 out of 79). Interestingly, more than a half (11 out of 19) of the H_2-emitting SNRs have [Fe II] emission features, as well (Figure 2.2). This may implies that the two emission lines are physically associated (see Section 2.4.1 for more details).

Figure 2.3 shows the [Fe II] and H_2 detection rates as a function of Galactic longitude. The number density of all the 79 SNRs falling in the survey area is presented in the black histogram. It peaks at the longitude of 10°–20°, and is gradually decreasing toward the high Galactic longitude. The low number density at $< 10°$ is due to the limitation of the survey coverage (i.e., the coverage is $7° < l < 62°$, but the longitude bin is starting at $l = 0°$ with a size of 10°.). On the other hand, the number density of [Fe II]- and H_2-emitting SNRs are presented in the green and red hatched histograms, and the detection rate at each longitude bin is over-plotted with the green diamond and the red triangle, respectively. The detection rate peaks at 40°–50° for the [Fe II] line and at 30°–40° for the H_2 line, and gradually decreases toward the low Galactic longitude. At each peak, the detection rate reaches up to around 50% even though the overall detection rate is only 24%. Since SNRs in lower galactic longitude may suffer higher interstellar extinction, the decrease of the detection rate toward the low Galactic

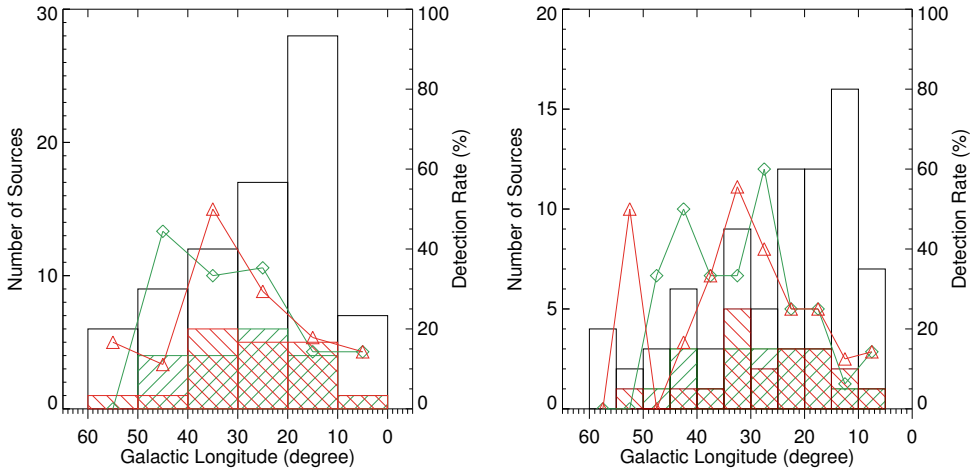

Figure 2.3 Number of SNRs as a function of Galactic longitude (black histogram). The red and green hatched histograms represent the number of SNRs showing either H_2 or [Fe II] emission line, respectively. The red and green solid lines are the detection rate at each bin range.

longitude can be explained by the increase of the interstellar extinction. However, the different peaks in the detection rates may not be explained by the interstellar extinction. As seen in Figure 2.3, the H_2 detection rate peaks at l =30°–40°, but is abruptly decreased at l =40°–50° where the [Fe II] detection rate is maximum. This may reflect the Galactic ecology, and we suggest two possible solutions. First, this different peaks may result from the different SN population between the two longitude bins. Let us assume that the H_2 emission arises from the SN shock, and reflects interaction between the SN shocks and the dense surrounding medium (SNR-MC interaction; see Section 2.4.3). If the progenitors are O type stars, their strong wind and radiation are enough to destroy their surrounding medium. On the other hand, the B type stars which have less strong wind and radiation cannot destroy the medium, so they eventually show SNR-MC interaction showing strong H_2 emission lines. This may imply that the progenitor stars in l =30°–40° may be dominated by B type stars, whereas those in l =40°–50° were dominated by O type stars. Second, it could be due to the

Table 2.4. [Fe II] Luminosities for the Galactic SNRs

G-Name	Other Name	Distance[a] (kpc)	N_H[b] (10^{22} cm^{-2})	$F_{[\mathrm{Fe\ II}]}$[c] ($erg\ s^{-1}\ cm^{-2}$)	$L_{[\mathrm{Fe\ II}]}$[d] ($L_\odot$)
$G8.7-0.1$	...	-		$1.00(0.60)\times10^{-14}$	
$G11.2-0.3$	...	4.4	2.0	$1.15(0.07)\times10^{-11}$	42
$G15.9+0.2$	...	?		$7.17(0.43)\times10^{-14}$	?
$G18.1-0.1$	...	?		$1.44(0.09)\times10^{-13}$	?
$G18.9-1.1$	...	2		$2.03(0.12)\times10^{-12}$	?
$G21.5-0.9$	...	4.6	2.2	$7.50(0.45)\times10^{-13}$	3.6
$G21.8-0.6$	Kes 69	$\sim$6.5	2.4	$5.48(0.33)\times10^{-12}$	$\sim$63
$G23.3-0.3$	W41	4.2		$5.11(0.31)\times10^{-12}$	?
$G27.4+0.0$	Kes 73	$\sim$8.5	2.5	$1.59(0.10)\times10^{-12}$	34
$G27.8+0.6$	...	-		$1.00(0.60)\times10^{-14}$	
$G28.6-0.1$	...	?	3.5	$1.82(0.11)\times10^{-12}$	?
$G31.9+0.0$	3C391	8.5	2.9	$3.91(0.24)\times10^{-11}$	1200
$G32.8-0.1$	Kes78	$\sim$7.1*	1.5	$6.30(0.38)\times10^{-12}$	?
$G34.7-0.4$	W44	2.8	1.0	$3.95(0.24)\times10^{-11}$	24
$G39.2-0.3$	3C396	8.5*	4.7	$8.77(0.53)\times10^{-12}$	1400
$G41.1-0.3$	3C397	10.6*	3.6	$1.86(0.11)\times10^{-11}$	1700
$G41.5+0.4$	...	-		$7.00(0.42)\times10^{-12}$	
$G43.3-0.2$	W49B	10	5.0	$4.65(0.28)\times10^{-11}$	13000
$G49.2-0.7$	W51	6	2.0	$4.85(0.29)\times10^{-12}$	33

[a]Distances taken from Green's Catalog; Kes78: Koralesky et al. 1998, Boumis et al. 2009, 3C 396: Lee et al. 2009, 3C 397: Park et al. 2013

[b]Column density taken from the references; G11.2-0.3, Kes 69, and 3C396: Andersen et al. 2011, G21.5-0.9: Safi-Harb et al. 2001, Kes 73: Gotthelf & Slane 2004, G28.6-0.1: Ueno et al. 2003, 3C391: Chen & Slane 2001, Kes78: Kalberla et al. 2005, W44: Harrus et al. 1997, 3C397: Safi-Harb et al. 2005, W49B: Hwang et al. 2000, W51: Koo et al. 2005

[c]Detected [Fe II] Brightness. Uncertainty in a bracket is a quadrature-sum of its photometric uncertainty (6% of total flux) and background random noise.

[d]Total luminosity ($L_\odot$) after correcting extinction estimated from the N_H.

different ages of SNRs in the two longitude bins. Since the [Fe II] and H_2 trace fast J-shock and slow non-dissociative C-shock, youger SNRs may have brighter [Fe II] but fainter H_2, and vice versa. The SNRs in l =40°–50° could be younger than thsoe in l =30°–40°, in general. In order to clear this out, we need to investigate those SNRs in more detail.

The total [Fe II] and H_2 fluxes of the SNRs are shown in Table 2.4 and 2.5, respectively. The most brightest SNR in [Fe II] 1.64 μm (extinction-uncorrected) is W49B, while W44 radiates the strongest H_2 2.12 μm line. The last column of the tables represents the extinction-corrected luminosity in the unit of solar luminosity.

Table 2.5. H_2 Luminosities for the Galactic SNRs

G-Name	Other Name	Distance[a] (kpc)	N_H [b] (10^{22} cm^{-2})	F_{H_2} [c] ($erg\ s^{-1}\ cm^{-2}$)	L_{H_2} [d] ($L_\odot$)
G9.9 − 0.8	...	?		$4.40(0.18) \times 10^{-13}$	?
G11.2 − 0.3	...	4.4	2.0	$6.69(0.27) \times 10^{-12}$	13
G13.5 + 0.2	...	?		$6.91(0.28) \times 10^{-13}$	?
G16.0 − 0.5	...	?		$3.77(0.15) \times 10^{-12}$	?
G18.1 − 0.1	...	?		$1.43(0.06) \times 10^{-12}$	?
G18.9 − 1.1	...	2	1.0	$2.18(0.09) \times 10^{-12}$	0.49
G21.6 − 0.8	...	-		$1.00(0.60) \times 10^{-13}$	
G21.8 − 0.6	Kes 69	∼6.5	2.4	$1.14(0.05) \times 10^{-11}$	∼62
G24.7 + 0.6	...	?		$1.65(0.08) \times 10^{-12}$	?
G27.4 + 0.0	Kes 73	∼8.5	2.5	$1.45(0.06) \times 10^{-13}$	1.4
G27.8 + 0.6	...	-		$1.00(0.60) \times 10^{-14}$	
G31.9 + 0.0	3C391	8.5	2.9	$1.04(0.04) \times 10^{-11}$	130
G32.1 − 0.9	...	4.6*	0.23	$2.50(0.10) \times 10^{-12}$	1.9
G32.8 − 0.1	Kes 78	∼7.1*	1.5	$1.21(0.73) \times 10^{-11}$	?
G33.2 − 0.6	...	?		$1.28(0.05) \times 10^{-12}$	?
G34.7 − 0.4	W44	2.8	1.0	$2.03(0.08) \times 10^{-10}$	90
G39.2 − 0.3	3C396	8.5*	4.7	$2.44(0.10) \times 10^{-12}$	88
G43.3 − 0.2	W49B	10	5.0	$1.04(0.04) \times 10^{-11}$	621
G54.4 − 0.3	HC40	3.3		$9.71(0.39) \times 10^{-13}$	?

[a]Distances taken from Green's Catalog; G32.1-0.9: Folgheraiter et al. 1997, Kes78: Koralesky et al. 1998, Boumis et al. 2009, HC40: Park et al. 2013, 3C396: Lee et al. 2009

[b]Column density taken from the references; G11.2-0.3, Kes 69, and 3C396: Andersen et al. 2011, G18.9-1.1: Tullmann et al. 2010, Kes 73: Gotthelf & Slane 2004, 3C391: Chen & Slane 2001, G32.1-0.9: Folgheraiter et al. 1997, Kes78: Kalberla et al. 2005, W44: Harrus et al. 1997, W49B: Hwang et al. 2000

[c]Detected H_2 Brightness. Uncertainty in a bracket is a quadrature-sum of its photometric uncertainty (4% of total flux) and background random noise.

[d]Total luminosity ($L_\odot$) after correcting extinction estimated from the N_H.

Due to the absence of either hydrogen column density ($N_{\rm H}$), distance, or both, the luminosity of some SNRs is not estimated. It is worth noticing that the luminosity of W49B is strongest in both surveys, and it accounts for more than 70% of total [Fe II] luminosity. The luminosity ranges 3.6–13,000 $L_{\odot}$ for [Fe II] and 0.49–620 $L_{\odot}$ for H_2. We can compare the [Fe II] luminosity with that of extra-galaxies reported in the previous studies: 26–720 $L_{\odot}$ for LMC (Oliva et al., 1989), 6–700 $L_{\odot}$ for M33 (Morel et al., 2002), 800–50,000 $L_{\odot}$ for M82 and NGC 253 (Alonso-Herrero et al., 2003), 70–800 $L_{\odot}$ for NGC 1569 (Labrie & Pritchet, 2006), 70–300 $L_{\odot}$ for NGC 5253 (Labrie & Pritchet, 2006), 70–3000 $L_{\odot}$ for NGC 6946 (Bruursema et al., 2014). The lowest luminosity of the Galactic SNRs is somewhat smaller than that in the extra-galaxies, but this might be due to different observational sensitivities; our deep narrow-band imaging survey can identify the weak [Fe II] emission features, more efficiently. Except the two starburst galaxies, M82 and NGC 253, the maximum [Fe II] luminosity in our Galaxy (13,000 $L_{\odot}$from W49B) is much larger than that in other extra-galaxies. The reason why W49B radiates very bright [Fe II] emission is unclear, and remains to be explored.

2.3.2 Spectroscopy of Four Galactic SNRs

G11.2−0.3

G11.2−0.3 is a young historical SNR which exploded in AD 386 and have a remarkably spherical morphology with $2'$ radius in radio, infrared and X-ray images. This remnant hosts the X-ray pulsar PSR J1811−1925 (Torii et al., 1997) and the pulsar wind nebula with a size of $\sim 1'$ (Roberts et al., 2003). Recently, several NIR imaging and spectroscopic studies have been carried out, and found bright [Fe II] and H_2 emission features around the remnant. The inner [Fe II] filaments have fast radial velocity of $\sim$ 1000 km s^{-1} which implies that they are SN ejecta mostly arising from the Fe core (Moon et al., 2009), whereas the bright south-eastern [Fe II] shell is composed of multiple thin filaments which is a mixture of the shocked SN ejecta and the shocked circumstellar material (Koo et al., 2007; Lee et al., 2013). Koo et al. (2007) found two small H_2 clumps in the south-eastern and north-eastern boundary of the remnant, and

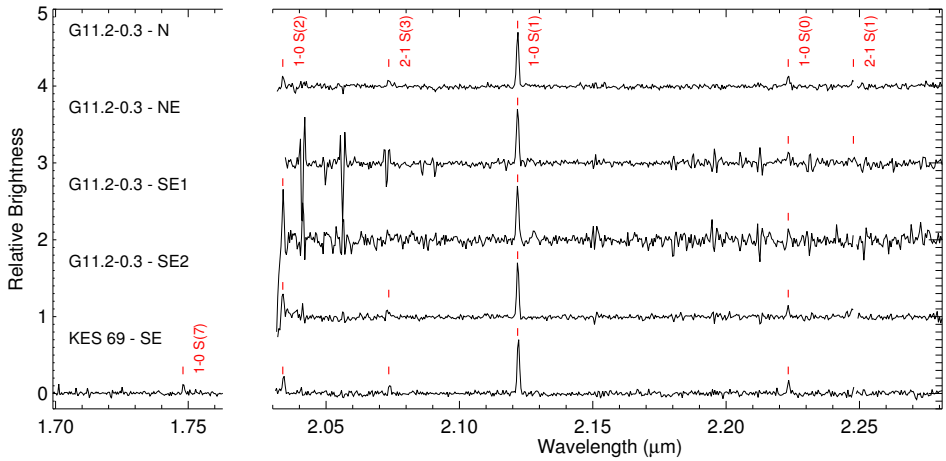

Figure 2.4 NIR H- and Ks-band spectra of H_2 filaments detected in G11.2−0.3 and KES 69.

suggested that they are dense clumps in the circumstellar wind material shocked by SN blast wave.

We detected both [Fe II] and H_2 emission features showing more detailed and dramatic structures compared to the previous NIR studies. Addition to the two bright H_2 clumps previously detected in Koo et al. (2007), we found diffuse and extended H_2 features far outside of the remnant's boundary. Especially in the northern region, the H_2 emission is detected nearly $2'$ away from nearby [Fe II] filaments or radio shell, which is corresponding to the $5'$ from the center of the remnant.

Our two long-slits of the Ks-band spectroscopy cover the extended H_2 filaments, which can be divided into four components (see Figure 2.1; hereafter N, NE, SE1, and SE2). Their one-dimensional spectra are shown in Figure 2.4. We clearly detected H_2 1–0 S(1) at 2.12 μm in all positions. Some of the filaments also have other H_2 lines from different ro-vibrational transitions. The radial velocity at the Local-Standard-of-Rest frame ($v_{\rm LSR}$) is constrained from +41–+47 km s^{-1} (Table 2.6), which is well consistent with the systematic velocity of the remnant (+45 km s^{-1}; Green et al., 1988), implying that they are indeed physically associated with the remnant. In order to examine

Table 2.6. Spectral Properties of H_2

SNR Name	Slit Name	v_{LSR}[a] (km s^{-1})	FWHM[b] (km s^{-1})	$F(H_2$ 1–0 S(1))[c] (10^{-15} erg s^{-1} cm^{-2})	H_2 1–0 S(7) 1.75 μm	H_2 1–0 S(2) 2.03 μm	H_2 2–1 S(3) 2.07 μm	H_2 1–0 S(0) 2.22 μm	H_2 2–1 S(1) 2.25 μm	References[d]
G11.2−0.3	N	47 (2)	139 (4)	11.0 (0.3)	—	0.27 (0.07)	0.17 (0.03)	0.19 (0.03)	0.09 (0.05)	1, 2
	NE	45 (3)	144 (6)	17.0 (0.9)	—	—	*	0.20 (0.08)	< 0.13	1, 2
	SE1	41 (3)	139 (6)	5.4 (0.3)	—	< 0.58	*	< 0.18	—	1, 2
	SE2	44 (1)	136 (3)	11.9 (0.4)	—	0.49 (0.13)	0.23 (0.06)	0.17 (0.05)	—	1, 2
KES 69	SE	57 (1)	141 (3)	23.0 (0.7)	0.23 (0.04)	0.28 (0.05)	0.16 (0.04)	0.20 (0.03)	—	3

Note. — Column 6–10 represent the extinction-corrected fluxes of the H_2 lines normalized by that of H_2 1–0 S(1) 2.12 μm shown in column 5. The symbol — indicates that the lines are located outside of the spectral coverage or detector gap (or 2–1 S(1)). We also mark *, when the lines are contaminated by strong OH airglow emission lines so we cannot measure their fluxes.

[a]Radial velocity of H_2 1-0 S(1) at Local Standard-of-Rest frame. The uncertainty in parenthesis is 1σ statistical error by a single Gaussian fitting, and does not include the wavelength calibration error which is roughly 3 km s^{-1}.

[b]Full Width at Half Maximum of H_2 1-0 S(1). The instrumental profile at ~ 2.12 μm has ~ 2.3 pixel width corresponding to ~ 140 km s^{-1}.

[c]Observed flux of H_2 1–0 S(1) 2.12 μm

[d]References for the hydrogen column density used for the extinction correction

References. — (1) Lee et al. (2013), (2) Borkowski et al. (2016), (3) Yusef-Zadeh et al. (2003),

the excitation mechanism of the extended H_2 filaments, we may use H_2 flux ratios (e.g., Burton, 1992). As seen in Table 2.6, the flux ratio of H_2 1–0 S(0) to 1–0 S(1) is $\lesssim 0.2$ in all filaments, which is consistent with that in the collisionally excited H_2 gas with a few 1000 K (~ 0.2; Black & van Dishoeck, 1987). Note that the ratio of UV fluorescence H_2 ranges from 0.4 to 0.6, which is higher than that by collisional process (Black & van Dishoeck, 1987). The weakness of the H_2 lines from high vibrational levels with $v \geq 2$ (H_2 2–1 S(3) at 2.07 μm and 2–1 S(0) at 2.25 μm) also supports the collisional process of the H_2 filaments.

KES 69

KES 69 have been widely studied in radio observations, and displays an incomplete radio shell morphology (e.g., Zhou et al., 2009). Multiple OH masers which seem to be associated with the remnant were detected in the north-eastern and the south-eastern regions (Green et al., 1997; Hewitt et al., 2008), and the remnant is believed to be one of the Galactic SNRs interacting with its surrounding molecular clouds (MCs). The X-ray emission appears interior to the radio shell (Bocchino et al., 2012, and references therein).

We detected bright H_2 filaments at the south-western border of the remnant where the brightness of the radio continuum is strongest. [Fe II] emission also arises from the south-western shell, but is relatively weak and diffuse compared to the H_2 emission. In the north-eastern region of the remnant, we also found additional complex H_2 features in the north-eastern region of the remnant where a strong OH maser was detected (Green et al., 1997).

Our NIR Jl, H, and Ks-band spectroscopic observations were done for the SW shell where bright H_2 filaments were detected (Figure 2.1). We detected five H_2 lines in H and Ks-band (Figure 2.4), but nothing in Jl-band. (We expected [Fe II] emission lines in Jl and H-band, but the exposure time of 240 seconds was not enough to detect the weak [Fe II] lines.) From a single Gaussian fitting for the H_2 lines, we derived their radial velocities, line widths, and relative fluxes (see Table 2.6). The radial velocity at the Local-Standard-of-Rest frame is ~ 60 km s^{-1}, which is somewhat smaller than the

systematic velocity of the SW shell (77–86 km s^{-1}; Zhou et al., 2009, and references therein). This discrepancy may imply either that the shocked H_2 filaments is moving toward us with -20 km s^{-1} at its systematic frame or that the kinematic distance of KES 69 is smaller than the previous estimation (5.2 kpc; Zhou et al., 2009). Assuming the flat Galactic rotation model with the IAU standard rotation constants ($R_\odot = 8.5$ kpc, $V_\odot = 220$ km s^{-1}), $v_{\rm LSR}$ of 60 ± 3 km s^{-1} of KES 69 yields $d = 4.1^{+0.2}_{-0.1}$ kpc. Like G11.2−0.3, the H_2 line ratios seem to be consistent with those in collionally excited H_2 gas, and this support the previous studies suggesting that KES 69 is now interacting with its surrounding MCs in the SW border of the remnant (Green et al., 1997; Hewitt et al., 2008).

KES 73

In radio and X-ray wavebands, KES 73 displays a limb-brightened shell-like morphology with $\sim 2'$ radius, and especially the western shell is relatively bright in both wavebands compared to the other regions. The remnant hosts an anomalous X-ray pulsar (1E 1841−045; Kriss et al., 1985; Vasisht & Gotthelf, 1997), which is believed to be a highly magnetized young neutron star (called magnetar). It is also bright in a mid-infrared 24 μm waveband, and the emission seems to arise from either the swept-up dust with 0.1 $M_\odot$ (Pinheiro Gonçalves et al., 2011) or strong mid-infrared forbidden lines (Carey et al., 2009).

In the UWIFE survey, we found a dozen of bright [Fe II] clumps inside the remnant, and their spatial distributions are very different to those of the radio and X-ray. In the western border of the remnant where strong radio and X-ray emission were detected, complex [Fe II] emission features as well as a small H_2 clump with a size of $5''$ were also detected. These western [Fe II] and H_2 clumps show clear anti-correlation, and the H_2 clump is located 2–$3''$ outside the [Fe II] clumps.

The NIR Jl and H-band spectroscopic observations cross one of the brightest [Fe II] clump near the center (Figure 2.1). The one-dimensional spectra show a dozon of bright [Fe II] lines with a $HI - Pa\beta$ line at 1.28 μm (see Figure 2.5). The LSR velocity of the knot is -30 ± 3 km s^{-1}, which is lower than the systematic velocity of the remnant

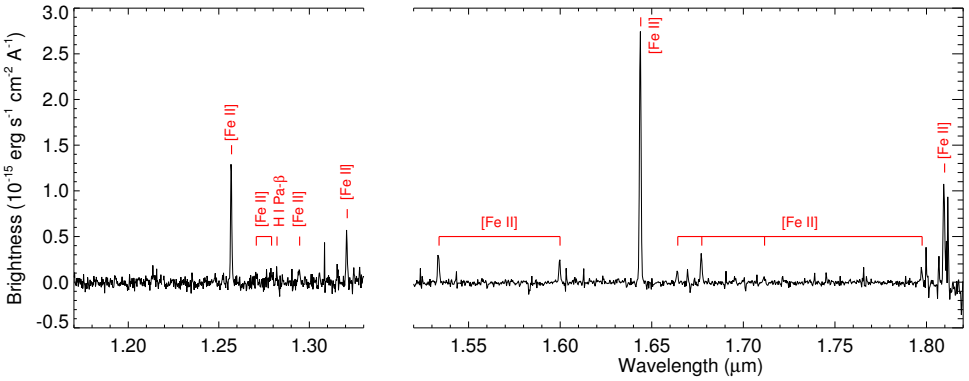

Figure 2.5 NIR J- and H-band spectra of a [Fe II] knot detected in KES 73.

estimated from previous radio observations. (+89–+110 km s^{-1}; Tian & Leahy, 2008; Kilpatrick et al., 2016). Since the [Fe II] knot is close to the center, therefore the expansion velocity of the [Fe II] knot is $\sim$ +100 km s^{-1} toward us, which can be regarded as slow, dense circumstellar medium rather than fast-moving SN ejecta. Note that the expected velocity of dense SN ejecta encountering the reverse shock is at most 2000 km s^{-1}, assuming that distance =7.5–9.8 kpc, age $\lesssim$ 2000 yrs, and radius $\sim$ 2 arcmin (Gotthelf & Vasisht, 1997; Tian & Leahy, 2008). Table 2.7 shows the detected emission lines in Jl and H-band and their relative fluxes. The detection of the recombination line of H (H I-Paβ) together with the non-detection of [P II] 1.189 μm emission line also implies that the knot has the circumstellar abundance (Koo et al., 2013; Lee et al., 2017). The electron density derived from the [Fe II] line ratios is $\sim 10^4$ cm^{-3} (e.g., Koo et al., 2016; Lee et al., 2017).

3C 391

3C 391 is one of the brightest mixed-morphology SNR, showing rim-brightened radio shell with center-filled thermal X-ray emission (Reynolds & Moffett, 1993). In the high resolution radio images, it shows a partial shell of 5′ radius, with a relative faint emission extended through the broken shell in the southeastern part (Reynolds & Moffett, 1993; Moffett & Reynolds, 1994). This “breakout” morphology together

Table 2.7. NIR Emission lines in KES 73

Wavelength (μm)	Identification (lower–upper)		Relative Flux	
			Observed	Dereddened[a]
1.1886	[P II]	$^3P_2$ - $^1D_2$	< 0.03	< 0.13
1.2570	[Fe II]	$a^6D_{9/2}$ - $a^4D_{7/2}$	0.41 (0.01)	1.42 (0.05)
1.2707	[Fe II]	$a^6D_{1/2}$ - $a^4D_{1/2}$	0.02 (0.01)	0.08 (0.04)
1.2791	[Fe II]	$a^6D_{3/2}$ - $a^4D_{3/2}$	0.05 (0.02)	0.17 (0.06)
1.2822	H I Paβ		0.04 (0.01)	0.12 (0.04)
1.2946	[Fe II]	$a^6D_{5/2}$ - $a^4D_{5/2}$	0.05 (0.02)	0.14 (0.05)
1.3209	[Fe II]	$a^6D_{7/2}$ - $a^4D_{7/2}$	0.14 (0.02)	0.38 (0.06)
1.5339	[Fe II]	$a^4F_{9/2}$ - $a^4D_{5/2}$	0.13 (0.01)	0.17 (0.02)
1.5999	[Fe II]	$a^4F_{7/2}$ - $a^4D_{3/2}$	0.09 (0.01)	0.10 (0.01)
1.6440	[Fe II]	$a^4F_{9/2}$ - $a^4D_{7/2}$	1.00	1.00
1.6642	[Fe II]	$a^4F_{5/2}$ - $a^4D_{1/2}$	0.05 (0.01)	0.05 (0.01)
1.6773	[Fe II]	$a^4F_{7/2}$ - $a^4D_{5/2}$	0.12 (0.01)	0.11 (0.01)
1.7116	[Fe II]	$a^4F_{5/2}$ - $a^4D_{3/2}$	0.03 (0.01)	0.02 (0.01)
1.7976	[Fe II]	$a^4F_{3/2}$ - $a^4D_{3/2}$	0.05 (0.01)	0.04 (0.01)
1.8099	[Fe II]	$a^4F_{7/2}$ - $a^4D_{7/2}$	0.37 (0.07)	0.26 (0.05)

[a]Extinction-corrected fluxes normalized by the [Fe II] 1.64 μm line assuming $N_{\rm H} = 2.6 \times 10^{22}$ cm^{-2} (Kumar et al., 2014) and the extinction model of the general interstellar dust (Draine, 2003).

with the CO line map coincide with the bright northeastern shell imply that the SN explosion took place in the edge of the northeastern molecular clouds (Wilner et al., 1998). Furthermore, the detection of two 1720 MHz OH maser spots in the remnant indicates that the remnant is now interacting with the surrounding molecular clouds (Frail et al., 1996).

In the [Fe II] narrow-band image, it shows complex filamentary structures filling inside the remnant boundary, and the overall distribution seems to be similar with that of the radio continuum. Furthermore, the [Fe II] emission peaks at the northwestern border, where the strongest radio shell is located. The H_2 emission is also detected in the remnant, but its distribution is very different to that of the radio continuum and [Fe II] emission. The strongest H_2 emission is arising from the southern portion of the remnant, where one of the OH maser spots is detected. The results of our morphological study are consistent with those in Reach et al. (2002), who carried out NIR [Fe II] 1.64 μm and H_2 2.12 μm narrow-band imaging observations for the

northeastern and southern regions of the remnant for the first time.

In the two H-band spectra of 3C 391 crossing the central diffuse [Fe II] filaments (Figure 2.1), we only detected [Fe II] 1.644 μm emission lines, and Figure 2.6 shows the position-velocity diagrams of the two slits at that wavelength. As seen in the figure, the central velocities of the [Fe II] filaments vary with the positions, but their $v_{\rm LSR}$ is only a few 100 km s^{-1} implying the circumstellar origin. In the middle of Slit 1, we also found a small velocity bump with a few 100 km s^{-1} from the central velocity. This may result from the inhomogeneous density distribution of its surrounding medium.

2.4 Discussions

2.4.1 "[Fe II] - H_2 reversals"

Among the 27 [Fe II]- and/or H_2-emitting SNRs, more than 40% of the SNRs show both emission lines (Section 2.3.1). This may imply that there are physical connections between the two NIR emission lines. Since SNRs are shock-dominated regions, the emission lines might be associated with the excitation process by SN shocks. In general, the [Fe II] line traces "fast" ($\gtrsim$ 50 km s^{-1}) dissociative J-shock, whereas the H_2 line traces "slow" ($\lesssim$ 50 km s^{-1}) non-dissociative C-shock. If the shocks are driven by the same SN blast wave, therefore, we expect the H_2 filaments to be closer to the explosion center than the [Fe II] filaments. The H_2 emission can also originates from the J-shock, if H_2 molecules reform in the further downstream from the [Fe II]-emitting region after the shock passage. Even in this case, the H_2 filaments are expected to be inside the [Fe II] filaments. For five SNRs emitting both [Fe II] and H_2 lines (G11.2−0.3, KES73, W49B, 3C 396, and W44), however, we found interesting morphologies which is different from what we expected; H_2 emission features were detected outside of the [Fe II] filaments. Especially, the extended H_2 filaments of G11.2−0.3 far beyond the [Fe II] and radio boundary is most interesting, because the H_2 emission is detected in almost twice of the remnant's radius from the center. (see Section 2.3.2). It is worth noticing that "[Fe II]-H_2 reversals" of several bright SNRs were already reported in previous NIR studies (Oliva et al. 1990, Burton & Spyromilio 1993 for RCW 103,

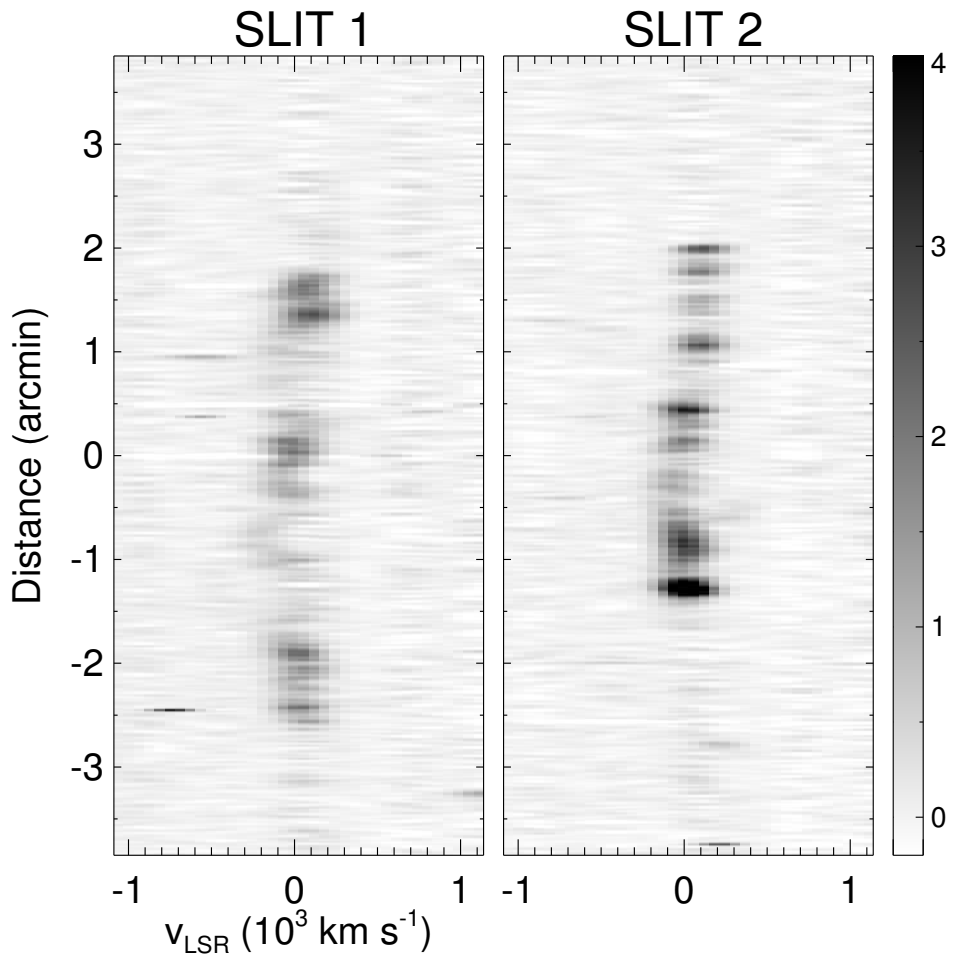

Figure 2.6 Position-velocity diagrams at [Fe II] 1.644 μm in (left) Slit 1 and (right) Slit 2 of 3C 391. Unit of the color bar is 10^{-17} erg s^{-1} cm^{-2} Å^{-1}.

Graham et al. 1991 for Cygnus loop, Koo et al. 2007 for G11.2−0.3, Keohane et al. 2007 for W49B, Lee et al. 2009 for 3C 396). In order to understand the origin of the "[Fe II]-H_2 reversal", we first need to investigate the excitation mechanism of the extended H_2 emission features. Several possible solutions explaining the extended emission have been suggested: (1) radiative/magnetic precursors, (2) UV fluorescence excitation, (3) complex projection effect of multi-shock, but, its origin is still not well understood so far.

For G11.2-0.3 showing the "[Fe II]-H_2 reversal" with extended H_2 filaments, we obtained the Ks-band spectra (Figure 2.4) and derived H_2 line fluxes (Table 2.6). In Section 2.3.2, we show that their flux ratios are well consistent with those of collisional process, and it is likely that the H_2 gas around the remnant is excited by slow ($v_s < 50$ km s^{-1}), non-dissociative C-shock. However, we cannot rule out a possibility that the excitation process involes the collisional heating of the H_2 gas by UV/X-ray radiation in high density regions ($\gtrsim 10^6$ cm^{-3}; Sternberg & Dalgarno, 1989; Burton et al., 1990). Another important physical parameter, which is useful to distinguish the excitation sources (shocks vs. UV/X-ray photons) is the line widths. If the shock is a dominant source of their heating, the H_2 line widths will be quite broad up to an order of the shock velocity (i.e., a few 10 km s^{-1}). If the gas is radiatively excited by high energy photons, on the other hand, they show very narrow line width with $\lesssim 5$ km s^{-1}, corresponding to the typical turbulent velocity of interstellar/molecular clouds. (Hollenbach & McKee, 1989; Burton, 1992). As seen in Table 2.6, however, all the lines we observed are almost unresolved with 140 ± 5 km s^{-1}, so we could not derive their intrinsic line widths. In order to clear this out, high resolution NIR spectroscopic observations will be needed.

2.4.2 Total [Fe II] Luminosity and Supernova Rate

Since supernovae are major sources of galactic turbulence and heavy elements, a supernova rate is a very important factor for understanding the kinematical and chemical evolution of galaxies. The direct way to estimate the SN rate is to count the SN events within a long control time, and indeed it was very useful to determine

the SN rates of extra-galaxies by using SN search programs(e.g., Palomar Supernova Search, Asiago Supernova Search, Lick Observatory Supernova Search) which had been done during the last several decades (e.g., Zwicky, 1938; Cappellaro & Turatto, 1988; Leaman et al., 2011). For our Milky Way galaxy, however, no supernova event has been detected after the invention of the telescope and only five SN events have been recorded during the last millennium in the ancient history books of East Asia and European countries (Stephenson & Green, 2002). There were various indirect ways to estimate the SN rate of our galaxy, using historical SN records with model simulations (Strom, 1994; Tammann et al., 1994; Adams et al., 2013), gamma-ray emission from the decay of ^{26}Al and ^{44}Ti (Timmes et al., 1997; Diehl et al., 2006; The et al., 2006), pulsar birth rates in our galaxy (Vranesevic et al., 2004; Faucher-Giguère & Kaspi, 2006; Keane & Kramer, 2008), and correlation between extragalactic SN rates and their total luminosities in a specific waveband (Cappellaro et al., 1993; Li et al., 2011). Even though the SN rate from those methods have large uncertainties, but the general consensus is that a few SN events have been occurred every one century in our galaxy.

Since NIR [Fe II] lines are bright in SNRs but relatively weak in H II regions (Graham et al., 1987; Koo & Lee, 2015, and references therein), they have been regarded as the tracer of SN shocks which are highly associated with the SN activities. (Greenhouse et al., 1991; Rosenberg et al., 2012). There were many efforts to find the correlation between the total [Fe II] luminosity of extra-galaxies and their SN rates (Morel et al., 2002; Alonso-Herrero et al., 2003; Rosenberg et al., 2012). Recently, Rosenberg et al. (2012) found the tight linear correlation between them. If we assume that the SN rate of our galaxy is a few per one century, the equation in Rosenberg et al. (2012) yields the expected total [Fe II]-1.64 μm luminosity of $\sim 10^{39}$ erg s^{-1}, corresponding to 2–3$\times10^5$ $L_\odot$. The observed total [Fe II] luminosity in our survey ($\sim 2 \times 10^4$ $L_\odot$) is only 10% of the expected one. It is worth noticing that, however, our survey covers only 27% of the known SNRs (79 out of 294). So we may simply multiply a factor of 4 to the observed [Fe II] luminosity, if we assume that the overall luminosity distribution of the Galactic SNRs is same as that in our survey area. This crude estimation yields $L_{[FeII]} \sim 8 \times 10^4$ $L_\odot$ which is still a few times fainter than the expected total [Fe II]

luminosity derived from the Galactic SN rate.

Why is the observed total [Fe II] luminosity fainter than the expected one? we suggest three possible solutions. First, it could be due to high interstellar extinction toward the galactic plane. In the extra-galaxies, the detection rate of [Fe II] lines in radio SNRs is 30–50% (Alonso-Herrero et al., 2003), whereas the overal detection rate in our survey area is only 24% which may due to high interstellar extinction. In Figure 2.3, indeed, the detection rate reaches up to 50% at l =40°–50°, but it gradually decreases toward the lower galactic longitude. Second, there could be more SNRs in our Galaxy, which have not been known so far. According to the theoretical calculation, around 1000 SNRs were expected to be visible at any time in our Galaxy (Tammann et al., 1994), but around 300 SNRs have been reported from multi-wavelength observations (Green, 2014). Third, the correlation between total [Fe II] luminosity and SN rates in extra-galaxies might be different to that in our Galaxy. According to Alonso-Herrero et al. (2003), more than 70% of the total [Fe II] flux of M82 and NGC 253 arises from diffuse emission features that does not seem to be associated with their SNRs. If so, there is a possibility that the expected total [Fe II] luminosity from the equation in Rosenberg et al. (2012) is overestimated by a factor of ~ 3.

2.4.3 SNR-MC Interaction

Most of massive stars with an initial mass of $\gtrsim 8\ M_{\odot}$ are born in giant molecular clouds (MCs) and end their lives as core-collapse SNe after $\lesssim 3 \times 10^7$ years. Unless the photo-ionizing photons and/or stellar winds from the progenitors have perfectly clear out the surrounding MCs, the SNRs will be interacted with the dense MC materials. Since more than 80% of the SNe are the core-collapse SNe, the "SNR-MC interaction" seems to be common phenomenon in nature. It is play an important role in triggering new star formations and is the most probable source of Galactic cosmic rays. The strongest observational evidence of the interaction is the detection of OH 1720 MHz maser, but there are a number of additional evidences supporting the SNR-MC interaction (Jiang et al., 2010): (1) detection of OH maser emission, (2) molecular line broadening, (3) morphological agreement with SNR features in molecular lines, (4) de-

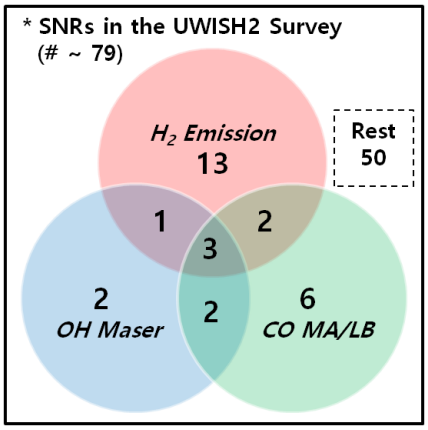

Figure 2.7 Venn diagram for the number of H_2-emitting SNRs (red circle). The numbers encircled by the green and blue area, on the other hand, represent the total numbers of SNRs that the detection of OH maser and either CO line broadening (LB) or CO emission features associated with SNRs (morphological agreement; MA) were reported in the previous radio observations.

tection of NIR H_2 emission lines. Among the 19 H_2-emitting SNRs in our survey area, one of third SNRs have either OH masers, CO line broadening, or CO emission features morphologically associated with the SNRs (see Figure 2.7), supporting the presence of SNR-MC interactions (Jiang et al., 2010). The rest of them have only H_2 line whose origins are unknown, and therefore, additional multi-wavelength studies will be needed to clear this out.

2.4.4 Origin of [Fe II] and H_2 associated with SNRs

According to previous studies, [Fe II] emission mainly arise from dense circumstellar/interstellar medium swept up by SN shock. For only two young SNRs, Cas A and G11.2−0.3, the detection of strong [Fe II] emission in their fast-moving (> 1000 km s^{-1}) SN ejecta were reported (Moon et al., 2009; Koo et al., 2013; Lee et al., 2017). Therefore, the radial velocity is an important physical parameter to identify their origins. In Section 2.3.2, we measured the radial velocities of [Fe II] lines detected in 3C 391 and KES 73, and showed their circumstellar origins with low line-of-sight velocities (a few 100 km s^{-1}). Despite of the same origin, their [Fe II] morphologies are very different.

[Fe II] emission features of 3C 391 is diffuse and extended, and their morphologies are simiar with that in radio continuum. On the other hand, the [Fe II] features in KES 73 are clumpy and very different to that in radio continuum. This may imply that their shocked surrounding mediums have different density distributions. In the case of 3C 391, we suggest that the ambient shock is slow ($\lesssim$ 100 km s^{-1}) and the surrounding medium have relatively homogeneous density distributions. So the [Fe II] emission features are diffuse and are similar with the radio morphology, since the [Fe II] lines arise from the post-shock cooling region just behind the ambient shock. For KES 73, on the other hand, it is likely that the ambient shock is fast ($\gtrsim$ 100 km s^{-1}) and non-radiative, so we cannot detect [Fe II] emission along the shock boundary. In the meanwhile, the SN shock propagating into the dense, clumpy medium can heat the gas up to 10^3–10^4 K and produce strong [Fe II] emission lines. We find similar morphologies of [Fe II] emission in the young SNR, Cas A. The previous NIR imaging and spectroscopic studies for Cas A showed that there are clumpy [Fe II] knots with very low radial velocity and that they are well coincide with the optical quasi-stationary flocculi, the dense circumstellar medium blown from the red giant phase of the progenitor (Gerardy & Fesen, 2001; Lee et al., 2017). We, therefore, suggest that the clumpy [Fe II] features in KES 73 are shocked, dense circumstellar medium, so the progenitor seems to be a red giant which results in a Type IIP or IIb/L SN explosion

Among the H_2-emitting SNRs, some of them also show Hα emission features (e.g., G9.9−0.8, G18.9−1.1, KES 78; Stupar & Parker, 2011). Since H_2 lines trace slow, non-dissociative C-shock, the recombination lines of H are not expected around the H_2 filaments. Therefore the detection of atomic and molecular hydrogen raises the question of the excitation mechanism H_2 lines and their origins. For G9.9−0.8, for example, we found that the detected H_2 features show strong anti-correlation with the Hα filaments (Stupar & Parker, 2011). This distribution is analogous to that in photo-dissociation regions, and it is possibility that they arise from UV fluorescence rather than the SN shock. To reveal the origin of the H_2 filaments, we need NIR spectroscopic observations for the filaments. The H_2 line ratio together with their line width can distinguish whether they are shocked or photo-excited H_2 gas (see Section 2.4.1).

2.5 Summary

We have searched [Fe II] 1.64 μm and H_2 2.12 μm emission line features around the Galactic SNRs using UWIFE and UWISH2 surveys. The bright emission lines with various morphologies were detected around 27 SNRs. We also performed NIR spectroscopic observations of four Galactic SNRs (G11.2−0.3, KES 69, KES 73, and 3C 391) which show either [Fe II], H_2, or both in the surveys. Several bright [Fe II] and H_2 emission lines were clearly detected in the spectra. From their line ratios and radial velocities, we investigated the origin of the emission lines. Our main results are listed in the following.

1. Among 79 Galactic SNRs fully covered by the surveys, we found 19 [Fe II]- and 19 H_2-emitting SNRs corresponding to 24% in detection rate for each, and 11 of them are emitting both [Fe II] and H_2 lines. Furthermore, more than a half of our detections are new discoveries, that have never been reported in previous studies.

2. Even though the overall detection rate of both emission lines is $\sim$ 24%, the detection rate reaches up to $\sim$ 50% at $l = 40°$–$50°$ for [Fe II] and at $l = 30°$–$40°$ for H_2, and is gradually decreasing toward the Galactic center which may due to increase of the interstellar extinction. The different peaks in the [Fe II] and H_2 detection rates can be explained by the different SN populations along the Galactic longitude, but this need to be investigated in more detail in the near future.

3. Several bright SNRs emitting both [Fe II] and H_2 lines clearly show "[Fe II]-H_2 reversal:" H_2 emission extends the outside of the radio and [Fe II] emission line boundary. Especially, the extended H_2 emission features detected in G11.2−0.3 far outside the remnant's boundary are of interest. The H_2 line ratios detected in NIR spectra of G11.2−0.3 imply that they are arising from the collisionally excited H_2 gas, but the exciting sources remain to be explored.

4. We measured the flux of the [Fe II] emission lines. The total [Fe II] luminosity in our survey is $\sim 2 \times 10^4\ L_\odot$, and W49B is responsible for more than 70% of them. The total [Fe II] luminosity of our Galaxy extrapolated from our observation is a few times fainter than that expected from the SN rate of our Galaxy. This may imply either that

there are many SNRs whose [Fe II] lines are undetected in the survey, or that there are many missing SNRs that have not been known so far.

5. The small radial velocities of [Fe II] lines detected in 3C 391 and KES 73 imply that they are the shocked circumstellar/interstellar medium, rather than the high speed SN ejecta. The [Fe II] morphologies of the SNRs, however, are very different, (i.e., diffuse [Fe II] emission in 3C 391 vs. small [Fe II] clump in KES 73) and this may be due to different density distributions of their surrounding medium.

Biblography

Adams, S. M., Kochanek, C. S., Beacom, J. F., Vagins, M. R., & Stanek, K. Z. 2013, ApJ, 778, 164

Alonso-Herrero, A., Rieke, G. H., Rieke, M. J., & Kelly, D. M. 2003, AJ, 125, 1210

Black, J. H., & Dalgarno, A. 1976, ApJ, 203, 132

Black, J. H., & van Dishoeck, E. F. 1987, ApJ, 322, 412

Bocchino, F., Bykov, A. M., Chen, Y., et al. 2012, A&A, 541, A152

Borkowski, K. J., Reynolds, S. P., & Roberts, M. S. E. 2016, ApJ, 819, 160

Bruursema, J., Meixner, M., Long, K. S., & Otsuka, M. 2014, AJ, 148, 41

Burton, M. G. 1992, Australian Journal of Physics, 45, 463

Burton, M. G., Hollenbach, D. J., & Tielens, A. G. G. M. 1990, ApJ, 365, 620

Burton, M., & Spyromilio, J. 1993, Proceedings of the Astronomical Society of Australia, 10, 327

Cappellaro, E., & Turatto, M. 1988, A&A, 190, 10

Cappellaro, E., Turatto, M., Benetti, S., et al. 1993, A&A, 273, 383

Carey, S. J., Noriega-Crespo, A., Mizuno, D. R., et al. 2009, PASP, 121, 76

Chernoff, D. F., McKee, C. F., & Hollenbach, D. J. 1982, ApJL, 259, L97

Diehl, R., Halloin, H., Kretschmer, K., et al. 2006, Nature, 439, 45

Diolaiti, E., Bendinelli, O., Bonaccini, D., et al. 2000, Proc. SPIE, 4007, 879

Draine, B. T. 1980, ApJ, 241, 1021

Draine, B. T. 2003, ARAA, 41, 241

Draine, B. T., & Roberge, W. G. 1982, ApJL, 259, L91

Dye, S., Warren, S. J., Hambly, N. C., et al. 2006, MNRAS, 372, 1227

Faucher-Giguère, C.-A., & Kaspi, V. M. 2006, ApJ, 643, 332

Frail, D. A., Goss, W. M., Reynoso, E. M., et al. 1996, AJ, 111, 1651

Froebrich, D., Davis, C. J., Ioannidis, G., et al. 2011, MNRAS, 413, 480

Froebrich, D., Makin, S. V., Davis, C. J., et al. 2015, MNRAS, 454, 2586

Gerardy, C. L., & Fesen, R. A. 2001, AJ, 121, 2781

Gotthelf, E. V., & Vasisht, G. 1997, ApJL, 486, L133

Graham, J. R., Wright, G. S., Hester, J. J., & Longmore, A. J. 1991, AJ, 101, 175

Graham, J. R., Wright, G. S., & Longmore, A. J. 1987, ApJ, 313, 847

Graham, J. R., Wright, G. S., & Longmore, A. J. 1990, ApJ, 352, 172

Greenhouse, M. A., Woodward, C. E., Thronson, H. A., Jr., et al. 1991, ApJ, 383, 164

Green, A. J., Frail, D. A., Goss, W. M., & Otrupcek, R. 1997, AJ, 114, 2058

Green, D. A., Gull, S. F., Tan, S. M., & Simon, A. J. B. 1988, MNRAS, 231, 735

Green, D. A. 2014, Bulletin of the Astronomical Society of India, 42, 47

Hewitt, J. W., Yusef-Zadeh, F., & Wardle, M. 2008, ApJ, 683, 189

Hollenbach, D., & McKee, C. F. 1989, ApJ, 342, 306

Jiang, B., Chen, Y., Wang, J., et al. 2010, ApJ, 712, 1147

Keane, E. F., & Kramer, M. 2008, MNRAS, 391, 2009

Keohane, J. W., Reach, W. T., Rho, J., & Jarrett, T. H. 2007, ApJ, 654, 938

Kilpatrick, C. D., Bieging, J. H., & Rieke, G. H. 2016, ApJ, 816, 1

Koo, B.-C., & Lee, Y.-H. 2015, Publication of Korean Astronomical Society, 30, 145

Koo, B.-C., Lee, Y.-H., Moon, D.-S., Yoon, S.-C., & Raymond, J. C. 2013, Science, 342, 1346

Koo, B.-C., Moon, D.-S., Lee, H.-G., Lee, J.-J., & Matthews, K. 2007, ApJ, 657, 308

Koo, B.-C., Raymond, J. C., & Kim, H.-J. 2016, Journal of Korean Astronomical Society, 49, 109

Kriss, G. A., Becker, R. H., Helfand, D. J., & Canizares, C. R. 1985, ApJ, 288, 703

Kumar, H. S., Safi-Harb, S., Slane, P. O., & Gotthelf, E. V. 2014, ApJ, 781, 41

Labrie, K., & Pritchet, C. J. 2006, ApJS, 166, 188

Leaman, J., Li, W., Chornock, R., & Filippenko, A. V. 2011, MNRAS, 412, 1419

Lee, H.-G., Moon, D.-S., Koo, B.-C., et al. 2013, ApJ, 770, 143

Lee, H.-G., Moon, D.-S., Koo, B.-C., Lee, J.-J., & Matthews, K. 2009, ApJ, 691, 1042

Lee, J.-J., Koo, B.-C., Lee, Y.-H., et al. 2014, MNRAS, 443, 2650

Lee, Y.-H., Koo, B.-C., Moon, D.-S., Burton, M. G., & Lee, J.-J. 2017, ApJ, 837, 118

Li, W., Chornock, R., Leaman, J., et al. 2011, MNRAS, 412, 1473

Lucas, P. W., Hoare, M. G., Longmore, A., et al. 2008, MNRAS, 391, 136

Moffett, D. A., & Reynolds, S. P. 1994, ApJ, 425, 668

Moon, D.-S., Koo, B.-C., Lee, H.-G., et al. 2009, ApJL, 703, L81

Morel, T., Doyon, R., & St-Louis, N. 2002, MNRAS, 329, 398

Mouri, H., Kawara, K., & Taniguchi, Y. 2000, ApJ, 528, 186

Neufeld, D. A., & Dalgarno, A. 1989, ApJ, 340, 869

Oliva, E., Moorwood, A. F. M., & Danziger, I. J. 1989, A&A, 214, 307

Oliva, E., Moorwood, A. F. M., & Danziger, I. J. 1990, A&A, 240, 453

Pinheiro Gonçalves, D., Noriega-Crespo, A., Paladini, R., Martin, P. G., & Carey, S. J. 2011, AJ, 142, 47

Reach, W. T., Rho, J., & Jarrett, T. H. 2005, ApJ, 618, 297

Reach, W. T., Rho, J., Jarrett, T. H., & Lagage, P.-O. 2002, ApJ, 564, 302

Reach, W. T., Rho, J., Tappe, A., et al. 2006, AJ, 131, 1479

Reynolds, S. P., & Moffett, D. A. 1993, AJ, 105, 2226

Rieke, G. H., Blaylock, M., Decin, L., et al. 2008, AJ, 135, 2245

Roberts, M. S. E., Tam, C. R., Kaspi, V. M., et al. 2003, ApJ, 588, 992

Rosenberg, M. J. F., van der Werf, P. P., & Israel, F. P. 2012, A&A, 540, A116

Stephenson, F. R., & Green, D. A. 2002, Historical supernovae and their remnants, Oxford: Clarendon Press

Sternberg, A., & Dalgarno, A. 1989, ApJ, 338, 197

Strom, R. G. 1994, A&A, 288, L1

Stupar, M., & Parker, Q. A. 2011, MNRAS, 414, 2282

Tammann, G. A., Loeffler, W., & Schroeder, A. 1994, ApJS, 92, 487

The, L.-S., Clayton, D. D., Diehl, R., et al. 2006, A&A, 450, 1037

Tian, W. W., & Leahy, D. A. 2008, ApJ, 677, 292-296

Timmes, F. X., Diehl, R., & Hartmann, D. H. 1997, ApJ, 479, 760

Tokunaga, A. T., & Vacca, W. D. 2005, PASP, 117, 421

Torii, K., Tsunemi, H., Dotani, T., & Mitsuda, K. 1997, ApJL, 489, L145

Vasisht, G., & Gotthelf, E. V. 1997, ApJL, 486, L129

Vranesevic, N., Manchester, R. N., Lorimer, D. R., et al. 2004, ApJL, 617, L139

Wilner, D. J., Reynolds, S. P., & Moffett, D. A. 1998, AJ, 115, 247

Yusef-Zadeh, F., Wardle, M., Rho, J., & Sakano, M. 2003, ApJ, 585, 319

Zajczyk, A., Gallant, Y. A., Slane, P., et al. 2012, A&A, 542, A12

Zhou, X., Chen, Y., Su, Y., & Yang, J. 2009, ApJ, 691, 516

Zwicky, F. 1938, ApJ, 88, 529

Chapter 3

High Resolution Near-Infrared Spectroscopy of Extended H_2 emission around Galactic Supernova Remnants

3.1 Introduction

Molecular hydrogen (H_2) is most abundant molecule in Universe, and plays an important role in the evolution of interstellar medium as a catalyst of chemistry and a major coolant at $T \gtrsim$ a few 1000 K (Burton, 1992). The ground state of H_2 can be easily excited via two major processes: (1) thermal process (collisional excitation) and (2) non-thermal process (radiative excitation), and then radiates strong near- and mid-infrared emission lines through various rotational-vibrational transitions. The thermal excitation process involves the collisional heating of the H_2 by either shock or UV/X-ray radiation in high density regions ($\gtrsim 10^6$ cm^{-3}; Sternberg & Dalgarno, 1989; Burton et al., 1990), and their level populations would be characterized by Boltzmann distribution with a single temperature. Since H_2 would be efficiently dissociated in high temperature condition greater than 4000–5000 K, H_2 lines may arise from warm H_2 gas with a narrow temperature range from 500 K to 3000 K. Furthermore, the ratio of

ortho-H_2 (two parallel proton spins) to para-H_2 (two anti-parallel proton spins) of the warm ($\gtrsim$ 200 K) H_2 gas in local thermodynamic equilibrium (LTE) is expected to be close to the ratio of their statistical weights (ortho-H_2 : para-H_2 $\sim$ 3 : 1; Smith et al., 1997; Takahashi, 2001). The non-thermal excitation of H_2, on the other hand, involves the absorption of far-ultraviolet (far-UV) photons. In the regions where the UV photon is dominant, e.g., photo-dissociation region, reflection nebulae around O/B stars, H_2 in the electronic ground state ($X^1\Sigma_g^+$) can be excited into higher electronic states ($B^1\Sigma_u^+$ and $C^1\Pi_u^+$; Lyman and Werner) by the absorption of FUV photons (11.2 eV – 13.6 eV). About 90% of the excited H_2 is then de-excited into the ground electronic state with high vibrational energy levels with $v \geq 13$ followed by the radiative cascade downwards into $v = 0$ (Black & Dalgarno, 1976; Black & van Dishoeck, 1987). This "top-down" process more populates $v \geq 3$ levels compared to the thermal process ("bottom-up"), so the H_2 level population diagram shows "sawtooth" pattern (e.g., Kaplan et al., 2017; Le et al., 2017). In contrast to the thermal process in LTE, the ortho-to-para ration seems to be less than 3 according to the previous NIR observations (Le et al., 2017, and references therein).

The previous near-infrared (NIR) observations found that the several Galactic SNRs show strong lines of H_2 together with the forbidden lines of a singly ionized Fe lines ([Fe II]), in entire $J/H/K$-bands, and these two NIR emission lines seem to be highly associated with the SN shocks (e.g., Oliva et al., 1990; Koo et al., 2007; Lee et al., 2009). Since a fast ($v_s > 50$ km s^{-1}) atomic shock can efficiently dissociate H_2, the emission lines seem to mainly arise from either (1) the post-shock cooling region of slow ($v_s < 50$ km s^{-1}), non-dissociative C-shocks (Draine, 1980; Chernoff et al., 1982; Draine & Roberge, 1982), or (2) the far downstream ($n_H \sim 10^{18-21}$ cm^{-2}) of dissociative J-shocks where the H_2 can be reformed (Hollenbach & McKee, 1989; Neufeld & Dalgarno, 1989). On the other hand, the NIR [Fe II] ($\gtrsim$ 0.8 μm) lines are believed to arise from electron collision of Fe^+ in the post-shock cooling region just behind the fast ($v_s > 50$ km s^{-1}), dissociative J-shocks (Mouri et al., 2000; Koo et al., 2016). Recently, two NIR narrow-band imaging surveys had been carried out for the first Galactic quadrant ($7^\circ < l < 62^\circ$ and $|b| < 1.^\circ3$) using [Fe II] 1.64 μm and H_2 2.12 μm filters,

which are the most strong emission lines in NIR [Fe II] and H_2 (Froebrich et al., 2011; Lee et al., 2014). Among the 79 SNRs falling in the survey area, we found 19 [Fe II]-emitting and 19 H_2-emitting SNRs, and then compared their spatial distributions (Lee, Y.-H. et al. 2017, in preparation). One of the most interesting results in the study is that five SNRs (G11.2-0.2, KES 73, W44, 3C 396, W49B) emitting both the emission features show extended H_2 filaments outside the [Fe II]/radio boundaries. This is opposite to the standard picture; if the shocks are driven by the same blast wave, we may expect the H_2 filaments to be closer to the explosion center than the [Fe II] filaments, because in general the former is from slower C-shocks whereas the latter is from fast J-shocks. The H_2 emission can also originate from a J-shock if H_2 molecules reform, but, again, it is further downstream from the [Fe II]-emitting region. Such "[Fe II]-H_2 reversal" accompanied by extended H_2 filaments had been known in several Galactic SNRs, since the early days of infrared studies (Oliva et al. 1990, Burton & Spyromilio 1993 for RCW 103, Graham et al. 1991 for Cygnus loop, Koo et al. 2007 for G11.2−0.3, Keohane et al. 2007 for W49B, Lee et al. 2009 for 3C 396). In order to explain the "[Fe II]-H_2 reversal," we first need to understand the excitation mechanism of the extended H_2 detected far beyond the [Fe II]/radio boundary. Several explanations have been suggested: (1) radiative/magnetic precursors, (2) UV fluorescence excitation, (3) complex projection effect of multi-shock, but it is still unclear so far.

In this paper, we perform high resolution NIR spectroscopy for the extended H_2 emission features detected around the five Galactic SNRs. The three physical parameters are important to understand the excitation mechanism of the H_2 lines: (1) flux ratios, (2) line widths, and (3) ortho-to-para ratio (Burton, 1992). If the H_2 gas is collisionally excited by the SN shocks, then their flux ratios will be analogous to that of Boltzmann distribution with an appropriate temperature and their line widths will be quite broad with a full-width at half-maximum (FWHM) of up to an order of the shock velocity (i.e., a few 10 km s^{-1}). In this case, the ortho-to-para ratio will be close to 3:1. If the H_2 lines arise from the UV fluorescence, on the other hand, they may show the relative bright H_2 lines from $v \geq 3$ levels compared to the thermal process, unless the density is larger than $\sim 10^6$ cm^{-3} (Sternberg & Dalgarno, 1989; Burton et al., 1990).

Furthermore, the UV-excited ambient H_2 gas is expected to have a very narrow line width with $\lesssim 5$ km s^{-1} corresponding to its typical turbulent velocity (Hollenbach & McKee, 1989; Burton, 1992), and an ortho-to-para ratio of less than 3. This paper is organized as follows. In Section 3.2, we outline our NIR spectroscopic observations and the data reduction procedures. In Section 3.3, we identify strong H_2 lines detected in *H*- and *K*-bands and derive their radial velocities, line widths, and fluxes from a single Gaussian fitting. From the three physical parameters, in Section 3.4, we discuss about the excitation mechanism of the H_2 lines we observed and the origin of the extended H_2 emission features detected around the SNRs. Finally, the paper is summarized in Section 3.5.

3.2 Observations and Data Analysis

NIR spectroscopy for the extended H_2 features around the five Galactic SNRs were carried out in 2014 May, 2015 June, and 2016 July, using Immersion GRating INfrared Spectrograph (IGRINS) attached on the 2.7 m Harlan J. Smith Telescope in the McDonald observatory. The IGRINS is a cross-dispersed NIR spectrograph with a spectral resolution of 40,000, which simultaneously covers the almost entire *H*- and *K*-band (1.5–1.8 μm and 1.9–2.5 μm; Yuk et al., 2010; Park et al., 2014). The slit width and length of IGRINS at the 2.7 m telescope are fixed to $1''$ and $15''$, respectively. Figure 3.1 shows the slit positions of the five SNRs. We carefully selected the slit positions in order for the slits to cover bright, extended H_2 filaments far outside the radio and [Fe II] boundaries. Since the size of the H_2 features are similar or larger than the slit length ($15''$), we took off-source sky frames just before or after the on-source science frames in order to remove sky background emission detected in the NIR waveband. The exposure time per frame was set to be 300 s and the position angle of all the slits was 90° (East-to-West direction). We also obtained several spectra of A0V standard stars near the targets at each day that are used for photometric calibration. Table 3.1 summarizes the observation logs.

All the data we obtained were preprocessed by the dedicated data reduction pipeline

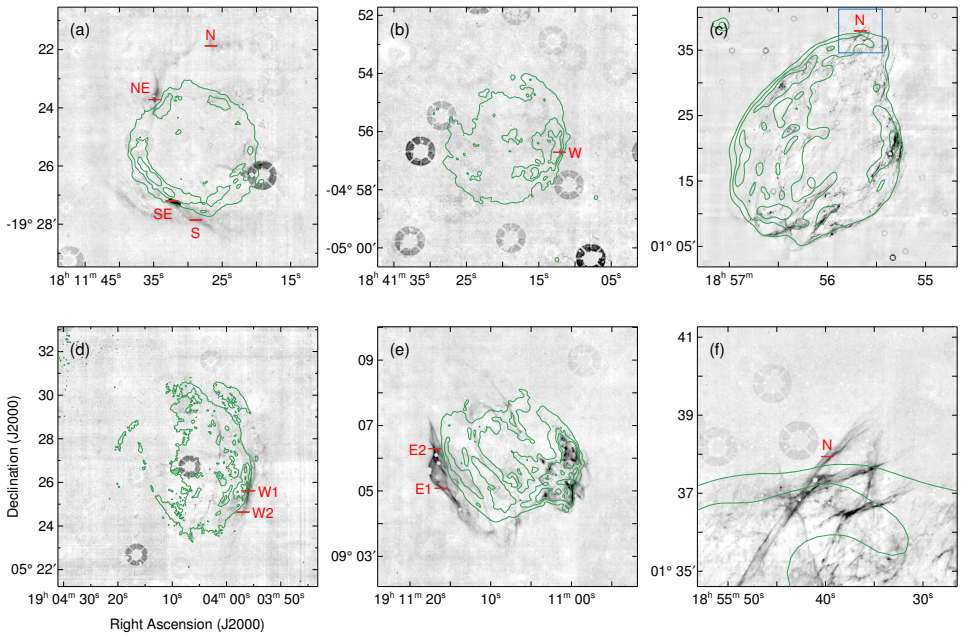

Figure 3.1 Slit positions of Five Galactic SNRs: (a) G11.2−0.3, (b) KES 73, (c) W44, (d) 3C 396, and (e) W49B. The background images show the continuum-subtracted H_2-2.12 μm narrow-band images obtained in UWISH2 survey (Froebrich et al., 2011). The enlarged image of the northern part of W44 (blue box) are shown in (f). The green contours represent the radio continuum.

Table 3.1. Log of NIR Spectroscopy

SNR Name	Slit Name	Slit Position [α(J2000)	δ(J2000)]	Exposure Time (seconds)
G11.2−0.3	N	18:11:26.64	−19:21:52.2	300 × 2
	S	18:11:28.85	−19:27:51.5	300 × 1
	SE	18:11:32.35	−19:27:12.0	300 × 1
	NE	18:11:34.82	−19:23:43.0	300 × 1
KES 73	W	18:41:12.15	−04:56:42.6	300 × 1
W44	N	18:55:39.80	+01:37:56.4	300 × 1
3C 396	W1	19:03:55.86	+05:25:36.9	300 × 1
	W2	19:03:56.94	+05:24:38.3	300 × 1
W49B	E1	19:11:16.14	+09:05:04.9	300 × 1
	E2	19:11:16.91	+09:06:17.5	300 × 1

Note. — All the slit are aligned along the East–West direction corresponding to a position angle of 90°.

for IGRINS written in Python[1]. First, the pipeline make a master flat image by median-averaging of all normalized flat frames, and all the observed frames were divided by the master flat in order to correct pixel-to-pixel variation of the detectors. The sky background emission in the on-source science frames was removed by subtracting their off-source frames. The pipeline also performed aperture extraction and distortion correction for every orders detected in the *H*- and *K*-band echellograms, and produced the preprocessed two-dimensional (2-D) spectra. We extracted the one-dimensional (1-D) spectrum of each target by integrating along the y-axis of the 2-D spectrum, and divided it by the mean spectrum of A0V standard stars for relative photometric calibration. The wavelength calibration was done by using bright, isolated OH airglow emission lines, and 2-D polynomial fitting for their central wavelengths over the observed *H*- and *K*-band echellograms provides the 1-sigma uncertainty of ~ 0.5 pixels corresponding to ~ 1 km s^{-1}.

[1]The pipeline package is downloadable at https://github.com/igrins/plp

Table 3.2. Kinematic Properties of H_2 1-0 S(1)

SNR Name	Slit Name	v_{LSR}[a] (km s^{-1})	FWHM[b](km s^{-1}) observed	FWHM[b](km s^{-1}) corrected[c]	1-0 S(0) / 1-0 S(1) observed	1-0 S(0) / 1-0 S(1) corrected[d]	References[e]
G11.2−0.3	N	47.4 (0.2)	14.5 (0.4)	12.7 (0.4)	0.20 (0.06)	0.17 (0.05)	1, 2
	S	46.6 (0.1)	14.9 (0.3)	13.2 (0.3)	0.17 (0.04)	0.15 (0.03)	1, 2
	SE	49.3 (0.1)	13.8 (0.1)	11.9 (0.1)	0.19 (0.01)	0.17 (0.01)	1, 2
	NE	49.0 (0.1)	13.8 (0.2)	11.9 (0.2)	0.20 (0.03)	0.17 (0.03)	1, 2
KES 73	W	99.2 (0.1)	13.5 (0.3)	11.5 (0.3)	0.23 (0.04)	0.20 (0.03)	3
W44	N	40.6 (0.1)	19.4 (0.3)	18.0 (0.3)	0.26 (0.04)	0.24 (0.04)	4, 5
3C 396	W1	55.2 (0.1)	12.8 (0.2)	10.7 (0.2)	0.26 (0.04)	0.22 (0.03)	6
	W2	56.6 (0.3)	13.8 (0.6)	11.9 (0.5)	0.16 (0.07)	0.14 (0.06)	6
W49B	E1	65.2 (0.1)	11.5 (0.2)	9.1 (0.2)	0.24 (0.03)	0.19 (0.02)	7
	E2	63.5 (0.1)	11.8 (0.1)	9.5 (0.1)	0.24 (0.02)	0.19 (0.02)	7

[a]Radial velocity of H_2 1-0 S(1) at Local Standard-of-Rest frame. The uncertainty within a parenthesis do not include the absolute uncertainty of a wavelength solution corresponding to about half pixel width ($\sim$ 1 km s^{-1}).

[b]Full Width at Half Maximum of H_2 1-0 S(1).

[c]Intrinsic FWHM of the line deconvolved with the instrument profile (7 km s^{-1}) assuming the both profiles are a single Gaussian shape.

[d]Extinction-corrected flux ratio assuming the general interstellar dust composition (Draine, 2003).

[e] References for the hydrogen column density used for the extinction correction in the 7th column.

References. — (1) Lee et al. (2013), (2) Borkowski et al. (2016), (3) Kumar et al. (2014), (4) Rho et al. (1994), (5) Shelton et al. (2004), (6) Lee et al. (2009), (7) Keohane et al. (2007)

3.3 Results

In all the spectra, we clearly detected H_2 1–0 S(1) 2.12 μm and 1–0 S(0) 2.22 μm. In the case of the brightest H_2 knot in G11.2−0.3 (G11.2−0.3 - SE), we found a dozen of H_2 lines in K-band. We performed a single Gaussian fitting for all the detected lines and derived their line-of-sight velocity corrected to Local Standard of Rest frame (v_{LSR}), line widths in Full Width at Half Maximum (FWHM), and fluxes normalized to those of H_2 1–0 S(1) 2.12 μm. Table 3.2 listed the three physical parameters.

In Table 3.3, we compared the mean v_{LSR} of H_2 lines with the systematic line-of-sight velocity of SNRs derived from the previous radio observations (CO emission, H I absorption, and OH maser). For all the SNRs, the v_{LSR} of H_2 lines are in the velocity range of either CO emission, H I absorption, or OH maser emission. The

Table 3.3. LSR Velocity of five SNRs

SNR Name	$v_{\rm LSR}$ (km s^{-1})				$d_{\rm kin}$[c] (kpc)	References[d]
	H_2[a]	CO	H I[b]	OH maser		
G11.2-0.3	+48	+29–+36	+45 (N)	-	4.7	1, 2
KES 73	+99	+100	+89–+110 (F)	-	9.3	2, 3
W44	+41	+30–+65	+42 (N)	+38–+47	2.8	4, 5, 6
3C 396	+56	+69, +84	+60–+80 (F)	-	9.4	4, 7, 8
W49B	+64	+14, +39	+40–+70 (F)	-	7.5	2, 9, 10

[a]Radial velocities of H_2 1-0 S(1) at Local Standard-of-Rest frame derived in this study.

[b]N or F in parentheses mean "near" or "far" side of its tangential point.

[c]Kinematic distances derived from the $v_{\rm LSR}$ of H_2 in the 2$^{\rm nd}$ column, assuming the flat Galactic rotation model with the IAU standard rotation constants ($R_\odot = 8.5$ kpc, $V_\odot = 220$ km s^{-1}).

[d]References of $v_{\rm LSR}$ derived from CO emission (3$^{\rm rd}$ column), H I absorption (4$^{\rm th}$ column), and OH maser observations (5$^{\rm th}$ column).

References. — (1) Green et al. (1988), (2) Kilpatrick et al. (2016), (3) Tian & Leahy (2008), (4) Caswell et al. (1975), (5) Seta et al. (1998), (6) Hewitt et al. (2008), (7) Lee et al. (2009), (8) Su et al. (2011), (9) Chen et al. (2014), (10) Zhu et al. (2014)

H_2 morphologies together with these $v_{\rm LSR}$ similar with the systematic velocity, implies that the H_2 filaments we see are physically associated with the SNRs. We measured the kinematic distances of the five SNRs from the observed $v_{\rm LSR}$ of H_2 lines, assuming the flat Galactic rotation model with the IAU standard rotation constants ($R_\odot = 8.5$ kpc, $V_\odot = 220$ km s^{-1}; see Table 3.3). Distances of the three SNRs, G11.2-0.3, KES 73, and W44, have been constrained in the previous studies, and our estimations are well consistent with them within 1 kpc. The distances of 3C 396 and W49B, however, have been controversial because of the complexity of the molecular clouds along the line-of-sight. In the previous studies, the distances of 3C 396 ranges from 6.2 kpc (at the tangential point) to 11.3 kpc (Caswell et al., 1975; Lee et al., 2009; Su et al., 2011), whereas that of W49B ranges from 8.0 kpc to 12.5 kpc (e.g., Lockhart & Goss, 1978; Moffett & Reynolds, 1994; Zhu et al., 2014) In this paper, we suggested the distance of 3C 391 and W49B of 9.4 and 7.5 kpc, respectively. It is worth noticing that the 7.5 kpc as a distance of W49B is the lowest value among the previous one that have ever been suggested so far.

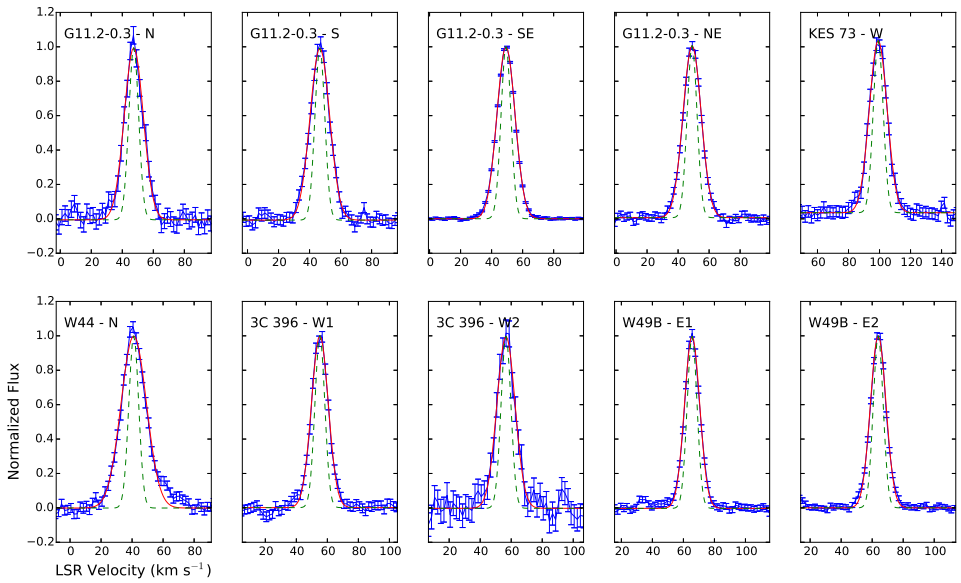

Figure 3.2 Line profiles of H_2 1–0 S(1) 2.12 μm lines. The blue represents the observed line profiles normalized by their peak intensities, and the red indicates their single Gaussian model. The instrumental profiles are shown in the green dashed lines.

Figure 3.2 shows the line profile of the observed H_2 1–0 S(1) 2.12 μm lines, together with a best-fit model and the instrumental profile with 7 km s^{-1}. As seen in the figure, all the line can be well explained by a single Gaussian model. This may imply that the H_2-emitting gas has a single velocity component, so their line widths reflect quadrature sum of intrinsic thermal broadening and turbulence broadening. The observed line widths of the H_2 line are 12–19 km s^{-1} which is much broader than that of the instrumental profile (Table 3.2). Using an Gaussian deconvolution, we derived the intrinsic line width of 9–18 km s^{-1} which is much larger than the typical turbulent velocity of ambient gas (1–5 km s^{-1}; Hollenbach & McKee, 1989). This is indeed broader than the H_2 line width observed in the reflection nebula NGC 7023 where the H_2 gas is radiatively excited (FWHM $\sim$ 2–6 km s^{-1} Le et al., 2017).

In Table 3.2, we also listed the flux ratio of H_2 1–0 S(0) to 1–0 S(1). These two lines have same vibrational transition from $v = 1$ to 0, but have different rotational

transition, so their ratio represents rotational temperature of the gas. Furthermore, they are either para- or ortho-hydrogen, the ratio is also affected by the ortho-to-para ratio of the gas. According to the previous theoretical study, the collisionally excited H_2 gas with $T = 2000$ K shows the flux ratio of ~ 0.2, whereas that from the radiatively excited H_2 gas ranges from 0.4 to 0.6 (Black & van Dishoeck, 1987). Those different line ratios were confirmed by a large number of NIR observations; the previous NIR observations for the shock-heated H_2 gas shows the ratio of 0.15–0.25 (Orion KL outflow, Herbig-Haro objects; Gredel, 1996; Oh et al., 2016a,b), whereas the flux ratio by UV fluorescence ranges from 0.43–0.62 (Giant H II region, reflection nebulae; Hasegawa et al., 1987; Puxley et al., 2000; Le et al., 2017) In our observation, the extinction-corrected H_2 flux ratios range from 0.13–0.25 (Table 3.2), which is consistent with that from the collisionally exited H_2 gas in the previous studies. In the southeast H_2 clump in G11.2−0.3, we clearly detected a dozen of ro-vibrational H_2 lines in K-band, transitions from upper levels with $T = 5000$ K to 20,000 K. Figure 3.3 shows its H_2 level population diagram. All the lines, including H_2 3–2 S(3) 2.20 μm from a high-excitation level (19086 K), are well fitted by a Maxwellian distribution with $T \sim 2500$K, and their distribution is contrast to the "sawtooth" pattern in photo-dissociation region or reflection nebula where the UV excitation (fluorescence) is dominant (e.g., Kaplan et al., 2017; Le et al., 2017).

3.4 Discussion

In Section 3.3, we showed that all the observed H_2 lines are broad ($\gtrsim 10$ km s^{-1}), and have thermal line ratios (see Table 3.2). This implies that the H_2 lines arise from the shock-heated H_2 gas in dense circumstellar medium or molecular clouds physically associated with the SNRs. The thermal broadening by the H_2 gas with $T \sim 3000$ K (see Figure 3.3) is only 6 km s^{-1} assuming Maxwellian distribution of H_2 molecules ($1/2\ m_{H2}\ v_{H2}^2 = 3/2\ k\ T_{H2}$). Therefore, the large fraction of the H_2 line width seems to be responsible for turbulence of the gas by the shock. Although the SN shock propagating into the ambient medium can be the most plausible source of the heating,

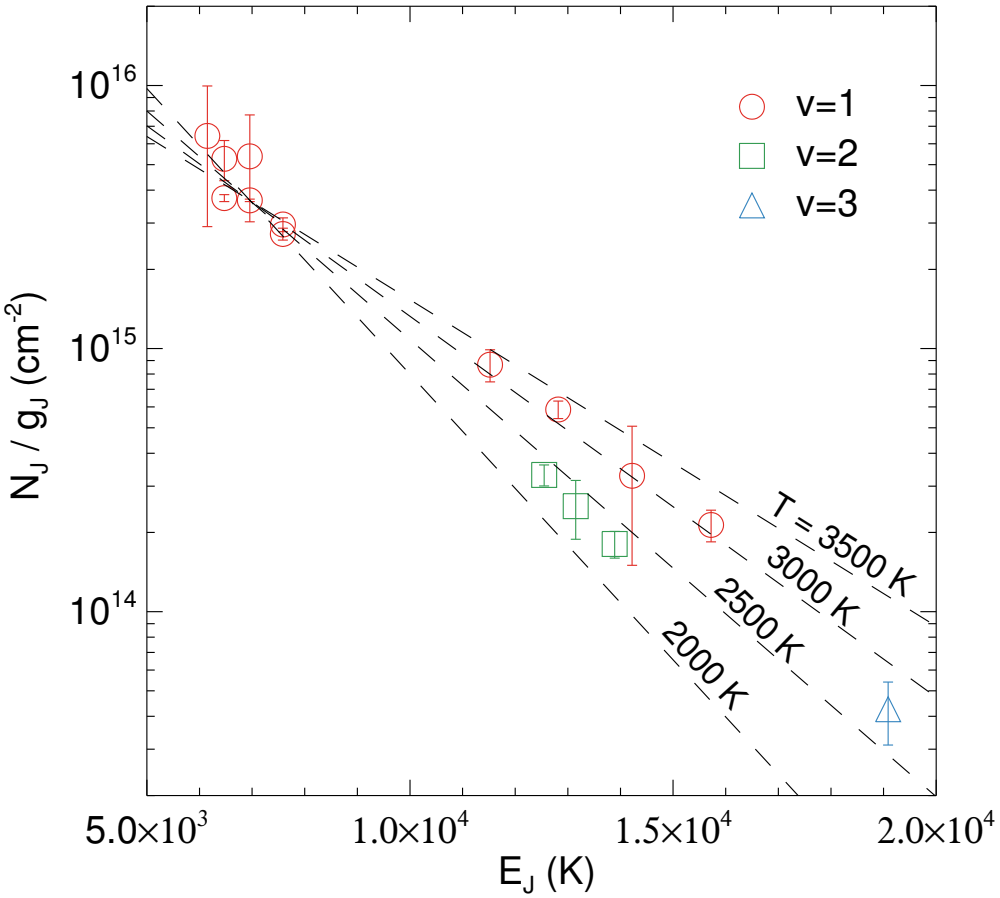

Figure 3.3 H_2 level population diagram of the brightest H_2 clump in G11.2−0.3 (G11.2−0.3 - SE).

it is not easy to be explained by simple J-type and C-type shock models considering the relative location of H_2 filaments (see Section 3.1). Here, we suggest three possible solutions: (1) magnetic precursor ahead of SN shock, (2) projection effect of SN shock, and (3) slow non-dissociative C-shock produced by the pre-SN wind.

When the magnetic field strength of the preshock gas with low ionization is high enough so that the magnetosonic speed exceeds the shock speed, then compressive wave in the plasma can propagate upstream ahead of the shock front (magnetic precursor) and heat the preshock gas before the shock is arrived (Draine, 2011). This is an intermediate stage between simple J-type and C-type shock (i.e., J-type shock with a magnetic precursor), and we may expected strong H_2 lines in the warm ($T \sim$ a few 1000 K) precursor followed by the strong [Fe II] lines in the postshock cooling region just behind of the J-shock front (Graham et al., 1991; McCoey et al., 2004; Keohane et al., 2007). According to the previous theoretical studies, the magnetic precursor can be extended to 10^{15}–10^{17} cm from the shock discontinuity depending on the magnetic field strength, shock velocity, and number density of the preshock gas (Graham et al., 1991; Draine & McKee, 1993; Draine, 2011). For KES 73, the H_2 clump in the western border of the remnant is detected only 2–3″ outside the [Fe II] filaments corresponding to a few 10^{17} cm assuming the remnant's distance of 9 kpc (Table 3.3). In this case, therefore, the magnetic precursor can be a solution explaining the "[Fe II]-H_2 reversal." In the case of other SNRs, however, the physical separation between [Fe II] and H_2 is a few 10^{18} cm, which is at least an order of magnitude larger than the length scale of the magnetic precursor expected in the previous theoretical studies.

Since the SNRs are not always spherical but significantly distorted by the surrounding medium as they evolved, projection effect is an important factor for considering the spatial distribution of the emission lines. Let us suppose that the two different shocks, i.e, fast atomic J-shock and slow non-dissociative C-shock, are propagating into different directions along the perpendicular to our line-of-sight. The good example is IC 443, one of the middle-aged SNRs in our Galaxy. The northeastern shell of the remnant swept-up by a fast atomic J-shock radiates bright [Fe II] emission lines, whereas the southern region where C-shock is propagating shows bright H_2 emission filaments (Rho

et al., 2001). In this case, we may expect the extended H_2 filaments far outside the [Fe II] filaments depending on the geometrical structure of the SNRs and the direction of our line-of-sight. Among the five SNRs we observed, the H_2 filaments detected in W44 could be the best case for explaining by the projection effect. As seen in Figure 3.1-(c) and (f), the northern H_2 filaments are bright and narrow, and are aligned along the SW-NE direction from the inside to the outside of the remnant shell without any brightness changes. It seems that there is no physical connection between the H_2 filaments and the radio-bright northern shell. In the other SNRs, in contrast, most of the H_2 features we observed are in contact with the [Fe II]/radio shell and almost parallel to the remnant's boundary. In the case of northern H_2 filaments in G11.2−0.3, however, it is not easy to explain the large physical separation between two NIR lines by using the projection effect. The H_2 filaments located $3\farcm7$ from the central compact source, corresponding to ~ 5 pc (assuming $d = 4.7$ kpc; Table 3.3). Assuming the age of 1400–2400 years (Borkowski et al., 2016), therefore, the expected mean velocity of the SN shock that can be heating the H_2 gas should be 2000–3500 km s^{-1}, which is a few times faster than the SN ejecta detected in the remnant (~ 1000 km s^{-1}; Moon et al., 2009). Furthermore, since the shock is fast and non-radiative, we may expect the strong X-ray-emitting gas inside the H_2 filaments. However, bright X-ray emission is only detected inside the radio boundary. At least, the northern H_2 filaments can not be explained by the SN shock.

Before SN explosions, the progenitors had made strong wind which results in the pre-SN shock propagating the surrounding medium. Unless the follow-up SN shock does not catch up the pre-SN wind shock, the pre-SN shock can be survived as long as $\sim 10^4$ years after the SN explosion (Draine, 2011). All the five SNRs, except W44, are young SNRs whose ages are only a few 1000 years, so their H_2 filaments outside the SN shock determined by the radio shell can be explained by the pre-SN wind shock (Note that W44 is an evolved, middle-aged SNR with age = 1–2 $\times 10^4$ years (Smith et al., 1985; Wolszczan et al., 1991)). The northern H_2 filaments in G11.2−0.3 seem to only be explained by the pre-SN shock.

3.5 Summary

We carried out high resolution ($R = 40,000$) NIR spectroscopy for the extended H_2 filaments around the five Galactic SNRs (G11.2-0.3, KES 73, W44, 3C 396, and W49B) showing "[Fe II]-H_2 reversal" phenomenon. In all slits, we clearly detected H_2 1–0 S(1) 2.12 μm and 1–0 S(0) 2.22 μm lines, and derived their radial velocities, line widths, and relative fluxes. Our main conclusions are listed below.

1. The observed $v_{\rm LSR}$ of H_2 lines are well consistent with the systematic velocity of the SNRs derived from the previous radio observations. The H_2 morphologies together with these $v_{\rm LSR}$ similar with the systematic velocity, imply the physical association between the remnants and the observed H_2 filaments. We determined the kinematic distance of the SNRs using the $v_{\rm LSR}$ of H_2 lines, and found that the distance of all the SNRs, except 3C 396 and W49B, are well consistent with the previous estimations within 1 kpc. In this paper, we suggested the distance of 3C 396 and W49B is 9.4 and 7.5 kpc, respectively. Our estimations are ~ 3 kpc larger or smaller than the previous estimations. The NIR H_2 lines can be an useful tool for investigating the kinematic distance of the Galactic SNRs interacting with the surrounding medium.

2. The observed H_2 lines show broad line widths (FWHM $\lesssim 10$ km s^{-1}) larger than the typical turbulent velocity of ambient gas (1–5 km s^{-1}). Furthermore, the flux ratios of H_2 1–0 S(1) 2.12 μm and 1–0 S(0) 2.22 μm are less than 0.25, which is consistent with that of collisional excitation models with $T =$ a few 1000 K. These two physical parameters imply that the H_2 emission lines detected far outside the remnants boundary are collisionally excited by shock.

3. We suggested three possible solutions for the origin of the shock: (1) magnetic precursor ahead of SN shock, (2) projection effect of SN shock, and (3) slow non-dissociative C-shock produced by the pre-SN wind. The H_2 filaments detected far outside the radio boundary of G11.2-0.3 might be excited by the pre-SN wind shock, rather than the SN shock, considering the large physical separation between the H_2 and [Fe II]/radio boundary and its young age. The exciting source of the bright H_2 filaments in W44, on the other hand, is likely the SN shock, and the "[Fe II]-H_2 reversal"

can be explained by projection effect. For the rest of the remnants (KES 73, 3C 396, and W49B), the reversal can be explained by both projection effect and pre-SN wind shock. For the H_2 clump in the western edge of KES 73, the magnetic precursor could be an another solution as an exciting source because the physical separation between H_2 and [Fe II] meets the typical length scale of the precursor ($\lesssim 10^{17}$ cm) expected in the previous theoretical studies.

Biblography

Black, J. H., & Dalgarno, A. 1976, ApJ, 203, 132

Black, J. H., & van Dishoeck, E. F. 1987, ApJ, 322, 412

Borkowski, K. J., Reynolds, S. P., & Roberts, M. S. E. 2016, ApJ, 819, 160

Burton, M., & Spyromilio, J. 1993, Proceedings of the Astronomical Society of Australia, 10, 327

Burton, M. G. 1992, Australian Journal of Physics, 45, 463

Burton, M. G., Hollenbach, D. J., & Tielens, A. G. G. M. 1990, ApJ, 365, 620

Caswell, J. L., Murray, J. D., Roger, R. S., Cole, D. J., & Cooke, D. J. 1975, A&A, 45, 239

Chen, Y., Jiang, B., Zhou, P., et al. 2014, Supernova Environmental Impacts, 296, 170

Chernoff, D. F., McKee, C. F., & Hollenbach, D. J. 1982, ApJL, 259, L97

Draine, B. T. 1980, ApJ, 241, 1021

Draine, B. T. 2003, ARAA, 41, 241

Draine, B. T. 2011, Physics of the Interstellar and Intergalactic Medium by Bruce T. Draine. Princeton University Press, 2011. ISBN: 978-0-691-12214-4,

Draine, B. T., & McKee, C. F. 1993, ARAA, 31, 373

Draine, B. T., & Roberge, W. G. 1982, ApJL, 259, L91

Froebrich, D., Davis, C. J., Ioannidis, G., et al. 2011, MNRAS, 413, 480

Graham, J. R., Wright, G. S., Hester, J. J., & Longmore, A. J. 1991, AJ, 101, 175

Gredel, R. 1996, A&A, 305, 582

Green, D. A., Gull, S. F., Tan, S. M., & Simon, A. J. B. 1988, MNRAS, 231, 735

Hasegawa, T., Gatley, I., Garden, R. P., et al. 1987, ApJL, 318, L77

Hewitt, J. W., Yusef-Zadeh, F., & Wardle, M. 2008, ApJ, 683, 189-206

Hollenbach, D., & McKee, C. F. 1989, ApJ, 342, 306

Kaplan, K. F., Dinerstein, H. L., Oh, H., et al. 2017, ApJ, 838, 152

Keohane, J. W., Reach, W. T., Rho, J., & Jarrett, T. H. 2007, ApJ, 654, 938

Kilpatrick, C. D., Bieging, J. H., & Rieke, G. H. 2016, ApJ, 816, 1

Koo, B.-C., Moon, D.-S., Lee, H.-G., Lee, J.-J., & Matthews, K. 2007, ApJ, 657, 308

Koo, B.-C., Raymond, J. C., & Kim, H.-J. 2016, Journal of Korean Astronomical Society, 49, 109

Kumar, H. S., Safi-Harb, S., Slane, P. O., & Gotthelf, E. V. 2014, ApJ, 781, 41

Le, H. A. N., Pak, S., Kaplan, K., et al. 2017, ApJ, 841, 13

Lee, H.-G., Moon, D.-S., Koo, B.-C., Lee, J.-J., & Matthews, K. 2009, ApJ, 691, 1042

Lee, H.-G., Moon, D.-S., Koo, B.-C., et al. 2013, ApJ, 770, 143

Lee, J.-J., Koo, B.-C., Lee, Y.-H., et al. 2014, MNRAS, 443, 2650

Lockhart, I. A., & Goss, W. M. 1978, A&A, 67, 355

McCoey, C., Giannini, T., Flower, D. R., & Caratti o Garatti, A. 2004, MNRAS, 353, 813

Moffett, D. A., & Reynolds, S. P. 1994, ApJ, 437, 705

Moon, D.-S., Koo, B.-C., Lee, H.-G., et al. 2009, ApJL, 703, L81

Mouri, H., Kawara, K., & Taniguchi, Y. 2000, ApJ, 528, 186

Neufeld, D. A., & Dalgarno, A. 1989, ApJ, 340, 869

Oh, H., Pyo, T.-S., Yuk, I.-S., et al. 2016a, ApJ, 817, 148

Oh, H., Pyo, T.-S., Kaplan, K., et al. 2016b, ApJ, 833, 275

Oliva, E., Moorwood, A. F. M., & Danziger, I. J. 1990, A&A, 240, 453

Park, C., Jaffe, D. T., Yuk, I.-S., et al. 2014, Proc. SPIE, 9147, 91471D

Puxley, P. J., Ramsay Howat, S. K., & Mountain, C. M. 2000, ApJ, 529, 224

Rho, J., Jarrett, T. H., Cutri, R. M., & Reach, W. T. 2001, ApJ, 547, 885

Rho, J., Petre, R., Schlegel, E. M., & Hester, J. J. 1994, ApJ, 430, 757

Seta, M., Hasegawa, T., Dame, T. M., et al. 1998, ApJ, 505, 286

Shelton, R. L., Kuntz, K. D., & Petre, R. 2004, ApJ, 611, 906

Smith, A., Jones, L. R., Watson, M. G., et al. 1985, MNRAS, 217, 99

Smith, M. D., Davis, C. J., & Lioure, A. 1997, A&A, 327, 1206

Sternberg, A., & Dalgarno, A. 1989, ApJ, 338, 197

Su, Y., Chen, Y., Yang, J., et al. 2011, ApJ, 727, 43

Takahashi, J. 2001, ApJ, 561, 254

Tian, W. W., & Leahy, D. A. 2008, ApJ, 677, 292-296

Wolszczan, A., Cordes, J. M., & Dewey, R. J. 1991, ApJL, 372, L99

Yuk, I.-S., Jaffe, D. T., Barnes, S., et al. 2010, Proc. SPIE, 7735, 77351M

Zhu, H., Tian, W. W., & Zuo, P. 2014, ApJ, 793, 95

Chapter 4

Near-Infrared Knots and Dense Fe Ejecta in the Cassiopeia A Supernova Remnant

(This chapter is published in The Astrophysical Journal[1]*.)*

4.1 Introduction

A massive star builds up onion-like layers of different chemical elements synthesized by hydrostatic nuclear burning processes during its lifetime. At the end of its evolution, the innermost Fe core collapses into a neutron star, which triggers a core-collapse supernova (SN) explosion. The detailed process of the explosion is complicated and poorly understood, but a consensus from theoretical studies suggests that the explosion should be asymmetric and turbulent, especially near the core (e.g., Sumiyoshi et al., 2005; Takiwaki et al., 2014; Gilkis & Soker, 2015, and references therein). Multi-dimensional numerical simulations have shown that the explosion also leads to extensive mixing and inversion among the stratified layers by hydrodynamic instabilities (e.g. Kifonidis et al., 2003, 2006; Hammer et al., 2010; Mao et al., 2015). A distinct method to explore the explosion dynamics of SNe, therefore, would be to investigate the detailed

[1]Lee et al. 2017, ApJ, 837, 118

chemical and kinematic properties of SN ejecta material in nearby young Galactic supernova remnants (SNRs) where the imprints of explosion remain.

Cassiopeia A (hereafter Cas A), at the age of ~ 340 years (Thorstensen et al., 2001; Fesen et al., 2006), is one of the best studied young Galactic SNRs. Its SN explosion was classified as Type IIb based on the optical spectra of light echoes (Krause et al., 2008; Rest et al., 2011), which implies that the progenitor was probably a star of 15–20 $M_{\odot}$ that had lost a significant portion, but not all, of its H-rich envelope before the explosion. Over the past several decades, Cas A has been extensively studied in almost all wavebands from radio to gamma-rays. The complex spatial distribution of *shocked* SN ejecta, such as the X-ray-emitting Fe-rich ejecta plumes beyond the Si-rich material and O/S-rich optical knots outlying the bright ejecta shell (e.g., Hughes et al., 2000; Hammell & Fesen, 2008), indicates an explosion resulting in an inversion of the chemical layers. Furthermore, the inhomogeneous distribution of *unshocked* SN ejecta radiating Si and Ti emission lines (Isensee et al., 2010; Grefenstette et al., 2014) implies that the explosion was turbulent near the progenitor core.

In the visible waveband, many bright optical knots are presented in and around Cas A. They have been classified into two major groups based on their proper motions and line-of-sight velocities: (1) fast-moving knots (FMKs) and (2) quasi-stationary flocculi (QSFs). The FMKs show large proper motions and high radial velocities, corresponding to expansion velocities of up to $\sim 10^4$ km s^{-1} (e.g., Fesen & Gunderson, 1996; Hammell & Fesen, 2008). They have spectral features strongly enhanced in O and other heavy elements (e.g., S and Ar) that are mostly synthesized from the nuclear burning process in a deep stellar layer, while showing no detectable H or He emission lines (e.g., Fesen & Gunderson, 1996; Hurford & Fesen, 1996). Based on their high expansion velocities and chemical composition, they have been regarded as dense material ejected from the disrupted layer of the progenitor after the SN explosion. The dynamical and chemical properties of the QSFs are very different from those of the FMKs. The QSFs have considerably slower velocities ($v < 500$ km s^{-1}), and so their typical expansion age is $11{,}000 \pm 2000$ years (van den Bergh & Kamper, 1985), which is much larger than the age of the remnant. They are bright in [N II] and Hα emission, with a handful of

other H and He emission lines, in optical spectra (e.g., Hurford & Fesen, 1996; Alarie et al., 2014). Considering these properties, QSFs are believed to be dense circumstellar medium (CSM) blown out from the progenitor prior to the SN explosion. In addition, some intermediate optical knots, that is, the so called fast-moving flocculi (FMFs) or nitrogen knots (NKs), were reported by Fesen et al. (1987). While their spectra, which show strong [N II] 6548, 6583 Å[2] accompanied by weak Hα without any lines of O and S, are analogous to those of QSFs (Fesen et al., 1987, 2006; Fesen, 2001), their proper motions are larger than $0\farcs3$ yr^{-1}, corresponding to $\sim$ 5000 km s^{-1} (Hammell & Fesen, 2008). Most of them have been found outside of the bright main ejecta shell. Therefore, these outlying N-rich knots have been interpreted as being fragments of the progenitor's photosphere expelled by the SN blast wave at the time of explosion.

The dynamical and chemical properties of these different types of optical knots have provided important clues to unveiling the SNR's origin and evolution. For example, the expansion center and age were determined from the proper motions of the FMKs (e.g., Thorstensen et al., 2001; Fesen et al., 2006, and references therein), and the three-dimensional (3D) structure of the ejecta knots reconstructed from spectral mapping observations has shown that the SN ejecta is expanding spherically but is systematically receding at a speed of 800 km s^{-1} at a distance of 3.4 kpc (Reed et al., 1995; DeLaney et al., 2010; Milisavljevic & Fesen, 2013; Alarie et al., 2014). The dense, slow-moving QSFs indicate that the progenitor had undergone significant and inhomogeneous mass loss during the red supergiant phase (Chevalier & Oishi, 2003).

Although this velocity-based classification is an efficient way to classify the knots as SN ejecta and CSM, which have distinctive expansion velocities, i.e., a few 1000 km s^{-1} vs. a few 100 km s^{-1}, it encounters limitations when characterizing the SN ejecta material from the different nucleosynthetic layers. According to previous numerical simulations for core-collapse SN explosions, the radial velocity profiles of heavy elements in SN ejecta are almost identical (Kifonidis et al., 2006; Joggerst et al., 2009). Several models in Joggerst et al. (2009) predict the velocity separation of up to $\sim$ 1000 km s^{-1} between different heavy elements. Their velocity profiles, however, are very broad (a

[2]All wavelengths listed in this paper are "air wavelengths."

few 1000 km s^{-1}), so that their distributions largely overlap. These numerical simulations may imply that SN material from different nucleosynthetic layers is barely distinguishable in velocity space. In order to comprehend the explosion dynamics, therefore, a more systematic classification of SN ejecta based on their chemical composition is needed.

In this paper, we report the results of broad near-infrared (NIR) spectroscopic observations toward the main ejecta shell of Cas A, focusing on classification of the emission knots based on their *spectrochemical* properties. The NIR study of Cas A has been relatively limited in the literature, although there are many bright forbidden lines of various elements in the NIR waveband, some of which may arise from the deep nucleosynthetic layers. As far as we are aware, the only NIR spectroscopic study covering the entire *JHK* bandpass was conducted by Gerardy & Fesen (2001), who obtained low-resolution ($R \sim 700$) spectra of five FMKs and three QSFs that were previously known. They showed that the spectra of the FMKs are dominated by [S II] 1.029, 1.032, 1.034, 1.037 μm (hereafter [S II] 1.03 μm multiplets) and [P II] 1.188 μm, as well as two high-ionization Si lines, [Si VI] 1.963 μm and [Si X] 1.430 μm, while those of the QSFs show strong He I 1.083 μm accompanied by H emission lines. A dozen bright [Fe II] lines are also detected in both FMKs and QSFs. Our spectra confirm these features. Here we present the spectrochemical classification of knots and discuss their characteristics. The organization of the paper is as follows. In Section 4.2, we outline our spectroscopic observations and data reduction procedures. An explanation of how we identified individual knots from two-dimensional (2D) dispersed images and derived their spectral properties is given in Section 4.3. In Sections 4.4 and 4.5, we carry out a classification of the knots using principal component analysis (PCA) and discuss the origin of knots in different classes. Finally, the paper is summarized in Section 4.6.

4.2 Observations and Data Reduction

4.2.1 Near-infrared Spectroscopy

We carried out NIR spectroscopic observations of Cas A using TripleSpec mounted on the Palomar 5 m Hale telescope. TripleSpec is a cross-dispersed NIR spectrograph that provides simultaneous wavelength coverage from 0.94 to 2.46 μm at a spectral resolving power of $R \sim 2700$ (Wilson et al., 2004; Herter et al., 2008). The spectrograph uses two adjacent quadrants, i.e., 2048×1024 pixels, of a Rockwell Scientific Hawaii-II array. The slit width and length are $1''$ and $30''$, respectively. On 2008 June 29 and August 8, we obtained spectra at eight slit positions along the main ejecta shell (Figure 4.1). The orientations of Slits 1 and 4 were set perpendicular to the shell, while those of the others were largely parallel to the shell. The nearby A0V star HD223386 was observed as a spectroscopic standard right before and/or after the target observations at similar airmasses. In addition to the target spectra, we also obtained spectra of sky background by dithering along the slit or taking spectra of nearby sky, depending on the complexity of the target fields. The total on-source exposure time at each slit position ranges from 300 to 1800 s. The detailed parameters of the spectroscopic observations are provided in Table 4.1.

We developed an IDL-based data reduction pipeline to reduce the obtained TripleSpec data. The pipeline first performed subtraction of a dark frame and flat fielding, followed by subtraction of sky background emission. For the latter, we used sky background emission obtained in a dithered frame or in a frame from nearby empty sky, depending on the complexity of the source emission in a given slit. Because of the non-uniform dispersion by the three cross-dispersing prisms in TripleSpec (Wilson et al., 2004; Herter et al., 2008), some orders of the TripleSpec spectra are severely curved. By carefully tracing the spectra of standard stars and airglow emission lines, we obtained a 2D wavelength solution for each order that can correct this effect in a satisfactory manner. We conducted fifth-order order polynomial fits to the wavelengths of the OH airglow emission lines (Osterbrock et al., 1997; Rousselot et al., 2000) in the TripleSpec spectra to obtain the wavelength solutions at 0.5 Å 1σ uncertainty for each order.

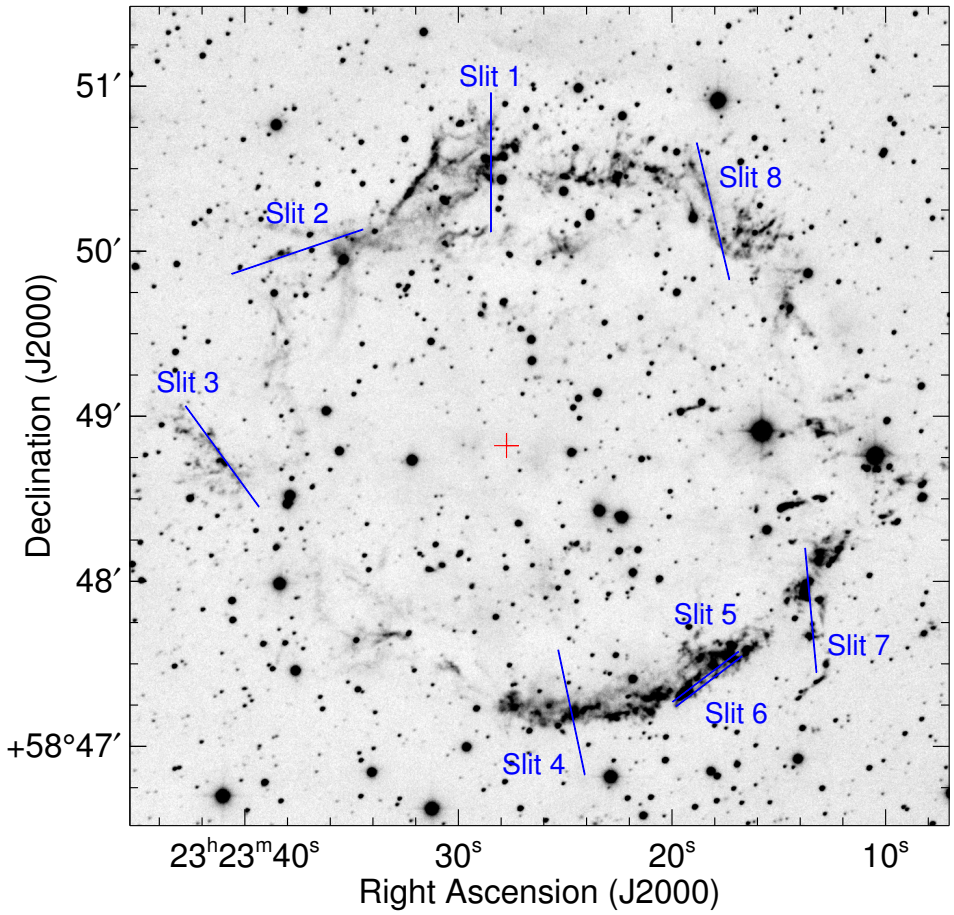

Figure 4.1 Finding chart for the eight long-slit positions. The background is a [Fe II] 1.644 μm narrow-band image observed in 2008 August. The red cross mark is the expansion center ($\alpha = 23^h23^m27^s.77 \pm 0^s.05$, $\delta = 58°48'49''.4 \pm 0''.4$ [J2000]) of the SN ejecta measured by Thorstensen et al. (2001). Note that the length of each blue bar represents the total effective slit coverage depending on the nodding offset (see Table 4.1). North is up and east is to the left.

Table 4.1. Parameters of the Spectroscopic Observations

Date (UT)	Slit	Central Coordinate α(J2000)	δ(J2000)	P.A. [a] (deg)	Mode [b]	Slit Length [c] ($''$)	Exposure (s)
2008 Jun 29	1	23:23:28.54	+58:50:32.2	0.0	Both	50.50	300 × 4
	8	23:23:18.13	+58:50:14.4	13.4	AB	51.00	300 × 5
	2	23:23:37.60	+58:49:59.7	288.7	AB	50.25	300 × 4
	ST[d]	23:48:53.97	+59:58:44.3	0.0	AB	30.00	30 × 6
2008 Aug 08	3	23:23:41.11	+58:48:45.2	36.1	AB	45.25	300 × 6
	4	23:23:24.77	+58:47:12.2	12.0	AB	46.25	300 × 6
	5	23:23:18.50	+58:47:25.1	307.3	OS	30.00	300 × 1
	6	23:23:18.33	+58:47:23.5	307.3	OS	30.00	300 × 1
	7	23:23:13.57	+58:47:49.2	5.2	AB	45.25	300 × 6
	ST[d]	23:48:53.97	+59:58:44.3	0.0	AB	30.00	30 × 8

[a]Position angle (counterclockwise from north on the plane of the sky)

[b]AB: ABBA nodding pattern, OS: Object-Sky pattern, Both: combined AB and OS

[c]Effective Slit Length = instrument slit length ($30''$) + Nodding offset length

[d]Standard Star, HD223386, for flux calibration

Heliocentric velocity correction was also performed when calculating the velocity of the emission line detected in the TripleSpec spectra. We used an A0V-type standard star (HD223386) in the photometric calibration and confirmed that the fluxes of the [Fe II] 1.644 μm emission line are consistent with those from the narrow-band imaging observations of the same areas (see Section 4.2.2).

4.2.2 Near-infrared Imaging

In 2005 August 28 and 2008 August 11, we performed NIR imaging observations for the remnant using the Wide-field Infrared Camera (WIRC; Wilson et al., 2003) attached to the Palomar 5 m telescope. The camera consists of a single 2048 × 2048 Rockwell Hawaii-II HgCdTe NIR detector with a pixel scale of $0\farcs2487$ pixel^{-1}, which provides a field of view of $8\farcm7 \times 8\farcm7$. We used an [Fe II] narrow-band filter that has a mean wavelength of 1.644 μm and a bandwidth of 252 Å. While the single exposure time per frame in 2005 and 2008 is 60 s and 200 s, the multiple dithering observations yield total integration times of 1200 s and 5400 s, respectively. We also obtained H-continuum narrow-band images (mean wavelength of 1.570 μm and bandwidth of

236 Å) in order to subtract the bright stars in the [Fe II] narrow-band images. The average seeing throughout our observations was $\sim 0\farcs9$ FWHM. We followed standard procedures for the reduction of NIR imaging data. First, the dark and sky background were subtracted from each individual dithered frame. Then, all of the frames were divided by the normalized flat image. The astrometric solution was derived on the basis of unsaturated stars around the remnant in the Two Micron All Sky Survey (2MASS) Point-Source Catalog (PSC; Skrutskie et al., 2006). We coadded all dithered frames which were astrometrically aligned. In terms of photometric calibration, the *H*-band magnitude in the 2MASS system was used by assuming that the [Fe II] narrow-band magnitude is the same as the *H*-band magnitude. The uncertainty in the zero-point magnitude we derived is less than 0.1 mag, corresponding to the 10% of the flux.

4.3 Identification of Knots and Line Parameters

Figure 4.2 shows 2D dispersed images of strong emission lines detected in our TripleSpec spectra: red for [Fe II] 1.644 μm, green for He I 1.083 μm, and blue for [P II] 1.188 μm + [S III] 0.953 μm. The emission features are complex, often with multiple peaks, and so the identification of individual 'knots' by visual inspection is not straightforward. We used the IDL routine CLUMPFIND (Williams et al., 1994), which was developed for the identification of clumps in molecular clouds. The routine identifies 'clumps' by searching for local maxima above some intensity threshold and following them down them to low-intensity levels. For a given 2D dispersed image, a "mask" locating individual knots was generated from [Fe II] 1.644 μm emission features or, if they are weak, [S III] 0.953 μm or [P II] 1.188 μm emission features, and shifted along the wavelength to find other emission lines associated with the knots. The details of this knot identification process are given in the Supplement Material of Koo et al. (2013). In total, we identified 63 knots of distinctive kinematical and spectral properties in the 2D dispersed images. Figure 4.3 shows their locations and Table 4.2 lists their positions, sizes, and radial velocities.

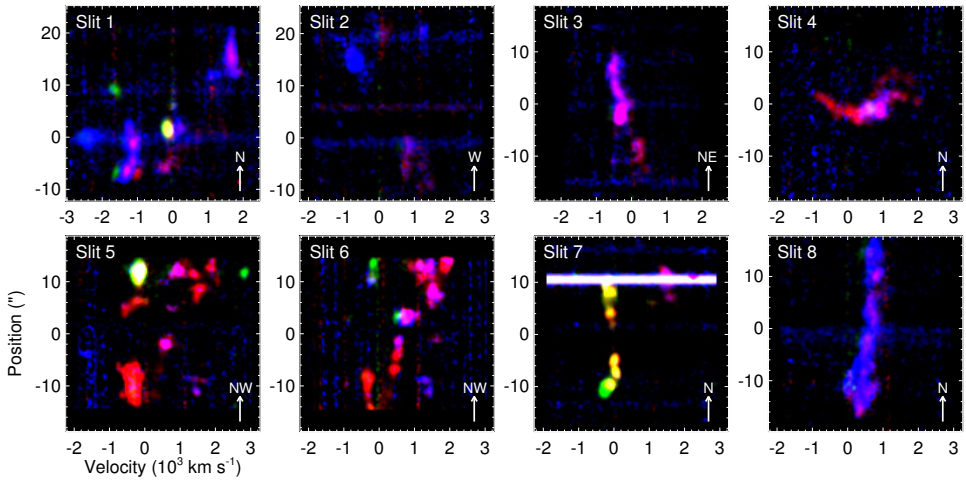

Figure 4.2 Two-dimensional dispersed image of bright emission lines in three colors: [Fe II] 1.644 μm in red, He I 1.083 μm in green, and [P II] 1.188 μm + [S III] 0.953 μm in blue. The y-axis represents the position along the slit length with zero corresponding to the slit center in Table 4.1. The dynamic ranges of RGB colors are the same, i.e., maximum to minimum intensity ratios of 10, while their maximum intensities have a ratio of 1:10:70 (R:G:B) in each slit image. Note that the continuous spectrum at $+10''$ in Slit 7 is of an adjacent star falling on the slit position. The slit direction is marked in the lower right of each panel (see Table 4.1 for details).

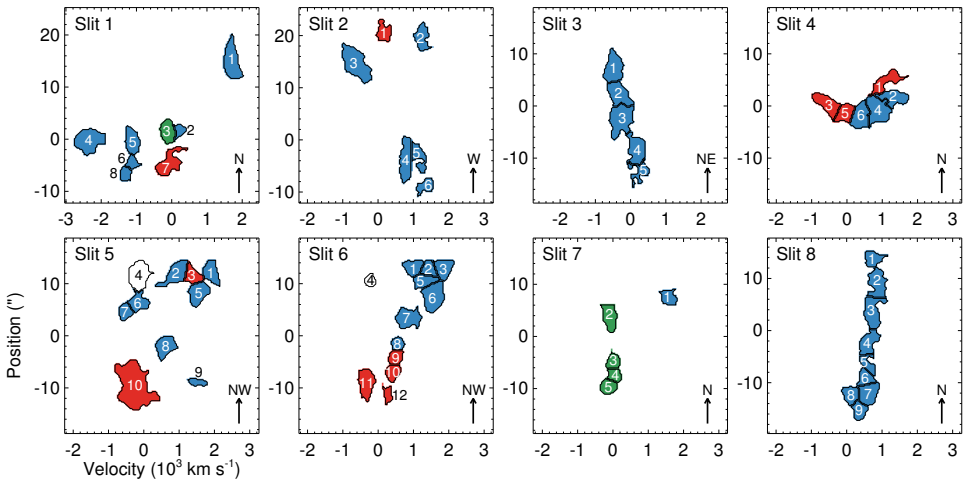

Figure 4.3 Sixty-three knots identified by the CLUMPFIND code in the 2D dispersed images. The colors represent the different types of knots: He-rich knots is in green, S-rich knots in blue, and Fe-rich knots in red. Knot 4 in Slits 5 and 6, which are not colored, are composed of two knots of different types with almost the same position and velocity (see Table 4.2). In Slit 7, there is another knot above Knot 2 (see Figure 4.2), but it spatially overlaps with a continuum source and was not identified as a clump by the CLUMPFIND code. The slit direction is marked in the lower right of each panel (see Table 4.1 for details).

Table 4.2. Physical Parameters of 63 Identified Knots

Slit No.	Knot No.	Central Position α(J2000)	Central Position δ(J2000)	Size[a] (″)	Knot Type[b]	A_V[c] (mag)	v_{rad} (km s^{-1})	[Fe II] 1.644 μm Flux[d] (10^{-17} erg s^{-1} cm^{-2})
1	1	23:23:28.54	+58:50:47.6	8.75	S	8.0 (0.5)	+1698 (2)	589 (8)
1	2	23:23:28.54	+58:50:34.1	3.25	S	10.6 (0.7)	+225 (2)	165 (4)
1	3	23:23:28.54	+58:50:33.8	5.00	He	5.8 (0.1)	−75 (2)	793 (5)
1	4	23:23:28.54	+58:50:32.3	5.50	S	3.3 (2.0)	−2234 (17)	96 (13)
1	5	23:23:28.54	+58:50:31.1	5.75	S	4.9 (0.2)	−1083 (2)	383 (3)
1	6	23:23:28.54	+58:50:27.6	3.00	S	3.3 (0.5)	−1091 (3)	132 (4)
1	7	23:23:28.54	+58:50:26.6	5.75	Fe	9.8 (0.4)	−17 (2)	561 (10)
1	8	23:23:28.54	+58:50:25.8	3.00	S	3.4 (0.4)	−1264 (2)	198 (5)
2	1	23:23:35.19	+58:50:06.0	4.50	Fe	5.5 (0.9)	+185 (6)	204 (10)
2	2	23:23:35.10	+58:50:06.3	5.75	S	9.3 (3.6)	+1271 (14)	75 (10)
2	3	23:23:35.83	+58:50:04.3	8.00	S	4.2 (1.7)	−653 (20)	140 (12)
2	4	23:23:38.21	+58:49:58.1	9.25	S	7.0 (0.5)	+814 (3)	480 (10)
2	5	23:23:38.21	+58:49:58.1	6.50	S	11.0 (1.0)	+1124 (3)	339 (12)
2	6	23:23:38.70	+58:49:56.8	3.75	S	9.2 (1.7)	+1337 (2)	164 (7)
3	1	23:23:41.64	+58:48:50.9	6.75	S	8.2 (0.3)	−473 (3)	460 (6)
3	2	23:23:41.28	+58:48:47.0	5.00	S	7.6 (0.3)	−397 (3)	310 (4)
3	3	23:23:40.92	+58:48:43.2	7.25	S	7.3 (0.1)	−297 (2)	972 (4)
3	4	23:23:40.52	+58:48:38.9	6.50	S	7.2 (0.3)	+222 (4)	434 (8)
3	5	23:23:40.16	+58:48:35.1	5.75	S	6.2 (1.2)	+341 (7)	121 (7)
4	1	23:23:24.90	+58:47:16.8	5.25	Fe	15.4 (1.4)	+1109 (5)	240 (6)
4	2	23:23:24.82	+58:47:13.9	3.75	S	10.6 (0.6)	+1306 (4)	289 (4)
4	3	23:23:24.77	+58:47:12.2	5.75	Fe	7.5 (0.4)	−491 (3)	298 (5)
4	4	23:23:24.73	+58:47:10.7	6.25	S	9.9 (0.3)	+907 (3)	606 (5)
4	5	23:23:24.73	+58:47:10.7	4.00	Fe	6.6 (0.4)	−31 (4)	236 (4)
4	6	23:23:24.72	+58:47:10.2	5.75	S	10.3 (0.3)	+390 (3)	577 (6)
5	1	23:23:17.21	+58:47:32.7	5.25	S	11.5 (0.8)	+1924 (3)	313 (7)
5	2	23:23:17.28	+58:47:32.3	5.25	S	8.8 (0.5)	+992 (3)	561 (10)
5	3	23:23:17.34	+58:47:32.0	4.50	Fe	8.7 (0.9)	+1388 (4)	286 (8)
5	4A[e]	23:23:17.26	+58:47:32.4	6.25	S	8.3 (0.3)	−109 (3)	537 (7)
5	4B[e]	23:23:17.34	+58:47:32.0	6.25	He	8.3 (0.1)	−109 (3)	2149 (7)
5	5	23:23:17.62	+58:47:30.3	5.25	S	9.3 (0.5)	+1550 (3)	456 (6)
5	6	23:23:17.88	+58:47:28.8	4.75	S	8.8 (0.8)	−177 (4)	273 (8)
5	7	23:23:18.00	+58:47:28.0	3.75	S	7.2 (0.6)	−492 (3)	215 (5)
5	8	23:23:18.72	+58:47:23.8	5.00	S	10.8 (0.5)	+624 (3)	492 (9)
5	9	23:23:19.41	+58:47:19.7	1.75	S	11.9 (1.8)	+1530 (8)	99 (5)
5	10	23:23:19.49	+58:47:19.3	9.75	Fe	7.9 (0.0)	−290 (3)	4959 (8)
6	1	23:23:17.02	+58:47:31.3	3.50	S	6.6 (0.9)	+1000 (6)	245 (8)
6	2	23:23:17.07	+58:47:31.0	3.25	S	9.0 (0.7)	+1412 (4)	340 (7)
6	3	23:23:16.94	+58:47:31.7	4.25	S	10.2 (0.3)	+1914 (3)	667 (7)
6	4A[e]	23:23:17.22	+58:47:30.0	2.75	He	10.0 (2.1)	−166 (6)	58 (6)
6	4B[e]	23:23:17.30	+58:47:29.6	2.75	S	10.4 (3.6)	−166 (6)	34 (6)
6	5	23:23:17.22	+58:47:30.0	3.00	S	7.4 (0.8)	+1343 (5)	272 (6)
6	6	23:23:17.53	+58:47:28.2	6.25	S	10.4 (0.4)	+1547 (3)	714 (8)
6	7	23:23:17.99	+58:47:25.5	4.50	S	7.8 (0.3)	+802 (3)	623 (8)
6	8	23:23:18.47	+58:47:22.6	2.75	S	9.3 (0.7)	+572 (4)	171 (5)
6	9	23:23:18.75	+58:47:21.0	2.75	Fe	8.3 (0.5)	+540 (4)	258 (5)
6	10	23:23:19.04	+58:47:19.3	3.50	Fe	7.3 (0.4)	+459 (3)	283 (5)
6	11	23:23:19.29	+58:47:17.8	6.50	Fe	6.9 (0.2)	−291 (3)	676 (7)
6	12	23:23:19.52	+58:47:16.4	4.25	Fe	9.9 (1.7)	+293 (6)	92 (6)
7	1	23:23:13.66	+58:47:56.4	3.25	S	10.2 (0.7)	+1591 (3)	161 (3)
7	2	23:23:13.62	+58:47:53.2	5.50	He	8.4 (0.2)	−83 (3)	424 (6)
7	3	23:23:13.51	+58:47:44.2	4.00	He	8.5 (0.2)	+42 (2)	647 (9)
7	4	23:23:13.49	+58:47:42.0	2.75	He	8.5 (0.3)	+78 (3)	480 (10)
7	5	23:23:13.46	+58:47:39.7	3.25	He	9.1 (0.2)	−63 (3)	516 (7)
8	1	23:23:18.56	+58:50:28.1	3.25	S	8.1 (0.9)	+727 (3)	180 (7)
8	2	23:23:18.43	+58:50:24.0	6.00	S	7.6 (0.5)	+841 (3)	369 (9)
8	3	23:23:18.22	+58:50:17.1	6.25	S	7.3 (0.4)	+737 (2)	443 (9)
8	4	23:23:18.07	+58:50:12.3	5.25	S	9.2 (0.4)	+621 (3)	364 (6)
8	5	23:23:17.93	+58:50:07.7	4.50	S	10.8 (1.6)	+606 (6)	170 (8)
8	6	23:23:17.88	+58:50:06.2	4.00	S	13.6 (1.7)	+478 (3)	139 (5)
8	7	23:23:17.76	+58:50:02.3	4.75	S	9.4 (0.7)	+627 (4)	378 (10)
8	8	23:23:17.76	+58:50:02.1	4.00	S	6.8 (0.8)	+146 (5)	239 (12)

Table 4.2 (cont'd)

Slit No.	Knot No.	Central Position α(J2000)	δ(J2000)	Size[a] ($''$)	Knot Type[b]	A_V[c] (mag)	v_{rad} (km s^{-1})	[Fe II] 1.644 μm Flux[d] (10^{-17} erg s^{-1} cm^{-2})
8	9	23:23:17.67	+58:49:59.1	4.00	S	8.1 (0.6)	+361 (3)	294 (6)

[a] Size along the slit length.

[b] He: He-rich knot, S: S-rich knot, Fe: Fe-rich knot

[c] Visual extinction derived from the flux ratio of [Fe II] 1.257 and 1.644 μm. We adopted the intrinsic [Fe II] line ratio of 1.36 (Deb & Hibbert, 2010) and the extinction curve of the Milky Way with $R_V = 3.1$ (Draine, 2003, see Section 4.4.1 for more details).

[d] The uncertainty in parenthesis is 1σ statistical error by a single Gaussian fitting, and does not include the absolute photometric error which is roughly 20% or less.

[e] Knot 4 in Slits 5 and 6 have been identified as a single knot by CLUMPFIND respectively, but a detailed inspection revealed that each of them are composed of two (A and B) components almost coincident both in space and velocity.

We extracted one-dimensional (1D) spectra of individual knots using their mask files (Figure 4.3). We identified 46 emission lines in total and derived their parameters by performing single Gaussian fits to the detected lines. Table 4.3 lists the derived line widths and fluxes. [Fe II] 1.644 μm line is detected in all 63 knots and their fluxes are also listed in Table 4.2. Among the 46 emission lines, 43 lines are previously detected lines in SNRs (Dennefeld & Andrillat, 1981; Rudy et al., 1994; Hurford & Fesen, 1996; Gerardy & Fesen, 2001), whereas three lines of [Fe III] at 2.145, 2.218, and 2.242 μm are detected for the first time in SNRs. The [Fe III] lines originate from transitions between levels in ^{3}G and ^{3}H terms with high excitation energies ($\gtrsim$ 30,000 K) and have been detected in a few objects, such as SgrA*/IRS16 complex (Lutz et al., 1993, and references therein), classical novae (Wagner & Depoy, 1996), H II regions (Okumura et al., 2001), and planetary nebulae (Likkel et al., 2006). Among the previously reported lines, on the other hand, the O I 1.1286, 1.1287 μm, [Fe II] 1.1881 μm, and [Si X] 1.430 μm lines are not detected in our spectra. Gerardy & Fesen (2001) reported detection of the O I lines in the FMKs in Cas A, but we were unable to confirm the detection with our spectra. They also reported detection of the highly ionized [Si X] 1.430 μm line, but again we were unable to confirm the detection. The [Fe II] 1.1881 μm line was included in the list of identified lines in three QSFs in Cas A and the Kepler SNR by Gerardy & Fesen (2001), but we consider that this was a misidentification of the [P II] 1.1883 μm line. The expected flux of the [Fe II] 1.1881 μm line in typical conditions (e.g., $T \lesssim 10^4$ K, $n_e \lesssim 10^5$ cm^{-3}) in SNRs is almost

Table 4.3. Observed NIR Line Parameters of Knots

Slit No.	Knot No.[a]	Line ID Transition (l - u)	λ_{rest}[b] (μm)	FWHM[c] (Å)	Observed Flux[d] (10^{-17} erg s^{-1} cm^{-2})	Note[e]
1	1	[S III] $^3P_2$ - $^1D_2$	0.95311	7.2 (0.2)	9233 (261)	
1	1	[C I] $^3P_1$ - $^1D_2$	0.98241	· (·)	· (15)	
1	1	[C I] $^3P_2$ - $^1D_2$	0.98503	· (·)	· (15)	
1	1	[S II] $^2D_{3/2}$ - $^2P_{3/2}$	1.02867	8.4 (0.1)	2317 (18)	LINE-FIX
1	1	[S II] $^2D_{5/2}$ - $^2P_{3/2}$	1.03205	8.4 (-)	3182 (-)	LINE-FIX
1	1	[S II] $^2D_{3/2}$ - $^2P_{1/2}$	1.03364	8.4 (-)	2185 (13)	LINE-FIX
1	1	[S II] $^2D_{5/2}$ - $^2P_{1/2}$	1.03705	8.4 (-)	1058 (-)	LINE-FIX
1	1	[N I] $^2D_{5/2}$ - $^2P_{3/2,1/2}$	1.03979	· (·)	· (12)	
1	1	[N I] $^2D_{3/2}$ - $^2P_{3/2,1/2}$	1.04074	· (·)	· (14)	
1	1	[S I] $^3P_2$ - $^1D_2$	1.08212	9.9 (0.5)	207 (15)	
1	1	He I $^3S_1$ - $^3P_{0,1,2}$	1.08302	· (·)	· (11)	
1	1	H I Paγ	1.09381	· (·)	· (9)	
1	1	[S I] $^3P_1$ - $^1D_2$	1.13059	· (·)	· (13)	
1	1	[P II] $^3P_1$ - $^1D_2$	1.14682	7.8 (0.7)	293 (48)	OH-CONT
1	1	[P II] $^3P_2$ - $^1D_2$	1.18828	9.8 (0.1)	736 (15)	
1	1	[Fe II] $a^6D_{7/2}$ - $a^4D_{5/2}$	1.24854	· (·)	· (7)	
1	1	[Fe II] $a^6D_{3/2}$ - $a^4D_{1/2}$	1.25214	· (·)	· (8)	
1	1	[Fe II] $a^6D_{9/2}$ - $a^4D_{7/2}$	1.25668	10.2 (0.3)	388 (15)	
1	1	[Fe II] $a^6D_{1/2}$ - $a^4D_{1/2}$	1.27035	· (·)	· (18)	
1	1	[Fe II] $a^6D_{3/2}$ - $a^4D_{3/2}$	1.27878	4.0 (0.6)	30 (6)	
1	1	H I Paβ	1.28181	· (·)	· (12)	
1	1	[Fe II] $a^6D_{5/2}$ - $a^4D_{5/2}$	1.29427	9.3 (1.0)	133 (22)	OH-CONT
1	1	[Fe II] $a^6D_{1/2}$ - $a^4D_{3/2}$	1.29777	· (·)	· (12)	
1	1	[Fe II] $a^6D_{7/2}$ - $a^4D_{7/2}$	1.32055	17.5 (2.6)	92 (18)	
1	1	[Fe II] $a^6D_{3/2}$ - $a^4D_{5/2}$	1.32778	12.3 (2.1)	67 (15)	
1	1	[Fe II] $a^4F_{9/2}$ - $a^4D_{5/2}$	1.53347	8.7 (0.9)	95 (12)	OH-CONT
1	1	[Fe II] $a^4F_{7/2}$ - $a^4D_{3/2}$	1.59947	9.8 (1.1)	76 (11)	OH-CONT
1	1	[Si I] $^3P_1$ - $^1D_2$	1.60683	· (·)	· (5)	
1	1	[Fe II] $a^4F_{9/2}$ - $a^4D_{7/2}$	1.64355	13.7 (0.1)	589 (8)	
1	1	[Si I] $^3P_2$ - $^1D_2$	1.64545	· (·)	· (7)	
1	1	[Fe II] $a^4F_{5/2}$ - $a^4D_{1/2}$	1.66377	14.0 (1.5)	73 (11)	OH-CONT
1	1	[Fe II] $a^4F_{7/2}$ - $a^4D_{5/2}$	1.67688	15.4 (0.5)	146 (8)	
1	1	[Fe II] $a^4F_{5/2}$ - $a^4D_{3/2}$	1.71113	· (·)	· (9)	
1	1	[Fe II] $a^4F_{3/2}$ - $a^4D_{1/2}$	1.74494	· (·)	· (5)	
1	1	[Fe II] $a^4F_{3/2}$ - $a^4D_{3/2}$	1.79710	· (·)	· (62)	
1	1	[Fe II] $a^4F_{5/2}$ - $a^4D_{5/2}$	1.80002	· (·)	· (240)	
1	1	[Fe II] $a^4F_{7/2}$ - $a^4D_{7/2}$	1.80939	· (·)	· (689)	
1	1	[Si VI] $^2P_{3/2}$ - $^2P_{1/2}$	1.96287	16.4 (0.6)	501 (27)	
1	1	[Fe II] $a^4P_{5/2}$ - $a^2P_{3/2}$	2.04601	· (·)	· (20)	
1	1	He I $^1S_0$ - $^1P_1$	2.05813	· (·)	· (12)	
1	1	[Fe II] $a^4P_{3/2}$ - $a^2P_{3/2}$	2.13277	· (·)	· (9)	
1	1	[Fe III] a^3H_4 - a^3G_3	2.14511	· (·)	· (10)	
1	1	H I Brγ	2.16553	· (·)	· (11)	
1	1	[Fe III] a^3H_6 - a^3G_5	2.21779	· (·)	· (13)	
1	1	[Fe II] $a^4G_{9/2}$ - $a^2H_{11/2}$	2.22379	· (·)	· (10)	
1	1	[Fe III] a^3H_4 - a^3G_4	2.24209	· (·)	· (13)	

Note. — This table is available in its entirety in a machine-readable form in the online journal.

[a] Knot 4 in Slits 5 and 6 has been identified as a single knot by CLUMPFIND, but a detailed inspection revealed that each of them are composed of two (A and B) components almost coincident both in space and velocity.

[b] Rest wavelengths in air.

[c] FWHM of lines.

[d] The uncertainty in parenthesis is the 1σ statistical error from a single Gaussian fitting and does not include the absolute photometric error which is roughly 20% or less. The uncertainty of the undetected lines was derived from the background rms noise around the wavelength. The emission lines falling in the bad atmospheric transmission window (e.g., [Fe II] lines near 1.80 μm) have much higher uncertainty in flux due to low signal-to-noise ratios.

[e] In the case of the lines which were contaminated by nearby lines of similar wavelengths either from the knot itself or from other knots, we carried out a simultaneous Gaussian fitting with possible constraints ("LINE-FIX" keyword in Note), e.g., by fixing their wavelengths and/or line widths based on the parameters of well-isolated lines, by fixing their intensities if they can be predictable theoretically (Froese Fischer (2006) for [C I], Kelleher & Podobedova (2008) for [Si I], Tayal & Zatsarinny (2010) for [S II], Deb & Hibbert (2010) for [Fe II]). "OH-CONT" keyword in Note represents the line which was significantly contaminated by nearby bright OH airglow emission lines so their true uncertainty could be much larger than what we measured from a single Gaussian fitting.

negligible, i.e., its flux relative to the [Fe II] 1.257 μm line is $\lesssim 10^{-5}$, whereas the [P II] 1.1883 μm line could be as strong as $\sim 1/10$ of the [Fe II] 1.257 μm line for cosmic abundance, or even higher if Fe atoms are locked into dust grains (Koo et al., 2013).

4.4 Principal Component Analysis of Knots' Spectral Properties

4.4.1 Method

In order to systematically characterize the spectral properties of the 63 knots, which have 46 emission lines in total, we applied the PCA method. PCA measures the variances among the original input variables (i.e., brightness of the emission lines in this study) and then sets new orthogonal axes called principal components (PCs) along the largest variances. Therefore, the largest variance (or information) is contained in the first PC (PC1), the second most in PC2, and so forth. If there are significant correlations among the original input variables, then the majority of the information is confined within the first few PCs, which makes it possible to categorize the objects into a few groups based on the first few PCs.

Before performing the PCA, we apply an extinction correction using the line ratio of the [Fe II] 1.257 and 1.644 μm emission. These two lines originate from the same upper level ($a^4D_{7/2}$) and therefore their intrinsic flux ratio ($[F_{1.257}/F_{1.644}]_{\rm int}$) depends on the Einstein A-coefficients ($A_{\rm ki}$) and their wavelengths, i.e., $[F_{1.257}/F_{1.644}]_{\rm int} = (A_{ki,1.257}/1.257)/(A_{ki,1.644}/1.644)$. The A-coefficients, however, are considerably uncertain so the line ratio ranges from 0.98 to 1.49 (Giannini et al., 2015; Koo & Lee, 2015, and references therein) in literature. We adopt a line ratio of 1.36, which is the value suggested by Nussbaumer & Storey (1988) and Deb & Hibbert (2010). (We found that the uncertainty of the theoretical line ratio does not affect our classification of the knots because they are well grouped in PC spaces, as we will show in Section 4.4.2. The criteria of the groups, however, may change depending on the intrinsic line ratio we adopt. In Section 4.4.2, we will describe this in more detail.) Then, by comparing the observed line flux ratio to the intrinsic ratio, we obtain the extinction of the knots

and deredden the observed fluxes of all of the lines. We use the general interstellar extinction curve derived from a carbonaceous-silicate grain model with a Milky Way size distribution for $R_V = 3.1$ (Draine, 2003). The derived extinctions are listed in Table 4.2. In our previous work (Lee et al., 2015), we showed that the extinction toward the west is systematically larger than that toward the east, which is consistent with the previous optical/X-ray extinction estimates (see Figure 1 in Lee et al., 2015). We further showed that the extinctions of red-shifted knots are systematically higher than those of the blue-shifted knots, implying the presence of a large amount of SN dust inside and around the main ejecta shell (see Lee et al., 2015, for details). The lines from the same upper level in the dereddened spectral data do not provide independent information any more, so that the number of attributes in the PCA are now reduced from 46 to 23. In order to prevent a few bright lines dominating the PCA, the line intensities are standardized by subtracting the mean and dividing by the standard deviation. Since we use the mean-subtracted data, the zero PCs represent the location of mean brightness, not the location of the zero fluxes of the lines (hereafter convergent point), which is important for our classification (see Section 4.4.2). In order to get the PC coefficients of a knot indicating the convergent point when all the emission lines of a knot get close to zero flux, we add one artificial knot into the data set that has emission lines with zero flux.

4.4.2 Results

Principal Components and Classification of Knots

Table 4.4 contains the relative and cumulative fraction of variances contributed by the 10 most significant PCs. The first three PCs account for the majority, i.e., ∼85%, of the spectral information; thus, we use them in our classification of the knots. Figure 4.4 shows the projection of the 23 attributes on the combination plane of the three most significant PCs. (This type of plots is known as an *h-plot*; see Ungerechts et al. (1997) and Neufeld et al. (2007).) While Figure 4.4(a) and 4.4(b) show 2D projections on the planes of (PC1 vs. PC2) and (PC1 vs. PC3), Figure 4.4(c) shows 3D projections for the three PCs together. The lengths of the vectors in the

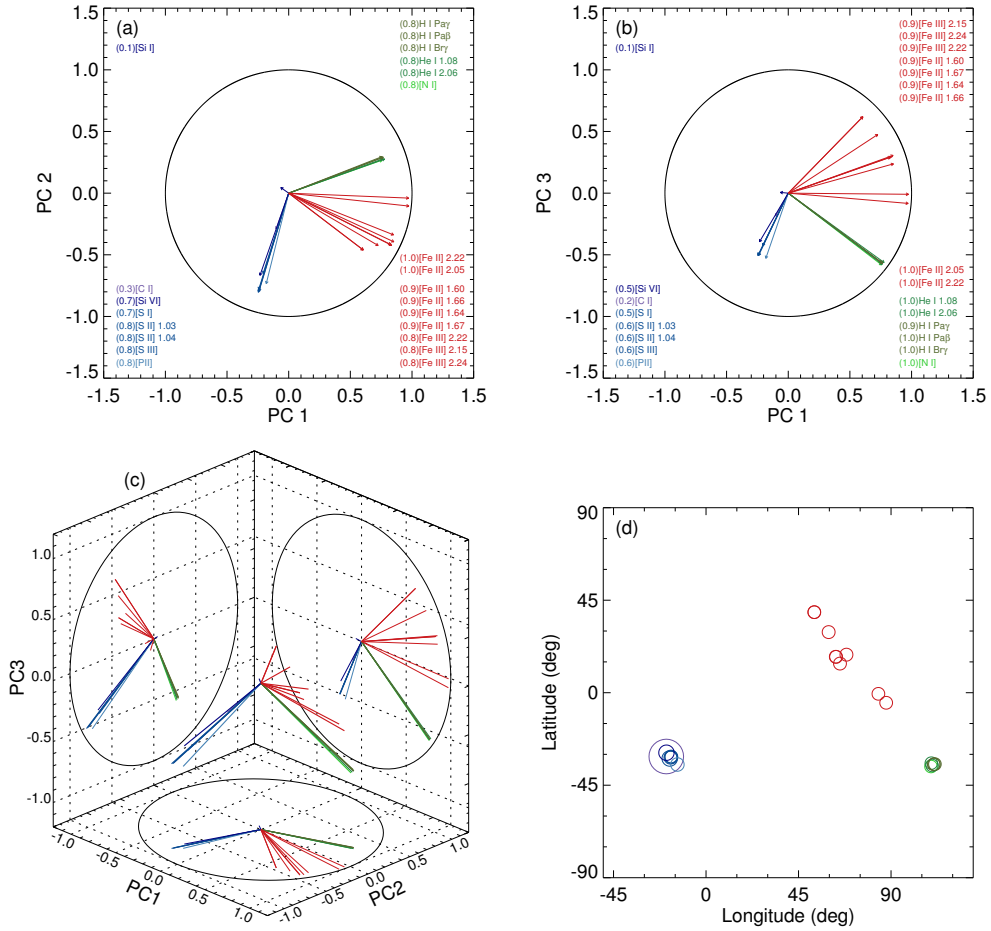

Figure 4.4 Projections of the 23 attributes (or spectral lines) on the plane of (a) PC1-PC2 and (b) PC1-PC3. A circle of unity radius is overplotted for comparison. The number within parentheses at the corners of (a) and (b) is radius from the center, that represents the normalized contribution of the line at each PC plane. The 3D projections and the projections within a sphere are in (c) and (d), respectively (see the text for details). The reference position in (d), where (Longitude, Latitude) = (0°, 0°), corresponds to (PC1, PC2, PC3) = (0, -1, 0), and Longitude and Latitude are measured toward east and north, respectively. The size of circles in (d) is inversely proportional to the length of the vector in (c). (An interactive 3D pdf version and it source code written in ASYMPTOTE are available in a tar.gz package in the electronic journal.)

Table 4.4. Individual and Cumulative Fraction of Variance

Number of PC	Eigenvalue	Fraction of Variance [%]	Cumulative Fraction [%]
1	9.8	42.7	42.7
2	5.1	22.2	64.9
3	4.7	20.4	85.3
4	1.1	4.7	90.0
5	1.0	4.2	94.2
6	0.4	1.8	96.0
7	0.3	1.3	97.4
8	0.2	0.7	98.1
9	0.1	0.5	98.6
10	0.1	0.4	98.9

plots are proportional to the fractional contributions by the spectral line to the given PC, and their quadratic sum is equal to unity. In Figure 4.4(d), we visualize the 3D projections using the coordinate of (Longitude vs. Latitude) representing the two projection angles on the surface of a sphere. We see in Figure 4.4 that the attributes can be largely divided into three groups, each of which is composed of several strongly correlated spectral lines. (Note that the cosine of the angle between the vectors on the plots measures the linear correlation between the emission lines; see Neufeld et al. (2007) for example.) The first group (hereafter 'He group') is composed of H I, He I, and [N I] lines. These lines are almost perfectly correlated with each other. The lengths of their vectors are close to unity in the PC1-PC3 plane, which means that these spectral lines are properly accounted for by PC1 and PC3. The second group ('S group') is composed of [Si VI], [P II], and ionized S emission lines. These lines are also strongly correlated with each other and mostly contributed by PC2 and PC3 in the direction orthogonal to the He group lines. The last group ('Fe group') is composed of ionized Fe emission lines, i.e., [Fe II] and [Fe III] lines. These lines are rather loosely correlated but are still generally well separated from the lines in the other two groups.

The [Fe II] 2.046 and 2.224 μm lines in particular appear somewhat distinct from the other [Fe II] lines. This might be caused by the higher excitation energies of the two lines than those of the other lines, i.e., $\sim$ 30,000 K vs. $\sim$ 10,000 K.

We plot the PC coefficients of the 63 knots on the PC planes in Figure 4.5. The central positions of the planes, where (PC1, PC2, PC3) = (0, 0, 0), represent the spectrum made by averaging all of the spectra of all 63 knots. In the lower panels of the figure, which are the enlarged plots of the central areas of the PC planes, we draw dashed lines in order to group the knots (see below) originating from (PC1, PC2, PC3) = (-0.10, 0.23, 0.10). This convergent point is the location of the virtual knot with zero flux (Section 4.4.1), and the radial distance from the convergent point is proportional to the brightness of the emission line. The distributions of the PC coefficients in Figure 4.5 are very similar to those in Figure 4.4. There appear to be three groups of knots in Figure 4.5 that have PC coefficients similar to those of the three groups in Figure 4.4, i.e., the He, S, and Fe groups. We therefore group the knots in Figure 4.5 as He-rich, S-rich, and Fe-rich knots using the dashed lines. As a result, we identify 7 He-rich knots, 45 S-rich knots, and 11 Fe-rich knots.

Figure 4.6 shows sample 1D spectra of the three groups. As expected, the He-rich knots have strong lines of He I 1.083 μm compared to [Fe II] and some of them also show several emission lines of H I, [N I], [P II], and [Fe III] as well. The H I and [N I] lines are detected only in the He-rich knots. The S-rich knots also have bright [Fe II] lines, but they have much stronger lines of [S III] 0.953 μm, [S II] 1.03 μm multiplets, [P II] 1.188 μm, and [Si VI] 1.963 μm. The low-ionized emission lines of refractory elements, i.e., [C I] and [Si I], are also detected in several S-rich knots. Although some S-rich knots show the He I 1.083 μm line, their intensities are significantly less than those of the He-rich knots. The Fe-rich knots have strong lines of [Fe II] and some of them have a weak He I 1.083 μm line as well. The brightest Fe-rich knot, Knot 10 in Slit 5, also emits [Fe III] lines in the K band. As in the He-rich knots, no lines of C, Si, and S are detected in the Fe-rich knots.

The three knot groups are easily distinguishable when the flux ratios of [S II] 1.03 μm multiplets, He I 1.083 μm, and [P II] 1.188 μm are compared (Figure 4.7). The He-rich

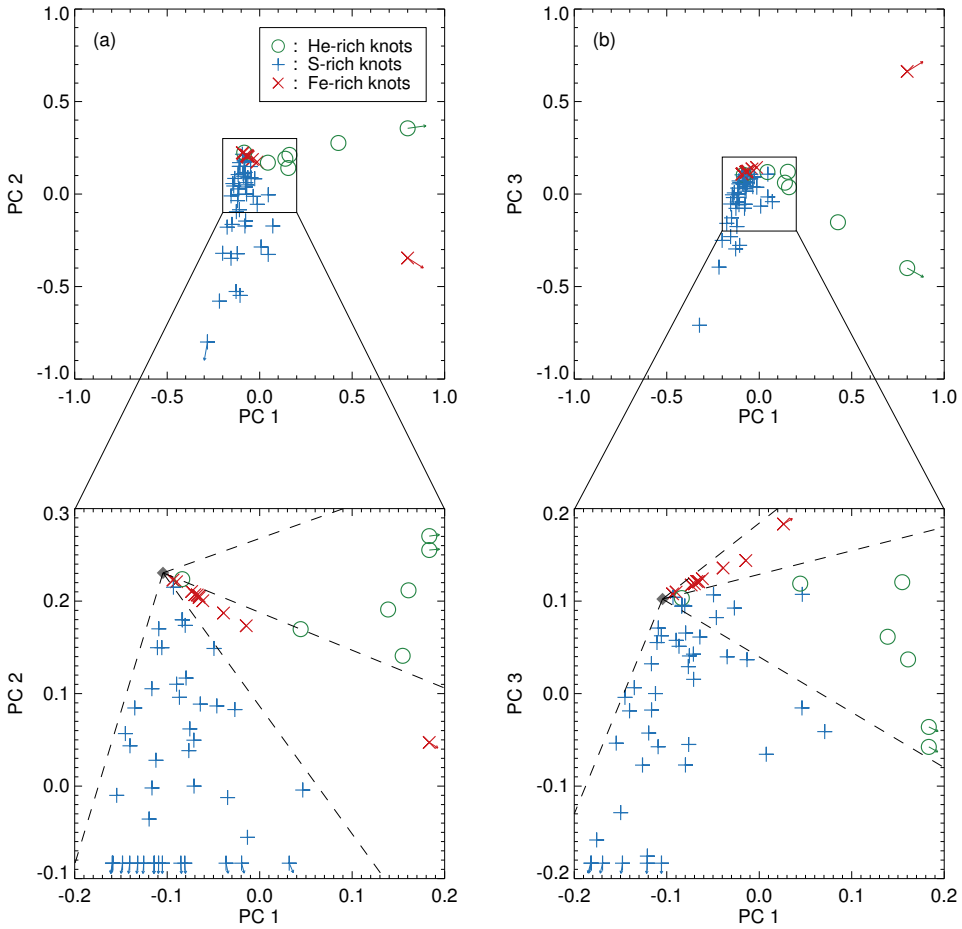

Figure 4.5 Projections of the 63 objects (or knots) on the plane of (a) PC1-PC2 and (b) PC1-PC3. The green open circles, blue crosses, and red X symbols indicate He-rich, S-rich, and Fe-rich knots, respectively. The enlarged views of the crowded central regions are shown in the lower panels. The black dashed lines in the lower panels represent the criteria of the groups, and the black diamond indicates the convergent point (see text for details). (An interactive 3D pdf version and it source code written in ASYMPTOTE are available in a tar.gz package in the electronic journal.)

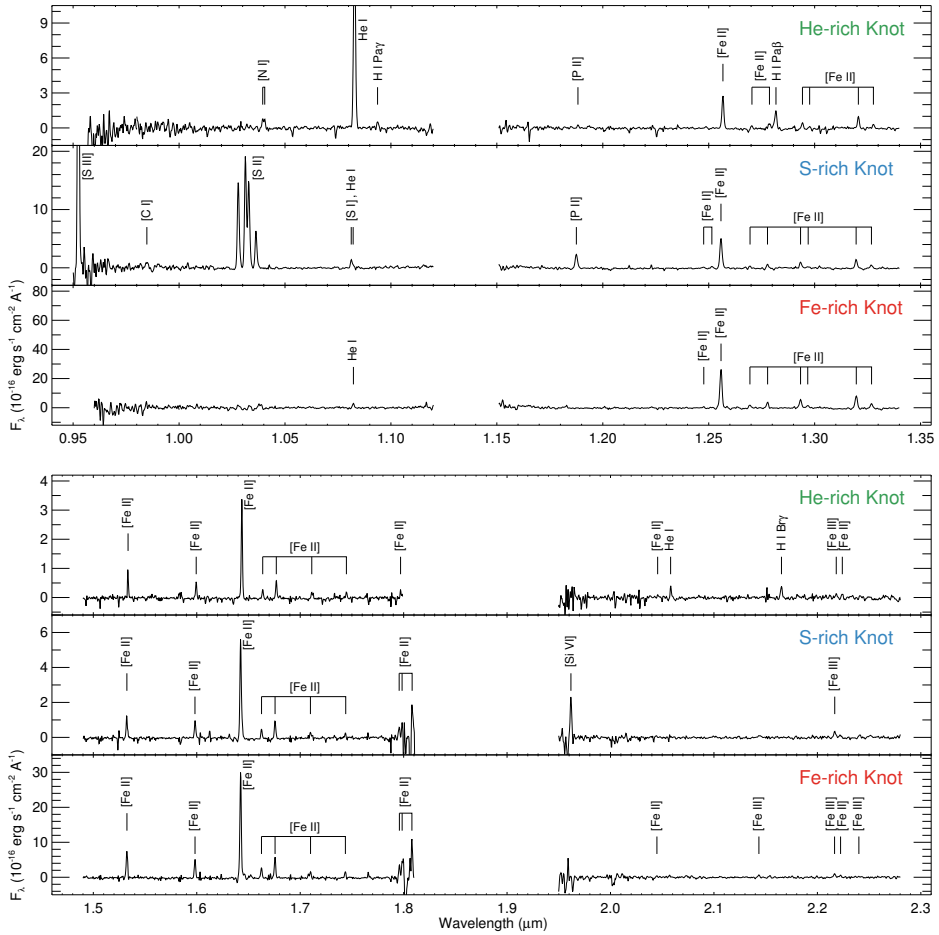

Figure 4.6 Sample 1D spectra of He-rich (Knot 5 in Slit 7), S-rich (Knot 3 in Slit 3), and Fe-rich (Knot 10 in Slit 5) knots. The spectra have been smoothed by a Gaussian kernel with an FWHM of 1 pixel (2–3 Å).

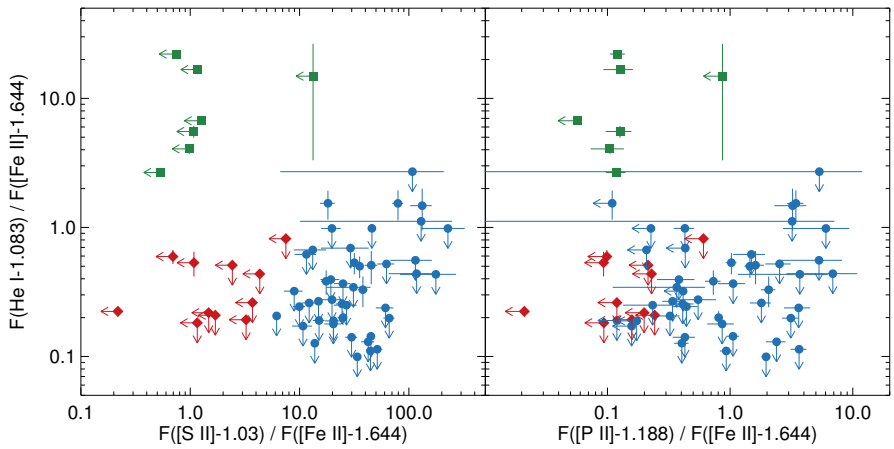

Figure 4.7 Flux comparisons among the lines of He I (1.083 μm), [S II] (1.03 μm multiplets), and [P II] (1.188 μm). The extinctions are corrected and the fluxes are normalized by the [Fe II] 1.644 μm line fluxes. The three knot groups are represented by green squares (He-rich knots), blue circles (S-rich knots), and red diamonds (Fe-rich knots). The arrows represent 3σ upper limits.

knots are well separated from the other groups in F(He I-1.083)/F([Fe II]-1.644), i.e., the ratio is greater than two for the He-rich knots but lower than two for the S-rich and Fe-rich knots. The F([S II]-1.03)/F([Fe II]-1.644) and F([P II]-1.188)/F([Fe II]-1.644) of the He-rich knots are mostly smaller than a few times 1.0 and 0.1, respectively. Although the S-rich and Fe-rich knots are not clearly distinguished in the F([S II]-1.03)/F([Fe II]-1.644) and F([P II]-1.188)/F([Fe II]-1.644) comparisons, we see that these ratios are higher in the S-rich knots than the Fe-rich knots, i.e., F([S II]-1.03)/F([Fe II]-1.644) $\gtrsim 5$ and F([P II]-1.188)/F([Fe II]-1.644) $\gtrsim 0.3$ for the S-rich knots and vice versa. It is worth noting that the flux ratios of the knots in Figure 4.7 and the criteria mentioned above are based on the assumption that the intrinsic flux ratio of [Fe II] 1.257 and 1.644 μm is 1.36 (Section 4.4.1). If we adopt different line ratios, e.g., 0.98 to 1.49 (Giannini et al., 2015; Koo & Lee, 2015, and references therein), then the criteria of those three flux ratios will be F(He I-1.083)/F([Fe II]-1.644) = 1.0–2.4, F([S II]-1.03)/F([Fe II]-1.644) = 2.3–6.0, and F([P II]-1.188)/F([Fe II]-1.644) = 0.19–0.34.

Physical Properties of Three Knot Groups

Figure 4.8 compares the distributions of the knot sizes, radial velocities, and line widths of the three knot groups. The angular sizes of most of the knots are in the range $2''$–$7''$ (or 0.03–0.1 pc at a distance of 3.4 kpc) and there is no significant difference among the three groups in their sizes, although some of the S-rich and Fe-rich knots are as large as $10''$. On the other hand, there are significant differences in their radial velocities and line widths. The radial speeds of He-rich knots are $\lesssim$ 200 km s^{-1}, while those of S-rich knots range from -2000 km s^{-1} to $+2000$ km s^{-1} with a median of $+630$ km s^{-1}. The radial velocities of Fe-rich knots range from -500 km s^{-1} to $+1500$ km s^{-1} with a median of $+330$ km s^{-1}. In line width, the He-rich knots have widths of 5–10 Å, while the S- and Fe-rich knots have widths of 10–35 Å. (Note that our spectral resolution at 1.64 μm is $\sim$ 6 Å.) Figure 4.8 also compares the distribution of the [Fe II] 1.644 μm line fluxes among the three knot groups. While the S-rich and Fe-rich knots have a similar distribution with an increased number of knots that have faint [Fe II] emission, the pattern is absent in the He-rich knots. There is no apparent

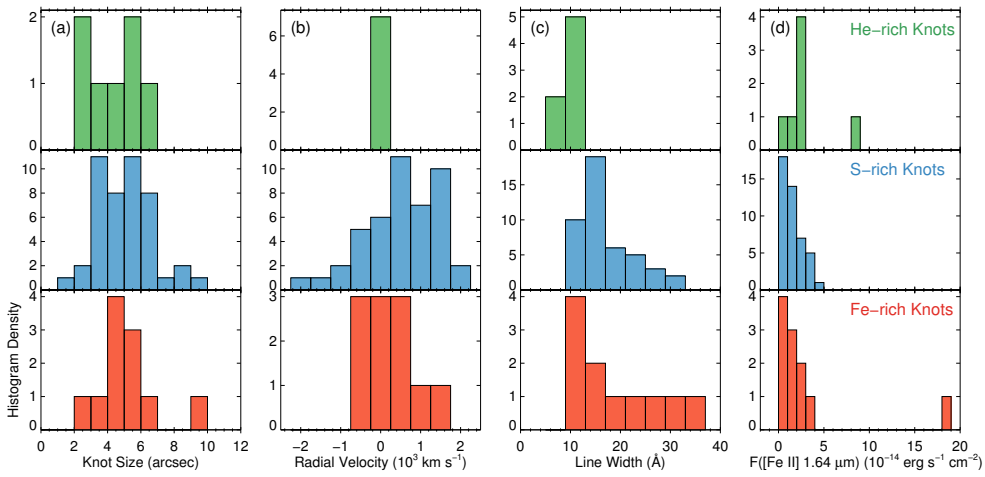

Figure 4.8 Histograms of (a) knot size, (b) radial velocity, (c) line width, and (d) extinction-corrected [Fe II] 1.644 μm flux.

correlation among the four physical parameters of the knots.

One of the physical parameters of the knots that can be straightforwardly obtained is electron density using [Fe II] lines originating from levels with similar excitation energies, because their ratios are mainly determined by electron densities (e.g., Koo et al., 2016). [Fe II] 1.644 μm and 1.677 μm are such lines, and Figure 4.9 compares their expected ratios as a function of density for the assumed temperatures of 5000, 10,000, and 20,000 K (left panel) with observed values as a function of the [Fe II] 1.644 μm flux (right panel). We see that the ratio is quite insensitive to temperature and can be used to estimate electron density in the range $\sim 10^3$–10^5 cm^{-3}. The electron density of the He-rich knots is a few 10^4 cm^{-3}, while the S-rich knots show electron densities over a broad range of 10^3 cm^{-3} to 10^5 cm^{-3}. The Fe-rich knots have somewhat lower (10^3–10^4 cm^{-3}) electron densities compared to the other two groups. There appears to be no correlation between the electron densities and [Fe II] 1.644 μm line fluxes.

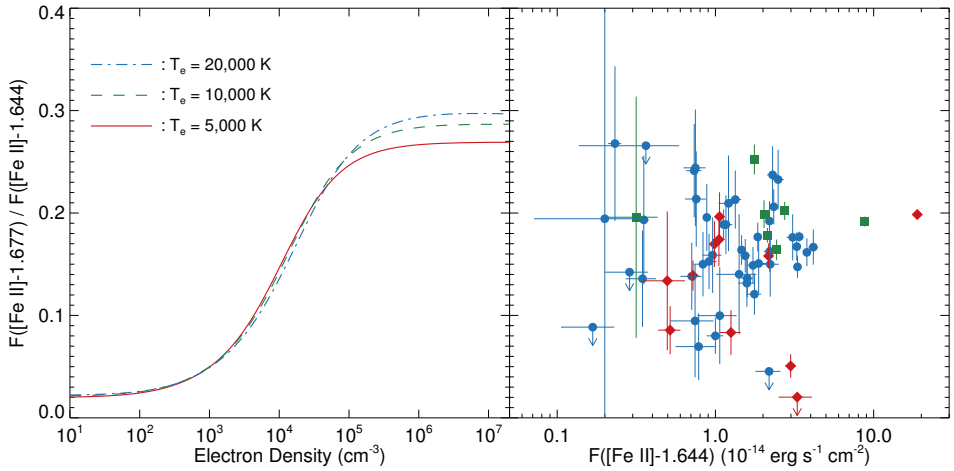

Figure 4.9 (Left) F([Fe II]-1.677)/F([Fe II]-1.644) ratio as a function of electron density for gas in statistical equilibrium at $T_e = 5000$ K, 10,000 K, and 20,000 K. (Right) F([Fe II]-1.677)/F([Fe II]-1.644) vs. F([Fe II]-1.644) of the knots. The symbols are the same as in Figure 4.7. All fluxes are extinction-corrected.

4.5 Discussion

In this section, we discuss the origin of the knots using their spectral characteristics described in the previous section.

4.5.1 He-rich and S-rich knots

The He-rich and S-rich knots have quite distinct spectral properties; the He-rich knots have high F(He I-1.083)/F([Fe II]-1.644) and low F([S II]-1.03)/F([Fe II]-1.644), F([P II]-1.188)/F([Fe II]-1.644), while the S-rich knots have low F(He I-1.083)/F([Fe II]-1.644) and high F([S II]-1.03)/F([Fe II]-1.644), F([P II]-1.188)/F([Fe II]-1.644). Their kinematic properties are also quite different; the He-rich knots have low ($\lesssim 200$ km s^{-1}) line-of-sight speeds, while the S-rich knots have high (up to ~ 2000 km s^{-1}) line-of-sight speeds. These spectral and kinematical properties suggest that the He-rich knots are dense, slow-moving CSM swept up by the SN blast wave, while the S-rich knots are fast-moving SN ejecta that have been shocked. The same conclusion was reached

by Koo et al. (2013), who performed an abundance analysis using [P II] 1.188 μm and [Fe II] 1.257 μm lines. They showed that the relative abundance of P (a major product of the stellar Ne-burning layer) to Fe (in number) for the He-rich knots is similar to the solar abundance, whereas that of the S-rich knots is 10–100 times higher than the solar abundance.

The characteristics of the two types of knots match well with those of QSFs and FMKs known from previous optical studies (see Section 4.1 for a summary of their properties). Similar to the optical QSFs, the He-rich knots have bright He I lines together with H I and [N I] lines; all the He-rich knots have a He I 1.083 μm line, 6 out of the 7 show H I Paβ, Brγ lines, and the three brightest ones also have [N I] 1.040, 1.041 μm lines. Like the optical FMKs dominated by lines of ionized heavy elements O, S, Ar, the S-rich knots show strong S lines plus [P II] and [Si VI] lines; all the S-rich knots have [S II] 1.03 μm multiplets, and 39 out of 45 S-rich knots also have [P II] 1.188 μm and/or [Si VI] 1.963 μm lines. Indeed, the overall spectra of He-rich and S-rich knots are similar to the NIR spectra of QSFs and FMKs obtained by Gerardy & Fesen (2001), respectively. Furthermore, the radial velocities of the two NIR knot groups are well consistent with those of the optical groups. For example, the radial velocity of the He-rich knots is -50 ± 90 km s^{-1}, while the generally accepted radial velocity of QSFs is -140 ± 300 km s^{-1} (van den Bergh & Kamper, 1985; Reed et al., 1995). In addition, the median line-of-sight velocity of S-rich knots is $+620$ km s^{-1}, while the systematic velocity of the FMKs is $+770 \pm 40$ km s^{-1} (Reed et al., 1995).

Rich emission lines of Si, P, and S in the S-rich knots and FMKs imply that they are the SN ejecta originated from the Ne- and O-burning layers. The two bright emission lines, [P II] 1.188 μm and [Fe II] 1.644 μm, have comparable excitation energies and critical densities, and so their line ratios are strongly dependent on their abundance ratio, X(P/Fe) (Koo et al., 2013). As seen in Figure 4.7, there is a large scatter in this line ratio for S-rich knots, which implies that the abundance ratio X(P/Fe) varies almost two orders of magnitude for these knots. We also found that 13 out of 45 S-rich knots have clear but relatively weak emission lines of He I and/or [C I]. The detection of the He, C, and Fe lines in the S-rich ejecta, which are either lighter or heavier

elements than the O-burning materials, might infer microscopic mixing during the SN explosion. In many S-rich knots, a highly ionized Si line, [Si VI] 1.963 μm, is detected, while in a few S-rich knots, a [Si I] 1.645 μm line is also detected. The detection of Si in very different ionization stages indicates the broad range of temperatures in the S-rich knots.

4.5.2 Fe-rich knots

In Section 4.4.2, we found that the Fe-rich knots exhibit intermediate characteristics between He-rich and S-rich knots; they emit strong [Fe II] lines without any Si, P, and S lines, but have high line-of-sight speeds of up to $\sim$ 1500 km s^{-1}. A few knots also emit an He I 1.083 μm line. The high velocities, however, suggest that they are not dense QSFs represented by the He-rich knots. Their line widths are also considerably broader than those of He-rich knots, i.e., 10–35 Å vs. 5–10 Å (Figure 4.8). On the other hand, the missing Si, P, and S lines indicate that the abundances of these Ne- and O-burning elements are very low in these Fe-rich knots. We can consider two possible explanations regarding the origin of the Fe-rich knots: (1) swept-up CSM around contact discontinuity (CD) or (2) shocked SN ejecta enriched with Fe elements that had been synthesized in explosive Si burning. The ambient medium that the Cas A SN blast wave is propagating into is believed to be CSM with an r^{-2} density distribution (e.g., Lee et al., 2014). In such a case, 1D similarity solutions show that the shocked CSM accumulates at the CD with infinite density asymptotically (Chevalier, 1982). We thus expect "dense" CSM expanding at a speed comparable to the shocked SN material. In the real situation, however, this interacting region between the shocked SN ejecta and the shocked CSM is hydrodynamically unstable and distorted, with the density of the shocked CSM limited to $\lesssim$ 10 times the density at the ambient shock (Chevalier et al., 1992; Blondin et al., 2001; van Veelen et al., 2009). The temperature of the shocked CSM near the CD, therefore, may be lower than the typical temperature ($\sim$ 2 keV) of the shocked CSM (Hwang & Laming, 2012), but probably no more than a factor of 10, and all of the Fe in the shocked CSM will be in high ionization stages. Furthermore, H I lines are not detected in all Fe-rich knots with an upper limit of F(H

I-Paβ)/F([Fe II]-1.257) $\lesssim$ 0.1. Note that the observed ratio of these line intensities ranges between 0.05 and 10 for SNRs while it is $\sim$ 50 for Orion, which should be the typical ratios for shocked and photoionized gases of cosmic abundance, respectively (Koo & Lee, 2015). Therefore, H must be depleted in Fe-rich knots. The non-detection of He and N lines might also indicate that the abundances of these 'circumstellar' elements are very low in Fe-rich knots, although this needs to be confirmed from other waveband observations. (See the next paragraph for an explanation of the faint He lines detected in some Fe-rich knots.) We may therefore conclude that the Fe-rich knots are not likely the shocked CSM.

This leaves the second possibility, i.e., the Fe-rich knots are Fe-enriched SN ejecta. The high velocities and large velocity widths are consistent with SN ejecta being swept up by the reverse shock. The low [P II] and [S II] fluxes compared to the [Fe II] flux, however, implies that the abundances of P and S, which are Ne- and O-burning materials, are very low, which is in sharp contrast to the S-rich knots. These characteristics strongly suggest that *the Fe-rich knots are most likely "pure" Fe ejecta synthesized in the deepest stellar interior.* The weak He I 1.083 μm line detected in some Fe-rich knots could be due to an α-rich freeze-out process during the explosive Si burning; just after the explosion, complete Si burning with an α-rich freeze-out occurs under high temperatures and low density conditions in the stellar deep layer, and many alpha particles are "frozen out" without participating in further nucleosynthetic processes (Woosley et al., 1973). Similar dense, Fe-predominant ejecta, likely from the α-rich freeze-out process, have been detected in another young core-collapse SNR G11.2-0.3 (Moon et al., 2009).

Pure Fe ejecta have been detected in X-rays (see below) but not in optical or NIR wavebands. This is surprising considering the extensive optical/NIR studies carried out for Cas A since its discovery. Figure 4.10 partly gives an answer. In the right panel of Figure 4.10, red is an [Fe II] 1.644 μm narrow-band image while green and blue are *Hubble Space Telescope* (*HST*) ACS/WFC F850LP and F775W images which are dominated by ionized S and O lines, respectively (Fesen et al., 2006; Hammell & Fesen, 2008). Previous optical observations had been mostly toward the northern ejecta

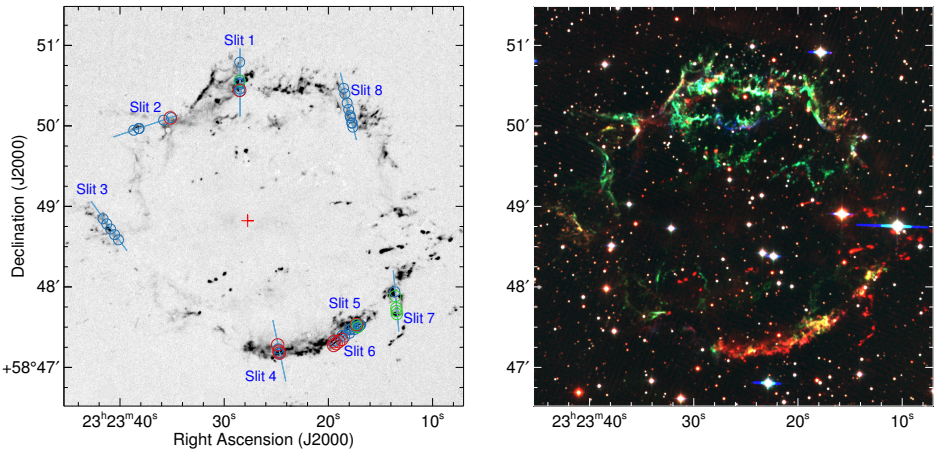

Figure 4.10 (Left) Locations of 63 knots in Table 4.2. (See Figure 4.3 for the knot numbers in each slit.) The He-rich, S-rich, and Fe-rich knots are marked in green, blue, and red, respectively. The background is the continuum-subtracted [Fe II] 1.644 μm narrow-band image in Figure 4.1. (Right) A three-color composite image of Cas A with an [Fe II] 1.644 μm narrow-band image in red, and *HST* ACS/WFC F850LP and F775W images in green and blue. The *HST* images are dominated by [S III] 9069, 9531 Å and [S II] 1.03 μm multiplets (F850LP) and [O II] 7319, 7330 Å lines (F775W), respectively (Fesen et al., 2006; Hammell & Fesen, 2008). The [Fe II] 1.644 μm image was observed in 2005 August. The *HST* ACS/WFC images are from the Hubble Legacy Archive (https://hla.stsci.edu) and they were taken in 2004 December (Fesen et al., 2006). To match their angular resolutions, the *HST* images were smoothed by using a Gaussian kernel with a FWHM of 0.″9.

shell bright in ionized O, S, and Ar lines (e.g., Chevalier & Kirshner, 1979; Hurford & Fesen, 1996; Fesen et al., 2001) or toward FMKs outside the main shell (e.g., Fesen et al., 1988, 2006; Fesen, 2001). Figure 4.10, however, shows that the southwestern (SW) main ejecta shell, which is bright in the [Fe II] line but faint in the ionized O and S lines, is the region where Fe-rich ejecta can be found. Indeed, our result shown in the left panel of Figure 4.10 confirms this; 9 out of 11 Fe-rich knots are located in Slits 4–6. (Note that the compact red knots in the interior and beyond the SW shell are mostly QSFs, and they are bright in [N II] 6548, 6583 Å and Hα images too (van den Bergh & Kamper, 1985; Alarie et al., 2014).) The slit positions are determined from an [Fe II] 1.644 μm image, so that some of them were placed toward the red portions of the main ejecta shell and, by decomposing the emission into individual velocity components, we were able to identify Fe-rich ejecta. It is worth noting that Rho et al. (2003) also noted the bright [Fe II] emission in the SW shell in their [Fe II] 1.644 μm image of Cas A. Meanwhile, we can see that the [Fe II] 17.9 μm emission is much brighter than the emission from O-burning elements such as Ar and S in the SW shell in the *Spitzer* mid-infrared maps of ionic lines (Ennis et al., 2006; Smith et al., 2009). Our result suggests that this [Fe II] emission-predominant area, i.e., the red area of the SW ejecta shell in Figure 4.10, is probably mainly composed of Fe ejecta.

It is not easy to identify the counterpart of Fe-rich knots in optical images because several velocity components are usually superposed along the line of sight toward the main ejecta shell. The brightest Fe-rich knot (Knot 10 in Slit 5; hereafter K10), however, is somewhat isolated and we can identify its counterpart. In Figure 4.11, the upper two images are [Fe II] 1.644 μm images at different epochs and they show that K10 is a clump of $\sim 10'' \times 3''$ elongated along the slit. The two [Fe II] images clearly show that the clump is moving fast tangentially. The proper motion is measured $0\farcs28$ yr^{-1}, implying a tangential velocity of 4500 ± 200 km s^{-1}. In the lower F775W and F850LP images, we see diffuse faint emission at the position of K10 (see the red contour). Its brightness distribution is different, with two small ($\lesssim 2''$) bright spots (S1 and S2 in the figure) in the lower part of the clump. One of these bright spots, S1, is coincident with an S-rich knot (Knot 9 in Slit 5), which is spatially coincident with

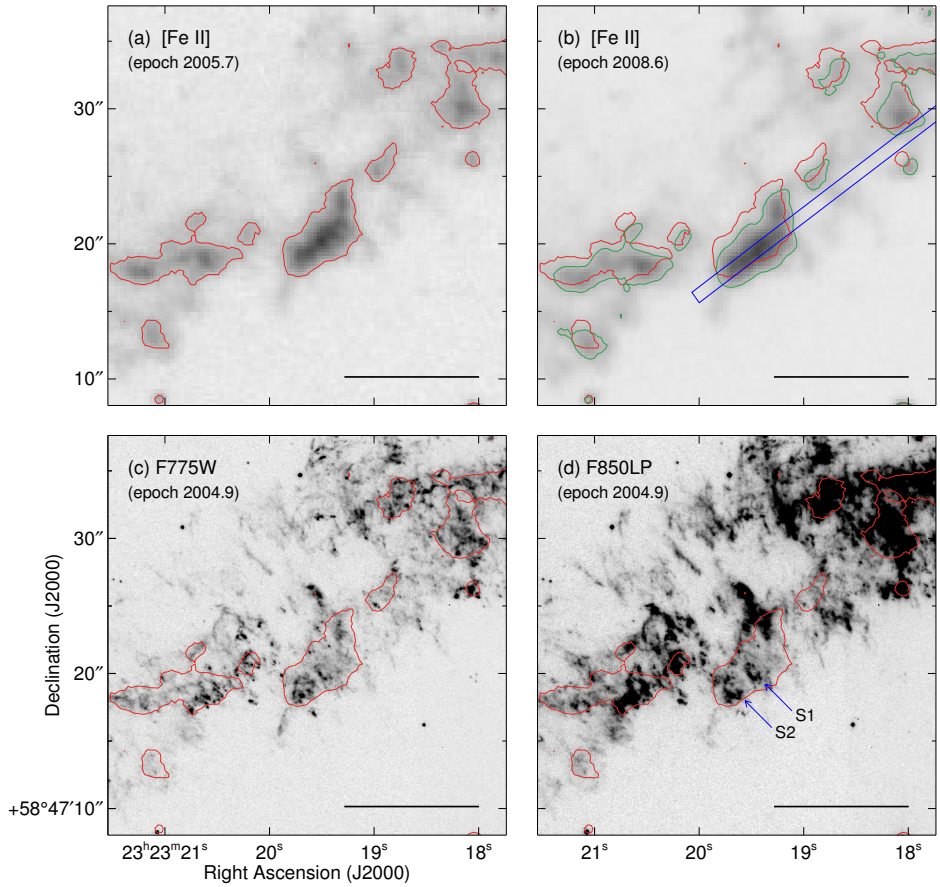

Figure 4.11 Enlarged views of the SW shell where the brightest Fe-rich knot (Knot 10 in Slit 5; K10) has been detected. (a)–(b) [Fe II] 1.644 μm narrow-band images obtained in 2005 August and in 2008 August. The red and green contours indicate the brightness level of 1×10^{-4} erg s^{-1} cm^{-2} sr^{-1} in the 2005 and 2008 images, respectively. The blue bar in the 2008 image represents the position of Slit 5 across Knot 10. (c)–(d) *HST* ACS/WFC F775W and F850LP images taken in 2004 December. The red contours overlaid on the images are the same as in (a). (d) S1 and S2 are the two bright knots mentioned in Section 4.5.2. The angular resolutions are 0.″1 and 0.″9 for the optical and [Fe II] images, respectively. The black scale bar in the lower right of each panel represents an angular scale of 10″, and the low and high thresholds of the grayscale are -5×10^{-5} and 5×10^{-4} erg s^{-1} cm^{-2} sr^{-1} in all images.

K10 but has a line-of-sight velocity (+1500 km s^{-1}) that is very different from that of K10 (−300 km s^{-1}). The other bright spot, S2, must also be due to an S-rich knot not detected in our spectroscopy. So excluding these two bright knots, K10 appears faint in F775W and F850LP images. We suspect that most of the diffuse emission in the F775W and F850LP images is due to optical [Fe II] lines. This can be confirmed by optical spectroscopy. Recently, there have been optical spectral mapping observations of Cas A (Reed et al., 1995; Milisavljevic & Fesen, 2013; Alarie et al., 2014) and, in principle, a similar analysis can be done to detect Fe-rich knots, although the optical [Fe II] lines, e.g., [Fe II] 7155 and 8617 Å lines, will be much fainter than the [Fe II] 1.644 μm line because of large interstellar extinction (A_V = 5–10 mag) toward Cas A (e.g., Eriksen et al., 2009; Hwang & Laming, 2012; Lee et al., 2015).

The distribution and amount of Fe ejecta in Cas A have been a subject of controversy. Previous X-ray studies detected hot and diffuse "pure" Fe ejecta with mass $\sim 0.1\ M_\odot$ that might have formed by α-rich freeze-out during the complete Si burning (Hwang & Laming, 2003, 2012). These X-ray-emitting shocked Fe ejecta are distributed mainly in the southeastern and northern regions of the remnant (Figure 4.12). On the other hand, the hard X-ray emission from the radioactive decay of ^{44}Ti has been detected in the interior of the main ejecta shell (Figure 4.12; Grefenstette et al., 2014). Since ^{44}Ti is essentially synthesized in complete Si burning with α-rich freeze-out in the innermost region (e.g., Magkotsios et al., 2010), ^{44}Ti traces "pure" ^{56}Ni or its stable nuclei ^{56}Fe. The majority of the observed ^{44}Ti is inside the reverse shock and therefore from unshocked Fe ejecta. The inferred mass of the unshocked Fe ejecta is $\sim 0.1\ M_\odot$ (Grefenstette et al., 2014). Such unshocked Fe ejecta, however, have not yet been detected, presumably because they are cool ($T \lesssim 40$ K; e.g., Barlow et al., 2010; Sibthorpe et al., 2010; Lee et al., 2015). Instead, the X-ray-emitting Fe ejecta located just outside the ^{44}Ti emission was attributed to the corresponding shocked ejecta (Figure 4.12; Grefenstette et al., 2014). However, the missing X-ray-emitting Fe ejecta toward the south and northeast directions from the explosion center have been puzzling. We note that the NIR [Fe II]-bright, red portion of the SW shell appears to be in contact with the interior ^{44}Ti-emitting region (Figure 4.12). This might be

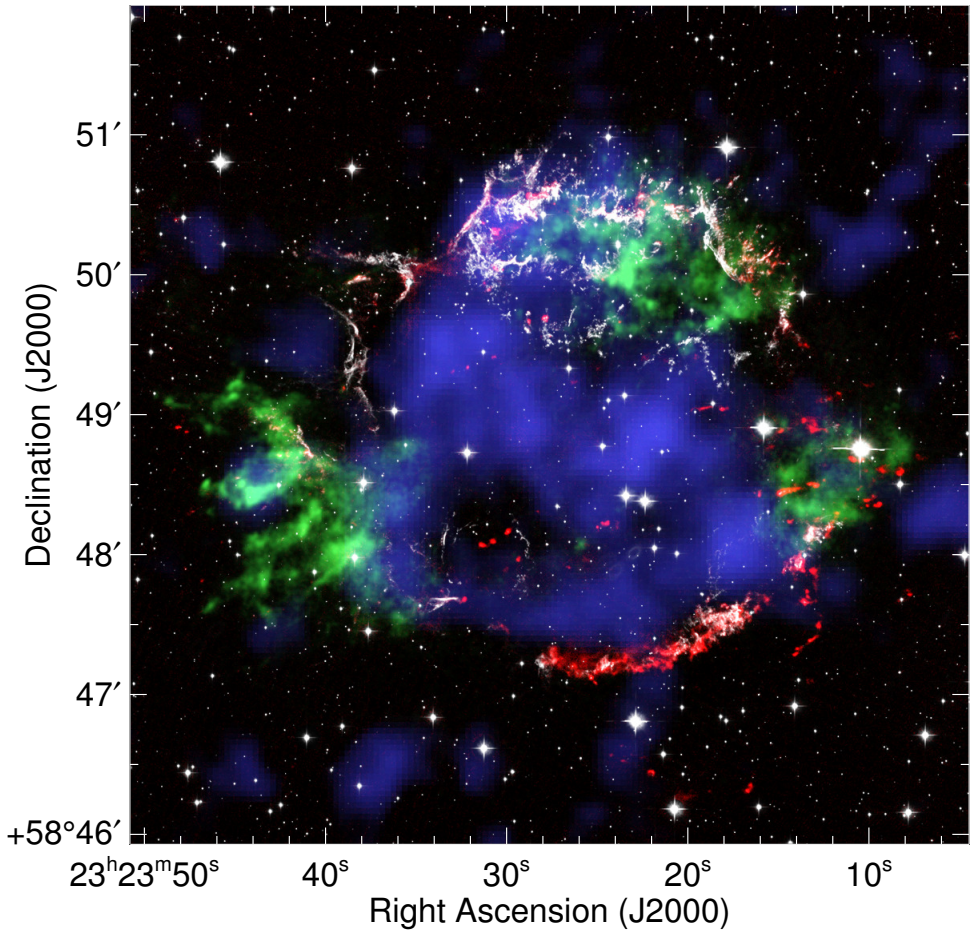

Figure 4.12 A four-color composite image of Cas A with the [Fe II] 1.644 μm narrow-band image in Figure 1 in red, the *Chandra* Fe K-shell (6.52–6.94 keV) image in green (Hwang et al., 2004), the *NuSTAR* hard X-ray ^{44}Ti (67.9 and 78.4 keV) image in blue (Grefenstette et al., 2014), and the *HST* ACS/WFC F850LP image in white (Fesen et al., 2006).

the case for the small red portion near Slit 2 in the northeastern shell, too. Therefore, if these [Fe II]-bright regions are composed of shocked, dense Fe ejecta, as implied from our spectroscopic result, it explains why we do not see X-ray-emitting diffuse Fe ejecta toward these directions; the unshocked "pure" Fe ejecta traced by the radioactive ^{44}Ti emission in the interior of the main shell is composed of both dense and diffuse ejecta, and when these are swept up by a reverse shock, we observe either NIR [Fe II] emission or X-ray emission depending on their densities. We do not see NIR emission associated with the central bright ^{44}Ti emission but this could be because the shock is face-on, as suggested by the large red-shifted central velocity (1100–3000 km s^{-1}) of the ^{44}Ti line (Grefenstette et al., 2014), or because the reverse shock has not yet reached the dense, unshocked Fe ejecta. Recent multi-dimensional simulations show that such global asymmetry in Fe (or ^{56}Ni) density can arise from the low-mode convection of the innermost region just after the core bounce (e.g., Wongwathanarat et al., 2013). Future NIR spectral mapping observations revealing the 3D distribution of the dense Fe ejecta will be helpful for understanding the SN explosion dynamics of the innermost region.

4.6 Summary

We have carried out NIR spectroscopic observations toward the main ejecta shell of the young SNR Cas A. In total, 63 individual knots were identified from eight slit positions by using a clump-finding algorithm. Each of these knots has distinct kinematical and spectral properties. Within the *JHK* spectral range (0.94–2.46 μm), we found 46 emission line features including a dozen bright [Fe II] lines, forbidden lines of other metallic species, and H and He lines. We employed the PCA method to classify the knots based on their relative line fluxes into three distinctive groups: He-rich knots of pre-supernova circumstellar wind material, plus S-rich and Fe-rich knots of SN ejecta material. The He-rich and S-rich knots correspond to QSFs and FMKs studied in the visible waveband, while Fe-rich knots, showing in general only [Fe II] emission lines, are likely 'pure' dense Fe ejecta from the innermost layer of the progenitor. We summarize

our main results as follows.

1. The PCA showed that the NIR spectral lines can be grouped into three groups: (1) Group 1, composed of H I and He I lines together with [N I] lines, (2) Group 2, composed of forbidden lines of Si, P, and S, and (3) Group 3, composed of forbidden Fe lines. The lines in the first two PCs are strongly correlated with each other, while the correlation is rather weak among the forbidden Fe lines in Group 3. These three spectral groups of the emission lines are almost independent in 3D PC space (Figure 4.4).

2. The distribution of the knots in the PC planes matches well with the above spectral groups, and we classified the knots into three groups: (1) He-rich, (2) S-rich, and (3) Fe-rich knots. The knots belonging to these three groups are well separated from each other in F([S II]-1.03)/F([Fe II]-1.644) vs. F(He I-1.083)/F([Fe II]-1.644) plane (Figure 4.7), so that one may use these line ratios to classify the knots in Cas A. It would be interesting to determine whether this classification methodology applies for other core-collapse SNRs.

3. The He-rich knots show bright emission lines of He I 1.083 μm and [Fe II] together with [N I] and H I lines. Their line-of-sight speeds are small ($\lesssim$ 200 km s^{-1}). From these chemical and kinematical characteristics, we conclude that the He-rich knots are dense CSM swept up by the SN blast wave. These knots correspond to the previously known QSFs.

4. The S-rich knots show strong forbidden lines of S together with [P II] and [Si VI], and their line-of-sight speeds reach a few 1000 km s^{-1}. These chemical and kinematical properties indicate that the S-rich knots are dense SN ejecta material mostly originating from the O-burning layers and swept up by a reverse shock. These knots correspond to the FMKs detected in previous optical studies.

5. The Fe-rich knots only show strong [Fe II] and [Fe III] lines, and no or weak He I 1.083 μm lines. Like the S-rich knots, they have large line-of-sight speeds (up to $\sim$ 1500 km s^{-1}) and broad line widths (10–35 Å), but they do not show the lines from Si, P, and S. Some Fe-rich knots show He I 1.083 μm but their fluxes compared to the [Fe II] lines are much weaker than those of the He-rich knots. These spectroscopic properties suggest that the Fe-rich knots are most likely "pure" dense Fe ejecta from

the innermost layer of the SN. The comparison of [Fe II] 1.644 μm images with the *HST* ACS/WFC F850LP and F775W and *NuSTAR* ^{44}Ti images reveals that these Fe ejecta are mainly distributed in the SW main ejecta shell, just outside the unshocked ^{44}Ti in the interior. This supports that there could be a large amount of unshocked "pure" Fe ejecta associated with ^{44}Ti. Together with the diffuse, X-ray-emitting "pure" Fe ejecta detected by *Chandra*, our result implies that the Fe ejecta synthesized in the innermost region develop large-scale non-uniformity during the SN explosion and are expelled asymmetrically. This seems to be consistent with the low-mode, convection-driven SN explosion model.

Biblography

Alarie, A., Bilodeau, A., & Drissen, L. 2014, MNRAS, 441, 2996

Barlow, M. J., Krause, O., Swinyard, B. M., et al. 2010, A&A, 518, L138

Blondin, J. M., Borkowski, K. J., & Reynolds, S. P. 2001, ApJ, 557, 782

Chevalier, R. A. 1982, ApJ, 258, 790

Chevalier, R. A., Blondin, J. M., & Emmering, R. T. 1992, ApJ, 392, 118

Chevalier, R. A., & Kirshner, R. P. 1979, ApJ, 233, 154

Chevalier, R. A., & Oishi, J. 2003, ApJL, 593, L23

Deb, N. C., & Hibbert, A. 2010, ApJL, 711, L104

DeLaney, T., Rudnick, L., Stage, M. D., et al. 2010, ApJ, 725, 2038

Dennefeld, M., & Andrillat, Y. 1981, A&A, 103, 44

Draine, B. T. 2003, ApJ, 598, 1017

Ennis, J. A., Rudnick, L., Reach, W. T., et al. 2006, ApJ, 652, 376

Eriksen, K. A., Arnett, D., McCarthy, D. W., & Young, P. 2009, ApJ, 697, 29

Fesen, R. A. 2001, ApJS, 133, 161

Fesen, R. A., Becker, R. H., & Blair, W. P. 1987, ApJ, 313, 378

Fesen, R. A., Becker, R. H., & Goodrich, R. W. 1988, ApJL, 329, L89

Fesen, R. A., & Gunderson, K. S. 1996, ApJ, 470, 967

Fesen, R. A., Hammell, M. C., Morse, J., et al. 2006, ApJ, 636, 859

Fesen, R. A., Hammell, M. C., Morse, J., et al. 2006, ApJ, 645, 283

Fesen, R. A., Morse, J. A., Chevalier, R. A., et al. 2001, AJ, 122, 2644

Froese Fischer, C. 2006, Journal of Physics B Atomic Molecular Physics, 39, 2159

Gerardy, C. L., & Fesen, R. A. 2001, AJ, 121, 2781

Giannini, T., Antoniucci, S., Nisini, B., et al. 2015, ApJ, 798, 33

Gilkis, A., & Soker, N. 2015, ApJ, 806, 28

Grefenstette, B. W., Harrison, F. A., Boggs, S. E., et al. 2014, Nature, 506, 339

Hammell, M. C., & Fesen, R. A. 2008, ApJS, 179, 195

Hammer, N. J., Janka, H.-T., Müller, E. 2010, ApJ, 714, 1371

Herter, T. L., Henderson, C. P., Wilson, J. C., et al. 2008, Proc. SPIE, 7014, 70140X

Hughes, J. P., Rakowski, C. E., Burrows, D. N., & Slane, P. O. 2000, ApJL, 528, L109

Hurford, A. P., & Fesen, R. A. 1996, ApJ, 469, 246

Hwang, U., & Laming, J. M. 2003, ApJ, 597, 362

Hwang, U., & Laming, J. M. 2012, ApJ, 746, 130

Hwang, U., Laming, J. M., Badenes, C., et al. 2004, ApJL, 615, L117

Isensee, K., Rudnick, L., DeLaney, T., et al. 2010, ApJ, 725, 2059

Joggerst, C. C., Woosley, S. E., & Heger, A. 2009, ApJ, 693, 1780

Kelleher, D. E., & Podobedova, L. I. 2008, Journal of Physical and Chemical Reference Data, 37, 1285

Kifonidis, K., Plewa, T., Janka, H.-T., Müller, E. 2003, A&A, 408, 621

Kifonidis, K., Plewa, T., Scheck, L., Janka, H.-T., Müller, E. 2006, A&A, 453, 661

Koo, B.-C., & Lee, Y.-H. 2015, Publication of Korean Astronomical Society, 30, 145

Koo, B.-C., Lee, Y.-H., Moon, D.-S., Yoon, S.-C., & Raymond, J. C. 2013, Science, 342, 1346

Koo, B.-C., Raymond, J. C., & Kim, H.-J. 2016, Journal of Korean Astronomical Society, 49, 109

Krause, O., Birkmann, S. M., Usuda, T., et al. 2008, Science, 320, 1195

Lee, J.-J., Park, S., Hughes, J. P., & Slane, P. O. 2014, ApJ, 789, 7

Lee, Y.-H., Koo, B.-C., Moon, D.-S., & Lee, J.-J. 2015, ApJ, 808, 98

Likkel, L., Dinerstein, H. L., Lester, D. F., Kindt, A., & Bartig, K. 2006, AJ, 131, 1515

Lutz, D., Krabbe, A., & Genzel, R. 1993, ApJ, 418, 244

Magkotsios, G., Timmes, F. X., Hungerford, A. L., et al. 2010, ApJS, 191, 66

Mao, J., Ono, M., Nagataki, S., et al. 2015, ApJ, 808, 164

Milisavljevic, D., & Fesen, R. A. 2013, ApJ, 772, 134

Moon, D.-S., Koo, B.-C., Lee, H.-G., et al. 2009, ApJL, 703, L81

Neufeld, D. A., Hollenbach, D. J., Kaufman, M. J., et al. 2007, ApJ, 664, 890

Nussbaumer, H., & Storey, P. J. 1988, A&A, 193, 327

Okumura, S.-i., Mori, A., Watanabe, E., Nishihara, E., & Yamashita, T. 2001, AJ, 121, 2089

Osterbrock, D. E., Fulbright, J. P., & Bida, T. A. 1997, PASP, 109, 614

Reed, J. E., Hester, J. J., Fabian, A. C., & Winkler, P. F. 1995, ApJ, 440, 706

Rest, A., Foley, R. J., Sinnott, B., et al. 2011, ApJ, 732, 3

Rho, J., Reynolds, S. P., Reach, W. T., et al. 2003, ApJ, 592, 299

Rousselot, P., Lidman, C., Cuby, J.-G., Moreels, G., & Monnet, G. 2000, A&A, 354, 1134

Rudy, R. J., Rossano, G. S., & Puetter, R. C. 1994, ApJ, 426, 646

Sibthorpe, B., Ade, P. A. R., Bock, J. J., et al. 2010, ApJ, 719, 1553

Smith, J. D. T., Rudnick, L., Delaney, T., et al. 2009, ApJ, 693, 713

Skrutskie, M. F., Cutri, R. M., Stiening, R., et al. 2006, AJ, 131, 1163

Sumiyoshi, K., Yamada, S., Suzuki, H., et al. 2005, ApJ, 629, 922

Takiwaki, T., Kotake, K., & Suwa, Y. 2014, ApJ, 786, 83

Tayal, S. S., & Zatsarinny, O. 2010, ApJS, 188, 32

Thorstensen, J. R., Fesen, R. A., & van den Bergh, S. 2001, AJ, 122, 297

Ungerechts, H., Bergin, E. A., Goldsmith, P. F., et al. 1997, ApJ, 482, 245

van den Bergh, S., & Kamper, K. 1985, ApJ, 293, 537

van Veelen, B., Langer, N., Vink, J., García-Segura, G., & van Marle, A. J. 2009, A&A, 503, 495

Wagner, R. M., & Depoy, D. L. 1996, ApJ, 467, 860

Williams, J. P., de Geus, E. J., & Blitz, L. 1994, ApJ, 428, 693

Wilson, J. C., Eikenberry, S. S., Henderson, C. P., et al. 2003, Proc. SPIE, 4841, 451

Wilson, J. C., Henderson, C. P., Herter, T. L., et al. 2004, Proc. SPIE, 5492, 1295

Wongwathanarat, A., Janka, H.-T., & Müller, E. 2013, A&A, 552, A126

Woosley, S. E., Arnett, W. D., & Clayton, D. D. 1973, ApJS, 26, 231

Chapter 5

Near-Infrared Extinction due to Cool Supernova Dust in Cassioepia A

(This chapter is published in The Astrophysical Journal[1]*.)*

5.1 Introduction

For the past decade, evidence for copious amounts of dust ($\geq 10^8\ M_\odot$) in high-redshift galaxies and quasars with $z > 5$ has been reported in many far-infrared (FIR) and sub-millimeter/millimeter studies (e.g., Wang et al., 2011; Leipski et al., 2013; Calura et al., 2014, and references therein), implying that dust should be produced within a very short timescale, less than 1 Gyr after the Big Bang. The most promising sites of dust formation in such an early universe are believed to be core-collapse supernovae (CCSNe), since their progenitors have very short lifetimes ($\sim 10^6$ years) compared to asymptotic giant branch stars, which are major sources of dust in the local universe (Morgan & Edmunds, 2003; Marchenko, 2006).

To understand the dust formation process in expanding supernova (SN) ejecta, many theoretical studies have been conducted to date (Nozawa et al., 2003, 2008, 2010;

[1]Lee et al. 2015, ApJ, 808, 98

Sarangi & Cherchneff, 2015). According to these theoretical studies, dust can form in an expanding He core with grain species determined by the elemental composition at the formation site. If an SN ejecta maintains its layered structure during expansion, a variety of grain species can form, e.g., carbon grains in the helium layer, silicate and oxide grains in the oxygen-rich layer, and Si/Fe grains in the innermost layer, the amounts of which depend on the progenitor mass. If the SN ejecta is mixed, however, it is mostly silicate and oxide grains that can form. The size of the grains depends on the gas density at the condensation time. In an SN IIP, which has a thick hydrogen envelope, the expansion is slow, so large grains with an average radius of ~ 0.1 μm can form (Nozawa et al., 2003). In an SN IIb with a low-mass hydrogen envelope as well as envelope-stripped SNe such as Type Ib/c, on the other hand, the SN ejecta expands rapidly, so only small grains with a size less than 0.01 μm can form (Nozawa et al., 2008, 2010). The size distribution and chemical composition of the dust, however, could be greatly affected by density enhancements due to clumping (Sarangi & Cherchneff, 2015). Theoretical studies predict that one CCSN can produce 0.1–1.0 $M_\odot$ of SN dust (Kozasa et al., 1991; Todini & Ferrara, 2001; Nozawa et al., 2003, 2008, 2010; Bianchi & Schneider, 2007), but the dust masses obtained from observations of nearby CCSNe are much smaller than this, e.g., $\lesssim 10^{-2}$ $M_\odot$ (Meikle et al., 2007; Kotak et al., 2009; Sakon et al., 2009; Szalai et al., 2011). A significant ($\gtrsim 0.1$ $M_\odot$) amount of dust has been observed in several young CC supernova remnants (SNRs), e.g., Cassiopeia A (Barlow et al., 2010; Sibthorpe et al., 2010; Arendt et al., 2014), Crab (Gomez et al., 2012; Owen & Barlow, 2015), and 1987A (Matsuura et al., 2011; Indebetouw et al., 2014), but the physical and chemical properties of the dust remain to be explored (see below).

Cassiopeia A (Cas A), which is a remnant of an SN IIb explosion (Krause et al., 2008), is an ideal target for examining the properties of SN dust. It is quite young (~ 330 years; Fesen et al., 2006), so the SN ejecta and freshly formed SN dust have not been significantly mixed with the circumstellar/interstellar medium (CSM/ISM), and it is relatively close (3.4 kpc; Reed et al., 1995), so the physical and chemical structures can be resolved. Therefore, Cas A has been a major target of infrared space missions.

The first direct evidence for SN dust in Cas A came from the *Infrared Space Observatory* (*ISO*), which performed mid-infrared (MIR; 2.4–45 μm) spectroscopic observations toward the bright ejecta shell (Lagage et al., 1996; Arendt et al., 1999; Douvion et al., 2001). The continuum spectra had a strong bump peaking at 21 μm together with a relatively weak bump at 9.5 μm, and Douvion et al. (2001) showed that the spectra can be fitted by two dust components at different temperatures, one at 90 K and the other at 350 K, with pyroxene ($MgSiO_3$), quartz (SiO_2), and aluminum oxide (Al_2O_3) as major components. The composition and distribution of this "warm" SN dust heated by a reverse shock have been studied in detail using the spectral mapping data of the *Spitzer Space Telescope* (Ennis et al., 2006; Rho et al., 2008; Arendt et al., 2014). These studies showed that the dust emission exhibits distinct spectral characteristics depending on the SN material with which it is associated. The most prominent dust emission is that with strong 9 and 21 μm bumps, which is associated with SN ejecta having strong Ar emission lines. The spectral features agree with the *ISO* spectra and can be reproduced by Mg protosilicate/$MgSiO_3$, $Mg_{0.7}SiO_{2.7}$, or SiO_2. The dust emission associated with SN ejecta having strong Ne lines is smooth without any silicate features and can be reproduced by Al_2O_3 dust or C glass. There is yet another type of smooth dust emission associated with X-ray Fe emission, but it is probably from swept-up CSM (Arendt et al., 2014). Meanwhile, Nozawa et al. (2010) showed that the observed spectral energy distribution (SED) of dust emission can be fitted by a physical model in which the SNR is expanding into a dense CSM, and the MIR emission is mostly from silicate grains (e.g., $MgSiO_3$, Mg_2SiO_4, and SiO_2) and MgO. The estimated total mass of warm dust ranges from 0.008 to 0.054 $M_\odot$.

A larger amount of SN dust, however, appears to reside in the interior of Cas A, where the SN ejecta is freely expanding. The first report was made by Dunne et al. (2003), who claimed the detection of 2–4 $M_\odot$ of cold (15–20 K) SN dust associated with Cas A from an 850 μm observation. It was found, however, that at least some of the 850 μm emission is from a foreground material (Krause et al., 2004; Dunne et al., 2009), and instead Sibthorpe et al. (2010) and Barlow et al. (2010), using the balloon-borne sub-millimeter telescope BLAST and infrared space telescopes *AKARI*

and *Herschel*, showed that there is faint FIR and sub-millimeter emission from Cas A that can be fitted by dust at 35 K with a total mass of $\sim 0.07\ M_{\odot}$. Arendt et al. (2014) also identified the FIR emission from this "cool" dust associated with unshocked SN ejecta (their "[Si II]" dust group) using the *Herschel* FIR data and derived an upper limit of 0.1 $M_{\odot}$ for the dust mass. However, the composition of the cool dust has been undetermined so far because the absorption cross sections of dust grains in the FIR are mostly smooth without prominent spectral features.

In this paper, we show that one can explore the characteristics of the cool SN dust in the interior of Cas A using extinction in the near-infrared (NIR). Recently, we performed NIR spectroscopy toward the main ejecta shell of Cas A, where we obtained the spectral and kinematical properties of 63 knots bright in [Fe II] emission lines (Koo et al., 2013). Most of these knots are SN material, and the extinctions toward these knots show clear evidence for the SN dust, which can be combined with thermal infrared dust emission to infer the dust composition. This paper is organized as follows. In Section 5.2, we outline our NIR spectroscopic observations and data reduction and then briefly describe the public MIR and FIR imaging data that we used in the paper. In Section 5.3, we derive the NIR extinction toward the knots using [Fe II] line ratios and show that there is a correlation between the extinction and the line-of-sight velocity, which implies extinction by SN dust. Then, in Section 5.4, by comparing the NIR extinction and the thermal dust infrared SED, we constrain the possible compositions and sizes of the SN dust. We discuss the implication of our result for dust production in Cas A in Section 5.5 and summarize our paper in Section 5.6.

5.2 Observations and Data Reduction

5.2.1 Near-infrared Spectroscopy

Eight long-slit NIR spectra of the main SN ejecta shell were obtained on 2008 June 29 and August 8 using TripleSpec mounted on the Palomar Hale 5 m telescope; this spectrograph provides a broadband spectrum simultaneously covering 0.94–2.46 μm with a moderate resolving power of ~ 2700. We also observed the spectra of an

A0V standard star (HD 223386) for flux calibration just before and after the target observations. To subtract sky OH airglow emission as well as background continuum, the observations were made with either a consecutive ABBA pattern or On-Off mode depending on the complexity of the field. Figure 5.1(a) shows the position of the slits on the continuum-subtracted [Fe II] 1.64 μm narrow-band image obtained in 2008 August.

We followed a general reduction procedure to make a two-dimensional dispersed image. Numerous sky OH airglow emission lines were used for wavelength calibration, and then we corrected it to the heliocentric reference frame. The absolute photometric calibration was made by comparing the observed spectrum of the standard star with the Kurucz model spectrum (Kurucz, 2003). Even though the absolute flux uncertainty goes up to 30% depending on the centering accuracy of the standard star observation, the relative fluxes are quite robust.

We found a total of 63 infrared knots using a clump-finding algorithm (Williams et al., 1994) and performed a single Gaussian fit for all the detected emission lines to derive their fluxes and line-of-sight velocities. For detailed descriptions of the data reduction and analysis as well as the full list of parameters of the detected emission lines, please refer to Koo et al. (2013) and Lee et al. (2017).

5.2.2 Mid- and Far-infrared Imaging Data

For an SED analysis of SN dust, we fully exploit the previously published archival data providing the highest spatial resolution and sensitivity in the MIR and FIR wavebands covering 10–500 μm, where the dust emission is dominant.

For short wavebands, we use the W3 channel image ($\lambda_{\rm iso} \sim 12$ μm) of the *Wide-field Infrared Survey Explorer* (*WISE*: Wright et al., 2010) with an angular resolution of $6\farcs5$. We first retrieved all 36 single-exposure images ("Level-1b") from the online service[2] and converted the pixel unit to MJy sr^{-1}. After subtracting the predicted brightness of zodiacal light calculated from the interplanetary dust model from each frame (Kelsall

[2] `http://irsa.ipac.caltech.edu/applications/wise/`

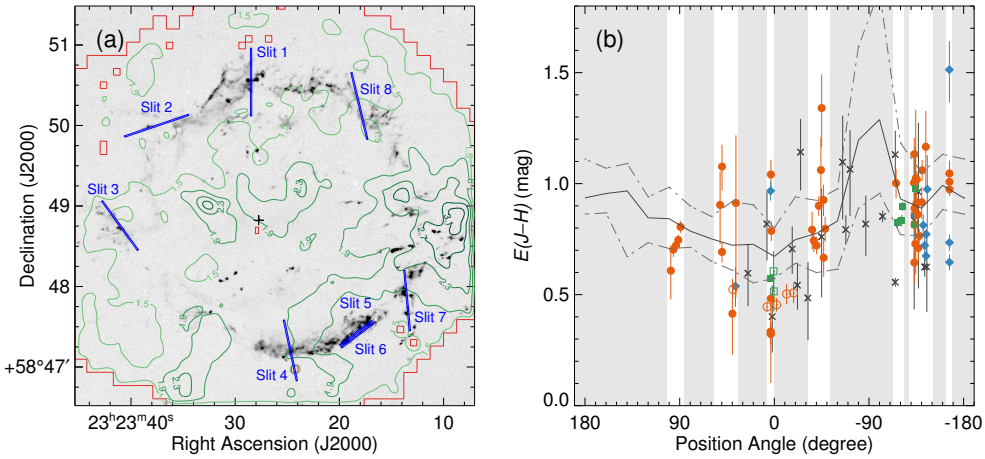

Figure 5.1 (a) Slit positions (blue bars) marked on the continuum-subtracted [Fe II] 1.64 μm narrow-band image obtained in 2008 August. The black cross mark corresponds to the center of expansion (Thorstensen et al., 2001). The green contours represent the hydrogen column density ($N_{\rm H}$) derived from a single-component fit of *Chandra* X-ray data (Hwang & Laming, 2012), and the levels are 1.5, 1.9, 2.3, 2.7, and 3.1×10^{22} cm^{-2}. The red solid line is the boundary of the $N_{\rm H}$ map. (b) Variation of $E(J-H)$ with position angle. The position angle is the angle along the perimeter of the remnant measured from north to east with $PA = 0$ corresponding to a line drawn due north from the expansion center (black cross mark) of Cas A. The filled symbols represent the 63 infrared knots detected (Koo et al., 2013), with green squares indicating He-rich knots, red circles indicating S-rich knots, and blue diamonds indicating Fe-rich knots. The seven optical knots of Hurford & Fesen (1996) are marked by open symbols: five FMKs and two QSFs appear as red circles and green squares, respectively. The 19 infrared knots observed in Eriksen et al. (2009) are also marked by black X symbols. The gray-shaded regions are the areas uncovered in our observation. The black solid line shows the variation of the average $E(J-H)$ along the iron-bright rim obtained from the $N_{\rm H}$ map of Hwang & Laming (2012), and the black dashed-dotted lines represent maximum and minimum $E(J-H)$ at each position angle (see the text for details).

et al., 1998), we co-added the individual frames using Montage software[3] to obtain the final image. Instead of the *WISE* W4 channel image ($\lambda_{\rm iso} \sim 22$ μm), we use the 24 μm band image of the Multiband Imaging Photometer for *Spitzer* (MIPS: Rieke et al., 2004) obtained in 2007 January (AORKEY: 17657088, 17657344)[4], which provides better spatial resolution (6″) than *WISE* W4. The data used here are the Post-BCD image ("Level 2"), which is automatically processed by the MIPS software pipeline (version: S18.12.0). As in the *WISE* data, zodiacal light is one of the significant sources of background radiation in this waveband. We therefore subtracted the background brightness from the mosaic image using the model calculation (Kelsall et al., 1998).

Recent FIR images of the remnant were observed with PACS and SPIRE on board *Herschel Space Observatory* (Pilbratt et al., 2010) in 2009 September and December. The two instruments have six photometric bands (70, 100, and 160 μm for PACS, and 250, 350, and 500 μm for SPIRE), and they provide spatial resolutions of 5.″2, 7.″7, 12″, 18″, 25″, and 37″, respectively. The fully calibrated data sets were downloaded from the *Herschel* Science Archive[5], and we use the data product levels of 2.5 and 2.0 for PACS and SPIRE, respectively. All imaging data have well-established zero-level brightness, whereas the PACS photometer images at level 2.5 do not (PACS Observer's Manual - version 2.5.1). To obtain the true zero point of the images, we calibrated the zero level by comparison with reference images whose zero point is well established. For the reference photometric calibrator, we used 60 and 100 μm images from Improved Reprocessing of the *IRAS* Survey (IRIS: Miville-Deschênes & Lagache, 2005) together with DIRBE 140 and 240 μm and *Planck* 350 and 550 μm maps. In Cas A, synchrotron radiation is a dominant source in the FIR waveband. This nonthermal component is subtracted by using the VLA radio image at 6 cm (Delaney, 2004). The expected brightness at each isophotal wavelength is extrapolated from the power law $S_\nu = C\ \nu^\alpha$ (erg cm^{-2} s^{-1} Hz^{-1}). In this paper, we adopt $\alpha = -0.682$ and $C = 2.50 \times 10^9$ erg cm^{-2} s^{-1} Hz^{-1}, which are derived from the total brightness of the remnant at 30, 44,

[3] `http://montage.ipac.caltech.edu/`
[4] `http://sha.ipac.caltech.edu/applications/Spitzer/SHA/`
[5] `http://www.cosmos.esa.int/web/herschel/science-archive/`

70, and 100 GHz using *Planck* (Planck Collaboration et al., 2011) archival data[6].

5.3 NIR Extinction by SN Dust

5.3.1 NIR Extinction Measurement

We derive the selective extinction or "color excess" between 1.26 and 1.64 μm, $E(J-H)$, toward the infrared knots from

$$E(J-H) \equiv A_{1.26} - A_{1.64} = 1.086 \ \ln \frac{[F_{1.26}/F_{1.64}]_{\rm int}}{[F_{1.26}/F_{1.64}]_{\rm obs}}, \tag{5.1}$$

where $A_{1.26}$ and $A_{1.64}$ are the total extinctions at 1.26 and 1.64 μm, and $[F_{1.26}/F_{1.64}]_{\rm obs}$ and $[F_{1.26}/F_{1.64}]_{\rm int}$ are the observed and intrinsic flux ratios of the [Fe II] 1.26 and 1.64 μm lines, respectively. These two strong [Fe II] lines share the same upper state ($a^4D_{7/2}$), so their intrinsic ratio is fixed by their Einstein A coefficients and wavelengths, i.e., $[F_{1.26}/F_{1.64}]_{\rm int} = (A_{ki,1.26}/1.26)/(A_{ki,1.64}/1.64)$. The ratio has been derived from both theoretical calculations and observations, and it ranges from 0.94 to 1.49 in previous studies (e.g., Giannini et al., 2015; Koo & Lee, 2015, and references therein). This large uncertainty of the intrinsic flux ratio hampers accurate measurement of the absolute extinction toward the remnant (this issue will be addressed in Section 5.3.3). It is, however, worth noting that the uncertainty does not affect the difference in $E(J-H)$ (Equation 5.1) among the knots, which gives the relative extinction to them. In this paper, we adopt the intrinsic line flux ratio of 1.36, which is the theoretical value proposed by Nussbaumer & Storey (1988) and Deb & Hibbert (2010).

5.3.2 Total Extinction to Cas A

In Figure 5.1(b), we plot $E(J-H)$ for the 63 infrared knots as a function of position angle. The colors and symbols represent the characteristic groups classified by Koo et al. (2013): helium-rich knots in green squares, sulfur-rich knots in red circles, and iron-rich knots in blue diamonds. In short, helium-rich knots are slowly moving

[6] http://irsa.ipac.caltech.edu/applications/planck/

($\lesssim$ 100 km s^{-1}) knots with strong He I lines, the properties of which match those of "quasi-stationary flocculi" (QSFs), the circumstellar material swept up by an SN blast wave (van den Bergh, 1971; Lee et al., 2014). Sulfur-rich and iron-rich knots are fast-moving ($\gtrsim$ 100 km s^{-1}) knots with strong [S II] and strong [Fe II] lines, respectively. They are SN ejecta material synthesized in different layers of the SN and correspond to fast-moving knots (FMKs) in previous optical studies (e.g., van den Bergh, 1971; Hammell & Fesen, 2008). For more detailed explanations on the spectroscopic and kinematic properties of these knots, please refer to Koo et al. (2013). For comparison, we also plot $E(J-H)$ for the optical and infrared knots measured in previous studies. Hurford & Fesen (1996) observed optical spectra of five FMKs and two QSFs located in the northern bright rim and measured $E(B-V)$ using ratios of the [S II] and the Balmer lines, respectively. We converted it to $E(J-H)(= 0.30 \times E(B-V))$ assuming the general interstellar dust composition with R_V of 3.1 (Draine, 2003), and the open red circles and green squares in the figure represent the FMKs and QSFs, respectively. Eriksen et al. (2009) performed NIR spectroscopy for four slit positions and derived the line ratio of [Fe II] 1.26–1.64 μm for 19 infrared knots without any classification of their origin. We obtained $E(J-H)$ using Equation 5.1 and marked the results by black X marks.

The derived $E(B-V)$ varies considerably over the remnant. It appears that the extinction toward the west is systematically larger than that toward the east, though there is a large scatter. This systematic variation is well known from previous radio and X-ray observations (e.g., Keohane et al., 1996; Reynoso & Goss, 2002; Hwang & Laming, 2012). For example, the green contours in Figure 5.1(a) show the column density ($N_{\rm H}$) map of Hwang & Laming (2012) obtained from an analysis of the *Chandra* X-ray data. The column density is large ((2–3) $\times 10^{22}$ cm^{-2}) toward the west and southwest directions, and molecular line studies showed that it is due to molecular clouds located in the Perseus Spiral Arm.

Figure 5.1(b) shows that the extinction varies considerably *within a slit*. For example, along Slit 4, $E(J-H)$ varies from 0.6 to 1.5 mag even though the emission is from a thin filament. This variation is significantly larger than what we would expect from

the variation in the foreground extinction. For example, the solid line in the figure represents an expected $E(J-H)$ variation along the ejecta shell derived from the $N_{\rm H}$ map in Figure 5.1(a). The ejecta shell is determined in the continuum-subtracted [Fe II] image where the brightness is greater than 3σ of the background rms noise, and the mean $N_{\rm H}$ is obtained at every 10° in position angle. The column density is converted to $E(J-H)$ using $N_{\rm H}/E(B-V) = 5.8\times10^{21}$ atoms cm^{-2} mag^{-1} (Bohlin et al., 1978) and $E(J-H) = 0.30 \times E(B-V) = N_{\rm H}/1.9\times10^{22}$ cm^{-2}. The dashed-dotted lines represent the maximum and minimum $E(J-H)$ at each position angle. It is obvious that, in several slits, the variation of $E(J-H)$ within a slit is much larger than the range allowed from the $N_{\rm H}$ map. As we show in the next section, this large variation is due to extinction *within the SN ejecta*.

5.3.3 Self-extinction within Cas A

An interesting correlation is found when we plot $E(J-H)$ as a function of radial velocity, which is shown in Figure 5.2(a). It is clear that the redshifted knots are generally more obscured than the blueshifted knots. Because we are observing an expanding shell, this suggests that the knots on the far side experience more extinction than those on the front side, or that there could be extinction originating *within* the remnant. To confirm this "self-extinction," it is necessary to remove the spatially varying foreground interstellar extinction. We subtract the extinction derived from the X-ray observation (Figure 5.1), and the result is shown in Figure 5.2(b). The correlation becomes slightly weaker, but it is still obvious that the redshifted knots are more heavily obscured than the blueshifted knots. Therefore, our result implies that there is extinction, which might be due to newly formed SN dust within the remnant. The large scatter in extinction for the same velocity knots might reflect differences among different sight lines, i.e., non-uniform distribution of SN dust.

Note in Figure 5.2(b) that the minimum $E(J-H) \sim -0.3$, which means that the $E(J-H)$ derived from the $N_{\rm H}$ map is higher than the $E(J-H)$ derived from [Fe II] line ratios. We can think of two possibilities for the negative $E(J-H)$. First, it could be due to the uncertainty of the theoretical [Fe II] line ratio. To compensate for the

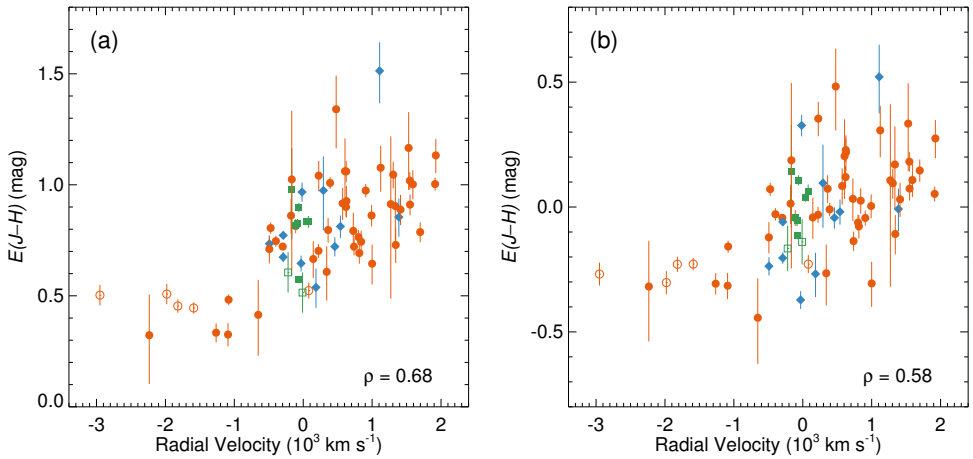

Figure 5.2 (a) Variation of $E(J-H)$ for the 70 knots as a function of radial velocity. Symbols and colors of the knots are the same as in Figure 5.1, and the correlation coefficient of the knots (ρ) is given in the bottom right. (b) Same as (a), but after the subtraction of the foreground extinction using the $N_{\rm H}$ map of Hwang & Laming (2012).

$E(J-H)$ of -0.3 mag, however, the theoretical flux ratio of [Fe II] 1.26–1.64 μm should be more than 1.8, which is considerably higher than the numerical value obtained in previous studies ($0.94 \leq [F_{1.26}/F_{1.64}]_{int} \leq 1.49$). Second, the $N_{\rm H}$ derived from X-ray data could be overestimated. Indeed, the mean column density from the X-ray studies is $\sim 1.5 \times 10^{22}$ cm^{-2} (Willingale et al., 2002; Hwang & Laming, 2012), which is higher than those of radio observations, e.g., $\sim 1.1 \times 10^{22}$ cm^{-2} (Troland et al., 1985; Keohane et al., 1996). We also note that the column densities of Hwang & Laming (2012) are higher by (0.4–0.7) $\times 10^{22}$ cm^{-2} than those of Lee et al. (2014), who carefully analyzed the X-ray spectra around the outer SNR shock. The difference of 0.3 mag in $E(J-H)$, which corresponds to $N_{\rm H} \approx 6 \times 10^{21}$ cm^{-2}, may therefore have resulted from the difficulty in background removal in the analysis of Hwang & Laming (2012). Another complication is that the X-ray-absorbing column also includes self-extinction, so the X-ray-based extinction overestimates the foreground extinction. Thus it appears difficult to obtain an accurate map of the foreground extinction from the X-ray data alone, but this uncertainty is not likely to erase the systematic correlation in Figure 5.2(b).

The non-uniform spatial distribution of SN dust and the uncertainty in the foreground extinction hamper the analysis of the correlation in Figure 5.2(b). However, in one slit (Slit 4), we detected convincing evidence for self-extinction without those sight-line-dependent complications. Figures 5.3(a) and (b) show that the velocity structure of the [Fe II]-line-emitting gas in Slit 4 is "arc"-like, suggesting that the slit crosses a portion of an expanding shell. This is consistent with the result of previous studies that the main ejecta shell is a thin shell expanding at 4000–5000 km s^{-1} (e.g., DeLaney et al., 2010; Isensee et al., 2012). In Slit 4, therefore, we have both blue and redshifted Fe knots along a given sight line, and the uncertainty due to different sight lines disappears. Now Figure 5.3(c) shows the $E(J-H)$ map obtained for pixels with an [Fe II] 1.64 μm brightness greater than 3σ above the background noise. A systematic increase in the extinction toward the redshifted knots is apparent. We computed an intensity-weighted $E(J-H)$ as a function of radial velocity, which is shown by the black solid line in Figure 5.3(d). We also divided the iron filament into three subregions along the slit (A–C in Figure 5.3(c)), and their mean $E(J-H)$ values are over-plotted on the

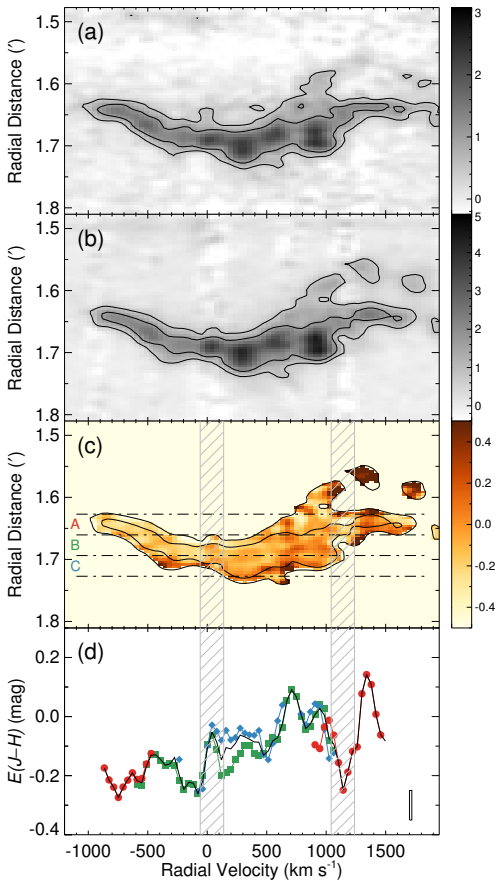

Figure 5.3 Position-velocity diagram at (a) 1.26 μm and (b) 1.64 μm in Slit 4, showing the brightness of [Fe II] 1.26 and 1.64 μm emission. The y-axis represents the radial distance in arcminutes from the expansion center (see Figure 5.1-(a)). The contour levels correspond to 2σ and 4σ for [Fe II] 1.26 μm and 3σ and 6σ for [Fe II] 1.64 μm above the background rms noise. Unit of the color bar on the right side of the panels is 10^{-17} erg cm^{-2} s^{-1} Å^{-1}. (c) Color excess ($E(J-H)$) map of Slit 4. The foreground extinction derived from the $N_{\rm H}$ map (Hwang & Laming, 2012) is subtracted from the observed $E(J-H)$. The gray hatched areas are the areas where the OH line contamination is significant compared to the [Fe II] emission. (d) One-dimensional $E(J-H)$ profile of the pixels above 4σ and 6σ rms noise for [Fe II] 1.26 and 1.64 μm, respectively. The black solid line represents the intensity-weighted extinction profile, whereas the red, green, and blue solid lines are the mean profiles obtained from the slices in (c). The mean velocity resolution and extinction error are indicated by the black solid box at the lower right.

figure with red, green, and blue solid lines. The total $E(J-H)$ within the ejecta shell from Figure 5.3(d) is 0.23 ± 0.05 mag with a systematic gradient of 0.13 ± 0.02 mag per 1000 km s^{-1}. This should be mostly, if not entirely, due to SN dust because the blue and redshifted ejecta materials in the slit are essentially along the same sight line. There are small-scale variations in $E(J-H)$ in Figure 5.3(d). They could be due to either incomplete subtraction of OH airglow emissions (e.g., gray-hatched areas in the figure) or very small dust clumps within the slit, or both.

The obtained $E(J-H)$ can be converted to the dust column density ($\Sigma_{\rm d}$) with an appropriate $\Delta\kappa_{JH} \equiv \kappa_{1.26} - \kappa_{1.64}$ (cm^2 g^{-1}), where $\kappa_{1.26}$ and $\kappa_{1.64}$ are the mass absorption coefficients at 1.26 and 1.64 μm, respectively:

$$E(J-H) = 1.086 \int \Delta\kappa_{JH}\ \rho_{\rm d}\ dl \approx 0.11 \left(\frac{\Delta\kappa_{JH}}{10^3\ {\rm cm^2\ g^{-1}}}\right)\left(\frac{\Sigma_{\rm d}}{10^{-4}\ {\rm g\ cm^{-2}}}\right) \quad (5.2)$$

This equation yields the column density of a given dust species required to explain the observed NIR self-extinction. For example, if it is Fe dust, which has $\Delta\kappa_{JH} \sim 10^3$ cm^2 g^{-1} (Semenov et al., 2003, see Figure 5.7), the required dust column is $\sim 10^{-4}$ g cm^{-2}.

5.4 FIR Emission and SN Dust Composition

5.4.1 FIR Emission from SN Dust

What dust species would produce the $E(J-H)$ of 0.2 mag detected in Slit 4? In this section, we constrain the dust species by investigating the FIR emission properties of SN dust.

Figure 5.4(a) shows the one-dimensional (1D) brightness profiles at 12, 24, 70, and 100 μm along the slit length in Slit 4. Note that these data have similar angular resolutions of 5.″2–7.″7 (Section 5.2.2). The profiles are background-subtracted using the mean brightnesses of an area just outside the ejecta shell (red square in Figure 5.4(b)) and are normalized by their peak brightnesses. All four profiles have maxima at 1.′67 where the iron filament is located (Figure 5.3). All emission drops to zero inside of the ejecta shell except for the 100 μm emission, which remains constant at $\sim$ 30% of its peak brightness. This excess emission at 100 μm must be mostly from the unshocked cool SN dust detected previously in the FIR (Barlow et al., 2010; Arendt et al., 2014).

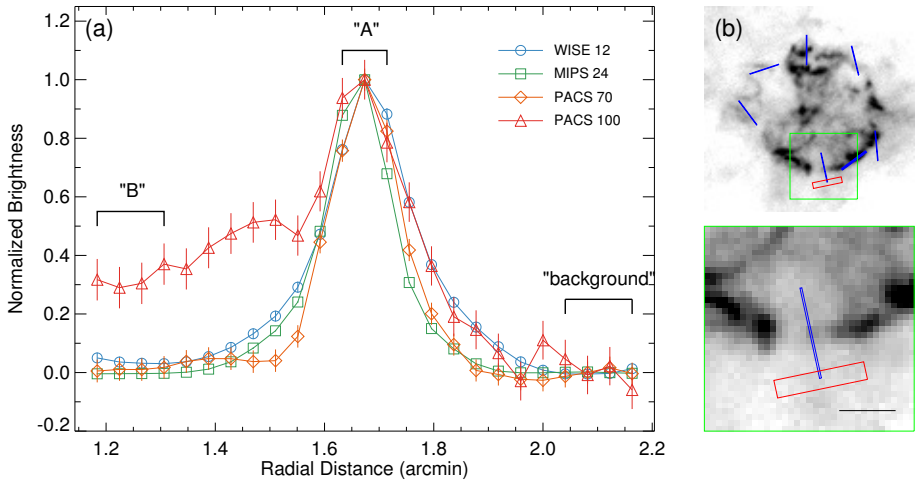

Figure 5.4 (a) One-dimensional profiles of 12, 24, 70, and 100 μm brightnesses along the length of Slit 4. Each profile is background-subtracted and normalized by the peak brightness at 1.′67. (b) Location of the background region (red box; $10'' \times 50''$ between 2.′0 and 2.′2 in radial distance) on the synchrotron-subtracted PACS 100 μm image. Slit positions are also marked with blue boxes. The bottom image is a zoomed-in image of the area in the green box in the top frame, and the black scale bar in the lower right represents an angular scale of $30''$.

We examine the SEDs at two positions (see Figure 5.4(a)): (1) the peak brightness position at 1.′67 with $\sim 6''$ aperture (hereafter position A) and (2) the inner 100 μm excess region between 1.′2 and 1.′4 (hereafter position B). For comparison, we also derive an interstellar dust SED just outside of the shell (red square in Figure 5.4(b)) where the radiation from the remnant is almost negligible. To derive accurate parameters for the SN dust, we first have to subtract the contributions of line emissions from the measured brightnesses. For this purpose, we retrieved the archival MIR and FIR spectra from *Spitzer* IRS[7] and *ISO* LWS[8] observations, respectively. We produced an IRS spectral data cube using CUBISM (Smith et al., 2007) and extracted 1D spectra within a $6''$ aperture at positions A and B as well as the background position. The strong emission lines falling in the *WISE* W3 and MIPS 24 μm bands are the [Ar II] 8.99 μm, [S IV] 10.5 μm, [Ne II] 12.8 μm, [Ne III] 15.6 μm, and [O IV]+[Fe II] 25.9 μm lines, and their contributions to the fluxes in the two bands have been estimated as 8.9% and 4.8% for position A, 4.6% and 16% for position B, and 2.0% and 1.8% for the background position, respectively. There are no corresponding FIR spectroscopic data, but an *ISO* LWS 1D spectrum (43–190 μm) from an area close ($\sim 50''$) to Slit 4 is available (#3 spectrum of Docenko & Sunyaev (2010)). According to this *ISO* spectrum, the strong emission lines falling in the PACS 70 and 100 μm bands are the [O I] 63.2 and [O III] 88.4 μm lines, respectively. Estimation of the contribution of these lines to the observed surface brightnesses at our positions is tricky because the *ISO* LWS beam is large, i.e., $\sim 80''$ (Lloyd, 2003), and covers both the Cas A ejecta shell and the background area. We estimated the line contribution by assuming that both emission lines come from the ejecta shell, not from the interstellar material. This assumption is plausible because the two lines are detected at several positions along the ejecta shell to show similar broad profiles, whereas there is little emission outside of the remnant (Docenko & Sunyaev, 2010). Under this assumption, the two lines contribute only to the brightness of A, which is estimated as 3.8% and 4.5% in the PACS 70 and 100 μm bands, respectively. In the PACS 160 μm band, there is the [O I] 146 μm

[7] http://sha.ipac.caltech.edu/applications/Spitzer/SHA/
[8] http://iso.esac.esa.int/ida/

Table 5.1. Observed and dust-continuum infrared brightnesses in Slit 4

Waveband	Observed[a]			Dust-continuum		
	A	B	Background	A	B	Background
WISE 12	24.0±1.1	7.9±0.4	6.6±0.5	21.9±1.0	7.5±0.3	6.5±0.5
MIPS 24	397±16	37.1±1.5	34.6±5.3	378±15	31.0±1.2	33.9±5.3
PACS 70	170±8	74.5±3.7	68.8±5.7	163±8	74.5±3.7	68.8±5.7
PACS 100	210±11	175±9	151±11	201±10	175±9	151±11
PACS 160	296±15	285±14	266±18	296±15	285±14	266±18
SPIRE 250	205±14	206±14	200±15	205±14	206±14	200±15
SPIRE 350	115±8	113±8	113±8	115±8	113±8	113±8
SPIRE 500	48.0±3.4	47.0±3.3	48.5±3.4	48.0±3.4	47.0±3.3	48.5±3.4

[a]The observed brightnesses include contribution from emission lines.

Note. — Brightnesses in units of MJy sr^{-1}. The uncertainties are derived from a quadrature sum of the photometric uncertainty and the brightness variation within the aperture.

line, but its contribution is almost negligible. The observed and line-subtracted dust continuum brightnesses at the three positions are listed in Table 5.1.

Figure 5.5 shows the line-emission-subtracted SEDs at positions A and B in red and blue solid lines, respectively. Both SEDs have broad thermal emission bumps peaking at 160 μm, which arise from the line-of-sight interstellar dust component at a temperature of ~ 20 K. This FIR SED matches well the SED of the background area outside the shell (black solid line), which represents the interstellar dust SED. The background-subtracted SEDs, which presumably represent "pure" SN dust SEDs, are shown in red and blue dotted lines in Figure 5.5. The SED at A now shows maximum brightness at 24 μm, and the brightness decreases toward longer wavelengths. On the other hand, that at B peaks at 100 μm, which implies that the dust temperature is much lower than that at A. These two SEDs should represent the SEDs of shocked (+unshocked) and unshocked dust species, respectively. We will analyze the SED at position A, where we obtained self-extinction of $E(J-H) = 0.23 \pm 0.05$.

Before doing a detailed analysis in the next section, we first show that the shocked warm dust component emitting the MIR emission cannot explain the NIR color excess

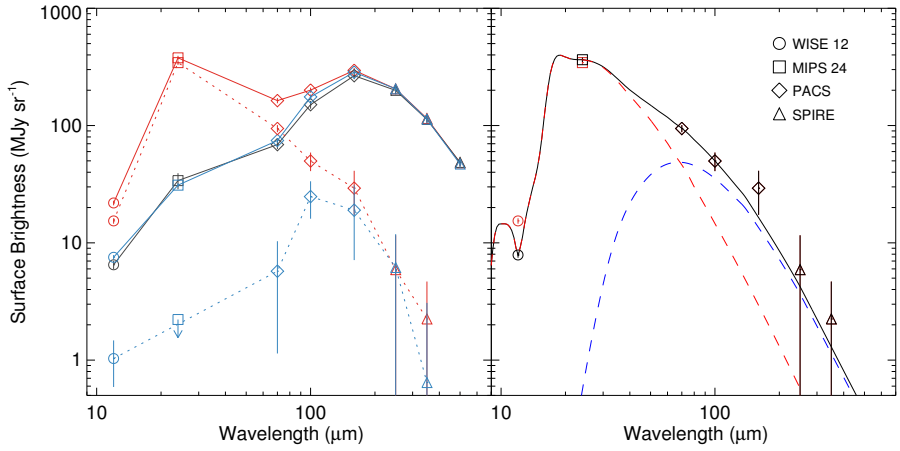

Figure 5.5 (Left) Spectral energy distribution (SED) of dust emission in Slit 4. The red and blue solid lines represent the SEDs of total dust continuum emission in regions A and B in Figure 5.4, and the black solid line is that of the background region (see Table 5.1). The red and blue dotted lines represent the background-subtracted SEDs in regions A and B, respectively, and therefore the SEDs of pure SN dust. The symbol with a downward arrow denotes the 1σ upper limit of the brightness. (Right) Two-component fit for the SED at position A. The warm dust (red dashed line) is assumed to be $MgSiO_3$, whereas the cool dust (blue dashed line) is assumed to have the general interstellar dust composition (see the text for details). Red and black symbols represent the measured and color-corrected brightnesses, respectively.

that we detected. Previous observations showed that the warm dust is silicate grains (e.g., Arendt et al., 2014), and we assume that it is $MgSiO_3$ grains with a size of 0.001–0.1 μm, which has $10^{-1} \lesssim \Delta\kappa_{JH} \lesssim 10^2$ cm^2 g^{-1} (Dorschner et al., 1995). (As we will show in the next section, assuming other silicate dust species will yield the same conclusion.) The SED at A has excess emission in the FIR, and we perform a two-temperature modified blackbody fit assuming that the cool dust has the optical properties of general interstellar dust (Draine, 2003), as in Sibthorpe et al. (2010). The surface brightness of each component at temperature T is calculated from

$$S_\nu = \kappa_{\mathrm{abs},\nu}\ B_\nu(T)\ \Sigma_\mathrm{d} \tag{5.3}$$

where $\kappa_{\mathrm{abs},\nu}$ is the mass absorption coefficient, and $B_\nu(T)$ is the Planck function. We used MPFIT (Markwardt, 2009), which is a nonlinear least-squares fitting routine within IDL, to derive the values of T and Σ_d at which χ^2 is minimum as well as their formal 1σ uncertainties. The SED is well fitted with warm dust at $T = 115 \pm 2$ K plus cool dust at $T = 40 \pm 6$ K (Figure 5.5). From this two-component fitting, we found that almost all of the brightnesses at 12 and 24 μm arise from the warm dust component, whereas more than 80% of the brightness in the FIR longer than 100 μm is from the cool dust component. The warm and cool dust components yield $\Sigma_\mathrm{d} = 3.2(\pm0.3)\times10^{-8}$ g cm^{-2} and $1.1(\pm0.8)\times10^{-6}$ g cm^{-2}, respectively. From Equation 5.2, therefore, the corresponding $E(J-H)$ of the warm dust with a size of 0.001–0.1 μm is $10^{-8} - 10^{-5}$ mag, and that of the cool dust is ~ 0.003 mag. The column density of warm dust required to explain the MIR emission is very small, and the resulting NIR extinction is several orders of magnitude smaller than the value we derived (0.23 ± 0.05 mag). Therefore, it must be the cool dust component that is responsible for the NIR extinction. (Note that the grain species of the warm dust component and therefore its contribution to the NIR extinction are rather well constrained.) However, the above result suggests that the cool dust component cannot have the optical properties of the general interstellar dust because then the NIR extinction is again two orders of magnitude less than the value we derived. The grain species of the cool dust should have large $\Delta\kappa_{JH}$ and/or small FIR opacity ($\kappa_{\mathrm{abs},\nu}$) compared to that of general interstellar

Table 5.2. Dust grain species considered in this work

Species	Condition[a]	Type	Density (g cm^{-3})	λ Coverage (μm)	References
C	u	Amorphous	2.28	4E-2 – 2E3	1
MgO	u	Crystalline	3.59	2E-3 – 625	2
$MgSiO_3$	m/u	Glassy	3.20	2E-1 – 500	3
Mg_2SiO_4	m/u	...	3.23	1E-1 – 1E5	4
Al_2O_3	m/u	Amorphous	4.01	2E-1 – 500	5
Si	u	Amorphous	2.34	1E-2 – 148[b]	6
SiO_2	m/u	Amorphous	2.66	1E-4 – 500	7
Fe	u	...	7.95	1E-1 – 1E5	4
FeS	u	...	4.87	1E-1 – 1E5	4
Fe_3O_4	m	...	5.25	1E-1 – 1E3	8

[a] u = unmixed SN explosion model, m = mixed SN explosion model

[b] The maximum of λ coverage is limited to 148 μm. In this case, we assume that the optical properties, n and k, do not vary at longer wavelengths.

References. — (1) Zubko et al. (1996), (2) Roessler & Huffman (1991), (3) Dorschner et al. (1995), (4) Semenov et al. (2003), (5) Koike et al. (1995) for $\lambda \leq 8$ μm and Begemann et al. (1997) for $\lambda > 8$ μm, (6) Piller (1985), (7) Philipp (1985), (8) A. Triaud and H. Mutschke (unpublished; see `http://www.astro.uni-jena.de/Laboratory/OCDB/mgfeoxides.html`).

dust.

5.4.2 SN Dust Composition

Dust Species and Their Optical Properties

For the composition of SN dust, we consider the grain species predicted by previous theoretical models for CCSNe (Todini & Ferrara, 2001; Nozawa et al., 2003, 2008, 2010). The grain species considered in this paper are summarized in Table 5.2 with references for their optical constants (n and k). Note that carbon grains are formed in the He layer, silicates ($MgSiO_3$, Mg_2SiO_4, and SiO_2) and oxides (Al_2O_3 and MgO) in the O-rich layer, and other heavy-element (Si, Fe, FeS) grains in the Si–S–Fe layer. In addition, various types of oxide grains (SiO_2, $MgSiO_3$, Mg_2SiO_4, Al_2O_3, and Fe_3O_4) are produced in the mixed SN models. According to Rho et al. (2008), the MIR spectra

of Cas A are well fitted by the combination of these grain opacity curves, which implies that these are the major dust species produced by the SN explosion. We calculated the absorption and extinction coefficients ($\kappa_{\rm abs,\nu}$ and $\kappa_{\rm ext,\nu}$) using the Mie theory (Bohren & Huffman, 1983) assuming a spherical grain with a radius of 0.001, 0.01, or 0.1 μm.

Figure 5.6 shows $\Delta\kappa_{JH}$ and $\kappa_{\rm abs,\nu}$ at 24 and 70 μm for the grain species with different sizes. As expected, the $\kappa_{\rm abs,\nu}$ values of dust species at 24 and 70 μm do not depend on the grain size except for Fe dust. For Fe dust, which is a metallic dust, not only the electric dipole but also the magnetic dipole is important for grains larger than 0.006 μm, the efficiency ($Q_{\rm abs}$) of which is proportional to the volume and not the size (Tanabe et al., 1984). Therefore, the FIR opacity ($\kappa_{\rm abs,\nu} = (\pi a^2 Q_{\rm abs,\nu})/(4/3\pi a^3 \rho)$, where $Q_{\rm abs,\nu}$ is the absorption efficiency) of Fe dust is proportional to the square of the size for large grains. Note that small Fe dust (≤ 0.01 μm) has an FIR dust opacity much smaller than those of the other dust grains, e.g., ≤ 0.2 cm^2 g^{-1} versus 2–100 cm^2 g^{-1} at 70 μm. $\Delta\kappa_{JH}$ in general does not depend on the grain size for $a \leq 0.01$ μm and increases with a for larger grains up to $a \gtrsim 0.1$ μm (Figure 5.7). This is the result of standard grain extinction properties: for small grains, i.e., $x \equiv 2\pi a/\lambda \ll 1$, $Q_{\rm ext} (= Q_{\rm abs} + Q_{\rm sca})$ is dominated by $Q_{\rm abs}$, which is proportional to x, so $\Delta\kappa_{JH} (\propto (Q_{\rm ext,J} - Q_{\rm ext,H})/a)$ is independent of the grain radius (except for Fe dust, which has $Q_{\rm abs} \propto a^3$). For larger grains up to $x \lesssim 1$, the scattering with $Q_{\rm sca} \propto x^4$ is more important, so $\Delta\kappa_{JH}$ increases. Because, in general, $Q_{\rm ext}$ increases to a value of $Q_{\rm ext} \approx 3-5$ near $|m-1|x \approx 2$, where $m (\equiv n + ik)$ is the complex refractive index, and then converges to 2 (Draine, 2011), $\Delta\kappa_{JH}$ reaches a maximum near $|m-1|x \approx 2$ and then rapidly drops to zero. For grains of $a = 0.1$ μm, $\Delta\kappa_{JH} = 10^2$–10^4 cm^2 g^{-1}. Fe grains have $\Delta\kappa_{JH} \sim 10^3$ cm^2 g^{-1} almost independent of their sizes. As discussed in the previous section, the dust grains responsible for the NIR extinction should have large $\Delta\kappa_{JH}$ and/or small FIR $\kappa_{\rm abs,\nu}$ compared to the general interstellar dust composition. In this sense, small Fe (or other metallic) dust grains seem to be a candidate for the cool dust.

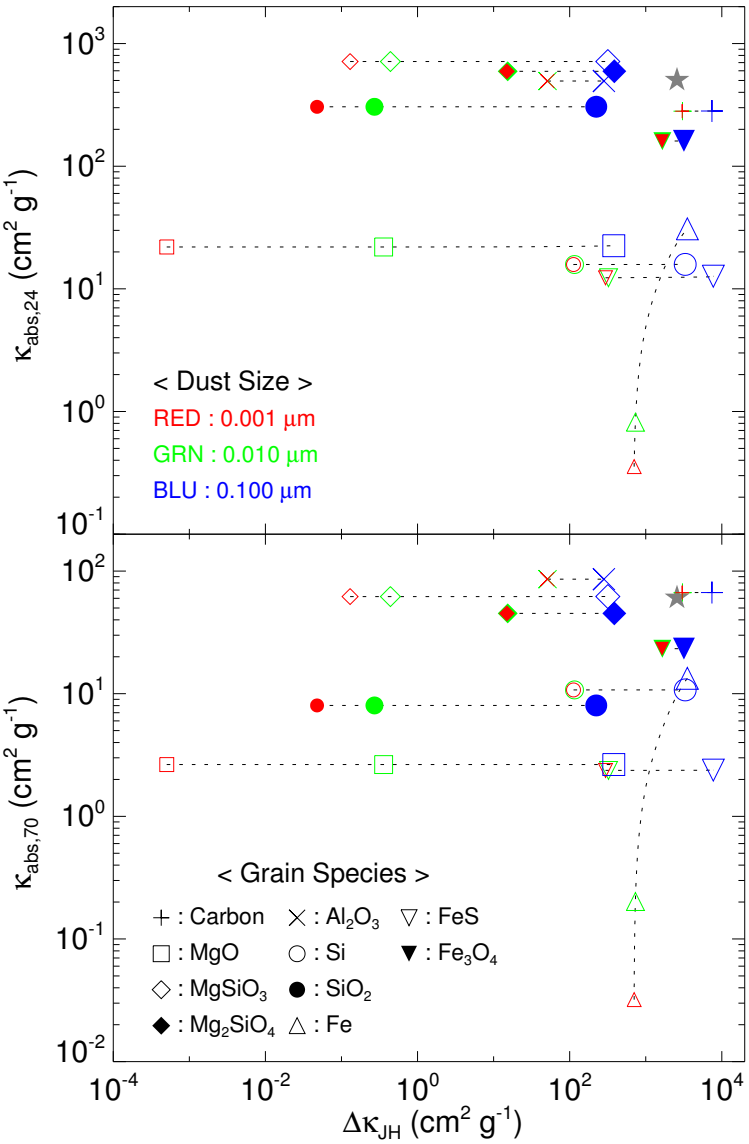

Figure 5.6 $\kappa_{\mathrm{abs},\nu}$ at 24 μm ($\kappa_{\mathrm{abs},24}$; upper panel) and 70 μm ($\kappa_{\mathrm{abs},70}$; lower panel) versus $\Delta\kappa_{JH}$ for 10 grain species in Table 5.2. Symbols and colors denote the grain species and sizes, respectively. We connect the same symbols with black dotted lines. For comparison, the general interstellar dust (Draine, 2003) is marked with a star symbol.

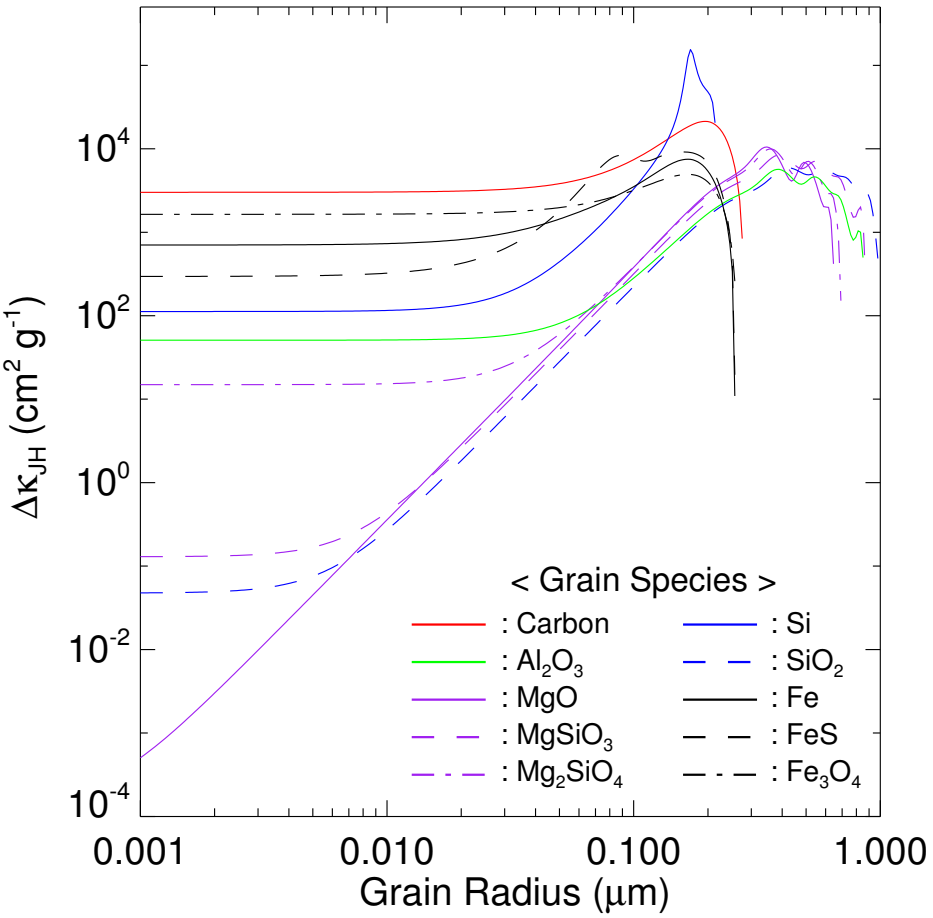

Figure 5.7 $\Delta\kappa_{JH}$ versus grain radius for 10 grain species.

Spectral Modeling

We now perform spectral fitting to the SN dust SED at position A. We assume that the SN dust is composed of two temperature components, i.e., warm and cool dust, as noted in Section 5.4.1. A single component cannot explain both the MIR peak and the FIR excess. We found that essentially all of the MIR emission is from the warm dust. Therefore, we simply assume that the 12 and 24 μm brightnesses are from the warm dust, which then yields the temperature and surface density of warm dust without fitting the entire SED. Color correction was made using the filter response curve at each band and the spectral shape of each grain model.

Figure 5.8(a) shows the derived temperature and surface density of warm dust for different species. Because the FIR $\kappa_{\mathrm{abs},\nu}$ values of dust grains, except for Fe dust, do not depend on their sizes (Figure 5.6), the derived temperature and column density of dust species are independent of the grain size. Not all of these dust species can match the FIR part of the SED. This is shown in Figures 5.8(c) and (d), where we compare the expected FIR brightnesses to the observed brightnesses (the red dashed and dotted lines). Note that it is acceptable if the expected brightness is less than the observed brightness because the difference can be contributed by cool dust, but not vice versa. Therefore, only three dust species can match the FIR part of the SED: $MgSiO_3$, Mg_2SiO_4, and SiO_2. The temperature and column density of the three grain models are 80 K $< T_{\mathrm{warm}} <$ 120 K and 10^{-8} g cm^{-2} $< \Sigma_{\mathrm{d,warm}} < 10^{-6}$ g cm^{-2}, respectively. The compositions and corresponding temperatures of this warm dust component are well consistent with previous observational and theoretical results (Rho et al., 2008; Nozawa et al., 2010). Figure 5.8(b) shows the expected $E(J-H)$ of warm dust estimated from their surface density using Equation 5.2. Note that the $E(J-H)$ values of the three dust species are less than $\sim 10^{-4}$ mag, which is a few orders of magnitude smaller than the observed $E(J-H)$, as we already pointed out in Section 5.4.1.

With the warm dust component constrained, we can now search for possible candidates for the cool dust component. We perform a two-temperature modified blackbody fit of the SED for each of the three possible warm dust species above, the temperature and surface density of which are fixed. The left column of Figure 5.9 shows the

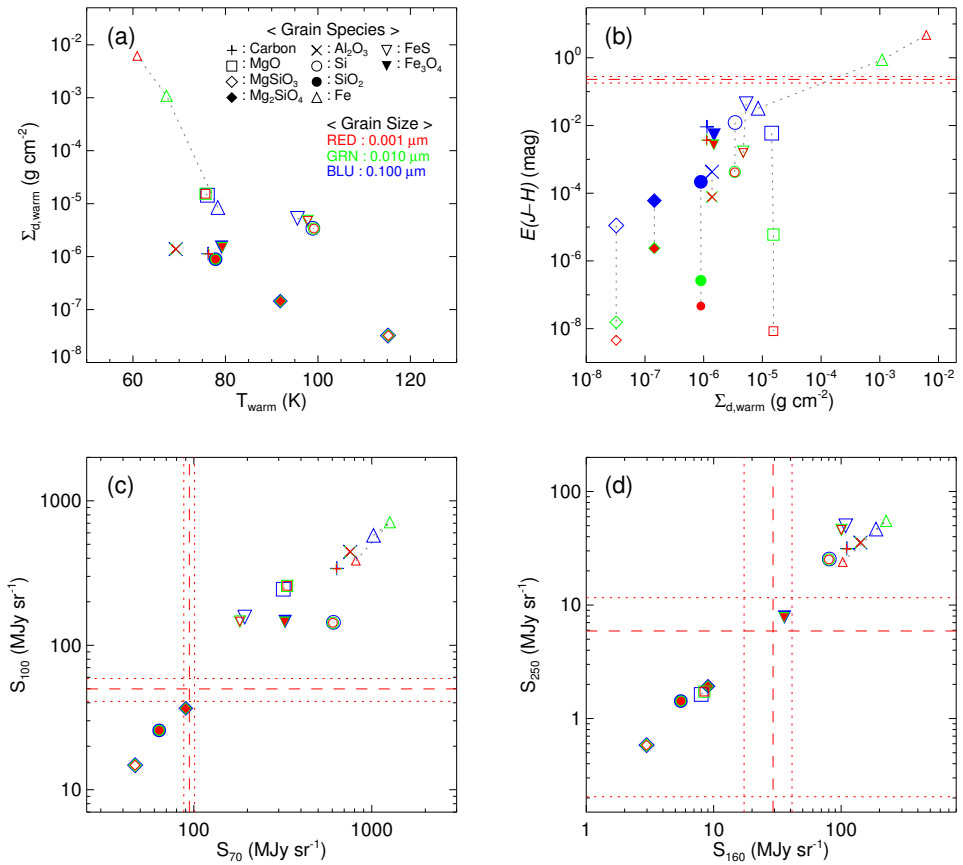

Figure 5.8 (a) Temperature and column density of warm dust grains obtained from the fit of MIR emission. Symbols and colors are the same as in Figure 5.6. (b) Predicted $E(J-H)$ of warm dust grains from their column densities in (a). The red dashed and dotted lines are the measured color excess and its 1σ uncertainty, respectively. (c) Expected brightnesses of warm dust grains at 70 and 100 μm. The red dashed and dotted lines represent the observed brightnesses and their 1σ uncertainty, respectively. (d) Same as (c) but for 160 and 250 μm brightnesses.

derived temperature and surface density of the cool dust for each warm dust species. All combinations can fit the observed SED within the 1σ uncertainty of the measured brightness except when the cool dust is MgO grains. The opacity of MgO has a small bump peaking at 100 μm, so it cannot properly fit the observed brightness at either 100 or 160 μm. The temperature of the cool dust ranges from 30 to 70 K depending on its composition. When the warm dust is Mg_2SiO_4, the cool dust temperature is systematically lower. The right column of Figure 5.9 shows the expected color excess of each cool dust species. We see that small ($\leq$ 0.01 μm) Fe grains can match the observed $E(J-H) \approx 0.2$ mag for any warm dust species with $\Sigma_{\rm d} = 2-5 \times 10^{-4}$ g cm^{-2}. None the other grain species can produce sufficient extinction.

Figure 5.9, however, shows that as the grain size increases, $E(J-H)$ increases because larger grains have higher $\Delta\kappa_{JH}$ (Figure 5.6), so perhaps grains larger than 0.1 μm might also produce $E(J-H) \approx 0.2$ mag. Figure 5.7 shows $\Delta\kappa_{JH}$ for each grain species as a function of grain radius. For oxide grains (i.e., MgO, $MgSiO_3$, Mg_2SiO_4, Al_2O_3, and SiO_2), $\Delta\kappa_{JH}$ reaches a maximum at $\sim$ 0.4 μm and then drops abruptly at $\gtrsim$ 0.6 μm, whereas for metallic grains (i.e., Si, Fe, FeS, and Fe_3O_4) and amorphous carbon, the transition occurs at somewhat shorter wavelengths. We find that pure Si grains with a radius of 0.16–0.21 μm can also explain the color excess we observed because of their large $\Delta\kappa_{JH}$ (Figure 5.7), although the permitted size range appears to be too narrow. Table 5.3 summarizes the parameters of the warm and cold dust grains that can explain both the FIR SED and the NIR extinction.

5.5 Discussion

5.5.1 Cool SN Dust Responsible for the NIR Extinction

According to our result, the cool dust that can explain the observed NIR extinction in the southern part of Cas A (i.e., in Slit 4) could be either small ($\lesssim$ 0.01 μm) Fe or large ($\gtrsim$ 0.1 μm) Si grains. In this section, we discuss these two possibilities.

In the Slit 4 position, the reverse shock is now encountering pure Fe ejecta in the innermost region (Koo et al., 2013). Considering this, cool SN dust mainly consisting

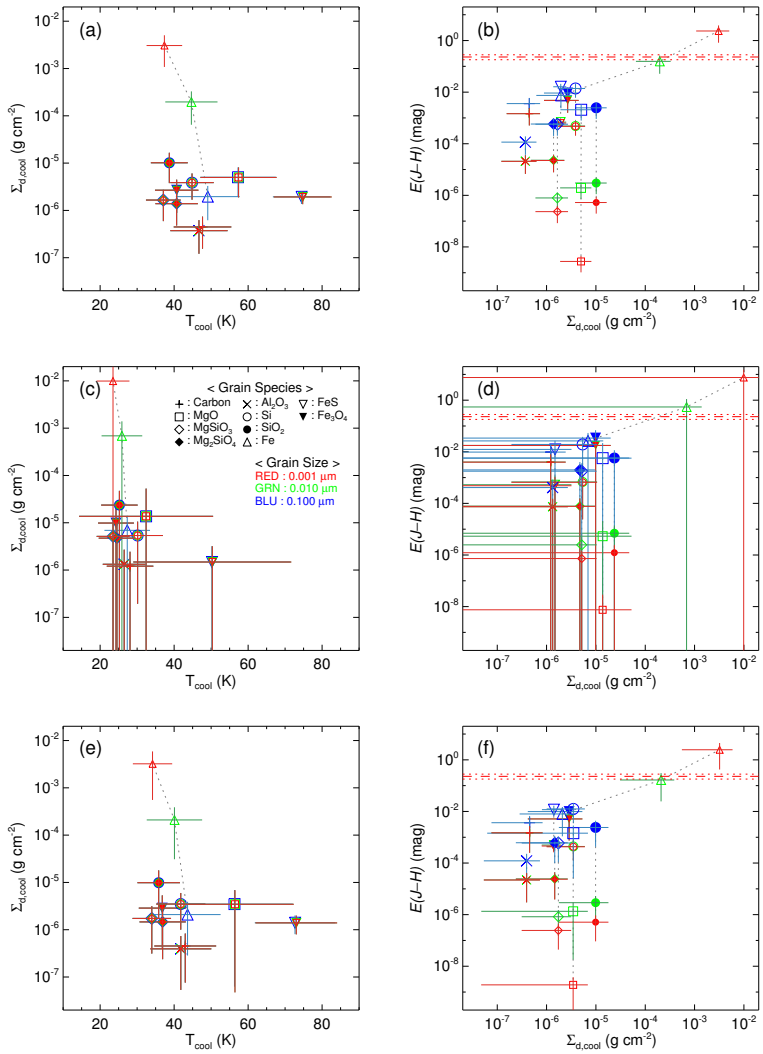

Figure 5.9 (a) Temperature and column density of various cool dust species obtained from the fit of FIR emission assuming that the warm dust component is $MgSiO_3$. (b) Predicted $E(J-H)$ of cool dust from the column density in (a). The red dashed and dotted lines are the measured color excess and its 1σ uncertainty, respectively. (c)–(d) Same as (a)–(b) but assuming the warm dust component is Mg_2SiO_4. (e)–(f) Same as (a)–(b) but assuming the warm dust component is SiO_2.

Table 5.3. Parameters of SN dust in Slit 4

Warm Dust				Cool Dust			
Species	T (K)	$\Sigma_{\rm d}$ (10^{-6} g cm^{-2})	$E(J-H)$ (10^{-4} mag)	Species	T (K)	$\Sigma_{\rm d}$ (10^{-4} g cm^{-2})	$E(J-H)$ (mag)
$MgSiO_3$ ($a = 0.1\mu$m)	115 ± 2	0.032 ± 0.005	0.11 ± 0.02	Si ($0.16 \leq a \leq 0.21\mu$m)	45 ± 6	0.039 ± 0.022	$0.15 - 0.65$
				Fe ($a \leq 0.01\mu$m)	$\leq 45 \pm 7$	$\geq 2.0 \pm 1.3$	$\geq 0.16 \pm 0.10$
Mg_2SiO_4 ($a = 0.1\mu$m)	92 ± 1	0.14 ± 0.02	0.60 ± 0.09	Si ($0.16 \leq a \leq 0.21\mu$m)	30 ± 7	0.054 ± 0.052	$0.21 - 0.90$
				Fe ($a \leq 0.01\mu$m)	$\leq 26 \pm 6$	$\geq 6.9 \pm 7.1$	$\geq 0.55 \pm 0.56$
SiO_2 ($a = 0.1\mu$m)	78 ± 1	0.9 ± 0.1	2.2 ± 0.3	Si ($0.16 \leq a \leq 0.21\mu$m)	42 ± 7	0.035 ± 0.025	$0.14 - 0.59$
				Fe ($a \leq 0.01\mu$m)	$\leq 40 \pm 7$	$\geq 2.1 \pm 1.8$	$\geq 0.17 \pm 0.14$

of Fe grains seems to be reasonable. The small size also appears to be consistent with the theoretical prediction that the average radius of newly formed SN dust grains in SN IIb is smaller than 0.01 μm because of low gas density in the expanding SN ejecta (Kozasa et al., 2009; Nozawa et al., 2010). On the other hand, theory also predicts that the gas density of the innermost ejecta is too low to produce pure Fe grains when the temperature of the region drops to 800 K, at which Fe grains can start to coagulate, so pure Fe dust is not expected to form in SNe IIb (Kozasa et al., 2009; Nozawa et al., 2010). However, the above conclusion assumes a spherically symmetric explosion with homogeneous and stratified ejecta. If the gas density is inhomogeneous and/or the SN explosion is asymmetric, we cannot rule out the possibility of pure Fe grain formation in the innermost SN ejecta, where the gas density is relatively high (Sarangi & Cherchneff, 2015). Indeed, the ejecta material emitting [Fe II] lines is dense, with electron densities of $\sim 10^4$ cm^{-3} (Koo et al., 2013).

Another possible grain species responsible for the large $E(J-H) \approx 0.2$ mag is large Si grains. This possibility may be supported by previous infrared studies; *Spitzer* spectral mapping observations found strong [Si II] emission together with [O IV] and [S III] lines in the interior of the remnant, which arises from the unshocked SN ejecta photoionized by UV and X-ray emission from the Bright Rim (e.g., Smith et al., 2009; Isensee et al., 2010; Arendt et al., 2014; Milisavljevic & Fesen, 2015). The presence of ionized silicon in the interior supports the suggestion that the cool dust could be Si and/or silicate grains. Theoretically, pure Si grains can form in the Si-rich layer, but the grain size is very small, i.e., $\lesssim 0.01$ μm (Nozawa et al., 2010). However, again if the SN ejecta is clumped, grains larger than 0.1 μm can form in dense clumps (Sarangi & Cherchneff, 2015), so large Si grains are not implausible.

5.5.2 Composition of SN Dust in Cas A

From previous studies, it is reasonably well established that there are two SN dust components in Cas A: warm ($\sim$ 100 K) dust swept up by the reverse shock and cool (30–40 K), unshocked dust residing in the interior of the remnant. The composition of the warm dust is relatively well specified from its MIR spectral features: Mg-silicates,

SiO_2, Al_2O_3, and/or C glass. The estimated total mass of warm dust ranges from 0.008 to 0.054 $M_\odot$. The composition of the cool dust has been essentially unknown because in the FIR, the SED is mostly smooth without prominent spectral features. Assuming the FIR absorption coefficients of the general interstellar dust (Sibthorpe et al., 2010) or silicates (Barlow et al., 2010), a total mass of $\sim 0.07\ M_\odot$ has been obtained.

Our analysis also showed that there are warm and cool dust components in the southern ejecta shell. The derived temperature (80–120 K) and composition ($MgSiO_3$, Mg_2SiO_4, or SiO_2) of the warm dust are consistent with previous results. For the cool dust, we were able to show for the first time that its composition is either small Fe or large Si grains. Their temperatures are 30–50 K. These grains are not expected in uniformly expanding stratified SN ejecta, but they can possibly form in dense clumps.

At first glance, the different compositions of warm and cool dust appear to be incompatible if we consider that the cool dust is swept up by the reverse shock and subsequently turns into warm dust with a temperature of $\sim$ 100 K. However, this can be understood if we consider that the SN ejecta is clumped. As we pointed out above, the cool dust responsible for the NIR extinction resides in dense clumps. When the dense clumps are swept up by the reverse shock, the shock speed is slow (e.g., $\lesssim$ 10 km s^{-1}), and the gas temperature is below 10^4 K (Koo et al., 2013), so the dust grains in the clumps are not heated to high temperature. On the other hand, when the diffuse ejecta is swept up by the reverse shock, the gas is heated to X-ray-emitting temperature ($\sim 10^7$ K), and the dust grains there are heated by collisions with electrons to high temperature. Therefore, it is the shock-heated warm grains in the diffuse ejecta that emit most of the MIR and FIR ($\lesssim 70\ \mu$m) emission (Figure 5.5), and their compositions could be different from those of grains in dense clumps. In summary, our observation can be explained if the SN ejecta is clumped and the grain species in diffuse material and dense clumps are different, i.e., silicate grains in the diffuse material and small Fe or large Si grains in the dense clumps. The cool dust that we detected could reside either in unshocked or shocked clumps, and it is these cool grains that are responsible for the NIR extinction.

When the cool dust is pure Fe grains, we can make a crude estimation of the dust

formation efficiency from our observation. The required Fe dust mass density of (2–5) $\times 10^{-4}$ g cm^{-2} corresponds to an Fe nucleus column density of (2–5) $\times 10^{18}$ cm^{-2}. For comparison, the characteristic size of [Fe II]-line-emitting clumps is 5″ or 0.08 pc at 3.4 kpc, and their average electron density is 2×10^4 cm^{-3} (Koo et al., 2013). For pure Fe ejecta clumps, because Fe is mostly in Fe^+, it means that the number density of Fe atoms is 2×10^4 cm^{-3}, and the characteristic Fe column density in the gas phase of Fe ejecta clumps is $N_{\rm Fe} \sim 5 \times 10^{21}$ cm^{-2}. Therefore, if there are $n_{\rm clump}$ such clumps along the sight line where $E(J-H) \approx 0.23$ in Slit 4, we obtain a dust-to-gas ratio of $0.4 - 1 \times 10^{-3}\ n_{\rm clump}^{-1}$.

The total flux of cool dust at 100 μm in the global SED is $\sim 30 \pm 10$ Jy (Barlow et al., 2010). The mass has been estimated to be $\sim 0.07\ M_\odot$ if we adopt the FIR absorption coefficients for silicates from Dorschner et al. (1995). The contribution of small Fe or large Si grains to this mass budget would depend on the volume filling factor of the clumps but is probably not large. To address this issue, one may carry out an analysis similar to that in this paper toward the entire ejecta shell.

5.6 Summary

We performed NIR spectroscopic observations of Cas A in which we obtained the spectral and kinematical properties of 63 [Fe II]-line-emitting knots spread over the main ejecta shell. All of the knots show strong [Fe II] 1.26 and 1.64 μm lines, the ratio of which provides a direct measure of the extinction. From an analysis of the extinction toward individual knots, we showed that the NIR extinction is due in part to SN dust within the remnant. We explored the nature of the SN dust responsible for the NIR extinction by analyzing its thermal infrared emission. Our main results are summarized below.

1. We found that [Fe II] emission from redshifted SN ejecta is in general more heavily obscured than that from blueshifted SN ejecta (Figure 5.2). We interpret the correlation as evidence for newly formed SN dust within the remnant. The amount of excess extinction varies considerably from one sight line to another, which suggests a highly

non-uniform distribution of SN dust.

2. One slit (Slit 4) is located across the southern [Fe II] ejecta filament, which has the velocity structure of an expanding shell. Along this particular sight line, we measured an excess NIR extinction of $E(J-H) = 0.23 \pm 0.05$ mag between the front and back sides of the shell, which must be entirely due to SN dust (Figure 5.3).

3. We analyzed the SED of thermal dust emission toward Slit 4 to show that there are warm ($\sim$ 100 K) and cool ($\sim$ 40 K) SN dust components along the sight line (Figure 5.5). Among the grain species predicted from theoretical dust formation models in CCSNe, only silicate grains (i.e., $MgSiO_3$, Mg_2SiO_4, SiO_2) can match the SED of warm SN dust which has a sharp 24 μm peak. The NIR extinction due to these warm silicate dust grains is negligible, so the observed excess NIR extinction should be due to the cool SN dust.

4. According to our analysis, only two grain species can explain both the SEDs of cool dust and the NIR excess extinction: (1) small ($\lesssim 0.01$ μm) Fe grains or (2) large ($\gtrsim 0.1$ μm) Si grains. However, neither would be consistent with the dust formation theory for SN IIb with uniformly expanding, layered ejecta (e.g., Nozawa et al., 2010), which predicts the formation of only small (< 0.01 μm) Si grains and no Fe grains. However, if the SN ejecta is clumpy, we might expect that Fe grains and large Si grains can be produced in dense clumps.

5. We suggest that the unshocked SN ejecta is clumpy and the grain species in diffuse material and dense clumps are different, i.e., silicate grains in diffuse material and small Fe or large Si grains in dense clumps. In the shocked ejecta, both still exist, but it is the shock-heated warm grains in the diffuse ejecta that emit most of the MIR and FIR ($\lesssim 70$ μm) emission. The cool dust that we detected could reside in either unshocked or shocked clumps, and it is these cool grains that are responsible for the NIR extinction. The contribution of each grain species to the total mass ($\gtrsim 0.1$ $M_\odot$) of cool SN dust in Cas A remains to be explored.

Biblography

Arendt, R. G., Dwek, E., Kober, G., Rho, J., & Hwang, U. 2014, ApJ, 786, 55

Arendt, R. G., Dwek, E., & Moseley, S. H. 1999, ApJ, 521, 234

Barlow, M. J., Krause, O., Swinyard, B. M., et al. 2010, A&A, 518, L138

Begemann, B., Dorschner, J., Henning, T., et al. 1997, ApJ, 476, 199

Bianchi, S., & Schneider, R. 2007, MNRAS, 378, 973

Bohlin, R. C., Savage, B. D., & Drake, J. F. 1978, ApJ, 224, 132

Bohren, C. F., & Huffman, D. R. 1983, Absorption and Scattering of Light by Small Particles (New York: Wiley)

Calura, F., Gilli, R., Vignali, C., et al. 2014, MNRAS, 438, 2765

Deb, N. C., & Hibbert, A. 2010, ApJL, 711, L104

Delaney, T. A. 2004, Ph.D. Thesis, Univ. Minnesota

DeLaney, T., Rudnick, L., Stage, M. D., et al. 2010, ApJ, 725, 2038

Docenko, D., & Sunyaev, R. A. 2010, A&A, 509, AA59

Dorschner, J., Begemann, B., Henning, T., Jaeger, C., & Mutschke, H. 1995, A&A, 300, 503

Douvion, T., Lagage, P. O., & Pantin, E. 2001, A&A, 369, 589

Draine, B. T. 2003, ApJ, 598, 1017

Draine, B. T. 2011, Physics of the Interstellar and Intergalactic Medium (Princeton: Princeton University Press), ISBN: 978-0-691-12214-4

Dunne, L., Eales, S., Ivison, R., Morgan, H., & Edmunds, M. 2003, Nature, 424, 285

Dunne, L., Maddox, S. J., Ivison, R. J., et al. 2009, MNRAS, 394, 1307

Ennis, J. A., Rudnick, L., Reach, W. T., et al. 2006, ApJ, 652, 376

Eriksen, K. A., Arnett, D., McCarthy, D. W., & Young, P. 2009, ApJ, 697, 29

Fesen, R. A., Hammell, M. C., Morse, J., et al. 2006, ApJ, 645, 283

Giannini, T., Antoniucci, S., Nisini, B., et al. 2015, ApJ, 798, 33

Gomez, H. L., Krause, O., Barlow, M. J., et al. 2012, ApJ, 760, 96

Hammell, M. C., & Fesen, R. A. 2008, ApJS, 179, 195

Hurford, A. P., & Fesen, R. A. 1996, ApJ, 469, 246

Hwang, U., & Laming, J. M. 2012, ApJ, 746, 130

Indebetouw, R., Matsuura, M., Dwek, E., et al. 2014, ApJL, 782, LL2

Isensee, K., Olmschenk, G., Rudnick, L., et al. 2012, ApJ, 757, 126

Isensee, K., Rudnick, L., DeLaney, T., et al. 2010, ApJ, 725, 2059

Kelsall, T., Weiland, J. L., Franz, B. A., et al. 1998, ApJ, 508, 44

Keohane, J. W., Rudnick, L., & Anderson, M. C. 1996, ApJ, 466, 309

Koike, C., Kaito, C., Yamamoto, T., et al. 1995, Icar, 114, 203

Koo, B.-C., Lee, Y.-H., Moon, D.-S., Yoon, S.-C., & Raymond, J. C. 2013, Science, 342, 1346

Koo, B.-C., & Lee, Y.-H. 2015, Publication of Korean Astronomical Society, 30, 145

Kotak, R., Meikle, W. P. S., Farrah, D., et al. 2009, ApJ, 704, 306

Kozasa, T., Nozawa, T., Tominaga, N., et al. 2009, in ASP Conf. Ser. 414, Cosmic Dust—Near and Far, ed. T. Henning, E. Grün, & J. Steinacker (San Francisco, CA: ASP), 43

Kozasa, T., Hasegawa, H., & Nomoto, K. 1991, A&A, 249, 474

Krause, O., Birkmann, S. M., Rieke, G. H., et al. 2004, Nature, 432, 596

Krause, O., Birkmann, S. M., Usuda, T., et al. 2008, Science, 320, 1195

Kurucz, R. L. 2003, http://kurucz.harvard.edu/

Lagage, P. O., Claret, A., Ballet, J., et al. 1996, A&A, 315, L273

Lee, J.-J., Park, S., Hughes, J. P., & Slane, P. O. 2014, ApJ, 789, 7

Lee, Y.-H., Koo, B.-C., Moon, D.-S., Burton, M. G., & Lee, J.-J. 2017, ApJ, 837, 118

Leipski, C., Meisenheimer, K., Walter, F., et al. 2013, ApJ, 772, 103

Lloyd, C. 2003, in ESA SP-481, in The Calibration Legacy of the *ISO* Mission, ed. L. Metcalfe, A. Salama, S. B. Peschke, & M. F. Kessler (Noordwijk: European Space Agency), 399

Marchenko, S. V. 2006, in ASP Conf. Ser. 353, Stellar Evolution at Low Metallicity: Mass Loss, Explosions, Cosmology, ed. H. J. G. L. M. Lamers, N. Langer, T. Nugis, & K. Annuk (San Francisco, CA: ASP), 299

Markwardt, C. B. 2009, in ASP Conf. Ser. 411, Astronomical Data Analysis Software and Systems XVIII, ed. D. A. Bohlender, D. Durand, & P. Dowler (San Francisco, CA: ASP), 251

Matsuura, M., Dwek, E., Meixner, M., et al. 2011, Science, 333, 1258

Meikle, W. P. S., Mattila, S., Pastorello, A., et al. 2007, ApJ, 665, 608

Milisavljevic, D., & Fesen, R. A. 2015, Science, 347, 526

Miville-Deschênes, M.-A., & Lagache, G. 2005, ApJS, 157, 302

Morgan, H. L., & Edmunds, M. G. 2003, MNRAS, 343, 427

Nozawa, T., Kozasa, T., Tominaga, N., et al. 2008, ApJ, 684, 1343

Nozawa, T., Kozasa, T., Tominaga, N., et al. 2010, ApJ, 713, 356

Nozawa, T., Kozasa, T., Umeda, H., Maeda, K., & Nomoto, K. 2003, ApJ, 598, 785

Nussbaumer, H., & Storey, P. J. 1988, A&A, 193, 327

Owen, P. J., & Barlow, M. J. 2015, ApJ, 801, 141

Philipp, H. R. 1985, in Handbook of Optical Constants of Solids, ed. E. D. Palik (San Diego, CA: Academic), 719

Pilbratt, G. L., Riedinger, J. R., Passvogel, T., et al. 2010, A&A, 518, L1

Piller, H. 1985, in Handbook of Optical Constants of Solids, ed. E. D. Palik (San Diego, CA: Academic), 571

Planck Collaboration, Ade, P. A. R., Aghanim, N., et al. 2011, A&A, 536, AA1

Reed, J. E., Hester, J. J., Fabian, A. C., & Winkler, P. F. 1995, ApJ, 440, 706

Reynoso, E. M., & Goss, W. M. 2002, ApJ, 575, 871

Rho, J., Kozasa, T., Reach, W. T., et al. 2008, ApJ, 673, 271

Rieke, G. H., Young, E. T., Engelbracht, C. W., et al. 2004, ApJS, 154, 25

Roessler, D. M., & Huffman, D. R. 1991, in Handbook of Optical Constants of Solids II, ed. E. D. Palik (San Diego, CA: Academic), 919

Sakon, I., Onaka, T., Wada, T., et al. 2009, ApJ, 692, 546

Sarangi, A., & Cherchneff, I. 2015, A&A, 575, A95

Semenov, D., Henning, T., Helling, C., Ilgner, M., & Sedlmayr, E. 2003, A&A, 410, 611

Sibthorpe, B., Ade, P. A. R., Bock, J. J., et al. 2010, ApJ, 719, 1553

Smith, J. D. T., Armus, L., Dale, D. A., et al. 2007, PASP, 119, 1133

Smith, J. D. T., Rudnick, L., Delaney, T., et al. 2009, ApJ, 693, 713

Szalai, T., Vinkó, J., Balog, Z., et al. 2011, A&A, 527, AA61

Tanabe, T., Onaka, T., & Kamijo, F. 1984, AP&SS, 98, 323

Thorstensen, J. R., Fesen, R. A., & van den Bergh, S. 2001, AJ, 122, 297

Todini, P., & Ferrara, A. 2001, MNRAS, 325, 726

Troland, T. H., Crutcher, R. M., & Heiles, C. 1985, ApJ, 298, 808

van den Bergh, S. 1971, ApJ, 165, 457

Wang, R., Wagg, J., Carilli, C. L., et al. 2011, AJ, 142, 101

Williams, J. P., de Geus, E. J., & Blitz, L. 1994, ApJ, 428, 693

Willingale, R., Bleeker, J. A. M., van der Heyden, K. J., Kaastra, J. S., & Vink, J. 2002, A&A, 381, 1039

Wright, E. L., Eisenhardt, P. R. M., Mainzer, A. K., et al. 2010, AJ, 140, 1868

Zubko, V. G., Mennella, V., Colangeli, L., & Bussoletti, E. 1996, MNRAS, 282, 1321

Chapter 6

Summary and Conclusion

I presented the near-infrared (NIR) imaging and spectroscopic studies for the Galactic supernova remnants (SNRs). The evolved SNRs show two strong emission lines, [Fe II] 1.64 μm and H_2 2.12 μm, from the shocked circumstellar and molecular clouds, whereas Cassiopeia A (Cas A) SNR, the second youngest Galactic SNR, shows strong lines of metallic elements in the SN ejecta which reflect the chemical abundance of the nucelar-burning materials. In this thesis composed of four individual chapters, I investigated their origins and environments. The detailed results and conclusions are summarized as follows.

Searching NIR [Fe II] and H_2 emission lines around the Galactic SNRs

In the first chapter, I searched two NIR emission lines, [Fe II] 1.64 μm and H_2 2.12 μm around the 79 Galactic SNRs in the first Galactic quadrant using UWIFE and UWISH2 survey data. I found 19 [Fe II]-emitting and 19 H_2-emitting SNRs, and more than a half of them are new discoveries. The overall detection rate of each survey is only $\sim$ 24% (19 out of 79) which is lower than that in the extragalxies, and this may due to high interstellar extinction through the Galactic plane. The detection rate peaks at l=40°–50° for [Fe II] and at l=30°–40° for H_2. The defferent peaks in the [Fe II] and H_2 detection rates can be explained by the different SN populations along the Galactic longitude. Among 11 SNRs emitting both the emission lines, five SNRs (G11.2−0.2, KES 73, W44, 3C 396, W49B) show clear "[Fe II]-H_2 reversal:" H_2 emission lines are

detected outside the [Fe II] or radio boundaries. The NIR spectroscopy for the extended H_2 filaments in G11.2−0.2 shows that the H_2 line ratios are consistent with those in collisional excitation, but the exciting sources remain to be explored. The total [Fe II] luminosity of our Galaxy estimated from our observations is a few times fainter than that expected from the Galactic SN rate, and this may implies either that there are many SNRs whose [Fe II] lines are undetected in the survey, or that there are many missing SNRs that have not been known so far. Among the 19 H_2-emitting SNRs, one of third SNRs have either OH masers, CO line broadening, or CO lines morphologically agreed with the SNRs, which are strong evidence of interaction between SNRs and surrounding molecular clouds. The NIR spectroscopy for [Fe II] emission features detected in KES 73 and 3C 391 show low radial velocity of the [Fe II] lines, which implies that they are dense circumstellar/interstellar medium swept up by the SN shocks. The different morphologies and distribution of the [Fe II] emission features in the two SNRs, on the other hand, may imply the different density distributions of their surrounding medium. Additional follow-up NIR spectroscopy for the [Fe II]-emitting and H_2-emitting SNRs is needed to reveal the origin and environments of the Galactic SNRs in more detail.

Investigating excitation mechanism of extended H_2 emission around the Galactic SNRs

In the second chapter, I investigated the excitation mechanism of the extended H_2 filaments as a part of the "[Fe II]-H_2 reversal" in the five Galactic SNRs (G11.2-0.3, KES 73, W44, 3C 396, and W49B) using high resolution (R = 40,000) NIR spectroscopy. The observed $v_{\rm LSR}$ of H_2 lines are well consistent with the systematic velocities of the SNRs, implying that the lines are indeed physically associated with the remnants. I also estimated the kinematic distances toward the remnants from the radial velocities, and constrained the distance of 3C 396 and W49B of 9.4 and 7.5 kpc, respectively. All the line are resolved in our spectrograph, and the line widths are broader than the typical turbulent velocity of ambient gas ($\gtrsim$ 10 km s^{-1} vs. 1–5 km s^{-1}). Furthermore, the flux ratios we derived are well consistent with those of collisional excitation models

with T = a few 1000 K. The line widths together with their flux ratios imply that the H_2 emission lines detected far outside the remnants boundary are collisionally excited by shock. In this thesis, I suggested three possible solutions for the origin of the shock: (1) magnetic precursor ahead of SN shock, (2) projection effect of SN shock, and (3) slow non-dissociative C-shock produced by the pre-SN wind. For G11.2−0.3, the extended H_2 filaments might be excited by the pre-SN wind shock, rather than the SN shock considering the large physical separation between the H_2 and [Fe II]/radio boundary. The exciting source of the bright H_2 filaments in W44, on the other hand, is likely the SN shock, and the "[Fe II]-H_2 reversal" can be explained by projection effect. For the rest of the remnants (KES 73, 3C 396, and W49B), the reversal can be explained by both projection effect and pre-SN wind shock. For the H_2 clump in the western edge of KES 73, the magnetic precursor could be an another solution as an exciting source because the physical separation between H_2 and [Fe II] meets the typical length scale of the precursor ($\lesssim 10^{17}$ cm) expected in the previous theoretical studies. Additional high resolution NIR spectroscopy of other H_2-emitting SNRs will be useful to understand the origin of the H_2 lines as well as the kinematic distances toward the remnants.

Detection of dense pure Fe ejecta in Cas A

In the third chapter, I reported the results of NIR spectroscopy of the second youngest Galactic SNR, Cas A. Sixty-three knots were identified in eight slit positions around the main ejecta shell, and 46 emission lines from various elements were clearly detected in the spectral coverage from 0.94 μm to 2.46 μm. Utilizing principal component analysis for the emission lines, I classified the knots into three distinctive groups: (1) He-rich, (2) S-rich, and (3) F-rich knots. The He-rich knots show prominent He I 1.083 μm and [Fe II] lines together with [N I] and H I lines. Their line-of-sight speeds are relatively small ($\lesssim 200$ km s^{-1}). These slow knots enriched by circumstellar elements like H, He, N, are likely the dense circumstellar medium swept up by the SN shock. The S-rich knots, on the other hand, are very fast (up to ~ 2000 km s^{-1}), and have bright forbidden lines from various metallic elements (e.g., [Si VI], [P II], [S II], [Fe II]).

These fast-moving, metal-enriched knots seem to be the dense SN ejecta, mostly from the oxygen-burning layer of the progenitor. The Fe-rich knots are of interested, because they have high radial velocities like the S-rich knots but show strong [Fe II] lines with/without He I 1.083 μm line. They are mainly distributed in the SW main ejecta shell, just outside the unshocked ^{44}Ti ejecta which are an important tracer of "pure" Fe ejecta. I suggested that the Fe-rich knots are most likey dense "pure" Fe ejecta from the innermost region of the progenitor, swept up by the reverse shock. Additional deep optical and NIR spectroscopy for the SW shell where we found the pure Fe ejecta will be needed to understand their detailed chemical compositions. Furthermore, NIR spectral mapping observations for the Cas A can reveal the three-dimensional distribution of the dense pure Fe ejecta, which is very important to understand the explosion mechanism near the collapsing core of the progenitor just after the SN explsion.

Investigating physical and chemical properties of cool SN dust in Cas A

In the last chapter, I measured the extinction toward the 63 knots using the flux ratio of [Fe II] 1.26 and 1.64 μm lines, which is a strong extinction indicator. I found that the redshifted SN ejecta is in general more heavily obscured than that from blueshifted SN ejecta. This internal "self-extinction" indicates the presence of a large amount of the SN dust inside or around the main ejecta shell. In the SW shell, I measured an excess NIR extiction of $E(J-H) = 0.23 \pm 0.05$ mag between the front and back sides of the shell, which must be entirely due to SN dust. Multicomponent dust SED fitting for the mid- and far-infrared emission in the SW region shows that there are warm ($\sim$ 100 K) and cool ($\sim$ 40 K) SN dust components and the later is responsible for the self-extinction I detected. I also found that the warm dust is likey silicate grains (i.e., $MgSiO_3$, Mg_2SiO_4, SiO_2), whereas the cool dust should be either (1) small ($\lesssim 0.01$ μm) Fe grains or (2) large ($\gtrsim 0.1$ μm) Si grains in order to explain both the thermal dust SED and the NIR self-extinction. Comparing our results with the previous theoratical studies, I suggested that the unshocked SN ejecta is clumpy and the small Fe or large Si grains mainly coarculated in the dense clumps. Although I in this thesis showed the presence of the cool, pure metallic dust around the Cas A, I could not derive their

total mass. NIR spectral mapping observations toward the Cas A in the near future will be useful to estimate the total mass of the SN dust, which is very important to understand the origin of the dust in early universe.

Future Prospects

The NIR is very promising waveband in the near future. Recently, state-of-the-art NIR spectrographs are actively developed, and are scheduled to be attached on new ground-based 20–30 m class telescopses (e.g., European Extremely Large Telescope[1] in Chille Giant Magellan Telescope[2] in Chille, Thirty Meter Telescope[3] in Hawaii). Especitially, Giant Magellan Telescope is now under construction, and will be operated in 2020–2021. Two NIR instruments, Near-IR IFU and Adaptive Optics Imager (GMTIFS) and IR Echelle Spectrograph (GMTNIRS) will be attached on the telescope as an early instrument. Furethermore, a new space telescope, James Webb Space Telescope[4], which is optimized for optical and near/mid-infrared wavebands (0.6–27 μm), is almost ready to be lunched (2018 Oct.), and will be operated in 2019. It has three NIR instruments: Near Infrared Camera (NIRCam), Near-InfraRed Imager and Slitless Spectrograph (NIRISS), and Near Infrared Spectrograph (NIRSpec). These advanced NIR instruments on the state-of-the-art ground- and space-based large telescopes will offer unprecedented resolution and sensitivity, which enable us to investigate the detailed studies for the many small, faint SNRs in our Galaxy as well as in nearby extra-galaxies (e.g., small/large magellaic clouds). These comprehensive works will play an important role in shedding light on the nature of the Galactic and extra-galactic SNRs.

[1] `https://www.eso.org/sci/facilities/eelt/`
[2] `http://www.gmto.org/`
[3] `http://www.tmt.org/`
[4] `https://www.jwst.nasa.gov/`

Chapter A

Short Descriptions on NIR SNRs in UWIFE and UWISH2 Surveys

A.1 G8.7−0.1

G8.7−0.1 is a member of W30 radio complex and was identified as a Galactic SNR by Odegard (1986). The young pulsar, PSR B1800−21, was discovered in the northern region of the remnant (Clifton & Lyne, 1986), but the physical association between the SNR and the pulsar is still controversal (Kassim & Weiler, 1990; Finley & Oegelman, 1994; Frail et al., 1994).

We found weak, complex [Fe II] emission features in the central region where the radio continuum is bright. It extends as large as $\sim 30'$ from the center to the north-eastern region of the remnant.

A.2 G9.9−0.8

This SNR was first identified by VLA 90 cm observation, and shows broken shell-like morphology with a radius of $6'$ (Brogan et al., 2006). Stupar & Parker (2011) detected Hα emission that seems to be associated with northwestern part of the remnant where the radio continuum is brightest.

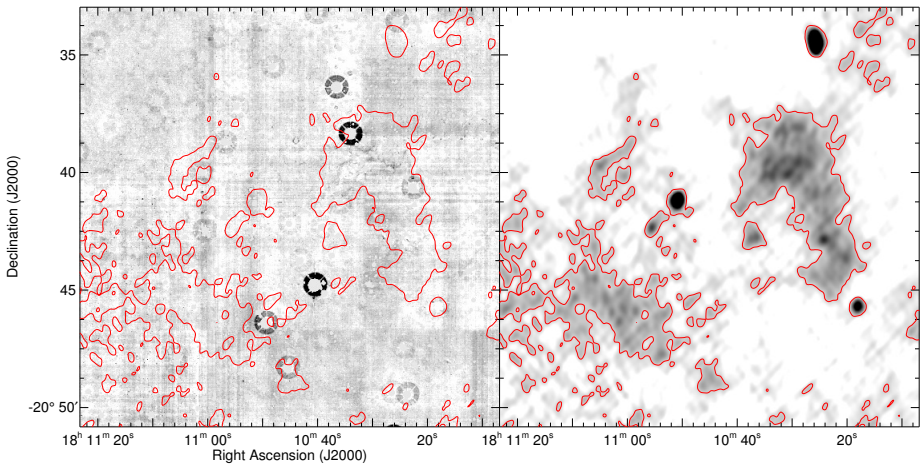

Figure A.1 (Left) continuum-subtracted H_2 2.12 μm narrow-band image of G9.9−0.8. (Right) VLA 20 cm continuum map. The red contours show the brightness distribution of the radio continuum.

In UWISH2 survey, complex H_2 filaments are also detected in the northwestern region. However, their distributions seem to be anti-correlated with that of Hα emission, which raises a question of the excitation mechanism of the H_2 emission.

A.3 G11.2−0.3

G11.2−0.3 is a young historical supernova remnant which exploded in AD 386 and have a remarkably spherical morphology with $2'$ radius in radio, infrared and X-ray images. This remnant hosts the X-ray pulsar PSR J1811−1925 (Torii et al., 1997) and the pulsar wind nebula with a size of $\sim 1'$ (Roberts et al., 2003). Recently, several near-infrared (NIR) imaging and spectroscopic studies have been carried out, and found bright [Fe II] and H_2 emission features around the remnant. The inner [Fe II] filaments have fast radial velocity of ~ 1000 km s^{-1} which implies that they are SN ejecta mostly arising from the Fe core (Moon et al., 2009), whereas the bright south-eastern [Fe II] shell is composed of multiple thin filaments which is amixture of the shocked SN ejecta and the shocked circumstellar material (Koo et al., 2007; Lee et al., 2013). Koo et al.

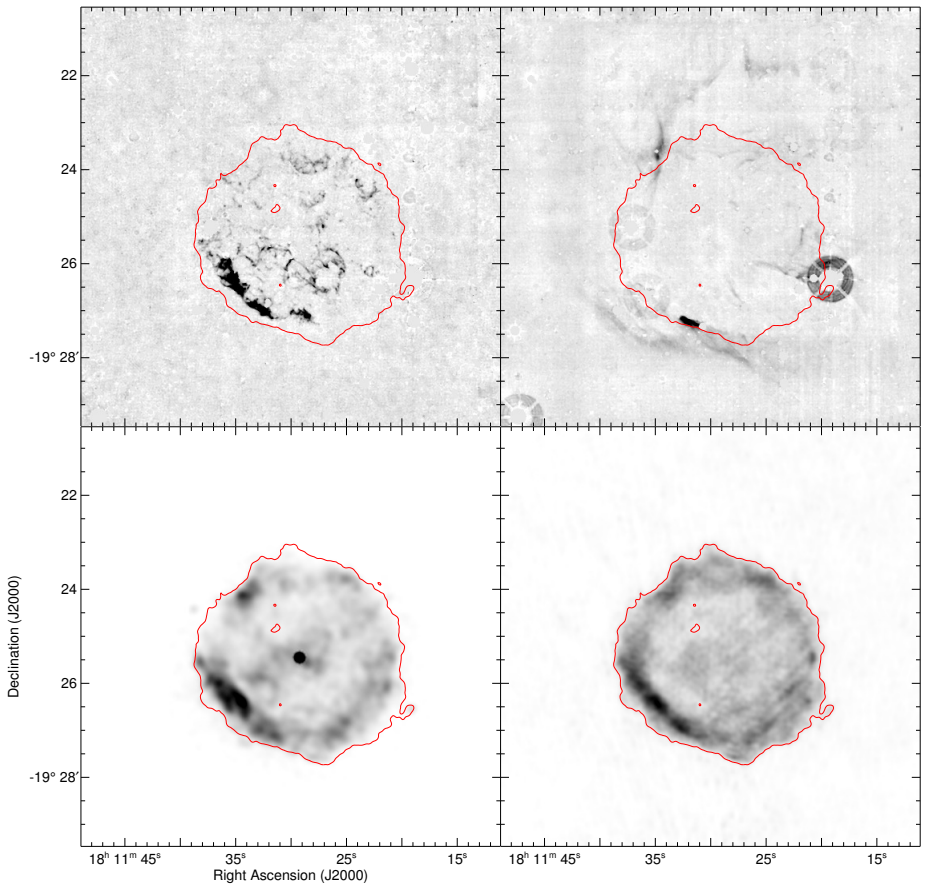

Figure A.2 Continuum-subtracted (top-left) [Fe II] 1.64 μm and (top-right) H_2 2.12 μm narrow-band images of G11.2−0.3. (Bottom-left) *Chandra* X-ray continuum map. (Bottom-right) VLA 20 cm continuum map. The red contours show the brightness distribution of the radio continuum.

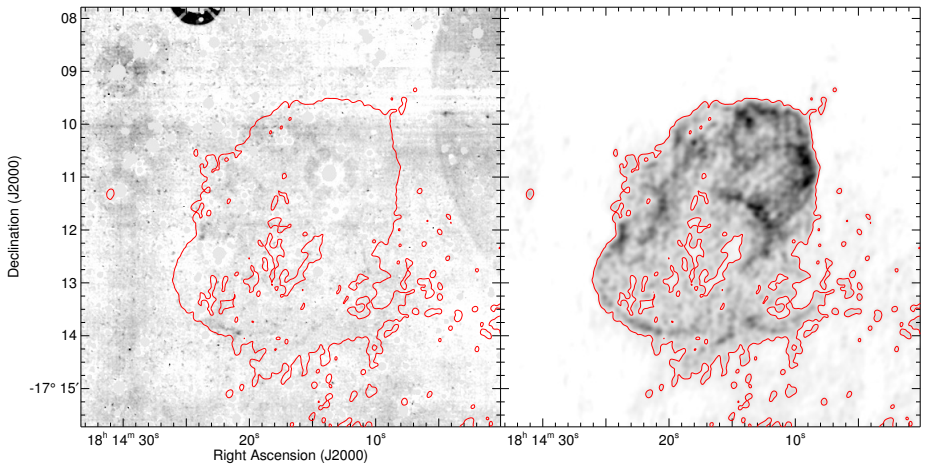

Figure A.3 (Left) continuum-subtracted H_2 2.12 μm narrow-band image of G13.5+0.2. (Right) VLA 20 cm continuum map. The red contours show the brightness distribution of the radio continuum.

(2007) found two small H_2 clumps in the south-eastern and north-eastern boundary of the remnant, and suggested that they are dense clumps in the circumstellar wind material shocked by SN blast wave.

We detected both [Fe II] and H_2 emission features showing more detailed and dramatic structures compared to the previous NIR studies. Addition to the two bright H_2 clumps previously detected in Koo et al. (2007), we found diffuse and extended H_2 features far outside of the remnant's boundary. Especially in the northern region, the H_2 emission is detected nearly $2'$ away from nearby [Fe II] filaments or radio shell, which is corresponding to the $5'$ from the center of the remnant.

A.4 G13.5+0.2

This elongated shell-like radio source with a size of $5' \times 4'$, is first classified as a Galactic SNR by Helfand et al. (1989). In radio continuum, the north-western part of the remnant is more complex and somewhat brighter than the rest of the remnant.

We found only two weak H_2 filaments in the western and southern borders of the

remnant, and they are well coincide with the radio continuum shell.

A.5 G15.9+0.2

G15.9+0.2 is known as a young ($\lesssim$ a few 1000 years) Galactic SNR (Reynolds et al., 2006). In the previous radio observations, it shows an elongated shell-like morphology with a size of $7' \times 5'$, including a bright spot at the eastern region of the remnant which is responsible for about 50% of the total flux density (Dubner et al., 1996). Caswell et al. (1982) suggested that the "eastern radio spot" is attributed to the large scale gradients in the interstellar medium (ISM). The *Chandra* X-ray observations revealed that it contains a compact X-ray source in the remnant's center, and has sharp outer edge in the south-east of the remnant (Reynolds et al., 2006).

We only detected a small ($\sim 4''$) [Fe II] clump in the south-western border, but there is no clear counterpart of the clump in both radio and X-ray images. The NIR spectroscopic observation will be needed to reveal the origin of the [Fe II] clump.

A.6 G16.0−0.5

This remnant was first identified as a Galactic SNR in centimeter radio observations (Brogan et al., 2006), and shows an incomplete shell-like morphology (Beaumont et al., 2011).

We found H_2 emission features around the eastern and southern border of the remnant, which is coincide with the filamentary arc detected in the previous radio observations. Furthermore, one H_2 clump with a size of $\sim 5''$ are detected outside the eastern radio shell, but we cannot find any physical association between the H_2 clump and the remnant.

A.7 G18.1−0.1

This remnant is a member of H II/SNR complex composed of at least four H II regions and one SNR. It is located in the western edge of the complex, and was first

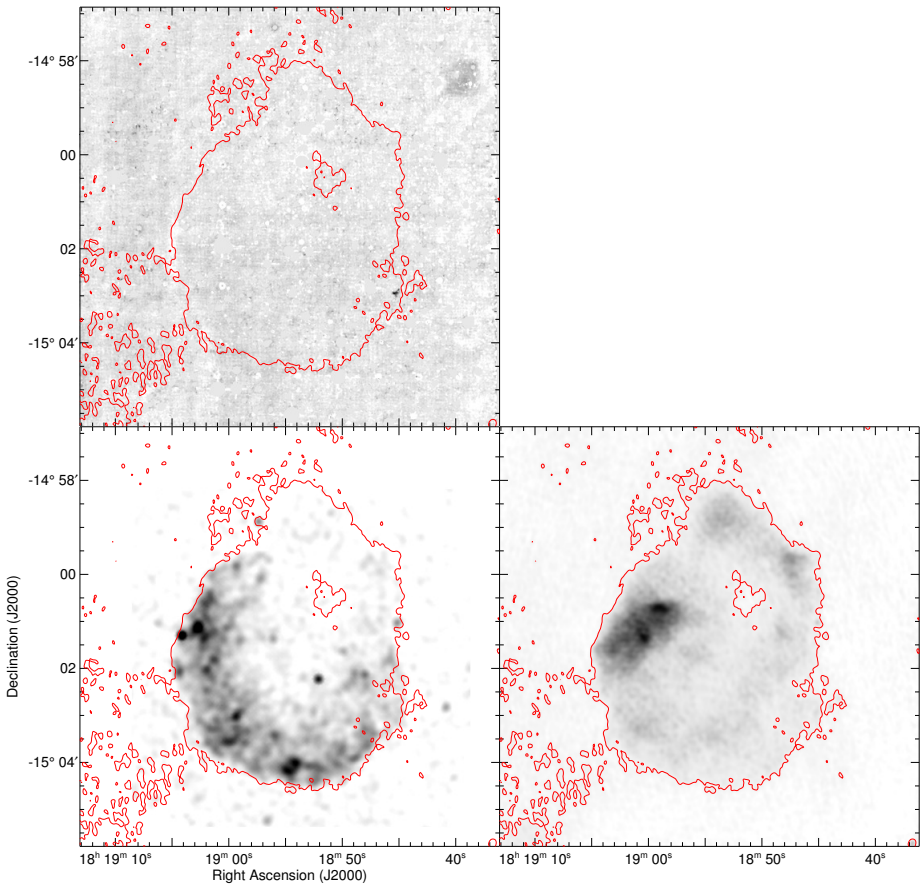

Figure A.4 (Top-feft) continuum-subtracted [Fe II] 1.64 μm narrow-band image of G15.9+0.2. (Bottom-left) *Chandra* X-ray continuum map. (Bottom-right) VLA 20 cm continuum map. The red contours show the brightness distribution of the radio continuum.

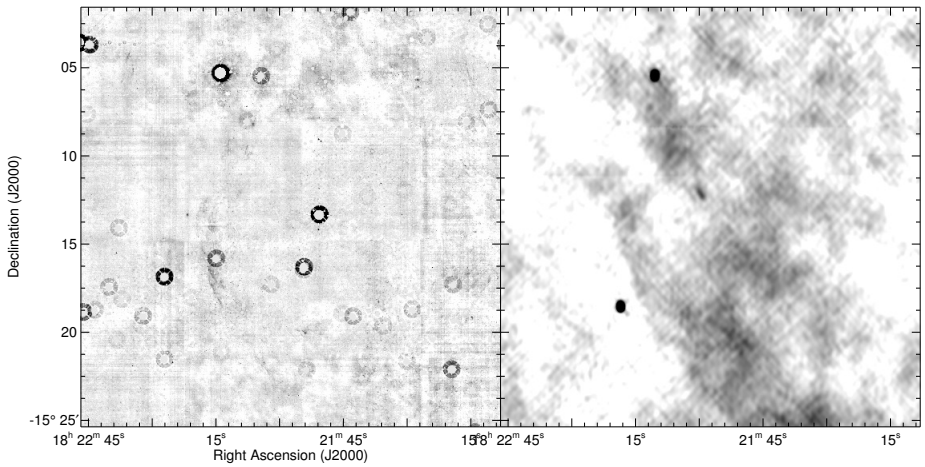

Figure A.5 (Left) continuum-subtracted H_2 2.12 μm narrow-band image of G16.0−0.5. (Right) VLA 20 cm continuum map.

confirmed as a SNR by Brogan et al. (2006). In radio continuum, it has a broken ring-like morphology with the bright northern and eastern arcs, and its the surface brightness is comparable with or weaker than the nearby H II regions. Although this remnant is close to the bright H II regions, it is still controversial whether they are physically associated or just in same line-of-sight far apart from each others (Paron et al., 2013; Leahy et al., 2014). From X-ray spectral analysis Leahy et al. (2014) argue that this SNR is in the adiabatic phase of evolution, and might have an explosion energy less than 10^{51} erg. One X-ray point source was detected near the northern shell, and it is seems to be an early O-type star radiating strong X-ray emission (Paron et al., 2013).

The strong, narrow filaments were detected in both [Fe II] and H_2 surveys, and mostly arise from the northern and eastern border of the remnant where the radio emission is also bright. However, the [Fe II] and H_2 distribution is somewhat different. We also found that some diffuse [Fe II] and H_2 lines arise from the nearby H II regions.

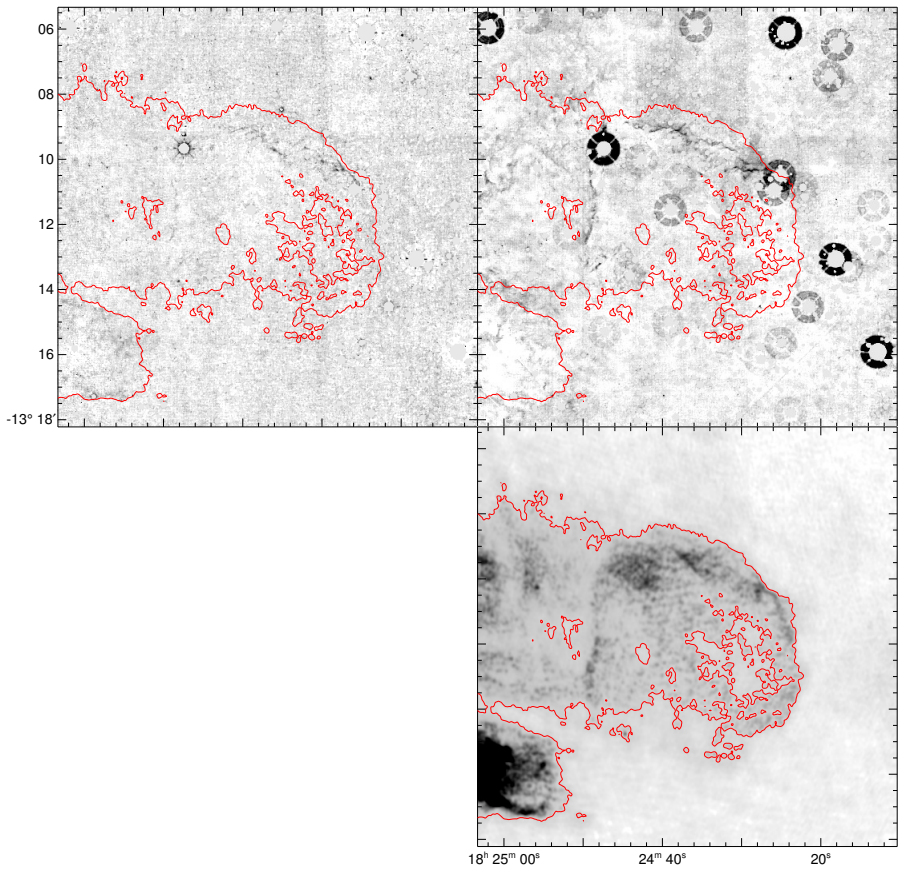

Figure A.6 Continuum-subtracted (top-left) [Fe II] 1.64 μm and (top-right) H_2 2.12 μm narrow-band images of G18.1−0.1. (Bottom-right) VLA 20 cm continuum map. The red contours show the brightness distribution of the radio continuum.

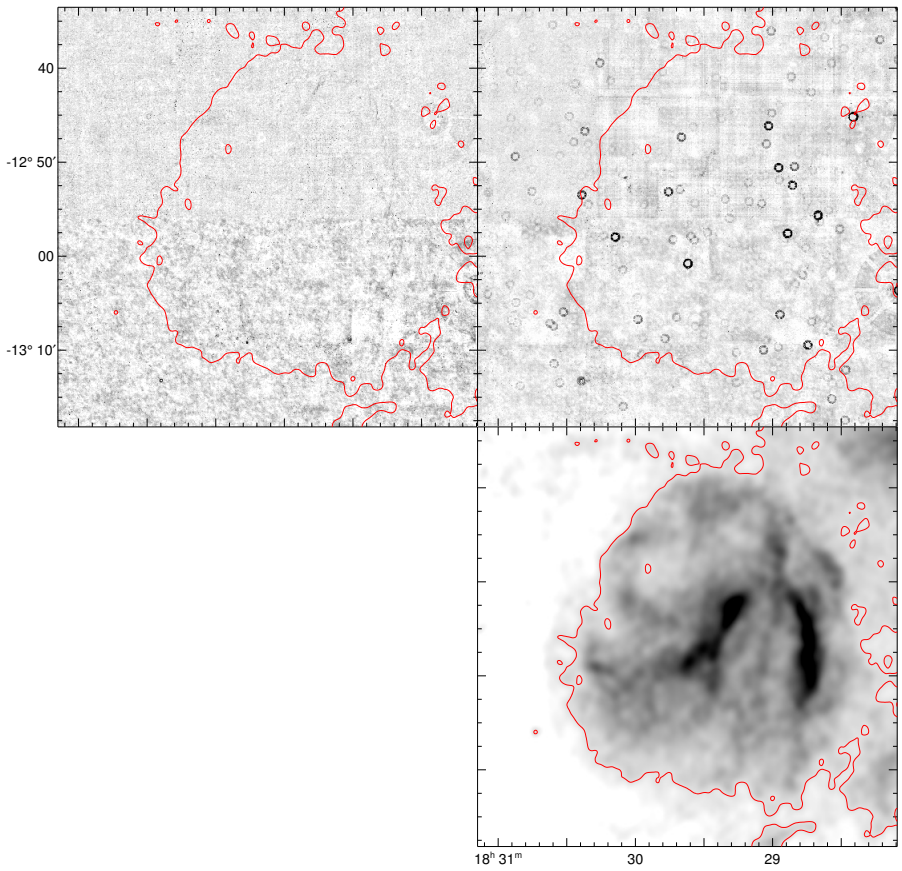

Figure A.7 Continuum-subtracted (top-left) [Fe II] 1.64 μm and (top-right) H_2 2.12 μm narrow-band images of G18.9−1.1. (Bottom-right) VLA 20 cm continuum map. The red contours show the brightness distribution of the radio continuum.

A.8 G18.9−1.1

G18.9−1.1 belongs to the composite type SNR with a size of larger than a half degree. Early radio observations (e.g., Furst et al., 1989) showed weak, diffuse radio continuum filling inside of the remnant together with two strong pillar-like features at the center and the western border. Several X-ray observations found a point-like hard X-ray source at the tip of the central radio pillar and smooth, extended features along the rest of the pillar (Harrus et al., 2004; Tüllmann et al., 2010). And they suggest that these strong X-ray features are well resemble with a typical characteristic of PWN.

We detected both [Fe II] and H_2 emission within the remnant, but their distributions are totally different. The [Fe II] emission mostly arises from the western shell corresponding to the western radio pillar, and some of weak, patchy [Fe II] emission is also detected in the northern and the north-eastern border of the remnant. The H_2 features, on the other hand, are composed of more than three strong filaments, are only detected around the center, a few arcminute east from the centeral radio pillar. We cannot find any counterpart of the central radio pillar in both [Fe II] and H_2 where the pulsar wind nebula is located.

A.9 G21.5−0.9

G21.5−0.9 have been extensively studied in radio and X-ray observations, and was revealed that it is one of composite type SNRs in our Galaxy. It is composed of (1) central X-ray source (PSR J1833-1034), (2) a radio and X-ray bright pulsar wind nebula (PWN) with a radius of $\sim 40''$, and (3) a diffuse X-ray halo extended to $\sim 150''$ from the center. Recently, a infrared study for this remnant has been carried out by Zajczyk et al. (2012). They reported the detection of [Fe II] 1.64 μm emission features in the north-east and the south-west of the PWN, showing a limb-brightened broken shell. They suggested that the [Fe II] emission arises from SN ejecta shocked by the PWN bubble.

The UWIFE survey shows the limb-brightened, complete ring-like [Fe II] structure in the central PWN together with the diffuse emission filling inside of the nebula. Some

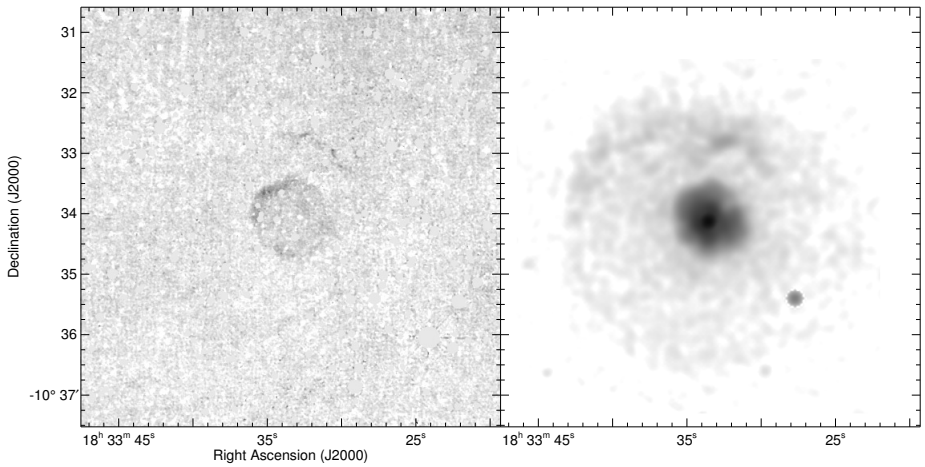

Figure A.8 (Left) continuum-subtracted [Fe II] 1.64 μm narrow-band image of G21.5−0.9. (Right) *Chandra* X-ray continuum map.

[Fe II] ffilaments are also detected in the north-west, $\sim 80''$ away from the center. This is well coincide with the bright "North Spur" confirmed in the previous X-ray and 1.4 GHz radio observations, that have been interpreted as the interacting SN ejecta with the H-rich stellar wind from the progenitor.

A.10 G21.6−0.8

Bietenholz et al. (2011) reported the detection of a shell-like SNR, G21.6−0.8, with $\sim 7'$ radius from the VLA 1.4 GHz radio image.

We found a long ($\sim 1'$), narrow H_2 filament around the western region of the remnant in which the radio continuum peaks, but the filaments is located around $2'$ outside the radio-bright shell. The physical association between the filament and the remnant is needed to be expored.

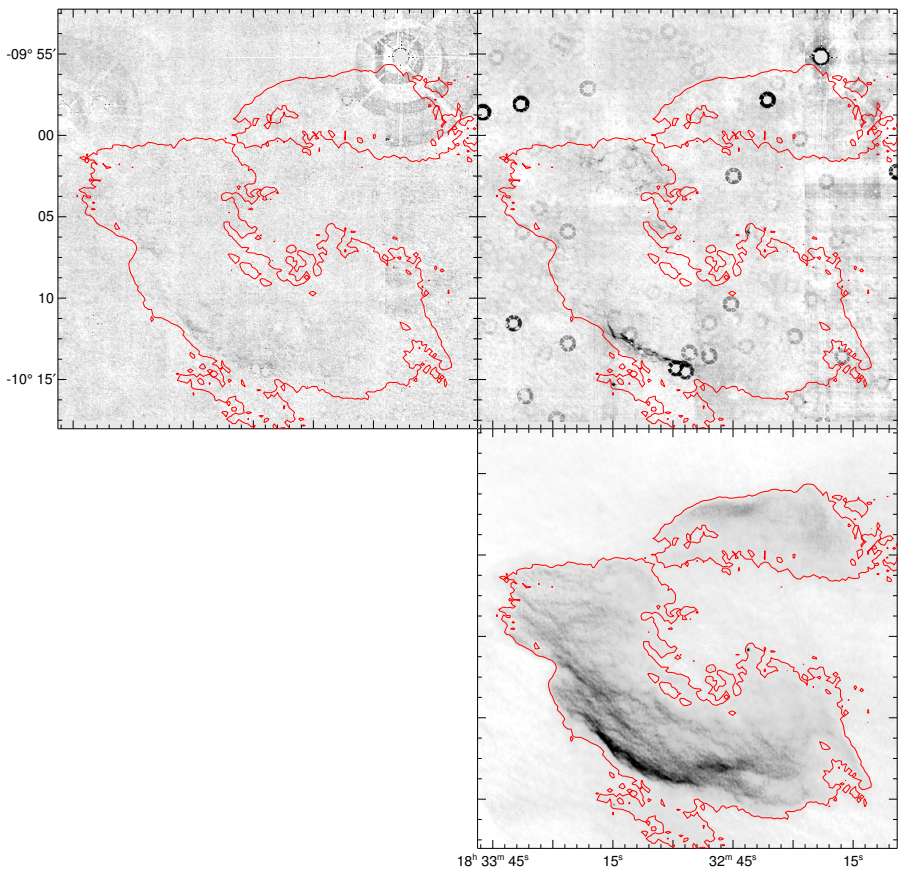

Figure A.9 Continuum-subtracted (top-left) [Fe II] 1.64 μm and (top-right) H_2 2.12 μm narrow-band images of KES 69. (Bottom-left) *Chandra* X-ray continuum map. (Bottom-right) VLA 20 cm continuum map. The red contours show the brightness distribution of the radio continuum.

A.11 Kes 69 (G21.8−0.6)

Kes 69 have been widely studied in radio observations, and displays an incomplete radio shell morphology (e.g., Zhou et al., 2009). Multiple OH masers which seem to be associated with the remnant were detected in the north-eastern and the south-eastern regions (Green et al., 1997; Hewitt et al., 2008), and the remnant is believed to be one of the Galactic SNRs interacting with its surrounding molecular clouds (MCs). The X-ray emission appears interior to the radio shell (Bocchino et al., 2012, and references therein).

We detected bright H_2 filaments at the south-western border of the remnant where the brightness of the radio continuum is strongest. [Fe II] emission also arises from the south-western shell, but is relatively weak and diffuse compared to the H_2 emission. In the north-eastern region of the remnant, We also found additional complex H_2 features in the north-eastern region of the remnant where a strong OH maser was detected (Green et al., 1997).

A.12 W41 (G23.3−0.3)

The previous radio studies show that W41 has a bright partial shell with an asymmetric morphology. This remnant have been most widely studied in high energy wavebands, since it possesses several high energy sources, the TeV γ-ray extension (HESS J1834−087; Aharonian et al., 2006), the GeV γ-ray source (2FGL J1834.3−0848; Nolan et al., 2012), the X-ray point source (XMMU J183435.3−084443/CXOU J183434.9−084443; Mukherjee et al., 2009; Misanovic et al., 2011), and the magnetar (Swift J1834.9−0846 D'Elia et al., 2011). An old pulsar (PSR J1833−0827), 20′ north-west from the remnant, also seems to be associated with the remnant (Gaensler & Johnston, 1995). These multi-wavelength studies may implies that it undergoes the interaction with the surrounding giant MCs.

We detected complex [Fe II] filaments near the western and south-western part of the remnant, and their distributions are well coincide with the bright radio filaments. Some [Fe II] emission also arises from near the X-ray and γ-ray point sources, but we

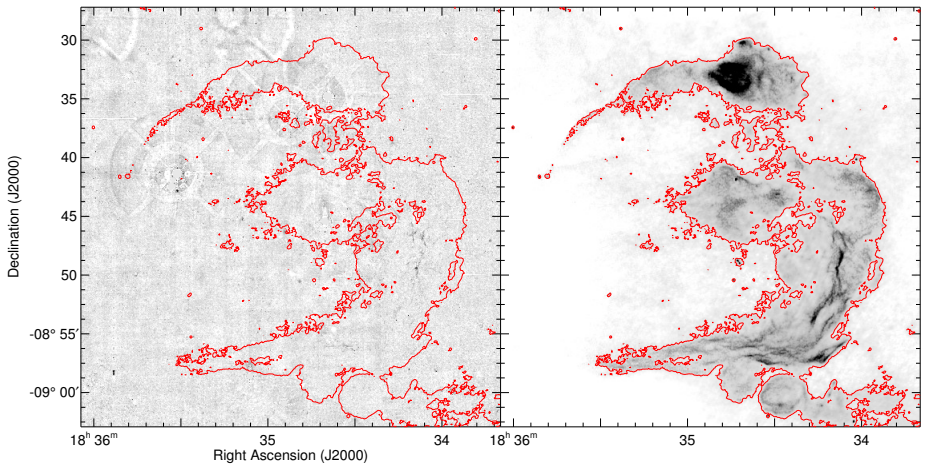

Figure A.10 (Left) continuum-subtracted [Fe II] 1.64 μm narrow-band image of W41. (Right) VLA 20 cm continuum map. The red contours show the brightness distribution of the radio continuum.

cannot find any clear evidence of their associations. There is no H_2 emission features around the remnant in our survey data.

A.13 G24.7+0.6

G24.7+0.6 is a Crab-like SNR, and is caracterized in radio wavebands by two bright incomplete shell with the filled central core which seems to be associated with the pulsar wind nebula powered by undetected pulsar (Becker & Helfand, 1987). The morphological agreement with the remnant and the molecular features (Petriella et al., 2008) together with the detection of a GeV γ-ray source (Nolan et al., 2012) may implies that it is an another SNR interacting with its surrounding MCs.

In the narrow-band H_2 image, we found bright and extended features around the southern and western region of the remnant. The southern H_2 features are relatively strong and more extended, and present a little coincide with the inner radio plateau. On the other hand, the the western features are narrow and clumpy, and do not have any clear counterpart in the radio image.

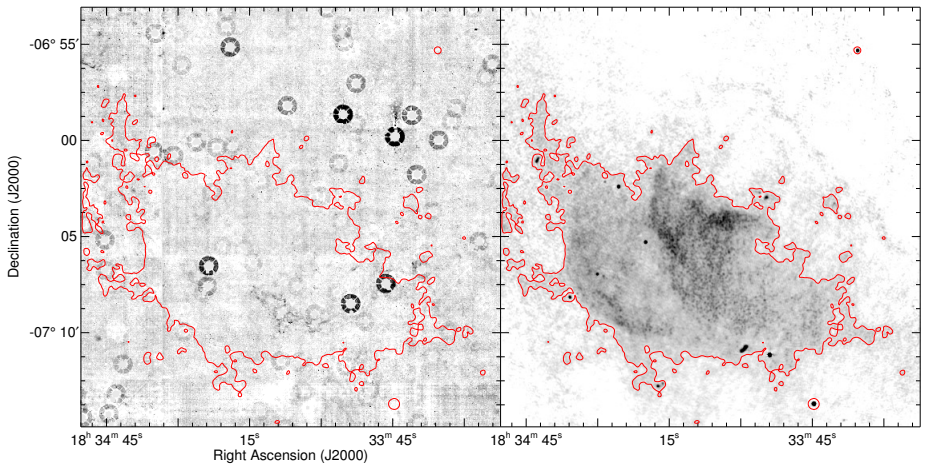

Figure A.11 (Left) continuum-subtracted H_2 2.12 μm narrow-band image of G24.7+0.6. (Right) VLA 20 cm continuum map. The red contours show the brightness distribution of the radio continuum.

A.14 Kes 73 (G27.4+0.0)

In radio and X-ray wavebands, Kes 73 displays a limb-brightened shell-like morphology with $\sim 2\farcm5$ radius, and especially the western shell is relatively bright in both wavebands compared to the other regions. The remnant hosts an anomalous X-ray pulsar (1E 1841−045; Kriss et al., 1985; Vasisht & Gotthelf, 1997), which is believed to be a highly magnetized young neutron star (called magnetar). It is also bright in a mid-infrared 24 μm waveband, and the emission seems to arise from either the swept-up dust with 0.1 $M_\odot$ (Pinheiro Gonçalves et al., 2011) or strong mid-infrared forbidden lines (Carey et al., 2009).

In the UWIFE survey, we found a dozon of bright [Fe II] clumps inside the remnant, and their spatial distributions are very different to those of the radio and X-ray. In the western border of the remnant where strong radio and X-ray emission were detected, complex [Fe II] emission features as well as a small H_2 clump with a size of $5''$ were also detected. These western [Fe II] and H_2 clumps show clear anti-correlation, and the H_2 clump is located 2–$3''$ outside the [Fe II] clumps showing the "[Fe II]-H_2 reversal."

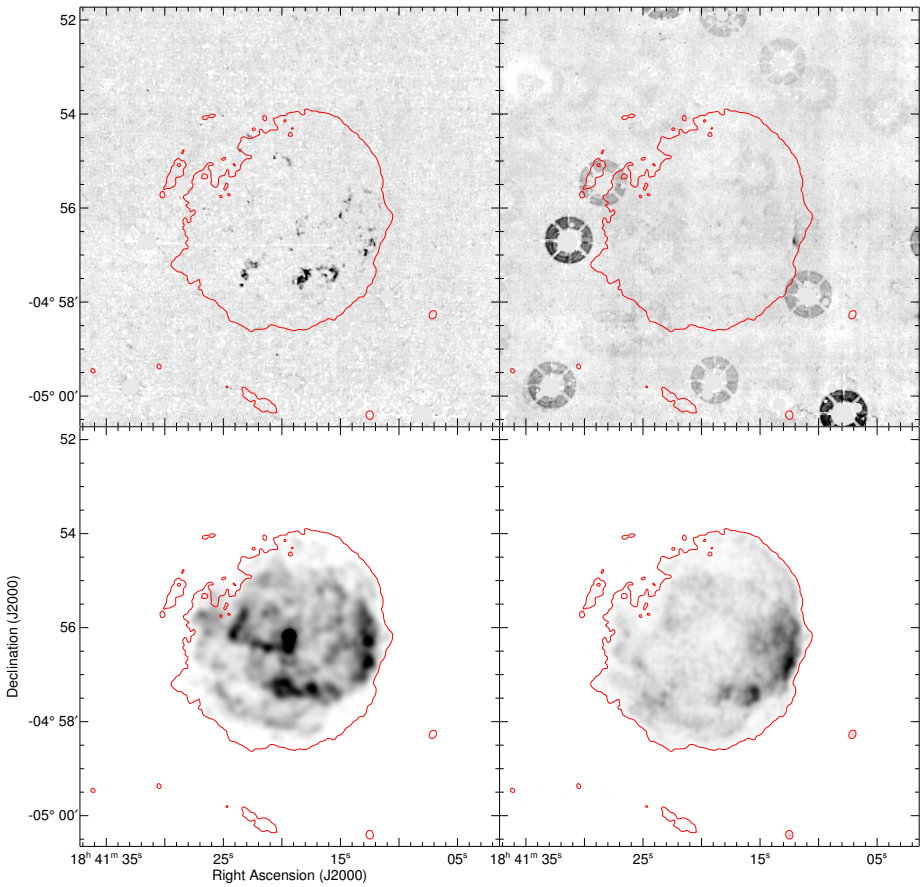

Figure A.12 Continuum-subtracted (top-left) [Fe II] 1.64 μm and (top-right) H_2 2.12 μm narrow-band images of KES 73. (Bottom-left) *Chandra* X-ray continuum map. (Bottom-right) VLA 20 cm continuum map. The red contours show the brightness distribution of the radio continuum.

A.15 G27.8+0.6

This SNR was identified as a center-filled SNR in radio observations (Reich et al., 1984), and the recent VLA 1.4 GHz observation shows multiple shell-like structures in the south-eastern region (Misanovic et al., 2010).

In UWIFE survey, weak and complex [Fe II] filaments were detected in the south-western region of the remnant. Their morphologies are similar with those in radio continuum, but the physical association between the [Fe II]/radio filaments and the center-filled SNR is unclear. In UWISH2 survey, on the other hand, we barely detected H_2 filaments at the south-eastern border of the remnant and their positions are well coincide with the radio shell. There are two small ($\lesssim 20''$) patches within the remnant, but we cannot find their radio counterpart. Some bright ring-like H_2 filaments with $\sim 30''$ radius were also detected, but they seem to arise from the planetary nebula, PN M 2-45, considering their spatial distributions centered on the source.

A.16 G28.6−0.1

From previous VLA 20 cm and 6 cm surveys, Helfand et al. (1989) resolved the radio complex around (l, b)=(28.6,-0.1) into 9 individual sources with names from A to I, and showed that radio sources C, E, and F have non-thermal spectra with a spectral index of $\alpha \sim 0.5$–0.6 implying some portions of possible Galactic SNRs (G28.6−0.1). Bamba et al. (2001) found a strong X-ray source (AX J1843.8-0352), and that the northern and southern rims of the X-ray source is well associated with the non-thermal radio sources, C and F identified in Helfand et al. (1989).

In UWIFE survey, two [Fe II] filaments are clearly detected around the remnant, and their morphologies are well resemble with those of the non-thermal radio sources, C and F. We cannot find any [Fe II] emission features around another non-thermal radio source E in the western part of the remnant.

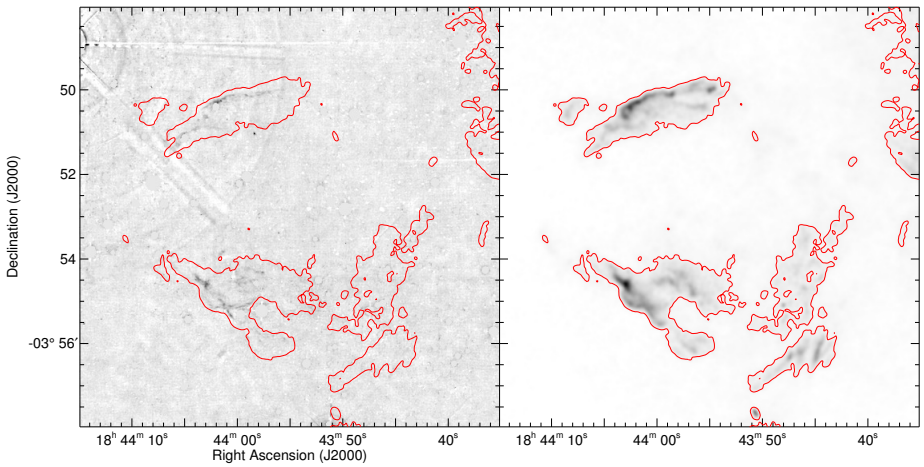

Figure A.13 (Left) continuum-subtracted [Fe II] 1.64 μm narrow-band image of G28.6−0.1. (Right) VLA 20 cm continuum map. The red contours show the brightness distribution of the radio continuum.

A.17 3C 391 (G31.9+0.0)

3C 391 is one of the brightest mixed-morphology SNR, showing rim-brightened radio shell with center-filled thermal X-ray emission (Reynolds & Moffett, 1993). In the high resolution radio images, it shows a partial shell of 5′ radius, with a relative faint emission extended through the broken shell in the southeastern part (Reynolds & Moffett, 1993; Moffett & Reynolds, 1994). This "breakout" morphology together with the CO line map coincide with the bright northeastern shell imply that the SN explosion took place in the edge of the northeastern molecular clouds (Wilner et al., 1998). Furthermore, the detection of two 1720 MHz OH maser spots in the remnant indicates that the remnant is now interacting with the surrounding molecular clouds (Frail et al., 1996).

In the [Fe II] narrow-band image, it shows complex filamentary structures filling inside the remnant boundary, and the overall distribution seems to be similar with that of the radio continuum. Furthermore, the [Fe II] emission peaks at the northwestern border, where the strongest radio shell is located. The H_2 emission is also detected

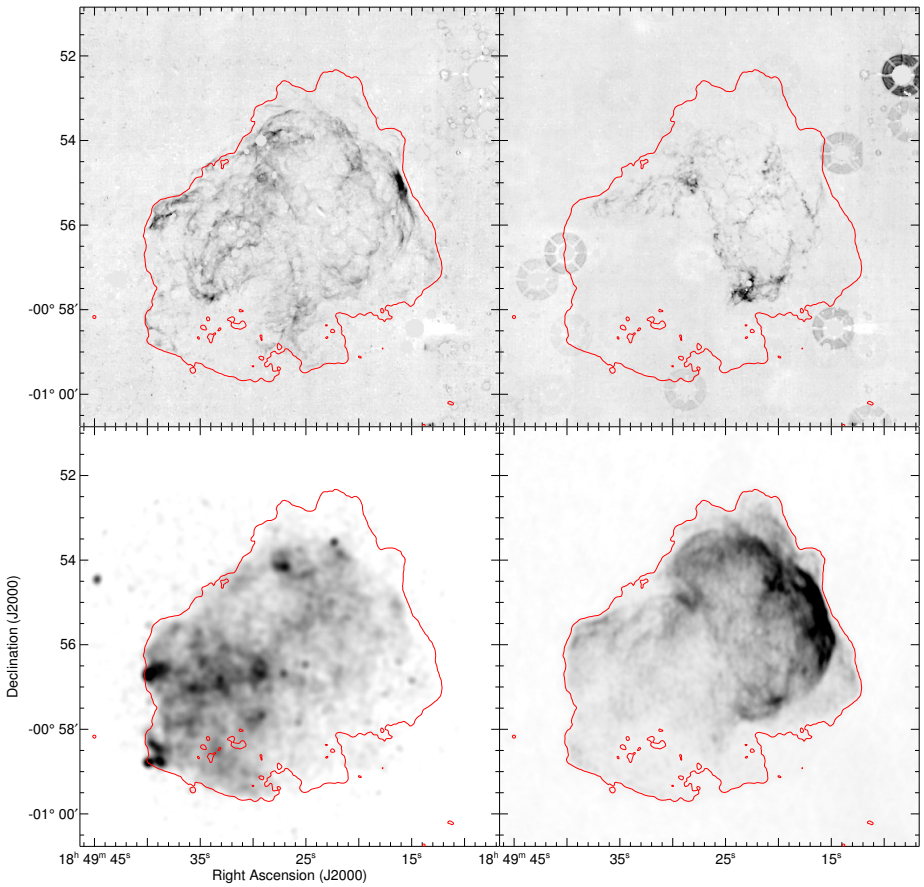

Figure A.14 Continuum-subtracted (top-left) [Fe II] 1.64 μm and (top-right) H_2 2.12 μm narrow-band images of 3C 391. (Bottom-left) *Chandra* X-ray continuum map. (Bottom-right) VLA 20 cm continuum map. The red contours show the brightness distribution of the radio continuum.

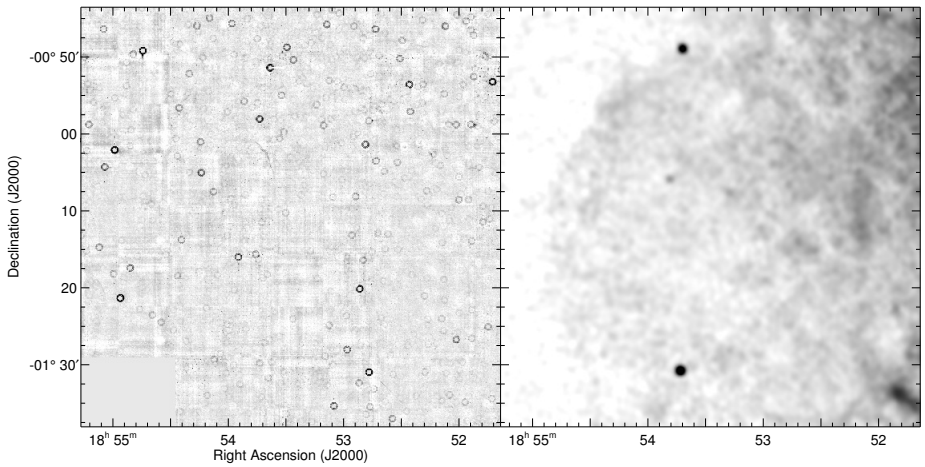

Figure A.15 (Left) continuum-subtracted H_2 2.12 μm narrow-band image of G32.1-0.9. (Right) VLA 20 cm continuum map.

in the remnant, but its distribution is very different to that of the radio continuum and [Fe II] emission. The strongest H_2 emission is arising from the southern portion of the remnant, where one of the OH maser spots is detected. The results of our morphological study are consistent with those in Reach et al. (2002), who carried out NIR [Fe II] 1.64 μm and H_2 2.12 μm narrow-band imaging observations for the northeastern and southern regions of the remnant for the first time.

A.18 G32.1-0.9

Previous ROSAT X-ray surveys found bright and extended emission features around the Galactic plane at l=32, and additional observations revealed that the source is composed of three X-ray spots and an extended emission within 15′ radius (Folgheraiter et al., 1997). Folgheraiter et al. (1997) argued that the X-ray source is probably an another center-filled Galactic SNR on the basis of the X-ray morpholgy and the spectrum, and the X-ray spots seem to be dense interstellar medium swept-up by the SN blast wave.

In UWISH2 data, we clearly detected long, narrow H_2 filaments at two different

regions. One filament is located near one of the X-ray spots in the northeastern region of the remnant (spot "A" in Folgheraiter et al., 1997). Another H_2 filament is detected near the northwestern border of the remnant, but we cannot find any clear counterpart of this filaments in the X-ray as well as the radio continuum.

A.19 Kes 78 (G32.8−0.1)

In radio wavebands, Kes 78 shows a elongated shell-like morphology with a size of $17' \times 10'$ (e.g., Caswell et al., 1975). The remnant also shows bright optical emission lines, and their morphology is well coincide with those of the radio continuum (Boumis et al., 2009; Stupar & Parker, 2011). The detection of high [S II]/Hα radio indicates shock-excitation of the optical filaments (Boumis et al., 2009). Koralesky et al. (1998) reported the detection of a OH maser spot in the eastern border of the remnant, implying the interaction of the SNR and the surrounding MCs.

We found weak and complex emission features in both [Fe II] and H_2 images around the remnant's shell. The bright, narrow H_2 filaments were detected around the eatern border of the remnant where the OH maser was detected, and an additional H_2 emission features were also detected in the southern edge. The [Fe II] emission was also detected in that regions, but is relatively weak and diffuse compared to the H_2 filaments. We also found additional diffuse [Fe II] emission features in the northern part of the remnant where the strong radio continuum is detected, but its morphology is somewhat different from that of the radio.

A.20 G33.2−0.6

This remnant shows an incomplete shell-like morphology with a size of $\sim 18'$ in the previous radio observations (e.g., Reich, 1982; Dubner et al., 1996).

We found strong H_2 filaments near the north-western edge in which the strongest radio emission is detected. There are also weak and diffuse H_2 features around the center of the remnant, but its brightness is much weaker than that of the north-western filaments.

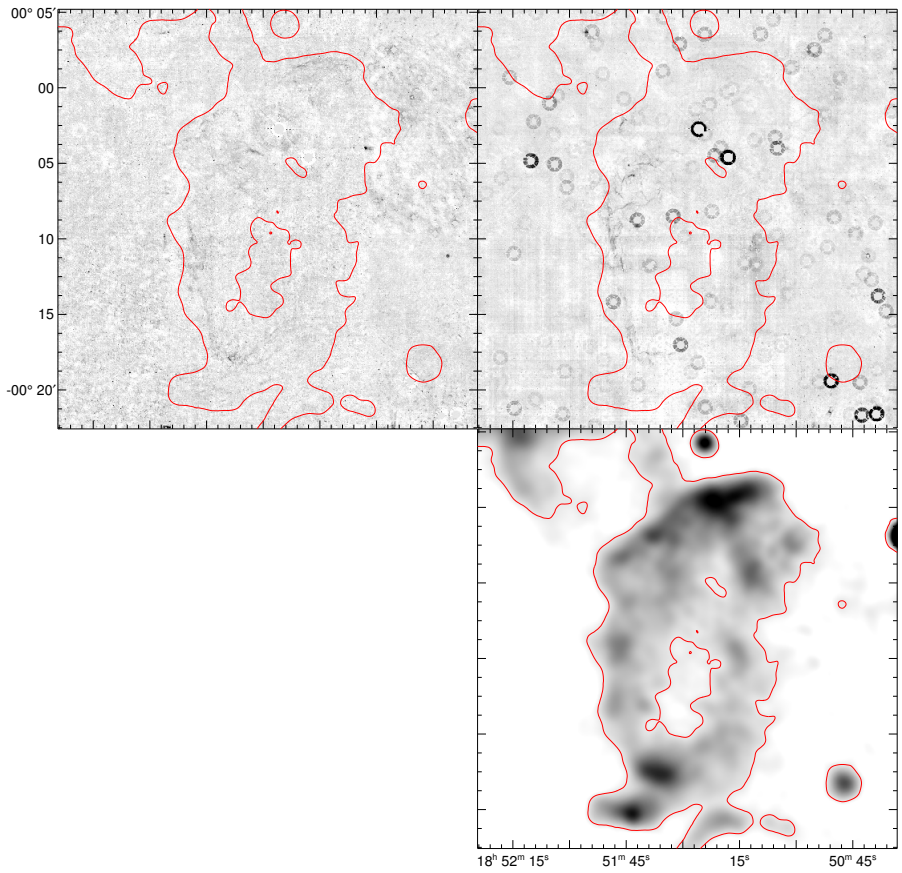

Figure A.16 Continuum-subtracted (top-left) [Fe II] 1.64 μm and (top-right) H_2 2.12 μm narrow-band images of KES 78. (Bottom-right) VLA 20 cm continuum map. The red contours show the brightness distribution of the radio continuum.

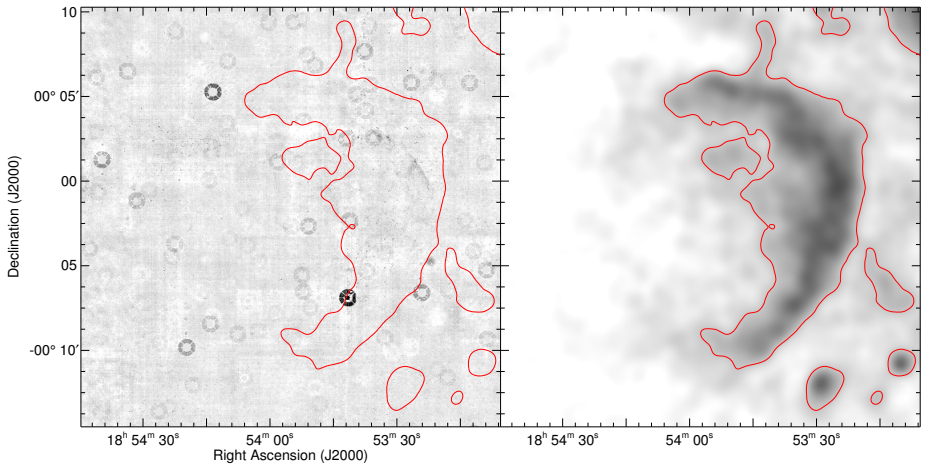

Figure A.17 (Left) continuum-subtracted H_2 2.12 μm narrow-band image of G33.2−0.6. (Right) VLA 20 cm continuum map. The red contours show the brightness distribution of the radio continuum.

A.21 W44 (G34.7-0.4)

We found bright and extended features of [Fe II] and H_2 inside of the remnant. Overall morphology of the [Fe II] is somewhat weak and diffuse compared with that of the H_2 and well resemble with that in the radio continuum. H_2 on the other hands, displays very bright and narrow H_2 filaments all over the remnant, and interestingly some of the H_2 features are detected slightly outside of the remnant boundary. The peak brightness in both [Fe II] and H_2 is arising in the western edge where the radio continuum is also strongest.

A.22 3C 396 (G39.2-0.3)

We detect both [Fe II] and H_2 emission features associated with the remnant. Addition to two bright [Fe II] knots identified in Lee et al. (2009), we also found weak and diffuse [Fe II] emission features which is smoothly filling inside of the radio boundary. The continuum-subtracted H_2 image shows complex filaments including two long

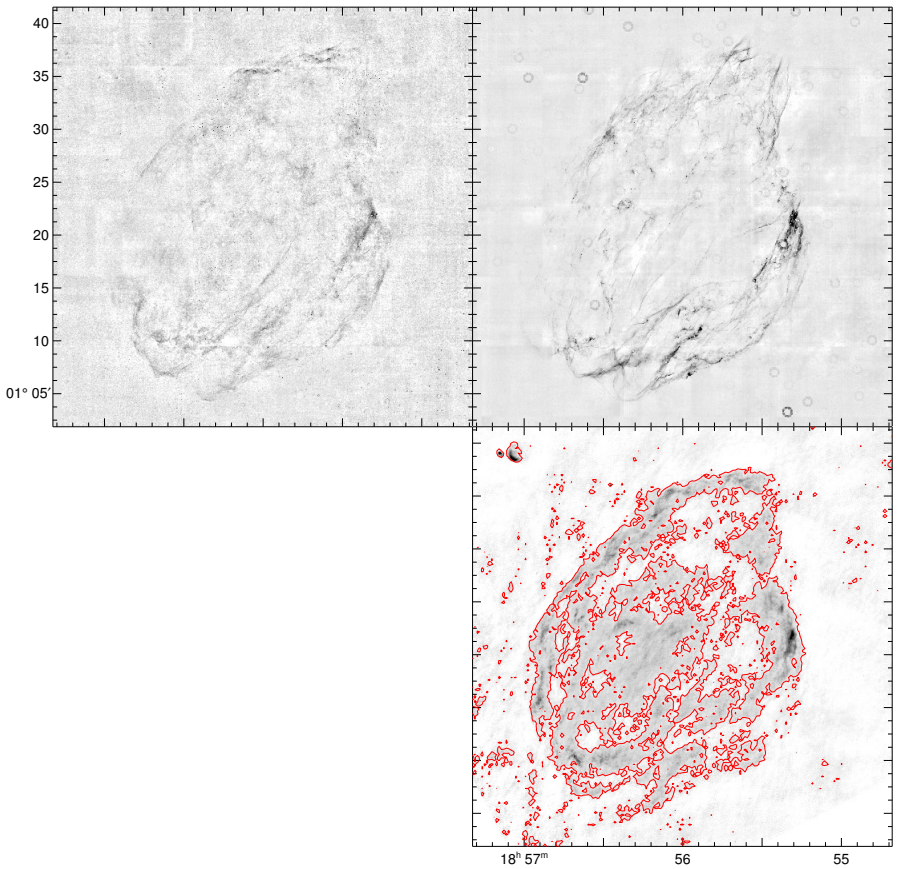

Figure A.18 Continuum-subtracted (top-left) [Fe II] 1.64 μm and (top-right) H_2 2.12 μm narrow-band images of W44. (Bottom-left) *Chandra* X-ray continuum map. (Bottom-right) VLA 20 cm continuum map. The red contours show the brightness distribution of the radio continuum.

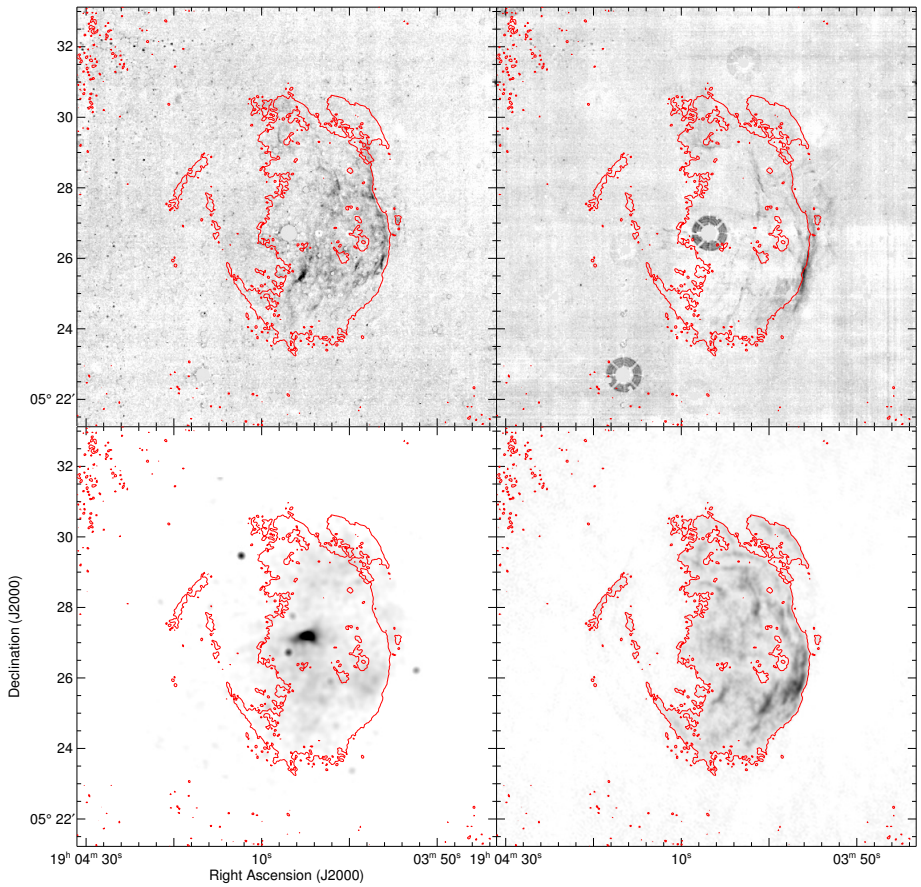

Figure A.19 Continuum-subtracted (top-left) [Fe II] 1.64 μm and (top-right) H_2 2.12 μm narrow-band images of 3C 396. (Bottom-left) *Chandra* X-ray continuum map. (Bottom-right) VLA 20 cm continuum map. The red contours show the brightness distribution of the radio continuum.

filaments along the north to south direction leaving an interval of $\sim 1'$. The peak brightness of H_2 emission is located near the western edge of the remnant, but is slightly outside of the [Fe II] and radio boundary.

A.23 3C 397 (G41.1-0.3)

We detected strong [Fe II] emission without any H_2 emission features, and it shows an elongated morphology with bright and complex features filling inside of the remnant. Contrast to the X-ray and Radio images showing bright emission features in south-western border of the remnant, the north-eastern shell is relatively bright in the [Fe II] emission.

A.24 G41.5+0.4

In 322 MHz VLA images, this remnant shows an incomplete shell in the north-east together with a compact core to the center (Kaplan et al., 2002).

In UWIFE survey, we clearly detected strong [Fe II] filaments almost all over the remnant. The brightest [Fe II] filaments are located in the center where the compact radio continuum is detected. Furthermore, the diffuse [Fe II] emission features in the north-eastern region of the remnant seem to be associated with the radio shell. We also found narrow [Fe II] filaments at the south-eastern and north-western border of the remnant.

A.25 W49B (G43.3-0.2)

The continuum-subtracted [Fe II] image shows a barrel-like morphology with very strong and narrow filaments mostly aligned along the north-east to south-west direction, which is quite similar with that in radio image. We also found some diffuse, "cirrus-like" [Fe II] emission features in the edge of the remnant, which seem to be perpendicular to the shell. The strong H_2 emission is detected in both eastern and western border of the remnant. The western H_2 structures show bright clumpy-like features.

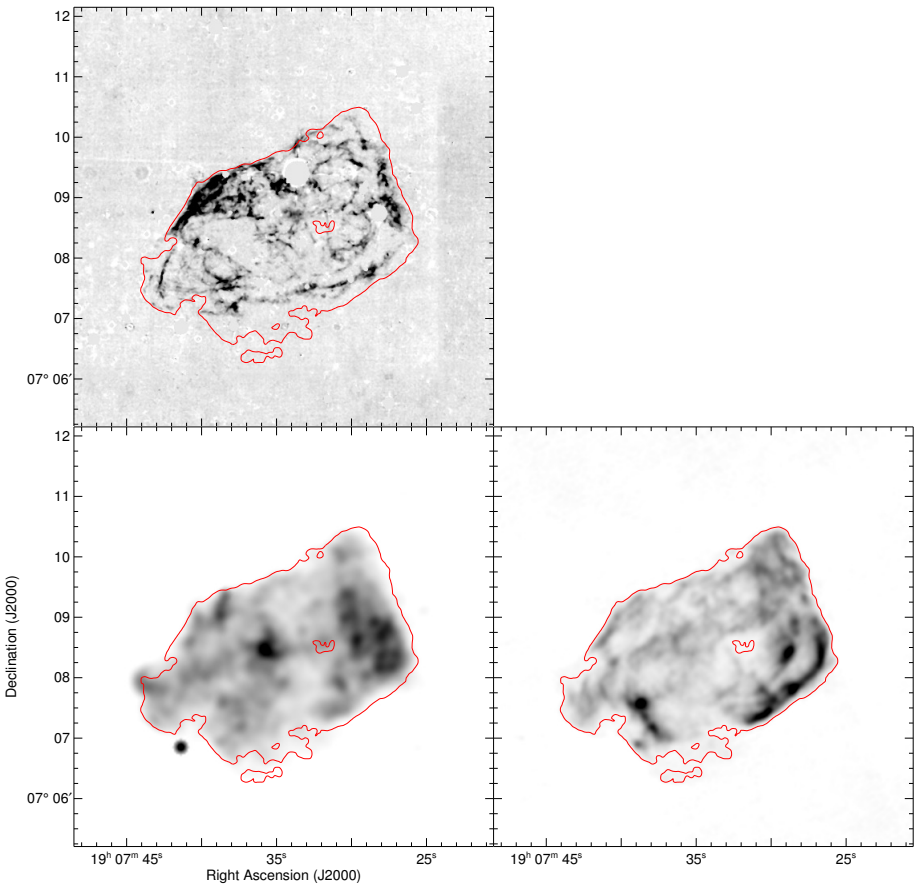

Figure A.20 (Top-left) continuum-subtracted [Fe II] 1.64 μm narrow-band image of 3C 397. (Bottom-left) *Chandra* X-ray continuum map. (Bottom-right) VLA 20 cm continuum map. The red contours show the brightness distribution of the radio continuum.

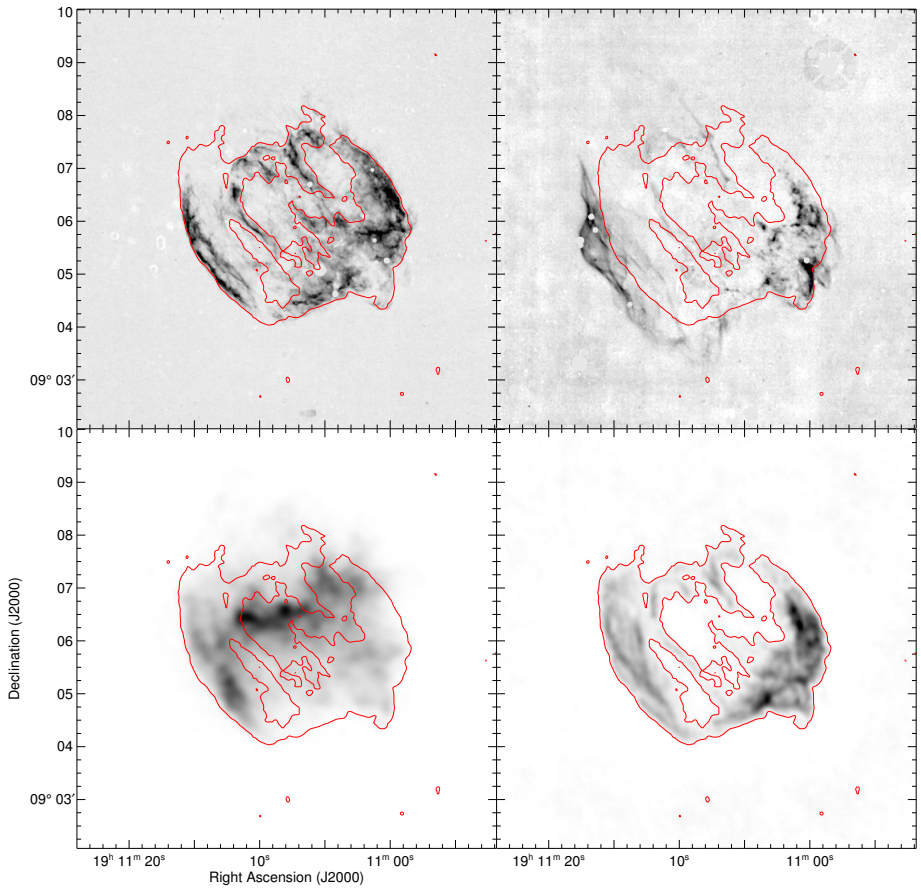

Figure A.21 Continuum-subtracted (top-left) [Fe II] 1.64 μm and (top-right) H_2 2.12 μm narrow-band images of W49B. (Bottom-left) *Chandra* X-ray continuum map. (Bottom-right) VLA 20 cm continuum map. The red contours show the brightness distribution of the radio continuum.

Although these are overlapped with the bright [Fe II] features, their distributions and morphologies are somewhat different. The H_2 features in the east seem to be composed of multiple narrow filaments as bright as the western H_2 clumps. These H_2 filaments are in a few 10 arcseconds outside the radio edge, as a part of "[Fe II]-H_2 reversal."

A.26 W51C (G49.2−0.7)

W51C is an old ($\sim 3 \times 10^4$ years; Koo et al., 1995) Galactic SNR and is member of the radio comples W51, which is composed of two large HII region (W51A and W51B) and one SNR (W51C). In radio wavebands, the remnant shows incomplete shell-like structures with its upper part opened. The detection of two OH maser spots associated with the remnant as well as the morphological agreement between H I and CO line maps imply that the remnant is interacting with surrounding MCs (Green et al., 1997; Koo & Moon, 1997).

We found the complex filamentary [Fe II] and H_2 structures within the W51 region. The strongest emission of [Fe II]and H_2 arises from the north-western part of the complex where the HII region W51B is located. Some diffuse and filamentary [Fe II] emission features were detected within W51C. They are composed of two long, narrow filaments aligned along the north-east to south-west direction, and seem to be associated with the remnant. One of them is detected along the south-eastern edge of the remnant, whereas the other is located in $\sim 10'$ inside from the outer filament.

A.27 HC40 (G54.4−0.3)

This remnant have been detected in previous radio observations, and shows an incomplete shell-like structure with $\sim 25'$ radius. Junkes et al. (1992) suggested that a CO shell is most likely the result of the interaction of the stellar wind from the progenitor with its surrounding MCs. And they also argue that the SN ejecta are still expanding in the stellar wind bubble. Diffuse optical emission of Hα and [S II] are detected in west and north/south edge of the remnant Boumis et al. (2005), the their flux ratio implies that the emissions arise from the shock heated gas.

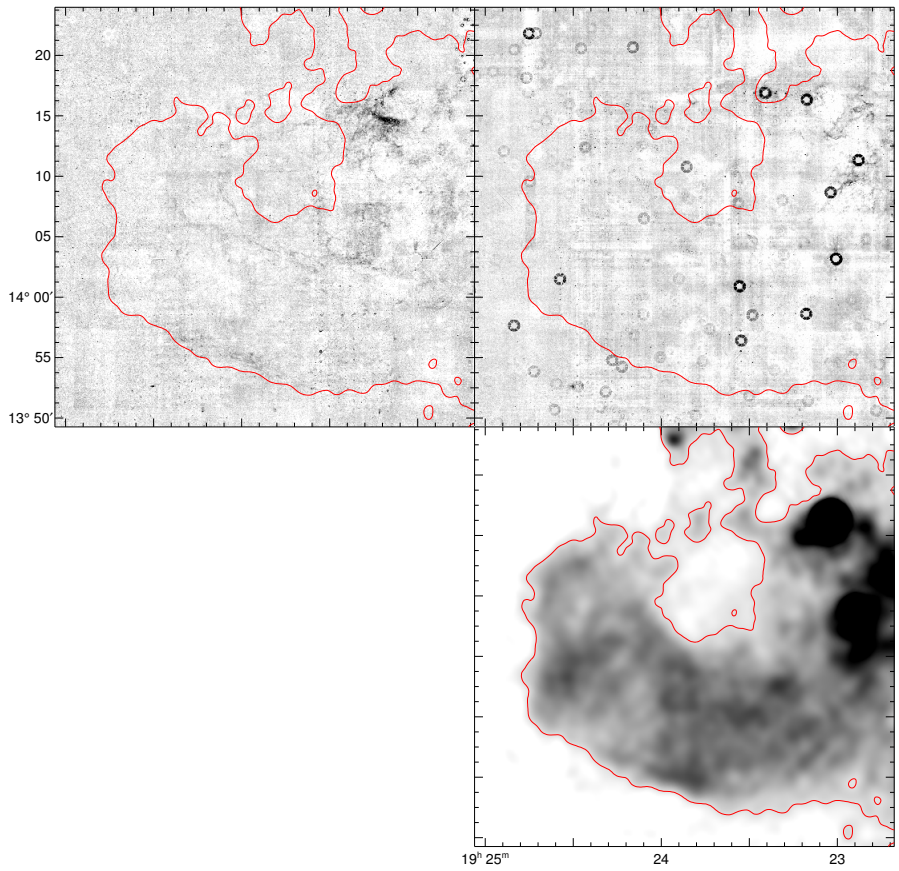

Figure A.22 Continuum-subtracted (top-left) [Fe II] 1.64 μm and (top-right) H_2 2.12 μm narrow-band images of W51C. (Bottom-right) VLA 20 cm continuum map. The red contours show the brightness distribution of the radio continuum.

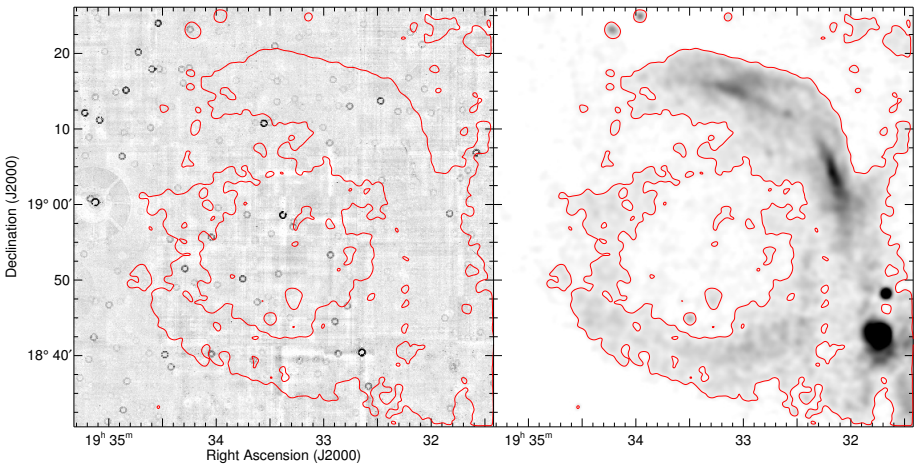

Figure A.23 (Left) continuum-subtracted H_2 2.12 μm narrow-band image of HC40. (Right) VLA 20 cm continuum map. The red contours show the brightness distribution of the radio continuum.

We found narrow H_2 filaments in the north-west border of the remnant, and they are coincide with the strongest radio shell. The spatial distribution of H_2 emission, however, is different from that of the Hα and [S II].

Biblography

Aharonian, F., Akhperjanian, A. G., Bazer-Bachi, A. R., et al. 2006, ApJ, 636, 777

Bamba, A., Ueno, M., Koyama, K., & Yamauchi, S. 2001, PASJ, 53, L21

Beaumont, C. N., Williams, J. P., & Goodman, A. A. 2011, ApJ, 741, 14

Becker, R. H., & Helfand, D. J. 1987, ApJ, 316, 660

Bietenholz, M. F., Matheson, H., Safi-Harb, S., Brogan, C., & Bartel, N. 2011, MNRAS, 412, 1221

Bocchino, F., Bykov, A. M., Chen, Y., et al. 2012, A&A, 541, A152

Boumis, P., Mavromatakis, F., Xilouris, E. M., et al. 2005, A&A, 443, 175

Boumis, P., Xilouris, E. M., Alikakos, J., et al. 2009, A&A, 499, 789

Brogan, C. L., Gelfand, J. D., Gaensler, B. M., Kassim, N. E., & Lazio, T. J. W. 2006, ApJL, 639, L25

Carey, S. J., Noriega-Crespo, A., Mizuno, D. R., et al. 2009, PASP, 121, 76

Caswell, J. L., Clark, D. H., & Crawford, D. F. 1975, Australian Journal of Physics Astrophysical Supplement, 37, 39

Caswell, J. L., Haynes, R. F., Milne, D. K., & Wellington, K. J. 1982, MNRAS, 200, 1143

Clifton, T. R., & Lyne, A. G. 1986, Nature, 320, 43

D'Elia, V., Barthelmy, S. D., Baumgartner, W. H., et al. 2011, GRB Coordinates Network, 12253, 1

Dubner, G. M., Giacani, E. B., Goss, W. M., Moffett, D. A., & Holdaway, M. 1996, AJ, 111, 1304

Finley, J. P., & Oegelman, H. 1994, ApJL, 434, L25

Folgheraiter, E. L., Warwick, R. S., Watson, M. G., & Koyama, K. 1997, MNRAS, 292, 365

Frail, D. A., Goss, W. M., Reynoso, E. M., et al. 1996, AJ, 111, 1651

Frail, D. A., Kassim, N. E., & Weiler, K. W. 1994, AJ, 107, 1120

Furst, E., Hummel, E., Reich, W., et al. 1989, A&A, 209, 361

Gaensler, B. M., & Johnston, S. 1995, MNRAS, 275, L73

Gotthelf, E. V., & Vasisht, G. 1997, ApJL, 486, L133

Green, A. J., Frail, D. A., Goss, W. M., & Otrupcek, R. 1997, AJ, 114, 2058

Harrus, I. M., Slane, P. O., Hughes, J. P., & Plucinsky, P. P. 2004, ApJ, 603, 152

Helfand, D. J., Velusamy, T., Becker, R. H., & Lockman, F. J. 1989, ApJ, 341, 151

Hewitt, J. W., Yusef-Zadeh, F., & Wardle, M. 2008, ApJ, 683, 189

Junkes, N., Fuerst, E., & Reich, W. 1992, A&A, 261, 289

Kaplan, D. L., Kulkarni, S. R., Frail, D. A., & van Kerkwijk, M. H. 2002, ApJ, 566, 378

Kassim, N. E., & Weiler, K. W. 1990, Nature, 343, 146

Koo, B.-C., Kim, K.-T., & Seward, F. D. 1995, ApJ, 447, 211

Koo, B.-C., & Moon, D.-S. 1997, ApJ, 475, 194

Koo, B.-C., Moon, D.-S., Lee, H.-G., Lee, J.-J., & Matthews, K. 2007, ApJ, 657, 308

Koralesky, B., Frail, D. A., Goss, W. M., Claussen, M. J., & Green, A. J. 1998, AJ, 116, 1323

Kriss, G. A., Becker, R. H., Helfand, D. J., & Canizares, C. R. 1985, ApJ, 288, 703

Leahy, D., Green, K., & Tian, W. 2014, MNRAS, 438, 1813

Lee, H.-G., Moon, D.-S., Koo, B.-C., et al. 2013, ApJ, 770, 143

Lee, H.-G., Moon, D.-S., Koo, B.-C., Lee, J.-J., & Matthews, K. 2009, ApJ, 691, 1042

Misanovic, Z., Kargaltsev, O., & Pavlov, G. G. 2010, ApJ, 725, 931

Misanovic, Z., Kargaltsev, O., & Pavlov, G. G. 2011, ApJ, 735, 33

Moffett, D. A., & Reynolds, S. P. 1994, ApJ, 425, 668

Moon, D.-S., Koo, B.-C., Lee, H.-G., et al. 2009, ApJL, 703, L81

Mukherjee, R., Gotthelf, E. V., & Halpern, J. P. 2009, ApJ, 691, 1707

Nolan, P. L., Abdo, A. A., Ackermann, M., et al. 2012, ApJS, 199, 31

Odegard, N. 1986, AJ, 92, 1372

Paron, S., Weidmann, W., Ortega, M. E., Albacete Colombo, J. F., & Pichel, A. 2013, MNRAS, 433, 1619

Petriella, A., Paron, S., & Giacani, E. 2008, Boletin de la Asociacion Argentina de Astronomia La Plata Argentina, 51, 209

Pinheiro Gonçalves, D., Noriega-Crespo, A., Paladini, R., Martin, P. G., & Carey, S. J. 2011, AJ, 142, 47

Reach, W. T., Rho, J., Jarrett, T. H., & Lagage, P.-O. 2002, ApJ, 564, 302

Reich, W. 1982, A&A, 106, 314

Reich, W., Furst, E., & Sofue, Y. 1984, A&A, 133, L4

Reynolds, S. P., Borkowski, K. J., Hwang, U., et al. 2006, ApJL, 652, L45

Reynolds, S. P., & Moffett, D. A. 1993, AJ, 105, 2226

Roberts, M. S. E., Tam, C. R., Kaspi, V. M., et al. 2003, ApJ, 588, 992

Stupar, M., & Parker, Q. A. 2011, MNRAS, 414, 2282

Torii, K., Tsunemi, H., Dotani, T., & Mitsuda, K. 1997, ApJL, 489, L145

Tüllmann, R., Plucinsky, P. P., Gaetz, T. J., et al. 2010, ApJ, 720, 848

Vasisht, G., & Gotthelf, E. V. 1997, ApJL, 486, L129

Wilner, D. J., Reynolds, S. P., & Moffett, D. A. 1998, AJ, 115, 247

Zajczyk, A., Gallant, Y. A., Slane, P., et al. 2012, A&A, 542, A12

Zhou, X., Chen, Y., Su, Y., & Yang, J. 2009, ApJ, 691, 516

요 약

우리 은하 초신성 잔해는 은하 내 성간 난류 및 거대 구조, 그리고 다양한 형태의 중원소의 원인이 되기 때문에, 우리 은하의 진화에 매우 중요한 역할을 한다. 네 부분으로 나누어진 본 학위논문에서는 우리 은하 초신성 잔해들에 대한 근적외선 사진 및 분광연구를 보고한다. 처음 두 부분에서는 주변물질과 상호작용하는 "진화된'' 초신성 잔해들에 대한 [Fe II] 1.64 μm 및 H_2 2.12 μm 방출선 연구를 소개하고, 나머지 두 부분에서는 초신성 폭발 정보가 남아있는 우리 은하에서 가장 젊은 초신성 잔해 중의 하나인 카시오페이아 A에 대한 근적외선 분광연구를 소개한다.

첫 번째 장에서는 UWIFE/UWISH2 서베이 자료를 이용하여 우리 은하 제 1 사분면 영역에 있는 초신성 잔해들의 [Fe II] 및 H_2 방출선 존재 유무를 보고한다. 서베이 영역에 위치한 총 79개의 우리 은하 초신성 잔해 중에서 19개의 [Fe II] 방출선을 내는 초신성 잔해들과 19개의 H_2 방출선을 내는 초신성 잔해들을 찾았다. 두 방출선의 검출율은 각각 24%이었다. [Fe II] 방출선의 검출율은 은경 40–50도에서 최대를 보이는 반면, H_2 방출선의 경우 은경 30–40도에서 최대 검출율을 보였다. 이러한 차이는 은경에 따라 초신성 생태계가 달라지기 때문일 것으로 예상된다. 계산된 초신성 잔해들의 총 [Fe II] 밝기는 우리 은하의 초신성 빈도로부터 예상되는 밝기에 비해 최소 2–3배정도 더 어두운데, 이는 서베이 검출 한계 때문이거나 혹은 현재까지 알려지지 않은 초신성 잔해가 우리 은하에 많이 있음을 암시한다. 두 방출선을 동시에 내는 11개의 초신성 잔해 중 5개에서 H_2 방출선이 [Fe II] 혹은 전파 경계보다 더 바깥쪽에서 검출되는, 이른바 "[Fe II]-H_2 역전현상''을 확인하였다. 나는 경계면 바깥에서 검출된 H_2 방출선 구조들의 근적외선 스펙트럼으로부터 그러한 H_2 방출선들이 충돌에 의해 흥분된 분자기체에서 발생된다는 사실을 확인하였지만, 흥분을 야기시키는 근원에 대해서는 추가적인 연구가 필요할 것으로 생각된다.

두 번째 장에서는 "[Fe II]-H_2 역전현상''에서 나타나는 확장된 H_2 방출선 구조를 보이는 5개의 초신성 잔해들(G11.2−0.3, KES 73, W44, 3C 396, W49B)에 대한 근적외선 분광결과를 보고한다. 모든 관측 슬릿에서 H_2 1–0 S(1) 2.12 μm 방출선과 1–0 S(0) 2.22 μm 방출선이 뚜렷하게 검출되었다. 그들의 시선속도는 각 초신성 잔해들의 시스템속도와 잘 일치하는데 이는 관측되는 H_2 방출선들이 실제 각 초신성 잔해들과 물리적인 연관성이

있음을 암시한다. 방출선들의 선폭은 10 km s^{-1} 이상 넓고 밝기비는 열적 흥분상태의 그것과 유사한데, 이는 확장된 H_2 방출선 구조가 충격파를 통해 열적으로 흥분되었음을 암시한다. 나는 충격파의 기원에 대한 세 가지 가능성을 제안한다: (1) 초신성 충격파 전면에 형성되는 자기 선행파, (2) 투영효과와 결합된 초신성 충격파, (3) 선조성의 항성풍에 의해 형성된 속도가 낮은 C형 충격파. 이 장에서는 세 가지 가능성을 이용하여 각 초신성 잔해들에서 나타나는 확장된 H_2 방출선 구조의 기원을 논의한다.

세 번째 장에서는 카시오페이아 A에 대한 근적외선 분광관측 결과를 보고한다. 8개의 슬릿 위치에서 얻은 2차원 스펙트럼에서 총 63개의 방출선 덩어리들을 식별하였고, 그들의 분광학적 특성을 알아보았다. 모든 덩어리들은 [Fe II] 방출선을 포함한 다양한 금속성 원소에서 발생되는 금지선들을 보여주고, 몇몇 덩어리들에서는 수소 및 헬륨 방출선들을 보여주기도 하였다. 63개의 방출선 덩어리에서 총 46개의 방출선들을 식별하였고, 그들의 밝기 및 시선속도를 측정하였다. 검출된 방출선들에 대한 주성분 분석을 통해 모든 방출선 덩어리들을 크게 세 개의 그룹으로 나눌 수 있었다: (1) He-rich, (2) S-rich, (3) Fe-rich 덩어리. He-rich 덩어리들은 시선방향으로의 속력이 상대적으로 낮고 ($\lesssim$ 200 km s^{-1}) 비교적 강한 He I 방출선 및 [Fe II] 방출선을 내는데, 이는 별 주변 물질로 알려진 광학영역의 quasi-stationary flocculi와 매우 닮았다. 반면, S-rich 덩어리는 매우 강한 산소-연소 물질의 방출선들과 함께 최대 $\sim$ 2000 km s^{-1}에 이르는 매우 빠른 시선속도를 보이는데, 이는 이들이 광학영역에서 fast-moving knots이라고 불리는 초신성 분출물임을 암시한다. Fe-rich 덩어리는 S-rich 덩어리처럼 매우 빠른 시선속도를 보이지만 산소-연소 물질의 방출선을 전혀 보이지 않는다. Fe-rich 덩어리들의 기원에 대한 논의과정을 통해 이들이 별 중심부근에서 합성된 순수한 철 분출물이라는 결론에 도달하였다. [Fe II] 사진과 여러 파장대역의 사진들과의 비교를 통해 이러한 밀도 높은 철 분출물이 주로 남서쪽의 충격파를 겪지 않은 ^{44}Ti 분출물 바로 바깥쪽에 분포한다는 사실을 알 수 있었고, 이는 ^{44}Ti 분출물과 연관된 충격파를 겪지 않은 철 분출물이 존재함을 암시한다.

마지막 장에서는 [Fe II]-1.26 μm 과 1.64 μm 방출선의 밝기비를 이용하여 카시오페이아 A의 분출물 껍질방향으로의 소광 측정 결과를 보고한다. 방출선 덩어리들의 시선속도와 근적외선 소광($E(J-H)$)사이에 좋은 상관관계, 즉 적색편이 된 덩어리들이 청색편이 된 것들에 비해 좀더 높은 소광을 보이는 현상을 확인하였다. 이러한 내부적 "자체 소광''은 많은 양의 초신성 먼지가 초신성 분출물 껍질 주변에 존재하고 있음을 암시한다. 특히 남쪽 껍질 부근에서 0.23 ± 0.05 mag의 초신성 먼지에 의한 소광량을 측정하였다. 초신성

먼지의 분광 에너지 분포를 분석함으로써 해당 지역에는 따뜻한 ($\sim$ 100 K) 먼지와 차가운 ($\sim$ 40 K) 먼지가 존재하며, 이 중 차가운 먼지가 관측된 자체 소광의 원인이 됨을 확인하였다. 관측된 근적외선 소광량과 중/원적외선 연속선과의 비교를 통해 두 온도 성분의 먼지들에 대한 가능성 있는 먼지의 종류와 크기를 조사해보았다. 그 결과 따뜻한 먼지는 주로 $MgSiO_3$, Mg_2SiO_4, SiO_2와 같은 규소질이고, 차가운 먼지는 0.01 μm 보다 작은 철 내지는 0.1 μm 보다 큰 실리콘이라는 사실을 확인하였다. 카시오페이아 A에 있는 이러한 따뜻한 먼지와 차가운 먼지는 각각 밀도가 낮은 초신성 분출물과 밀도가 높은 분출물 덩어리에서 주로 생성되었을 것으로 생각된다.

주 요 어: 먼지, 소광 — 적외선: 성간 물질 — 성간 물질: 개별 천체 (카시오페이아 A, G11.2−0.3, KES 73, W44, W49B, 3C 396) — 성간 물질: 분자 — 성간 물질: 초신성 잔해 — 방출선: 식별 — 서베이

학 번: 2011-30129